



**Miguel Araújo Machado**

Mechanical Engineering Master

## **Development of Non-Destructive Testing by Eddy Currents for Highly Demanding Engineering Applications**

Thesis to obtain the PhD Degree in  
Mechanical Engineering

Supervisor: Telmo Jorge Gomes dos Santos  
Associate Professor  
Faculdade de Ciências e Tecnologia  
Universidade Nova de Lisboa

Co-supervisor: Pedro Miguel dos Santos Vilaça da Silva  
Associate Professor  
School of Engineering  
Aalto University

Chairperson: Doctor Jorge Joaquim Pamies Teixeira

Examiners: Doctor Helena Maria dos Santos Geirinhas Ramos  
Doctor Pedro Miguel Guimarães Pires Moreira

Members of the Committee: Doctor Jorge Joaquim Pamies Teixeira  
Doctor Altino de Jesus Roque Loureiro  
Doctor Telmo Jorge Gomes dos Santos  
Doctor Nuno Miguel Carvalho Pedrosa



**December 2018**



Development of Non-Destructive Testing by Eddy Currents for Highly Demanding Engineering Applications

Copyright © 2018 Miguel Araújo Machado

Faculdade de Ciências e Tecnologia, Universidade Nova de Lisboa

A Faculdade de Ciências e Tecnologia e a Universidade Nova de Lisboa têm o direito, perpétuo e sem limites geográficos, de arquivar e publicar esta dissertação através de exemplares impressos reproduzidos em papel ou de forma digital, ou por qualquer outro meio conhecido ou que venha a ser inventado, e de a divulgar através de repositórios científicos e de admitir a sua cópia e distribuição com objetivos educacionais ou de investigação, não comerciais, desde que seja dado crédito ao autor e editor.





# ACKNOWLEDGMENTS

To all of those who, directly or indirectly, contributed to the accomplishment of this work, my deepest thanks. In particular:

Prof. Telmo Santos, my research supervisor, for his guidance, fruitful discussions, support and advices throughout the work. It has been an honour to be his first PhD student. The joy and enthusiasm for his research was contagious and motivational for me. Prof. Pedro Vilaça, my co-supervisor, who generously received me in Aalto University, for his significant contributions and many valuable comments to my work during my stay. Prof. Rosa Miranda for her insightful comments, encouragement and valuable suggestions. Prof. Pamies Teixeira for sharing his knowledge and for the kind observations. Prof. Luís Rosado for the help in experimental tests and for letting me use his electronics. Prof. Helena Geirinhas Ramos, member of the Thesis Advisory Committee, for the support, availability and valuable comments. To Gonçalo Sorguer and Kim-Niklas Antin for the help, support and hospitality during my stay in Aalto University. To Mr. António Campos and Mr. Paulo Magalhães for the assistance provided during the realization of the work and for the teachings shared in particular in the machining operations. To my colleagues from NOVA NDT Lab., special thanks to Patrick Inácio (you are next) and Diogo Pereira, for sharing their ideas, experiences, opinions and difficulties with me. To my family, for the constant friendship and support, which in their own way also contributed decisively to the accomplishment of this work. To my parents for all the support and concern, and for challenging me to do more and better. To my wife Mariana for the love and friendship shown whenever given the opportunity providing me strength and motivation to face new challenges. To my baby daughter Matilde for making me finish my daily routine with a smile, due to her constant unbelievable good humour.

To the companies that came up with the challenges, provided samples and allowed the experimental validations in their industrial setting. Finally, to Fundação para a Ciência e a Tecnologia (FCT-MCTES) for its financial support via the PhD scholarship FCT-SFRH/BD/108168/2015.



# ABSTRACT

Defect detection with Non-Destructive Testing (NDT) is essential in accidents prevention, requiring R&TD to generate new scientific and procedural knowledge for new products with high safety requirements. A current challenge lies in the detection of surface and sub-surface micro defects with NDT by Eddy Currents (EC).

The main objective of this work was the development of applied research, technological innovation and experimental validation of EC customized systems for three highly demanding inspection scenarios: micro defects in tubular geometries; brazed joints for the automotive industry; and high-speed moving composite materials. This objective implied starting from the scientific fundamentals of NDT by EC to design and simulate EC probes and the prototypes developed were tested in industrial environment, reaching a TRL  $\approx$  5.

Another objective, of a more scientific and disruptive nature, was to test a new technique for the creation of EC in the materials to be inspect, named Magnetic Permeability Pattern Substrate (MPPS). This technique consists on the development of substrates/films with patterns of different magnetic permeabilities rather than the use of excitation bobbin coils or filaments of complex geometry.

The experimental results demonstrated that the prototypes developed for the three industrial applications studied outperformed the state of the art, allowing the detection of target defects with a very good signal-to-noise ratio: in tubular geometries defects with depth of 0.5 mm and thickness of 0.2 mm in any scanning position; in the laser brazed weld beads pores with 0.13 mm diameter and internal artificial defects 1 mm from the weld surface; in composite materials defects under 1 mm at speeds up to 4 m/s and 3 mm lift-off.

The numerical simulations assisted the probe design, allowing to describe and characterize electrical and magnetic phenomena. The new MPPS concept for the introduction of EC was validated numerically and experimentally.



# RESUMO

A deteção de defeitos com Ensaio Não Destrutivo (END) é fundamental na prevenção de acidentes, existindo a necessidade de I&DT para criar conhecimento científico e processual para novos produtos com elevados requisitos de segurança. Um desafio atual é detetar micro defeitos superficiais e sub-superficiais com END por Correntes Induzidas (CI).

O objetivo principal deste trabalho foi desenvolver investigação aplicada, inovação tecnológica e validação experimental de sistemas de CI customizados para três cenários de inspeção de elevada exigência: micro defeitos em geometrias tubulares, juntas brasadas para a indústria automóvel; e materiais compósitos a alta velocidade. Foram aplicados os fundamentos científicos dos END por CI para conceber e simular o funcionamento de sondas de CI, e os protótipos desenvolvidos foram testados em ambiente industrial, tendo-se atingido um TRL  $\approx$  5.

Outro objetivo, de carácter mais científico e disruptivo, foi testar uma nova técnica para a criação de CI nos materiais a inspecionar, batizada *Magnetic Permeability Pattern Substrate* (MPPS). Esta técnica consiste no desenvolvimento de substratos ou filmes com padrões de diferentes permeabilidades magnéticas, alternativos à utilização convencional de bobinas ou filamentos de excitação de geometria complexa.

Os resultados experimentais mostraram que os protótipos desenvolvidos para as três aplicações industriais superaram o estado da arte, permitindo a deteção dos defeitos alvo com boa relação sinal/ruído: nos tubos foram detetados defeitos com 0.5 mm profundidade e 0.2 mm de largura em qualquer orientação; nas juntas brasadas detetaram-se poros com 0.13 mm de diâmetro e defeitos artificiais internos a 1 mm da superfície; nos materiais compósitos identificaram-se defeitos inferiores a 1 mm à velocidade de 4 m/s com as sondas afastadas 3 mm da superfície.

As simulações numéricas auxiliaram a conceção das sondas, permitindo descrever e caracterizar alguns fenómenos elétricos e magnéticos do seu funcionamento. O novo conceito MPPS para a introdução de CI foi validado numérica e experimentalmente.



## **KEY-WORDS**

Non-Destructive Testing (NDT)

Eddy Currents (EC)

Probes

Defects

Carbon Fibre Reinforced Polymer (CFRP)

## **PALAVRAS-CHAVE**

Ensaio Não Destrutivo (END)

Correntes Induzidas (CI)

Sondas

Defeitos

Polímero Reforçado com Fibra de Carbono (PRFC)





# CONTENTS

ACKNOWLEDGMENTS .....	v
ABSTRACT .....	vii
RESUMO .....	ix
KEY-WORDS.....	xi
PALAVRAS-CHAVE .....	xi
CONTENTS .....	xiii
LIST OF FIGURES .....	xvii
LIST OF TABLES .....	xxv
LIST OF ABBREVIATIONS AND SYMBOLS.....	xxvii
Chapter 1      INTRODUCTION .....	1
1.1. – Motivation .....	1
1.2. – Scientific and technological objectives.....	2
1.3. – Work performed.....	3
1.4. – Results and conclusions.....	4
1.5. – Industrial impact and application of the work developed .....	6
1.6. – Document structure .....	7
Chapter 2      STATE OF THE ART.....	9
2.1. – Introduction.....	9
2.2. – Non-Destructive Testing.....	10
2.3. – Main NDT techniques and their fundamentals .....	10
2.4. – Eddy Currents Testing.....	13
2.4.1.– Operating modes .....	18
2.4.2.– Flat EC probes .....	20
2.4.3.– Eddy current array .....	21
2.4.4.– High speed eddy current testing.....	22
2.5. – Inspection of tubular geometries .....	23
2.6. – Inspection of bimetallic joints for automotive industry.....	24

2.7.	– NDT inspection of unidirectional carbon fibre reinforced polymer composites.....	28
2.8.	– Conventional EC generation mode.....	30
2.9.	– Summary.....	32
Chapter 3	CUSTOMIZED EC PROBES FOR CIRCULAR GEOMETRIES INSPECTIONS .....	35
3.1.	– Introduction.....	35
3.2.	– Motivation .....	36
3.3.	– Material and defects characterization .....	37
3.4.	– Probe design.....	38
3.4.1.	Excitation winding – Element 1 .....	38
3.4.2.	Pick-up coils array – Element 2.....	39
3.4.3.	Probe chassis – Element 3 .....	42
3.5.	– Experimental results and discussion .....	42
3.6.	– Summary.....	47
Chapter 4	NON-DESTRUCTIVE INSPECTION OF LASER BRAZED WELD BEADS.....	49
4.1.	– Introduction.....	49
4.2.	– Motivation .....	50
4.3.	– Geometrical and material characterization .....	52
4.4.	– Numerical simulations.....	55
4.5.	– Customized NDT system development .....	60
4.5.1.	– Functional prototype chassis .....	60
4.5.2.	– Eddy current probes .....	62
4.5.3.	– Four-point probe for potential drop measurement .....	64
4.5.4.	– Laboratorial set up.....	65
4.6.	– Experimental results and discussion .....	65
4.6.1.	– Industrial environment – Real defects.....	65
4.6.2.	– Laboratory conditions – Artificial defects.....	67
4.7.	– Summary.....	76
Chapter 5	CONTACTLESS HIGH-SPEED ECT OF CARBON FIBER REINFORCED POLYMER .	77
5.1.	– Introduction.....	77
5.2.	– Material characterization .....	78
5.3.	– Defects Characterization .....	81

5.4.	– Numerical simulation of Eddy Currents in CFRP.....	83
5.5.	– Functional prototype for low speed inspection .....	85
5.6.	– Functional prototype for high speed inspection .....	86
5.7.	– Probe design.....	90
5.8.	– Experimental results and discussion .....	98
5.8.1.	– Low speed experimental tests.....	98
5.8.2.	– High speed experimental tests .....	102
5.9.	– Summary.....	105
Chapter 6	MAGNETIC PERMEABILITY PATTERN SUBSTRATE .....	107
6.1.	– Introduction.....	107
6.2.	– Motivation .....	108
6.1.	– Theoretical concept.....	108
6.2.	– Numeric simulation of the MPPS .....	109
6.3.	– Experimental concept validation.....	112
6.3.1.	– Magnetic field measurement .....	112
6.3.2.	– Induction heating with thermography.....	114
6.4.	– Eddy current probe with the MPPS technology .....	118
6.5.	– Summary.....	120
Chapter 7	CONCLUSIONS AND FUTURE WORK.....	121
7.1.	– Introduction.....	121
7.2.	– Conclusions.....	122
7.3.	– Future work .....	124
7.4.	– Publications and Patents .....	125
REFERENCES	.....	127
APPENDIX	.....	145
Appendix 1	– CoDeSys routine .....	145
Appendix 2	– EC tailored probes prototypes for the CFRP inspection .....	146
Appendix 3	– EC tailored probes for the CFRP inspection numeric simulations .....	149



# LIST OF FIGURES

Figure 1.1 – Objectives layout.....	3
Figure 2.1 – Magnetic fields and eddy currents generated by an EC probe.....	13
Figure 2.2 – Eddy currents generated by an EC probe and its deflection by the crack. ....	14
Figure 2.3 – EC impedance plan. ....	15
Figure 2.4 – Deflection of the eddy currents by the imperfections.....	16
Figure 2.5 – Intensity and location of the EC generated by an EC probe (cut view).....	17
Figure 2.6 – Stainless steel penetration depth with different magnetic permeabilities. ....	17
Figure 2.7 – Distortion of eddy current flow at the edge of a part.....	18
Figure 2.8 – Schematic representation of an EC probe operating in: a) absolute mode; b) bridge differential mode. ....	19
Figure 2.9 – Schematic representation of an EC probe operating in: a) reflection mode; b) reflection differential mode.....	20
Figure 2.10 – Flexible eddy current array probe.....	22
Figure 2.11 – Side panel and roof connection solutions: roof drip moulding and laser brazing. .....	25
Figure 2.12 – Different types and varieties of geometrical seam imperfections.....	27
Figure 2.13 – Laser brazed joint in the automotive industry: a) joints cross section view of the laser brazed welds of roof/body side panel; b) a schematic illustrating the principle of laser brazing. ....	27
Figure 2.14 – Magnetic flux generated by a bobbin coil: a) without core nor shield; b) with a ferrite core; c) with a ferrite shield. ....	31
Figure 3.1 – ITER main components illustration. ....	36
Figure 3.2 – ITER tubular sample. a) profile view with dimensions in mm, b) isometric view. ..	36
Figure 3.3 – Schematic of the sensitive and excitation coils with axial zigzag (left side) and twisted zigzag (right side). The twisted excitation coil ensures that the defect will have EC passing through it at least once. ....	39
Figure 3.4 – Pick-up coils - Planar parallelogram spiral coils in flexible PCB.....	40
Figure 3.5 – Schematic of currents flow direction in circular spiral (left) and in parallelogram spiral coils (right). The proposed EC probe with parallelogram spiral coils avoids, with one array, the blind zones of the conventional probes. ....	40

Figure 3.6 – Circular spiral coils (left) vs rectangular spiral coils (middle) vs parallelogram spiral ones (right). An axial defect may not be detected by a conventional circular or rectangular spiral coil where both parallelogram spiral coils would. ....	41
Figure 3.7 – Probe designed in Altium Design software. ....	42
Figure 3.8 – Chassis examples; a) inner surface inspection probe; b) outer surface inspection probe; c) outer surface section inspection probe. ....	42
Figure 3.9 – Inner surface inspection probe for the inspection of the ITER sample. ....	43
Figure 3.10 – Output signal obtained with each probe when scanning defect #1 and #2 in the axial scanning position 1. ....	43
Figure 3.11 – Output signal obtained at 500 kHz of defect #2 in different axial scanning positions (1 to 5). ....	44
Figure 3.12 – EC probe and steel sample; a) inner perimeter inspection probe; b) tube cut view with defects represented. ....	44
Figure 3.13 – Output signal obtained at 500 kHz of the steel sample in the axial scanning position 1. ....	44
Figure 3.14 – Outer surface inspection probe; a) flat flexible pick-up coils inside the chassis; b) EC probe around the steel sample. ....	45
Figure 3.15 – ST 52 steel sample with the four artificial defects depicted. ....	45
Figure 3.16 – Output signal obtained at 500 kHz of the steel sample in the axial scanning position 1. ....	45
Figure 3.17 – Outer surface section inspection probe; a) probe over the sample; b) pick-up coils of the probe. ....	46
Figure 3.18 – Aluminium AA2024 120 mm diameter pipe with artificial produced defects. ....	46
Figure 3.19 – Output signal obtained at 500 kHz of the aluminium sample in the axial scanning position 1. ....	46
Figure 4.1 –Weld profile macro. ....	50
Figure 4.2 – Inspection methods envisaged. a) eddy currents testing b) potential drop measurement. ....	51
Figure 4.3 – Weld profile being digitalized to a CAD model. ....	52
Figure 4.4 – Weld profile uniformness along its length. a) profiles overlapped to access its uniformness along its length; b) Profile variation is not significant in the inspection zone. ....	53
Figure 4.5 – a) Weld profile macrograph with the different components; b) four-point probe used to measure the electrical conductivity. ....	53
Figure 4.6 – Set up for the resistance measurement of the filler wire. ....	54

Figure 4.7 – a) CAD model used in the numeric simulations; b) Mesh representation with the tetrahedral elements. ....	55
Figure 4.8 – Eddy current testing simulation with a 100-winding coil at a frequency of: a) 10 kHz; b) 3 MHz. ....	56
Figure 4.9 – Four-point probe simulation: a) pins positioning towards the profile; b) current flow through the weld.....	56
Figure 4.10 – Current flow behaviour in a weld with different defects.....	57
Figure 4.11 – Potential along the current flow direction with different defects.....	57
Figure 4.12 – Potential drop along the transversal line that contains all the pins. ....	58
Figure 4.13 – Potential distribution from the top with an increasing defect. ....	59
Figure 4.14 – Alternative pin distribution (cross shape). ....	59
Figure 4.15 – Potential distribution along the blue longitudinal line for different defects with increasing length L. ....	60
Figure 4.16 – Device chassis designed in the iterative process to reach the pretended solution.....	61
Figure 4.17 – Preliminary device chassis with bearing tin wheels on the right and bearing 3D printed on the left. ....	61
Figure 4.18 – Scanning device with step motors for movement. a) top view of the device over a weld specimen; b) bottom view;.....	62
Figure 4.19 – Final scanning device for robotic arm movement. a) front view of the device; b) back view; .....	62
Figure 4.20 – Probe design sequence. ....	63
Figure 4.21 –EC bobbin probe: a) final probe assembled over a conductivity standard for impedance characterization; b) probe geometric parameters.....	63
Figure 4.22 – Set of tailored EC probe holder.....	64
Figure 4.23 – Tailored EC probes. a) EC individual bobbin; b) device with a set of two bridge differential bobbins; c) device over the weld testing the spring that maintains the probe constant lift-off.....	64
Figure 4.24 – Four-point probe. ....	65
Figure 4.25 – Inspection set-up: a) equipment structure; b) voltage source and drivers for the step motors.....	65
Figure 4.26 – Relevant environment experimental result where a 0,23 mm diameter notch was detected with 250 kHz and with 750 kHz. ....	66
Figure 4.27 – Relevant environment experimental result where two notches were found with 250 kHz, 750 kHz and 1 MHz.....	66

Figure 4.28 – Relevant environment experimental result where a notch was detected with 250 kHz and 750 kHz. ....	67
Figure 4.29 – Relevant environment experimental result where three notches were found with 250 kHz and 750 kHz. ....	67
Figure 4.30 – Sample 2LH with enlarged defects 1 to 4.....	68
Figure 4.31 – Sample 2LH with enlarged defects 5 to 8.....	68
Figure 4.32 – EC probe output signal of sample 2LH at a frequency of 250 kHz. ....	69
Figure 4.33 – EC probe output signal of sample 2LH at a frequency of 750 kHz. ....	69
Figure 4.34 – EC probe output signal of sample 2LH at a frequency of 1 MHz.....	69
Figure 4.35 – Four-point probe output signal of sample 2LH. ....	70
Figure 4.36 – Sample 3LH with enlarged defects 1 to 4.....	70
Figure 4.37 – Sample 3LH with enlarged defects 5 to 8.....	71
Figure 4.38 – EC probe output signal of sample 3LH at a frequency of 750 kHz. ....	71
Figure 4.39 – Sample 4LH with enlarged defects 1 to 7.....	72
Figure 4.40 – EC probe output signal of sample 4LH at a frequency of 250 kHz. ....	72
Figure 4.41 – EC probe output signal of sample 4LH at a frequency of 750 kHz. ....	73
Figure 4.42 – EC probe output signal of sample 4LH at a frequency of 1 MHz.....	73
Figure 4.43 – Test piece with 1 surface and 2 sub-surface defects and respective output signals at high and low frequency.....	74
Figure 4.44 – Test piece with one surface and one sub-surface defect and respective output signal at high and low frequency. ....	74
Figure 4.45 – Prototype developed for the inspection of 3 m long samples at higher speeds. .	75
Figure 4.46 – EC probe output signal of sample 3LH at a higher speed. ....	75
Figure 5.1 – 3D perspective of the carbon fibre tension member system with four parallel CFRP elements, protected by a polymer coating. ....	78
Figure 5.2 – Dimensions of the cross-section of the individual CFRP elements (in millimetres). ....	78
Figure 5.3 – Cross-section of the tension member evidencing the four CFRP elements with 5 × 2.5 mm cross section and the polyurethane coating with about 1 mm thickness. ....	78
Figure 5.4 – Directions used to measure the electrical conductivity of the CFRP element.....	79
Figure 5.5 – Micrographs showing the contact between individual carbon fibres: a) Transversal view; b) Longitudinal view .....	80
Figure 5.6 – X-ray microtomography 50 µm apart showing the fibre waviness and contact: a) transversal section (Z = 0); b) transversal section (Z = 50 µm) .....	80
Figure 5.7 – Tested CFRP samples with the location of the defects. ....	83



Figure 5.8 – Geometrical model used in the simulation of the eddy current induced by the excitation filament of the EC probe: a) geometric model; b) mesh representation.....	84
Figure 5.9 – Field of eddy current density on an isotropic material (Aluminium) with different excitation orientations: a) excitation with 90°; b) excitation with 45°; c) excitation with 0°. ...	84
Figure 5.10 – Field of eddy current density on an CFRP anisotropic material (carbon fibre) with different excitation orientations: a) excitation with 90°; b) excitation with 85°; c) excitation with 45°; d) excitation with 0°.....	85
Figure 5.11 – Inspection prototype CAD design.....	85
Figure 5.12 – Low speed inspection prototype. a) inspection with the prototype at the vertical position; b) inspection with the prototype at the horizontal position. ....	86
Figure 5.13 – Lift-off regulation by screw. ....	86
Figure 5.14 – Equipment acquired for the high speed movement; a) Slider bearing rodless linear actuator - LCB060; b) SMH100 brushless motor; c) Compax3 Single Axis Drive. ....	87
Figure 5.15 – Aluminium frame with all the devices required for the actuator operation. ....	87
Figure 5.16 – Schematic design of the high-speed inspection prototype (not to scale), a) before the inspection; b) after the inspection.....	88
Figure 5.17 – Set up for the high-speed inspection with the linear guide and the CFRP guiding structure.....	88
Figure 5.18 – Hand held device used in the high-speed tests.....	89
Figure 5.19 – The EC probe can be adjusted with relative precision to the CFRP elements. ....	89
Figure 5.20 – Inspection device holder and test reference. ....	89
Figure 5.21 – PCB EC probes designed and manufactured for testing with correspondent secondary magnetic field: a) Circular spiral coil probe with transversal excitation – PCB Probe #1; b) Circular spiral coil probe with curved excitations – PCB Probe #2; c) Rectangular spiral coil probe with parallel excitation – PCB Probe #3; d) 45° parallelogram spiral coil probe with transverse excitation – PCB Probe #4.....	92
Figure 5.22 – Vectorial field of the EC in the CFRP element when excited with a parallelogram probe when operating in bridge differential mode. ....	93
Figure 5.23 – PCB probe #3 variant with winded excitation coil. ....	94
Figure 5.24 – Schematic representation of the model used for the probe simulation: a) Isometric view of the element with the two coils; b) Top view of the coils and its dimensions. ....	94
Figure 5.25 – Mesh representation with about 2.7 million tetrahedral elements: a) With a top cross cut defect; b) With a lateral cut defect. ....	95

Figure 5.26 – Field of EC density on the top of the element with the lateral cut defect in three distinct positions. ....	96
Figure 5.27 – Numerical simulated output signal of the parallelogram bridge differential probe of a top cross and lateral cut defect scanning. ....	96
Figure 5.28 – PCB probes assembled in the 3D printed chassis. ....	97
Figure 5.29 – Array versions of the PCB Probe #4 with 45° parallelogram spiral coil overlapped with the four CFRP elements: a) Version with four individual coils; b) Version with two individual coils. ....	97
Figure 5.30 – PCB probes assembled in the 3D printed chassis. ....	97
Figure 5.31 – Total of EC tailored probes produced and experimentally tested. ....	98
Figure 5.32 – EC probes lift-off: a) EC probe #5; b) EC probe #6b. ....	98
Figure 5.33 – Output signal of EC probe #5 inspecting a saw cut sample at 4 MHz, assessed from the defective side. ....	99
Figure 5.34 – Output signal of EC probe #5 inspecting an impact damage sample at 4 MHz, assessed from the defective side. ....	99
Figure 5.35 – Output signal of EC probe #6b inspecting a saw cut sample at 4 MHz. ....	99
Figure 5.36 – Output signal of EC probe #6b inspecting an impact damage sample at 4 MHz. ....	100
Figure 5.37 – Output signal of tailored EC Probes inspecting the Sample 1 at low speed at 8 MHz, except PCB Probe #4 in bridge mode at 6 MHz. ....	101
Figure 5.38 – Output signal of EC PCB Probe #4 inspecting the Sample 1 at 8 MHz at low speed comparing to the Ionic Probe at 8 MHz and commercially EC absolute pencil probe with 3 mm diameter with a fixed air loaded reference coil in bridge mode at 6 MHz. ....	102
Figure 5.39 – Output signal of EC PCB Probe #4 operating in bridge differential mode inspecting Sample 2 at 6 MHz at 3.5 m/s. ....	102
Figure 5.40 – Comparison between experimental results and numerical simulation by Finite Element Method (FEM) testing the lateral cut defect LC05 at 6 MHz and 3.5 m/s. ....	103
Figure 5.41 – Comparison between experimental results and numerical simulation by Finite Element Method (FEM) testing the cross top cut defect 3PTB at 6 MHz and 3.5 m/s. ....	103
Figure 5.42 – Output signal of EC PCB Probe #4 (Figure 5.29 – b) operating in bridge differential mode inspecting Sample 2 at 6 MHz at 3.5 m/s. ....	104
Figure 5.43 – Output signal of EC PCB Probe #4 operating in reflection mode inspecting Sample 2 at 3 MHz at 2 m/s. ....	104
Figure 5.44 – Output signal of EC commercial probe inspecting Sample 2 at 6 MHz at 2 m/s. ....	104
Figure 5.45 – Output signal of EC PCB Probe #4 inspecting Sample 3 at 6 MHz at 4 m/s. ....	105
Figure 5.46 – Output signal of EC PCB Probe #4 inspecting Sample 4 at 6 MHz at 4 m/s. ....	105

Figure 5.47 – Output signal of EC PCB Probe #4 inspecting Sample 4 at 6 MHz at 4 m/s zoomed in on the lateral cut defect.....	105
Figure 6.1 – Model used for the simulation of a zigzag pattern substrate.....	109
Figure 6.2 – Simulation results using a zigzag pattern on an aluminium specimen; a) eddy currents vector field; b) eddy currents density intensity.....	109
Figure 6.3 – Model of the simulation using a circular coil and a cross shaped pattern.....	110
Figure 6.4 – Simulation results using a circular coil and a cross shaped pattern; a) eddy currents vector field; b) eddy currents density intensity.....	110
Figure 6.5 – Model of the simulation using a linear excitation and a ring-shaped pattern.....	110
Figure 6.6 – Simulation results using a linear excitation and a ring-shaped pattern; a) eddy currents vector field; b) eddy currents density intensity.....	111
Figure 6.7 – Model of the simulation; a) using a linear excitation and several substrate rectangles creating a zigzag EC pattern; b) using a linear excitation and three substrate rectangles with different orientations.....	111
Figure 6.8 – Simulation results using a linear excitation and several substrate rectangles creating a zigzag EC pattern; a) eddy currents vector field; b) eddy currents density intensity.....	111
Figure 6.9 – Simulation results using a linear excitation and three substrate rectangles with different orientations; a) eddy currents vector field; b) eddy currents density intensity.....	112
Figure 6.10 – Neodymium permanent magnet: a) image; b) magnetic poles and dimensions, c) Hall sensor Honeywell SS496A1.....	112
Figure 6.11 – Magnetic field measured with a Hall sensor at 64 mm with 1 mm resolution...	113
Figure 6.12 – 3D printed magnetic iron PLA filter with zigzag pattern.....	113
Figure 6.13 – Validation of the MPPS as a magnetic filter; a) set up used; b) magnetic field measured by the Hall sensor.....	114
Figure 6.14 – Induction heating for thermography: a) setup used for the validation; b) ferrite sheet used as MPPS.....	114
Figure 6.15 – Test performed without MPPS: a) induction coil; b) thermography image of the heat produced by the eddy currents.....	115
Figure 6.16 – Components required for the EC probe assembly as presented in §3.4: 3D printed chassis; complex twisted excitation coil; sensitive coils array.....	118
Figure 6.17 – Components required for the MPPS EC probe assembly: 3D printed chassis; simple circular winding; MPPS; sensitive coils array.....	118
Figure 6.18 – Eddy current probe for inner diameter tube inspection with the MPPS technology assembly sequence.....	119

Figure 6.19 – Simulation using a linear excitation and pattern simulating the twisted excitation; a) model of the simulation; b) simulation result of the eddy currents density intensity..... 119

## LIST OF TABLES

Table 2.1 – Different NDT technique and their applicability to the inspection. ....	28
Table 3.1 – Artificial defects in the ITER sample. ....	37
Table 3.2 – ST 52 steel sample defects dimensions. ....	45
Table 3.3 – Aluminium AA2024 artificial produced defects dimensions. ....	46
Table 4.1 – Resistivity and conductivity measured with four-point probe. ....	53
Table 4.2 – Voltage and resistance measured with different currents. ....	54
Table 4.3 – Penetration depth for different frequencies. ....	55
Table 5.1 – Electrical resistivity and conductivity of the CFRP sample for XYZ directions. ....	80
Table 5.2 – Machined and real defects in the four CFRP samples. ....	82
Table 5.3 – First EC tailored probes prototypes. ....	91
Table 6.1 – Schematic representation of the MPPS geometry and its respective thermography. ....	116
Table 6.2 – Schematic representation of the MPPS geometry and its respective thermography. ....	117
Table A1 – First EC tailored probes prototypes. ....	146



# LIST OF ABBREVIATIONS AND SYMBOLS

$\vec{Z}$	Electric impedance vector [ $\Omega$ ]
$f$	Frequency [Hz]
$\text{Im}(\vec{Z})$	Electric impedance vector – Imaginary part [ $\Omega$ ]
$\text{Re}(\vec{Z})$	Electric impedance vector – Real part [ $\Omega$ ]
$X, x$	Length [m]
$\varnothing$	Diameter [m]
$\delta$	Eddy currents penetration depth [m]
$\sigma$	Electric conductivity [ $\text{S}\cdot\text{m}^{-1}$ ] or [% IACS]
DAQ	Data acquisition
DEMI	Departamento de Engenharia Mecânica e Industrial
EC	Eddy Currents
FCT	Faculdade de Ciências e Tecnologia
FIT	Finite Integration Technique
GUI	Graphical User Interface
$H_p$	Magnetic field
$H_s$	Secondary magnetic field
IACS	International Annealed Copper Standard
ISQ	Instituto de Soldadura e Qualidade
NDT	Non-Destructive Testing
NI	National Instruments™
NTI	Núcleo de Tecnologia Industrial
PMMA	Methyl Polymethacrylate
RFT	Remote Field Testing
UNL	Universidade Nova de Lisboa
UT	Ultrasonic Testing
MPPS	Magnetic Permeability Pattern Substrate
FDM	Fused Deposition Modelling
CFRP	Carbon Fibre Reinforced Polymer
ITER	International Thermonuclear Experimental Reactor
TRL	Technology Readiness Level
PCB	Print Circuit Board





# CHAPTER 1

## INTRODUCTION

### 1.1. – Motivation

Non-destructive testing (NDT) consists in the application of a vast group of inspection methodologies and techniques to evaluate and/or monitor the condition of materials, components or equipment, without any material properties or functional performance modified [1]. This is determinant in components maintenance and reliability, preventing accidents, deaths, and economic and environmental damage [2].

However, technological research and development (TR&D) is required to create scientific know-how in this area, due to the crescent use of products with new materials and manufacture technologies with high safety requirements.

Detection of surface and sub-surface micro defects with NDT, such as Eddy Currents (EC), is a big challenge. The actual main problems are: i) minimum defect size detected not sufficient due to noise generated by the probe vibration (lift-off) that can mask the defect signal; ii) the difficulty in generating EC tailor-made patterns in the materials to inspect and iii) probe complexity with many assembled elements in one configuration.

## 1.2. – Scientific and technological objectives

Three main objectives were defined in this work, comprising both technological and scientific nature, according to Figure 1.1.

The central objective was the development of applied research, innovation, numerical simulation and knowledge generation for the development of customized Non-Destructive Testing (NDT) systems based on Eddy Currents (EC).

A second objective consisted on technological innovation, in order to produce and experimentally validate customized eddy current systems for three highly demanding engineering applications, namely the inspection of: i) micro defects in tubular geometries; ii) brazed joints for the automotive industry and iii) unidirectional composite materials at high-speed. This objective implied starting from the scientific fundamentals of NDT by EC, to analyse and characterize materials, to design and numerically simulate the EC probes, and to test the prototypes in relevant industrial environment, reaching a Technological Readiness Level (TRL)  $\approx$  5/6.

The third objective, of a more scientific and disruptive nature, was to test a new technique for the creation of EC in the materials to be inspected, an alternative to the conventional use of bobbin coils. This technique, baptized *Magnetic Permeability Pattern Substrate (MPPS)*, consists on the development of substrates/films with patterns of different magnetic permeabilities rather than the use of excitation bobbin coils or filaments of complex geometry.

These three objectives represent a huge technological potential, which will be duly exploited. Simultaneously, some of them present scientific challenges, requiring new procedural knowledge and more fundamental research, since they involve concepts, theoretical fundamentals, materials, manufacturing processes and geometries never before investigated in NDT, from a systematic point of view.

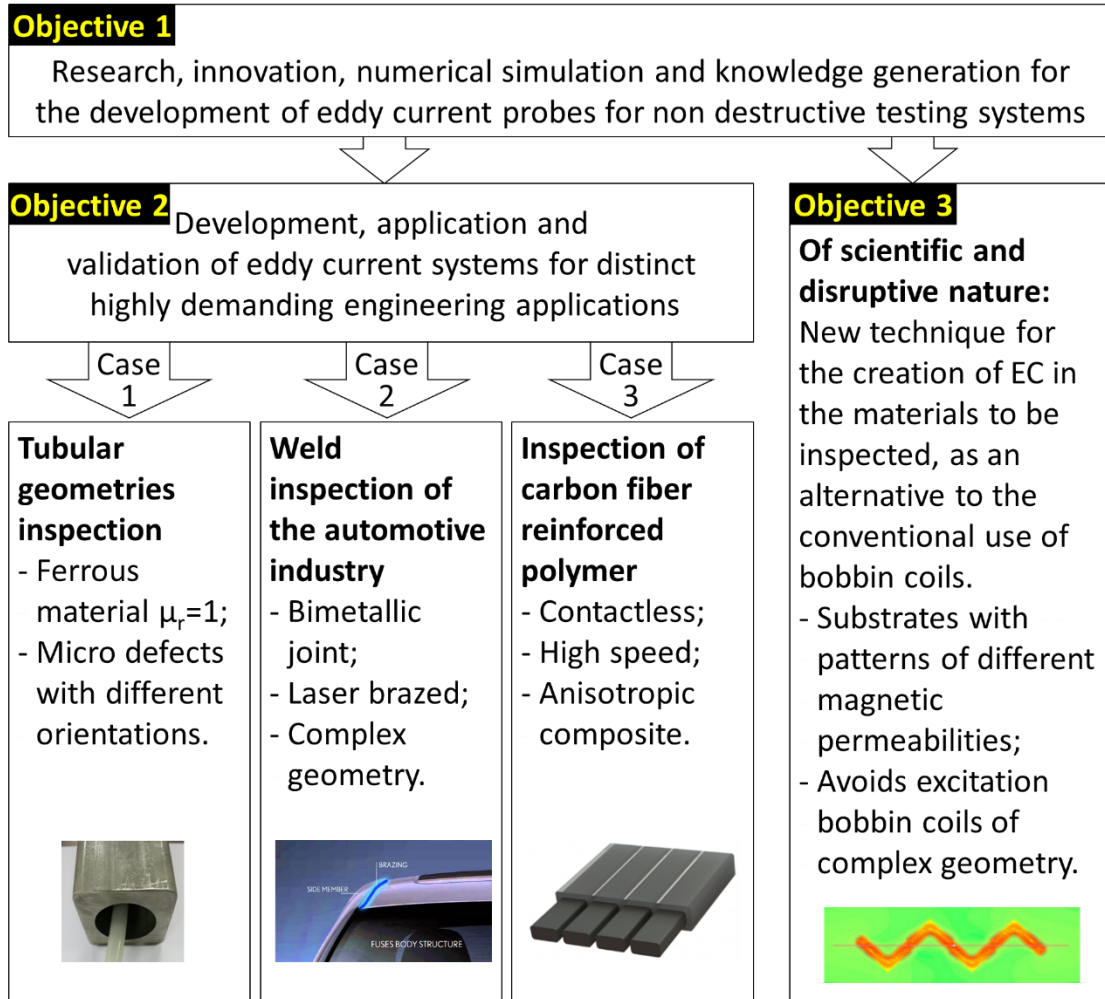


Figure 1.1 – Objectives layout.

### 1.3. – Work performed

The present work started by performing a bibliographic review in the area of NDT and in particular, electric and magnetic methods. Different types of EC probes and operating modes were studied, and a simplification of the probe manufacturing process was seen to be needed.

Three case studies were presented in which real inspections needs were required. The first case was a particularly demanding and complex inspection of the inner surface of a tubular component in austenitic stainless steel from the International Thermonuclear Experimental Reactor (ITER). The major difficulties relied on the defect positioning and size as well as on the material. A customized Eddy Currents (EC) probe was designed for the inspection of the inner perimeter of this tubular geometry. The experimental results were successfully validated, and the probe concept was applied to other materials and geometries.

The second case study required a non-destructive testing solution for a laser brazed weld bead inspection for automotive industry. A concept solution was designed, and numerical simulations were performed to validate its feasibility. An inspection prototype using both eddy currents and potential drop measurement techniques in the same customized chassis was designed, produced and validated. Specimens were inspected with real and artificially made defects. The experimental validation was successfully performed in both laboratorial conditions and industrial conditions.

The third case study involved an NDT need for a unidirectional Carbon Fibre Reinforced Polymer (CFRP) tension members inspection with a few particularities. Various NDT methods were considered in §2.7 but the need for the inspection to be contactless and at high speed made eddy currents the only feasible technique. The CFRP tension members were characterized and several artificially made defects were produced. Numerical simulation was performed in order to assist the probe design. Several EC probes, with 3D printed chassis and wound coils, were designed, produced and benchmarked. With that knowledge Print Circuit Board (PCB) probes were designed for the final implementation. A low speed prototype was designed and produced for the probes benchmarking as well as a high-speed prototype for laboratorial tests with speeds closer to the final application. Industrial environment experimental tests were also performed successfully.

An alternative method of applying eddy currents with different orientations rather than the exciting coil was studied. It consists on the application of a magnetic permeability subtract between the test piece and the excitation coil which was denominated Magnetic Permeability Pattern Substrate (MPPS). Numerical simulation was performed in order to prove that the EC are influenced by the MPPS and change their orientation accordingly. Experimental validation with thermographic tests and magnetic field measurements was performed successfully. Since the EC in the test piece does not need to follow the excitation coil orientation anymore, this technology allows the simplification of EC probes. A probe concept for inner circular geometries inspection was created and successfully simulated numerically.

#### **1.4. – Results and conclusions**

A customized eddy current probe for the inspection of tubular geometrics inner perimeter was designed, produced and validated experimentally and evidenced a superior reliability when compared to a commercial probe used in these applications, since it was able to detect all defects, at a depth of 0.5 mm, 0.2 mm width and 2 mm length in any scanning position. The

twisted excitation windings and trapezoidal sensing coils evidenced a superior reliability, since the EC are generated in the orientation that maximizes the EC perturbation by the defects and the flexible substrate allows a closer proximity to the tube surface, thus increasing the coil sensitivity. 3D printing proved to be a very good alternative in the production of the chassis as it allows a faster, cheaper and easily customizable solution.

A prototype created for the inspection of the laser brazed weld beads was successfully validated. The prototype holds two sets of EC probes, one designed for low frequencies and the other for high frequencies that aim the detection of sub-surface and surface defects, respectively. Each probe was comprised of two bobbin probes operating in bridge mode, one bobbin was over the weld being inspected while the other was over a reference (good weld). That distinction was possible with the two set of probes since the low frequency (20 kHz) EC probe was able to detect both surface and sub-surface cracks and porosities and the high frequency (3 MHz) probe detected the surface ones only, as intended. For the lack of bonding, the potential drop measurement technique was used, with a customized four-point probe, which was also part of the prototype. The conventional linear pins position was numerically simulated and was considered unfit for this specific application. Different pins positions were simulated and a new disposition for the pins that made the inspection possible was found, in a cross shape. However, the aimed defects were quite hard to recreate artificially.

A prototype for high-speed inspection of CFRP tension members was designed, manufactured and experimentally validated. The prototype contains four-in-one EC probes for each element. Several tailored planar EC probes were designed, manufactured and experimentally validated. These probes demonstrated superior performance when compared to commercial pencil probes or conventional circular spiral absolute probes. The parallelogram shaped coils probe was selected since, demonstrated a very good performance especially when operating in bridge differential mode with speeds up to 4 m/s being the fibre breaks the defects to obtain the best signal to noise ratio even though the use of very high lift-offs ( $\approx 3$  mm). Using the PCB technology to produce the probes enabled a faster and consistent reproducibility and parametrization for different specimen dimensions. Numerical simulations allowed better understanding of the EC behaviour in the CFRP component and thus were an essential tool in assisting the probe design. The experimental results were consistent with the numerical simulations performed.

The MPPS technology is still at an early stage and there is still some work ahead. Despite, the concept has been validated both by simulation and experimentally. The numerical

simulations have demonstrated that the eddy currents acquired the shape of the MPPS pattern. Two different validation techniques were used. The technique with a permanent magnet and magnetic fields measurement with a Hall sensor allowed the visualization of the pattern designed in a 3D printed filter. It is possible to conclude that the MPPS does indeed change the magnetic field and that the eddy currents created by it do change accordingly. With the thermography technique, it was possible to visualize the heat produced by the eddy currents and the different patterns when applying different MPPS. A probe concept, for tubular geometries, was designed with this technology which allows a faster and simplified probe assembly which was numerically simulated.

### **1.5. – Industrial impact and application of the work developed**

The use of NDT inspection methods is increasing in several kinds of industries from the automotive industry to the oil and gas. And, the benefits of non-destructive testing have increased over time as well. From the point of view of safety, reliability and affordability. NDT can be conducted to determine if a component or system is compromised or in need of repair, if properly implemented and acted upon, accidents can be prevented, hence the safety as mentioned. NDT can provide reliability since there are a range of available methods and techniques that complement each other eliminating the risk of overlooking or inaccuracy. Finally, affordability since NDT can not only anticipate the replacement or repair of equipment before malfunction can occur but, might avoid destructive testing which is typically expensive and does not guarantee the correct functioning of the rest of the lot. Given the benefits it is understandable the demand for NDT solutions. However, although standard solutions are available from several suppliers, for specific applications often a customized solution is required. That is where these case studies presented in this thesis come into play. All three case studies came from real inspection needs from international companies and an entirely customized solution was created for each necessity. All the prototypes created were successfully validated on samples provided by the industry in need and in two of them the prototypes were successfully validated in relevant environment reaching a TRL  $\approx$  5/6.

## 1.6. – Document structure

This thesis is structured in seven chapters.

Chapter 2 presents the bibliographic review made, where the main topics involved in this thesis are described, in particular Non-Destructive Testing (NDT) by eddy currents. The bibliographic review starts with an approach to NDT in general and in §2.4 the EC method in particular. In the EC review, the different operating modes (§2.4.1) are described as are the different types of probe sensors geometries (§2.4.2) and high-speed inspections are also covered (§2.4.4). Applications of NDT in tubular geometries (§2.5), bimetallic joint in the automotive industry (§2.6) and CFRP tension members (§2.7) are also discussed.

Chapter 3 presents the first case study: customized eddy current probes for circular geometries inspections. The problem and objectives are addressed, followed by the probe design in §3.4. The three key features of the probe are explained, and the target defects are characterized in §3.3. The experimental results are shown in §3.5 validating the probe concept.

Chapter 4 presents the second case study of this thesis: the non- invasive inspection of laser brazed weld beads. The problem and objectives are addressed followed by a material and geometrical characterization in §4.3. A solution is presented supported by numerical simulations of both EC and potential drop measurements in §4.4. The functional prototype is described as are the probes designed and manufactured and the laboratorial set up is described in §4.5. Finally, the experimental results are shown both in laboratorial condition and in relevant environment in §4.6.1 and §4.6.2.

Chapter 5 presents the third case study: contactless high-speed EC testing of a carbon fibre reinforced polymer. A material characterization is performed, and several artificial defects made are presented in §5.2 and §5.3. Numerical simulation was made to assist the probes design §5.4. Two functional prototypes, in which the tests were made, are described and depicted, a low speed and a high-speed prototype §5.5 and §5.6. Finally, the experimental results are shown in §5.8 and §5.8.2.

Chapter 6 presents a new method to induce eddy currents in a specimen reducing the EC probes complexity. Numerical simulations were performed to access its viability (§6.2) and experimental validation was done using a permanent magnets (§6.3.1) and induction heating thermography (§6.3.2). A new probe concept using this technology is also presented (§6.4).

Chapter 7 summarizes the research conclusions and future work proposals are discussed.





## **CHAPTER 2**

### **STATE OF THE ART**

#### **2.1. – Introduction**

This chapter presents the literature review where the Non-Destructive Testing (NDT) by electric and magnetic methods are characterized, particularly, NDT by eddy currents (EC). The bibliographic review starts with an approach to NDT in general (§2.2) and the EC method in particular (§2.4). In the EC review the different operating modes (§2.4.1) are described as are the different types of probe sensors geometries (§2.4.2) and high-speed inspections are also covered (§2.4.4). Applications of NDT in tubular geometries (§2.5), bimetallic joint in the automotive industry (§2.6) and CFRP tension members (§2.7) are also discussed.

## **2.2. – Non-Destructive Testing**

Non-Destructive testing (NDT) is a term used for the examination of materials and components in such a way that allows materials to be examined without changing or destroying their usefulness. NDT plays a crucial role in everyday life and is necessary to assure safety and reliability. Typical examples are found in aircrafts, motor vehicles, pipelines, bridges, trains, power stations, refineries and oil platforms, which are all, inspected using NDT [3].

Currently, NDT techniques are industrial relevant since, they allow the materials and equipment condition monitoring, which can be done in finished and unfinish components [4]. The correct inspection method can provide information as the degradation state of a component, indicating eventual defects it may have, as well as their location and dimensions [5].

NDT is widely used in the industry for being economic, time consumption wise, and for not compromising the future use of the inspected components.

The main applications are:

- Inspection of the base material before processing – defect detection of material inherent imperfections;
- Product inspection in production – process quality control;
- Inspection of finished products – quality control of finished products – Defect detection of imperfections originated in the production process;
- Inspection of components in service – equipment monitoring – defect detection of imperfections originated in service;
- Material properties and metrology characterization – measurement of electrical conductivity, sound speed, coatings and paint thickness, structural variations and microstructures characterization.

## **2.3. – Main NDT techniques and their fundamentals**

There is a wide NDT techniques variety [6–8], which are variants of the six main NDT methods [9], that are: i) visual inspection; ii) liquid penetrant; iii) magnetic particle; iv) radiological; v) electromagnetic testing (ET) (including EC) and vi) ultrasonic (UT).

NDT usually involves the following steps: i) application of the test medium on the specimen (source of energy or other); ii) modification of the test medium by the defects, or material

properties; iii) detection and conversion of this change through a suitable sensor; iv) interpretation of the information obtained.

Visual inspection is one of the most used NDT methods for the detection of discontinuities. The inspection process may be done using such behaviours as looking, listening, feeling, smelling, shaking, and twisting. It includes a cognitive component wherein observations are correlated with knowledge of structure and with descriptions and diagrams from service literature [10]. It can alternatively, be carried out with devices like mirrors, magnifying glasses, microscopes, borescopes, fiberscopes, digital video borescopes, computer enhanced systems, camera systems and robotic crawler systems. Endoscopy is based on the use of an optical instrument (endoscope) to inspect component interiors intrusively, in the search for cracks [11,12].

Dye penetrant inspection (DPI) uses a dye which is applied over the surface to inspect and penetrates in the material discontinuities by capillarity [9]. The excess dye is then removed and afterwards, a nonaqueous wet developer is applied to increase the visibility of the dye left in the discontinuities. A new technique very similar to dye penetrants is being developed where bacterial cells are used instead of dye penetrant [13–20]. A suspension with bacterial cells stained with fluorescent dye is applied on the sample surface. After the deposition of the bacterial suspension, the excess liquid is mechanically removed, similarly as in the dye penetrant technique. The only bacterial cells left are in the discontinuities which are fed and grow until they are observable with UV light.

Magnetic particles inspection consists in the analysis of the magnetic particles disposition near surface discontinuities. These particles are concentrated there due to the magnetic poles resulting from the leakage fields caused by the distortion of magnetic field lines [21,22].

Radiology methods have as variants: the X-ray [23–25] and gamma ray radiography [26–28]; digital radiography [29,30], neutron imaging [31–33] and X-ray computed tomography (CT) [34–38].

The main electromagnetic testing techniques are: sinusoidal alternated current conventional EC [9,21,39,40], pulsed EC [41], EC measured by GMR [42,43] and SQUID [44], remote field testing (RFT) [45,46], magnetic flux leakage (MFL) [47–49], alternating current field measurement (ACFM) [50,51], alternating current potential drop (ACPD) [52–54] and EC probes with particular specificities like MWM [55]. Conventional EC method measures the electric impedance variation at the coil terminals when subjected to an alternated electric current, at frequencies normally between 1 kHz and 12 MHz. Pulsed EC variant consists in exciting the

probe with square waves, to increase the penetration depth of the EC in the material. GMR and SQUID EC probes differ from the conventional for the reception signal measured by magnetic resistances and magnetometers, respectively. The excitation and the reception are done by distinct elements. Both the ACPD and the ACFM techniques are particularly suited for measurement of the size of surface cracks and the ACFM technique can also be used for detection [56,57].

UT methods contain: conventional pulse echo UT [58], creeping UT [59], phased array ultrasonic (PAUT) [60,61], time of flight diffraction ultrasonic (TOFD) [62], guided ultrasonic waves [63–65] and air coupled UT [66,67]. UT methods are based in the transmission of high frequency sound waves in the specimen [68]. Conventional pulse echo analyses the ultrasonic waves reflections to detect and localize the material discontinuities. The ultrasonic wave is generated by piezoelectric effect inside the probe, penetrating and propagating through the material. Reflected echoes due to discontinuities reach back the probe, and by inverse piezoelectricity effect generates a signal proportional to the discontinuity dimension, and with a delay proportional to the distance between the discontinuity and the material surface. Phased array comprises a matrix of piezoelectric crystal UT probes, which are excited with different temporal delays between them, allowing the generation of front waves with different shapes and directions. TOFD variant analyses the time frame diffracted signals from the defect's extremities take to go from the emitting to the receiving probe. Instead of measuring response high amplitude of the reflected energy, as in conventional UT, TOFD measures the time of low amplitude waves created by the diffraction in the defect's extremities.

Other less often used methods or employed in a smaller scale: holographic interferometry [69,70], and thermography [71–75]. An infrared thermographic scanning system can measure, and view temperature patterns based upon temperature differences. Infrared thermographic testing may be performed during day or night, depending on environmental conditions and the desired results [76].

There are also some hybrid NDT variants, grounded on more than one physic phenomena, as laser ultrasonic (LUT) [77,78], Electromagnetic acoustic transducer (EMAT) [79,80], thermosonics [81,82] and Acoustic Emission Testing (AET) [83,84]. LUT uses the ultrasonic waves created from the surface thermic expansion of the material when hit by a high frequency pulse laser beam.

The crescent use of new materials and manufacturing processes in high safety requirements products requires a superior NDT reliability. Examples of these applications are: composite

aircraft fuselage, dissimilar and multi-material joints [85,86], high temperature inspection [87–90], railways high speed monitoring, in-line inspection of additive manufacturing products [91–93].

These recent developments have not been accompanied by the consistent development of NDT techniques, since these were developed in a different inspection paradigm. Thus, it is urgent new scientific knowledge and new NDT technologies development for these emerging applications.

Critic imperfections detection is confined to the material's surface, due to fatigue [94], stress conditions and more severe conditions [95,96]. For these cases, EC systems have to be developed focussing on the customization for each specific application in order to maximize the potential of EC in defect detection and condition monitoring.

#### 2.4. – Eddy Currents Testing

Eddy Currents testing has been widely applied in the inspection and characterization of metallic parts. The method allows measuring properties such as conductivity and thickness and is particularly suited for the detection of imperfections located at the part surface [97,98].

The Faraday Induction Law and the electric impedance variation of the bobbin coil establish the fundamentals of the NDT method by EC [99]. Typically, the generation of eddy currents is attained when a non-constant electric current is imposed to a coil, e.g. helicoidal spiral coil, thus creating a non-constant magnetic field ( $H_p$ ) as shown in Figure 2.1 case (a). When the coil is placed over a conductive test part, electrical currents are created in the part, known as eddy currents, as shown in Figure 2.1 case (b).

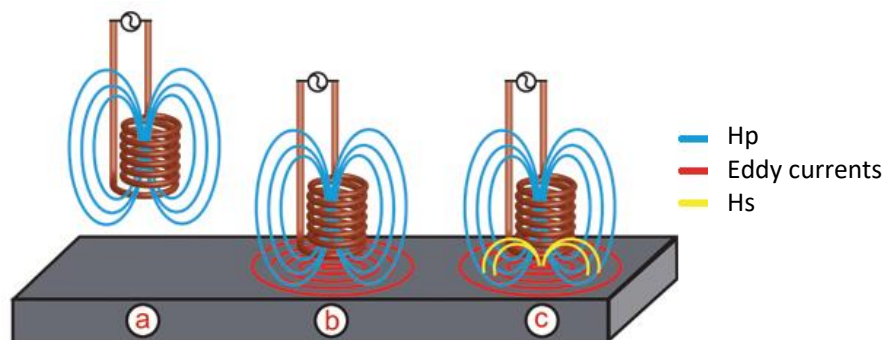


Figure 2.1 – Magnetic fields and eddy currents generated by an EC probe [100].

On the other hand, the eddy currents in the test part create a secondary magnetic field,  $H_s$ , which opposes the primary field  $H_p$  and induces a current in the coil. The reduction of the primary  $H_p$  field causes an increase in resistance and a change in inductance.

The opposition that a circuit presents to an alternating current when a voltage is applied is measured by the Electrical Impedance ( $Z$ ). Impedance, measured in ohm defined by Eq. 2.1, where the real part is the resistance ( $R$ ) and the imaginary part the reactance ( $X$ ). The reactance can be inductive ( $X_L$ ) if positive or capacitive ( $X_C$ ) is negative. Eddy current circuits typically have only  $R$  and ( $X_L$ ) components. For an eddy current circuit with resistance and inductive reactance components, the total impedance is calculated using the following Eq. 2.2. Impedance also has an associated angle, denominated phase, which can be calculated by Eq. 2.3 [101].

$$Z = R + jX \quad \text{Eq. 2.1}$$

$$Z = \sqrt{R^2 + X_L^2} \quad \text{Eq. 2.2}$$

$$\tan \theta = \frac{X_L}{R} \quad \text{Eq. 2.3}$$

In the presence of defects in the part, the trajectory of the EC will be disturbed and may be deviated or limited (Figure 2.2) [9,102]. The effect of the opposition of these currents to the field  $H_p$  (see Figure 2.1c) will be smaller, changing the electrical impedance of the coil. This method is only applicable to electrically conductive materials, whether ferromagnetic or not.

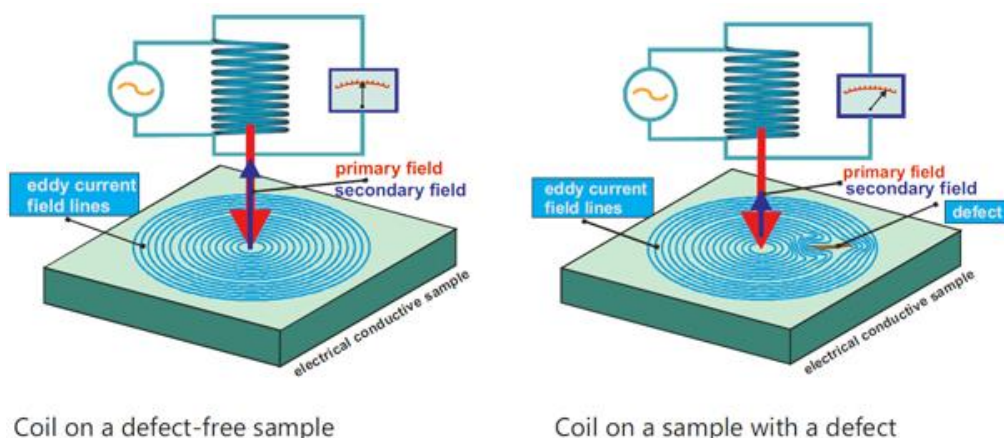


Figure 2.2 – Eddy currents generated by an EC probe and its deflection by the crack [103].

As seen in Figure 2.3 the EC signal in the impedance plane changes in a different direction according to the test material magnetic permeability or the EC strength. If a coil is in the air and

then placed over an aluminium specimen, the circuit resistance will increase, since the EC generated in the test piece is consuming energy from the coil, and the coil's inductive reactance decreases due to the secondary magnetic field, produced by the EC, having an opposing effect on the primary field resulting in a magnetic field with a net effect weaker. The presence of a crack in the test piece will decrease the resistance since there are less EC generated and the inductive reactance will increase. Conductivity changes in the test piece on the other hand changes the signal in a different way [101].

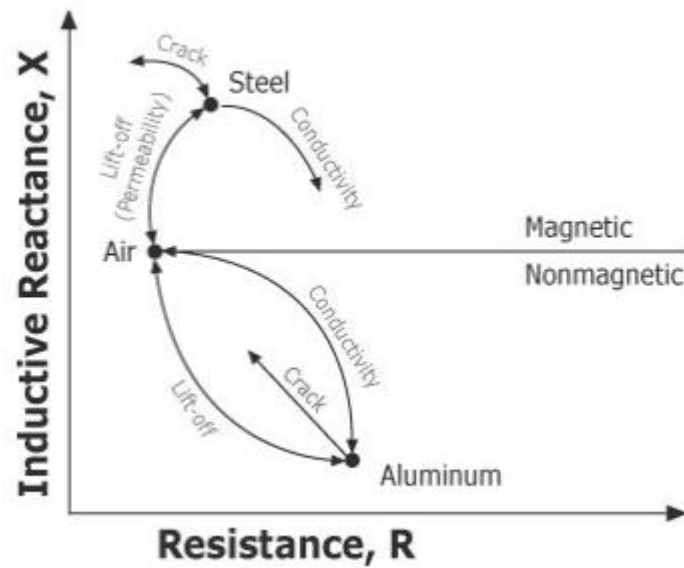


Figure 2.3 – EC impedance plan [101].

With magnetic materials such as steel the probe signal has a different behaviour. With magnetic conductors, when the EC are generated, energy is taken from the coil which results in a coil resistance increase as it happens with non-magnetic conductors. And the EC also generate a secondary magnetic field which also opposes the primary but, the reactance increases instead of decreasing like on non-magnetic conductors. This is due to the magnetic permeability which concentrates the coil's magnetic field. This increased magnetic field entirely surpasses the secondary magnetic field generated by the EC. A defect or a change in the electrical conductivity will have a similar behaviour in the EC signal as a non-magnetic conductor [101].

The EC are concentrated in the material surface (skin effect), decreasing exponentially its density with the depth increase according to Eq. 2.4. In which  $I_x$  [ $A \cdot m^{-2}$ ] is the current density at the depth of  $x$  [m],  $I_0$  [ $A \cdot m^{-2}$ ] is the current density at the surface,  $f$  [ $s^{-1}$ ] excitation frequency,  $\mu$  [ $H \cdot m^{-1}$ ] magnetic permeability ( $\mu = \mu_0 \cdot \mu_r$ ) and  $\sigma$  [ $S/m$ ] electrical conductivity.

$$I_x = I_0 \cdot e^{-x\sqrt{\pi \cdot f \cdot \mu \cdot \sigma}} \quad \text{Eq. 2.4}$$

Due to this phenomenon, it is possible to detect only surface and sub-surface defects. Although, as seen in Eq. 2.5, decreasing the frequency reduces the skin effect, allowing the detection of deeper defects.

The maximum EC penetration depth or standard depth penetration,  $\delta$  [m], was agreed as the depth for which the current density ( $I_x$ ) is  $e^{-1}$  ( $\simeq 37\%$ ) of the current density at the material surface ( $I_0$ ) assuming a plane wave magnetic field (although this condition is rarely observed on the conventional coil probes). Changing these values in Eq. 2.4, results in the penetration depth according Eq. 2.5 in which  $f$  [ $s^{-1}$ ] excitation frequency,  $\mu$  [ $H \cdot m^{-1}$ ] magnetic permeability ( $\mu = \mu_0 \cdot \mu_r$ ) and  $\sigma$  [S/m] electrical conductivity.

$$\delta_{(f,\mu,\sigma)} = \frac{1}{\sqrt{\pi \cdot f \cdot \mu \cdot \sigma}} \quad \text{Eq. 2.5}$$

However, EC penetrate deeper than the standard depth of penetration. In fact, depending on the probe geometry, current intensities slightly higher than 37%, at deeper depths, can be achieved. Ionic EC probes have experimentally validated this [104].

Defects perpendicular to the surface will be easier to detect than parallels. As shown in Figure 2.4, defects transversal to the EC orientation creates a greater deflection of the currents. This deflection is almost inexistent when the defect has the same direction as the EC.

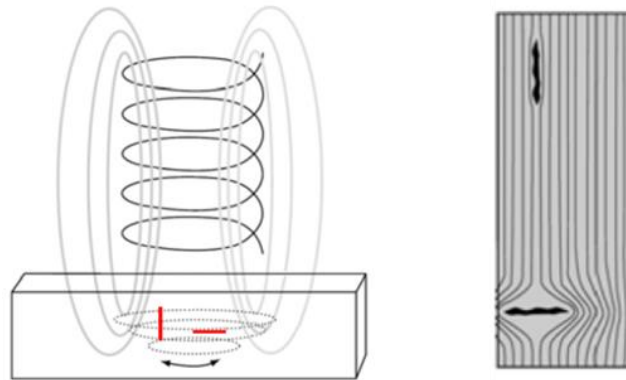


Figure 2.4 – Deflection of the eddy currents by the imperfections.

This method presents some limitations and specificities, namely:

Lift-off effect: defined by changes in the relative position of the probe to the test piece (Figure 2.5). These position changes produce variations in its electrical impedance and may be higher than the variation caused by the defects. When this happens, the detection becomes very



difficult since the changes caused by the defect are absorbed by the noise of the lift-off [105–107];

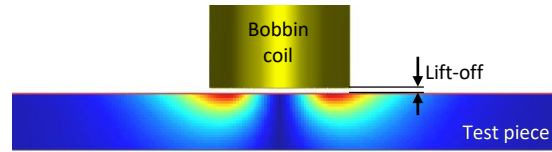


Figure 2.5 – Intensity and location of the EC generated by an EC probe (cut view) [108].

**Skin effect:** As shown in Figure 2.5, the eddy currents have a limited penetration depth in the material, which limits the ability to detect sub-surface defects. However, for surface defects, this is an advantage because sensitivity is increased. The penetration depth can be increased using lower frequencies [109];

**Magnetic Permeability:** consists in the ability to create a magnetic field in a material: the greater the magnetic permeability, the greater the ease of inducing a magnetic field. In ferrous materials the relative magnetic permeability is greater than one ( $\mu_r \gg 1$ ) and in the non-ferrous materials it is approximately equal to ( $\mu_r \approx 1$ ), which causes the impedance variation curve to assume different trajectories as is shown in Figure 2.3 [21] and, increases significantly the skin effect since, as seen in Eq. 2.5 the magnetic permeability plays a major role in the penetration depth. For example, a 3 %IACS stainless steel with a magnetic permeability of 1 has a greater penetration depth than a steel with relative magnetic permeability of 500 as shown in Figure 2.6;

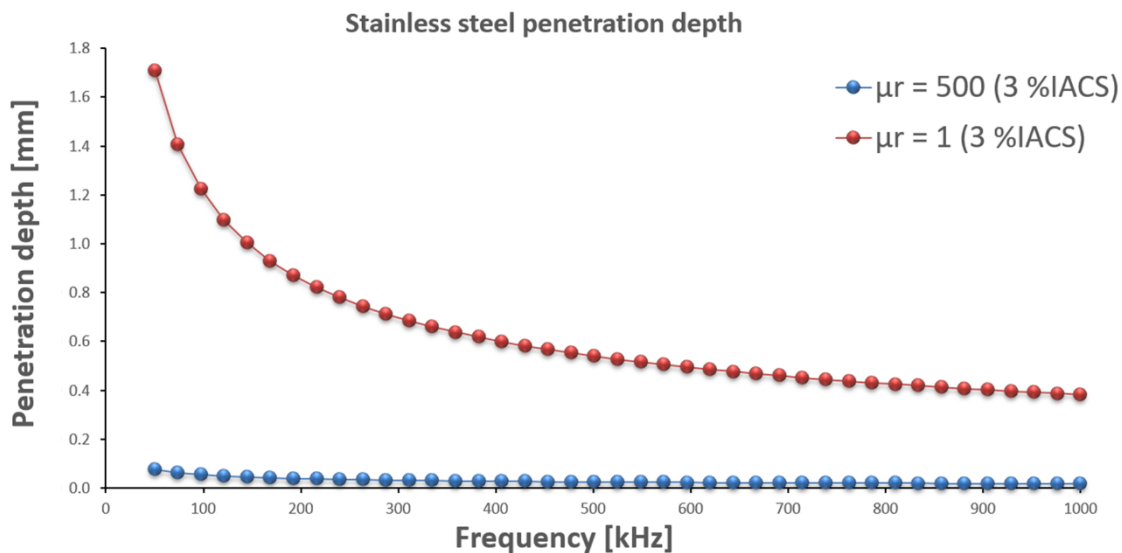


Figure 2.6 – Stainless steel penetration depth with different magnetic permeabilities.

**Edge effect:** when the probe approaches the ends of the workpiece, a distortion of the eddy currents occurs, similar to that observed when there is a defect. This phenomenon can mask

defects at or near the extremities, since these distortions produce signals of great amplitude (Figure 2.7);

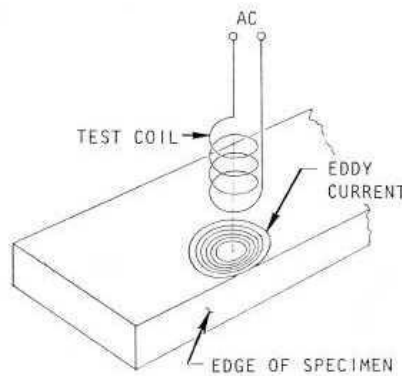


Figure 2.7 – Distortion of eddy current flow at the edge of a part [110].

Another limitation of EC probes consists on their structure and several distinct elements (excitation/sensitive coils, ferrite cores, shielding, chassis) [111] produced by different technologies that are irreversibly assembled in a single operating configuration. Moreover, EC are typically generated exclusively through excitation (often complex) coils or filaments, which limits the creation of EC with a more favourable tailor-made patterns [98,112].

#### **Pulsed eddy currents**

Pulsed eddy currents (PEC) led to the development of a technique that has been used for the corrosion and cracking detection and quantification of aircraft structures and in the nuclear power industry. It has as advantages a greater penetration depth, greater defect information, lower interference sensitivity and lower energy consumption. The PEC consists of a probe excitation with a square wave, which allows, with a single step, more information; the use of multifrequency, achieving a penetration depth of about 10% higher than that achieved by conventional methods [41,113–115]. One of this technique limitations concerns the defects direction in the parts. Although the defects found perpendicular to the eddy currents are easily detectable, the parallels and those of great length are difficult to detect as in EC in general.

#### **2.4.1.– Operating modes**

EC probes can have different configurations and operation modes. The configuration is directly linked with the coil geometry, number and adaptation to the test piece. The operation mode depends on the way the wiring is done and the interface with the measuring equipment. There are four main operation modes which are: absolute, differential, reflection and hybrid [101].

### Absolute probes

EC absolute probes usually operate with one bobbin coil in contact with the testing material and it works as both the driver and pick-up coil. These probes are widely used for flaw detection, conductivity measurements, lift-off measurements and thickness measurements. These probes can have a fixed air-loaded reference coil (Figure 2.8a), that can compensate for ambient temperature variations, which can be in the probe housing, in the probe connector or in an adapter [101]. This is the so-called absolute bridge probe. However, when the probe inductance value is not close enough to the reference coil value it does not allow for proper calibration of the instrument. The result is poor performance (noise or poor sensitivity) or no response (signal saturation).

### Differential Probes

Differential EC probes have two coils over the test piece and are usually wound in opposition. The coils are wired in an electrical bridge and the instrument balances the bridge and any change in balance is displayed with a signal variation (Figure 2.8b). When the coils are over a homogenous test piece, there is no differential signal formed between the coils. However, when one probe is over a defect and the other over a defect free part, a differential signal is created. This configuration allied with the operating mode is very sensitive to defects and consequently fairly insensitive to slow varying properties as gradual dimensions or temperature changes. Wobbling is also reduced in this type of probe. The signal can be very easy to interpret for small defects but for long flaws, longer than the spacing between coils, it is quite the opposite. Bridge type probes allow a limited range of frequencies on older instruments, since they had to balance an electric bridge using other arms (X and R controls). In modern instruments, the bridge is usually formed with fixed precision resistors, or a transformer fixed in its interior. Signals detected this way are processed electronically without any "mechanical" adjustments, which means a greater balancing ability over a wider frequency range.

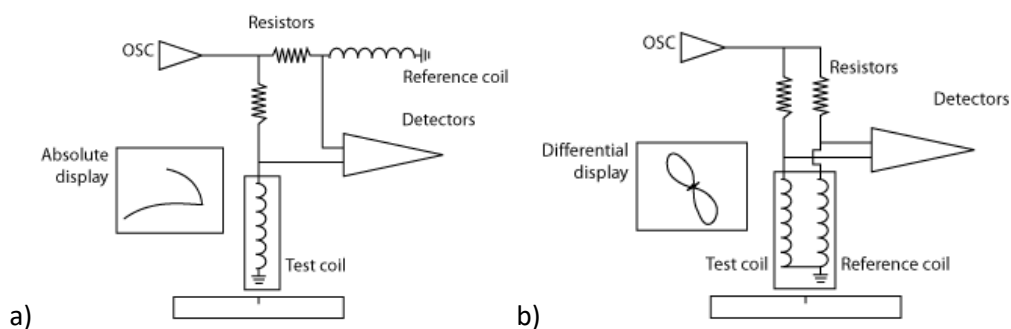


Figure 2.8 – Schematic representation of an EC probe operating in: a) absolute mode; b) bridge differential mode [116].

### Reflection probes

EC reflection probes are also composed of two bobbin coils but one of the coils is used exclusively to induce the EC in the test piece and the other works as a sensor (Figure 2.9a). The duo is usually referred as driver and pick-up coils. The main advantage of these probes is the possibility of separately optimize each coil for each intended purpose. The driver is required to create a strong and uniform flux field near the pick-up coil and, the pick-up coil can be smaller to increase its sensitivity to very small defects. Reflection probes allow a higher gain, particularly if they are "tuned" to a specific frequency, but usually the difference is on average about 6 dB. These probes duplicate the signal which, in critical applications, is favourable. Also, these probes do not need to balance both coils (excitation and reception), which allows for a wider frequency range. As long as the excitation coil produces the EC, the pick-up coil will detect them and display some signal.

### Hybrid probes

A hybrid probe can be a reflection differential probe. These probes can have a driver coil and two or more pick-up coils operating in differential mode. These probes are usually very sensitive to surface cracks (Figure 2.9b). Other hybrid probes are composed of conventional driver coils to induce the EC in the test piece and use other sensors for the detection of defects. These sensors can be Hall effect sensors [117] or Giant Magnetoresistances (GMR) [42]. Hybrid probes are usually specially designed for specific applications.

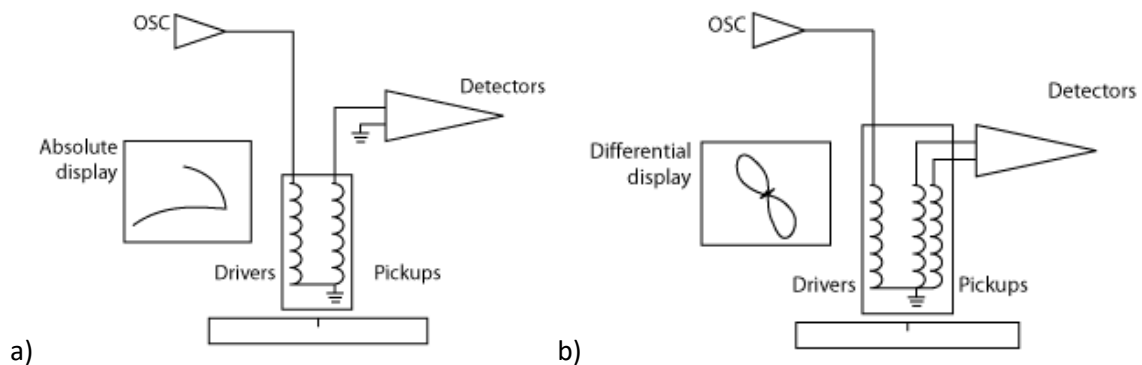


Figure 2.9 – Schematic representation of an EC probe operating in: a) reflection mode; b) reflection differential mode [116].

#### 2.4.2.– Flat EC probes

Flat EC probes composed of one or more planar coil display a great potential in EC testing and offers some very attractive features in the detection of surface imperfections in electrical conductor materials. Some of the benefits of flat coils are: higher sensitivity to cracks due to the

small effective lift-off; straightforward EC probe production using printed-circuit-board (PCB) technology; easy and unobtrusive permanent attachment to the part being inspected; and the prospect of inspecting complex surface geometries if coil is printed on a flexible substrate that allows the coil to conform to the surface [118]. Furthermore, it is simple to print multiple coils on the same board to create a multi-coil array thereby increasing inspection coverage and reducing inspection times.

The use of planar rectangular eddy-current coils has been reported in the NDE literature for defect detection [119–121], materials characterization [122] and coating thickness measurement [123]. Rectangular spiral coils exhibit the same overall advantages as circular spiral coils in eddy-current NDT [124]: good electromagnetic coupling with the substrate, low physical profile and a generally large normalized response to long surface-breaking defects. Rectangular spiral coils, however, display a range of more interesting behaviours than circular spiral coils because it is possible to vary the coil aspect ratio and coil orientation as well as the winding width (inner and outer radii). The main advantages of rectangular spiral coils over circular spiral coils are improved packing when tiled into arrays, less sensitivity to edge effects [119], and simpler artwork [125]. Other coil geometries have been successfully tested with improved sensibility for example in the detection of root defects in Friction Stir Welding FSW [102,126,127]. Other sensors geometries consist of flat triangular coils combined into an array.

Triangular forms allow flexibility on the desired shapes of the generated electromagnetic (EM) field. The elements are arranged so that they can create several possible EM configurations, thereby, avoiding the mechanical movement of the sensor occurred in conventional characterization. The basic idea rests on the fact that the EM fields generated by two parallel wires traversed by currents with the same amplitude and in opposite direction cancel each other. This property is exploited to generate different field forms, acting only on the excitation currents' distribution. The application of the proposed sensor on a sample of CFRP shows its capability to detect the plies' orientations and their stacking order by acting only on the excitation currents. This sensor can thus be an alternative to the mechanical rotating sensors and the rectangular sensors [128].

### **2.4.3.– Eddy current array**

Eddy Current Arrays (ECA) are EC probes composed of several coil elements disposed in a matrix that provides a much wider area to be inspected at once. Although, to avoid a sensitivity loss, multiplexing may be required [129]. Multiplexing activates and deactivates coils in certain sequences to leverage probe width [161]. Also, increases the probe resolution and the

interference between adjacent coils is reduced. ECA probes eliminate the raster scanning required for EC pencil probes which translates into faster inspection speeds [130–132]. When comparing to single coil EC testing, ECA is a major improvement as it allows: faster inspection speeds, wider coverage area, it is less operator dependent as eddy current array probes yield more consistent results compared to manual raster scans, easier analysis because of simpler scan patterns, improved positioning and sizing because of encoded data, eddy current array probes can be designed to be flexible or shaped to specifications (Figure 2.10), making hard-to-reach areas easier to inspect.



Figure 2.10 – Flexible eddy current array probe [133].

#### **2.4.4.– High speed eddy current testing**

Velocity effects on eddy currents (EC) have been demonstrated in specimens with simple shapes, such as, bars, tubes, and wires which are moving [134]. Very low frequencies were simulated (40 Hz) and speeds up to 1000 m/s [135]. The higher the employed frequency, the smaller the speed effect is. For instance, assuming an inspection speed of 4 m/s, the travelled distance during one cycle of 1 MHz EC testing is 4  $\mu\text{m}$ , far less than the sensitive area of any practical probe, leaving valid a stationary assumption. Beside this, it is only required that the demodulation of EC testing signals is accomplished with enough bandwidth to accommodate for the defect signal. The bandwidth required can be assumed the inverse of the time required for a given test location to travel across the employed probe. As an example, for the same inspection speed, the required bandwidth using a 4 mm sensitive area probe is roughly 1 kHz. In other EC testing methods velocity can even be a beneficial factor [43,136]. In fact, eddy current arrays have been used to measure the velocity of moving conductors with considerable accuracy [137].

## 2.5. – Inspection of tubular geometries

Eddy Currents (EC) is one of the main non-destructive testing technique used to inspect metallic pipes and tubes [97]. The inspection of the outer pipe surface is typically performed during production with encircling EC probes, while inner pipe inspection is mostly performed after installation and in service, in industrial environments, for instance in steam generator pipes for nuclear power plants or boilers [138–140]. Despite being a very common technique, some difficulties remain, especially in the inspection of circumferential micro defects on the inner surface.

Conventional bobbin probes for inner pipe inspections are typically composed of circumferential windings inducing circumferential eddy currents. Defects with transversal orientation towards the EC direction produce output signals with greater amplitude, while defects with parallel orientation with the EC direction produce smaller output signals. In conventional coaxial windings probes, circumferential defects are parallel to the EC, thus, its poor proficiency to detect circumferential oriented defects [141].

In order to avoid the conventional probes limitations, different approaches have been essayed, such as the inclination of the bobbin windings allowing, for instance, different orientation between the pickup and the excitation coils which can be parallel, symmetric or twisted [142]. With this approach, EC are no longer parallel to the circumferential direction. These probes proved to have more sensitivity when compared to conventional ones, however, there were circumferential positions, in which, defects remain parallel to the coils, and thus, being overlooked without mechanical rotation of the probe.

Another approach for pipe inspection consists of a rotating field eddy current probe with bobbin pickup coil that generates a rotating magnetic field, avoiding mechanical rotation of the probe [143]. The authors used three identical coils located on axes of  $120^\circ$  apart and a balanced three-phase source. The vector sum of the fields generates a field that rotates circumferentially around the pipe. The probe was validated using artificial defects characterized by through wall square holes of  $3.5 \times 4 \text{ mm}^2$  and  $4 \times 4 \text{ mm}^2$  in Inconel® 600 pipes, with a conductivity of  $9.69 \times 10^5 \text{ S/m}$ . The probe is sensitive to defects of all orientations in the tube wall and both depth and location to be estimated from a single line scan data. Later, this research group developed a new probe using a GMR as a sensor [144] with promising results. The prototype probe is sensitive to both axial and circumferential notches and the C-scan image clearly shows the defect location and orientation.

Probes composed of planar spiral coils arrays in flexible substrates, have shown to have superior reliability for micro defect detection, especially in reflection mode [98,102,145–147]. The planar spiral coils adhere to a conformable substrate, producing a very thin and flexible sensor allowing a greater proximity to the surface, reducing the lift-off and increasing the sensitivity [148–151]. Micro-fabrication techniques allow to produce reliable and repeatable cost-effective sensors [43,107,152,153].

Commercial EC probes dedicated to the detection of circumferential defects are available but these are usually complex and expensive [154–160], and thus, a growing demand of reliable NDT probes remains [161]. A particular example of high demanding inspection consists of a round-in-square jacket profile in austenitic steel JK2LB [162], which constitutes the casing for the central solenoid conductor coils of the International Thermonuclear Experimental Reactor (ITER) [163,164]. These components require extremely high-quality control, thus the need for probes with greater sensitivity to micro defects aligned with any orientation [118,165,166]. The material has a very low magnetic permeability, similar to air ( $\mu_r \approx 1$ ), and low electric conductivity.

## **2.6. – Inspection of bimetallic joints for automotive industry**

Laser brazing has become decisive as a joining process for sheet metal joining in the automotive industry. Laser brazing is nowadays widely used, and it became a standard process in automotive industries around the world replacing the conventional roof drip moulding (Figure 2.11). The outcome of the quality of the laser brazing joints in comparison to other joining processes has better performance and many advantages such as: higher car body stiffness; smoother car design; low heat input; no distortion; no additional sealing; highly productive; reliable seam tracking for 3D contours available; saving costs in the long run [167]. Laser brazing joints are ductile and leak proof at low processing temperatures and produce robust joints [168]. One of the major advantages is the minimum thermal impairment to the substrate metal and low thermal distortion for the welding parts which is major drawback for conventional fusion welding joints. In addition, laser brazed joints exhibit very high-quality surfaces and the process can be fully automated. Due to these unique qualities of the process, it is widely used in car body manufacturing especially for the components in the visible areas such as roof joints and tail gates [169]. The most common filler material used in the automotive steels is silicon copper (CuSi3). Even though the process outcome has a better performance, various types of weld imperfections still appear in the final joints.



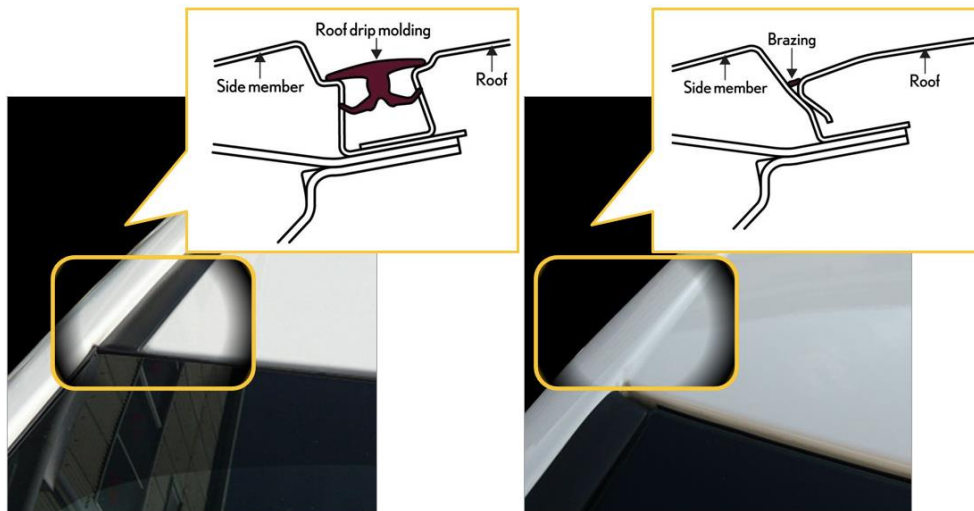


Figure 2.11 – Side panel and roof connection solutions: roof drip moulding and laser brazing [170].

The imperfections can be related to metallurgical reactions like an unintentional melting of the base metals or the formation of brittle intermetallic compounds [171]. These intermetallic compounds formation can deteriorate the joint quality. The results are similar to the joining of dissimilar metals using conventional fusion welding techniques. The most commonly used dissimilar materials combinations in automobiles are aluminium and stainless steel. Conversely, there are some serious problems encountered across these joint interfaces when arc welding practices are used for instance gas metal arc welding [172], laser welding [173], TIG arc welding–brazing [174]. On the contrary, solid state joining has been contemplated as a trustworthy welding method for incompatible metals (such as steel to aluminium, titanium to steel, steel to magnesium, aluminium to titanium, copper to aluminium, etc.) that are very difficult to conventionally fusion weld. These combinations are successfully joined by using solid state welding methods for example friction stir welding [175–180], friction welding [180–189], explosive welding [190], diffusion bonding [191,192] and magnetic pulse welding [193–195]. There are a few types of joint combinations with the formation of intermetallic, to suppress the further formation an interlayer mechanism was used [196–199]. But, all these joining techniques are not suitable for mass production due to several problems such as limited shape of the base metals, the initial preparation of the surfaces, material loss, long weld duration of diffusion bonding and low range of process parameters selection [200].

In contrast, brazing technique is one of the most beneficial and high-quality joining processes for dissimilar metals. Laser brazing welding became an efficient process to solve the weld joint problems and it has several advantages, complex structures and thin sheets can be brazed with high feasibility. Laser welding brazing process is an exceptional tool for governing

the heat input and fusion zone extent, all are beneficial for maintain weld temperature in weld zone and reaction time of solidification in the dissimilar metals joining [201].

The roof top connection to the side panel of automobiles is extremely important in what concerns its structural integrity. In the automotive industry, most of the quality control is typically done with destructive testing. In every 200-500 cars, one is destroyed in order to evaluate the weld quality, and the rest of the lot is statistically estimated based on these.

Being a structural joint in which the bead form and integrity is crucial, porosities and/or internal cracks, lack of bonding and the lack of bead height (thickness reduction) compromises the mechanical resistance of the joint. Therefore, in the event of a collision or rollover of the vehicle, endangers the safety of the occupants. Given the importance of this joint, it is necessary to ensure that there are no internal defects and the bead height must comply with the construction standards. It must be equal or greater than 70% of the filler thickness. Under that (around 0.5 mm) is considered that the joint has no structural strength, depending on manufacturers.

In order to create an inline quality control system for the detection of imperfections and defects in brazed joints, these imperfections first need to be classified. There are three different basic types of weld bead surface imperfections, which may appear in various sizes and intensities and are shown in Figure 2.12. In detail, the three types can be described as follows:

- Sporadically occurrence of pores, including small pores, big pores and pore clusters (1st column of Figure 2.12).
- Joint disruptions in the shape of large cavities, joint discontinuities, lack of bonding and one-sided wetting (2nd column of Figure 2.12).
- Surface irregularities in the form of scaly or wavy seam surfaces, also including surfaces with protruding bits of non-fused brazing wire (3rd column of Figure 2.12).

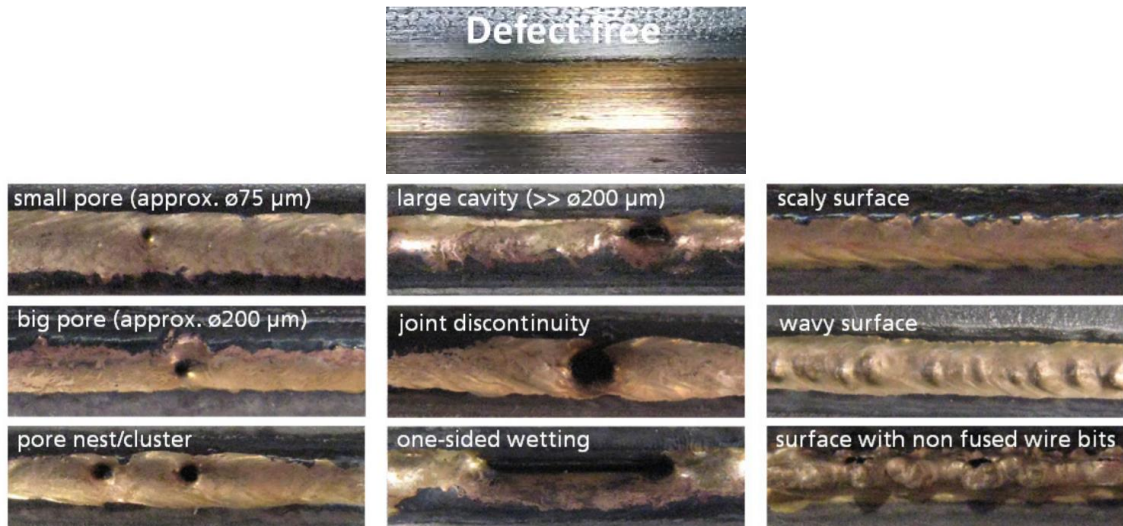


Figure 2.12 – Different types and varieties of geometrical seam imperfections [202].

The brazed joint is performed between two thin curved steel sheets, which makes non-destructive inspection particularly difficult (Figure 2.13). There are systems with image processing algorithms that detect pores in a brazed seam. The principle of triangulation is used to control the quality of the joint. But all these systems operate in a post process configuration. To avoid these time and cost consuming off-line inspections and to enhance the efficiency of the quality control, the development of an on-line quality control system is highly desired by the industry [203,204]. Table 2.1 summarizes the main difficulties for different NDT techniques available in the market.

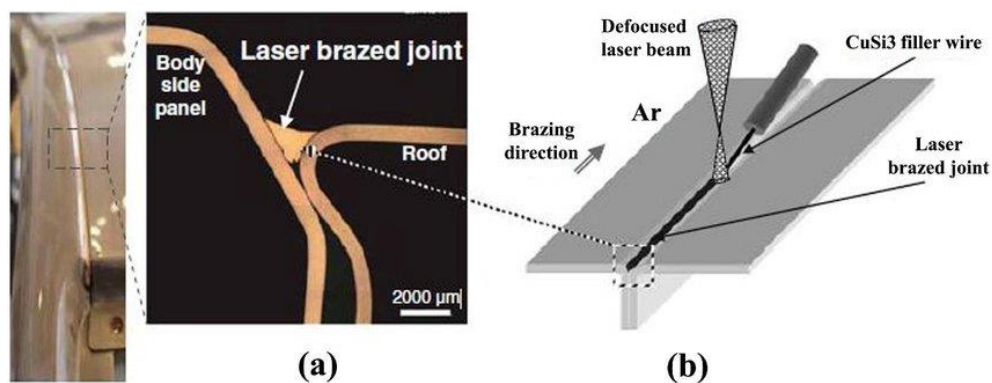


Figure 2.13 – Laser brazed joint in the automotive industry: a) joints cross section view of the laser brazed welds of roof/body side panel; b) a schematic illustrating the principle of laser brazing [205].

Table 2.1 – Different NDT technique and their applicability to the inspection.

NDT method	Applicability	Limitations and observations
X ray	Reduced/ incomplete	<ul style="list-style-type: none"> <li>- Complex and non-orthogonal geometry to the direction of radiation (whichever);</li> <li>- Technological implementation tends to be complex (due to the need for access to both sides of the joint), time consuming inspection.</li> <li>- Problems with operator safety due to radiation.</li> </ul>
Ultrasounds	Reduced/ impossible	<ol style="list-style-type: none"> <li>1) Complex and non-rectilinear geometry: difficult coupling of the probe near the brazed zone.</li> <li>2) Curvature between probe coupling and brazed zone: complex path of echo reflected and subject to lateral echoes that may make it impossible to detect reflected echoes.</li> <li>3) Thin sheet: difficulty in the introduction of longitudinal ultrasound waves.</li> </ol> <p>Thus, the US does not detect porosities, nor does it allow assessing the height of the bead. The most recent US variants, such as phased array and Time-of-flight diffraction (TOFD), introduce specific advantages under certain inspection conditions, but do not override the limitations intrinsic to the physical phenomenon on which they are based. The foregoing is generally valid for any US-based techniques.</p>
Dye penetrants	Reduced/ incomplete	<ul style="list-style-type: none"> <li>- Surface defects only</li> <li>- Unable to automate</li> </ul>

From the above, it is possible to reason that NDT techniques based on electromagnetic phenomena such as eddy current (EC) or electrical phenomena, such as Alternating Current Potential Drop Measurement (ACPD), are best suited to the nature of the inspection problem (Figure 4.2). However, given the inspection condition and the technological specificity, a commercial solution is not available, and it is therefore necessary to design, produce and validate a dedicated NDT system.

## 2.7. – NDT inspection of unidirectional carbon fibre reinforced polymer composites

Unidirectional carbon fibre reinforced polymer composites (UD CFRP) are high performance materials for structural components [206–208], but present low damage tolerance [209–212]. The use of synthetic fibre ropes, like CFRP, has significant potential to replace steel wire ropes in civil engineering and hoisting applications. The high strength-to-weight ratio and corrosion resistance are beneficial in stationary applications such as suspended bridges [179,213,214], offshore anchoring as well as hoisting applications [215–217]. Although the application of non-

destructive testing methods is mature and well established for metallic ropes [218], the same does not apply to synthetic fibre ropes. Several methods for online monitoring of fibre ropes have been suggested [219], such as methods based on the electrical resistivity of the fibres [220] and optical methods monitoring mechanical stiffness [221] and vibration [222]. X-ray inspection can give high-resolution volumetric information of the damage state of a rope [223], but inspection speeds are quite slow for online monitoring and there is a large volume to be inspected. Electrical resistivity works well for small samples [224], but it does not provide information on the location of damage. Furthermore, the relative increase in resistance caused by a small fraction of broken fibres is low compared to the total resistance of a long rope. It is possible to detect local changes by using embedded optical fibres [225], however, they only provide strain values, which are an indirect indication of damage. Moreover, matrix and interface damage, such as micro-cracking, delamination, environmental aging and debonding, does not cause an increase in strain although it can reduce the strength and service life of a rope [226]. The TSA analysis is one typical method applied to polymer composites, including CFRP, to detect different kinds of damage, but most sensitive to delamination [227–229]. The reflection or transmission of ultrasonic waves, at high frequency, can be used to detect interfaces or heterogeneities in CFRP components [227,230]. The principle of ultrasonic inspection is similar to the thermal waves of the TSA phase image and is therefore especially sensitive to delamination [227,231,232]. Contact ultrasonic testing provides damage location and morphology [219], but the online monitoring is not viable at high speed, due to coupling issues, inadmissibility of component wetting or insufficient sample rating. Radiography is a contactless alternative to damage localization and characterization, but even when radiation hazard issues are not critical, it typically needs long exposure times [223], compromising high speed inspection. Thermo-elastic stress analysis is faster, but it does not penetrate protective surface coatings, limiting the inspection to the coating polymer or delamination between coating and CFRP elements. Damage can be detected by observing the surface with optical methods [221,222], but they require a contrast pattern. Similarly, optical fibres can be used to observe local changes in strain [213], but they need to be embedded in the structure. Far field microwave NDE using time reversal mirror has been done with GFRP and metal-composites in  $150 \times 150$  mm samples where disbonding defects, drilled holes and impact damage have been detected [233]. It can be performed without contact, but measurements require 10 min and CFRP has not been tested yet. Electric based methods, on the other hand, can use the conductivity of the carbon fibres themselves for damage detection. Resistance [234] and capacitance [235] monitoring can be used to detect strain, fibre breaks and even matrix damage [236,237]. However, resistance measurements do not provide information about the damage location nor morphology.

Furthermore, the relative increase in resistance caused by broken fibres may be very low compared to the total resistance of a large component. This method is also not reliable if the defects consists of a delamination between unidirectional fibres, since the resistivity is not changed along the longitudinal direction.

In contrast, local and contactless electromagnetic methods can be conducted using eddy current testing [238]. ECT can be used in several ways to inspect carbon fibre composites [239]. It is typically used for inspecting undulations in carbon fibre reinforcement fabrics, quality control of stacking sequence, fibre orientation and curing effects [240–244]. Electrical properties can be characterized through various orientations with EC testing techniques [245,246]. Delamination detection has been proposed [247] and shown with artificial delamination made with interply release film [248] and extensive delamination during tension testing [249]. Artificial cracks made by slitting the fabric before lamination have been detected [250] as well as impact damage [251,252]. Planar EC probes have demonstrated a superior sensitivity in the detection of imperfections in other low conductive materials [98,118].

There is a growing demand for non-destructive testing techniques for inline condition monitoring of CFRP ropes [253]. Static techniques are insufficient since these ropes can be in movement, or even at high speeds, for example in hoisting applications. The sensors coupling is also crucial since the contact between the probe and the CFRP can damage the elements [254].

There are commercially available solutions [255] especially designed for the non-contact and continuous testing of carbon fibre rovings. The testing system utilizes the electrical conductivity of the carbon fibres to gain information such uniformity of the carbon fibre tow or yarn [256]. However, the present case presents significant differences, since it consists on the condition monitoring of the CFRP composite in operation, and the fibres are covered by a polymeric coating of about 1 mm thickness, increasing the EC probe lift-off. This allows monitoring of actual components during use, instead of just having quality assurance of raw materials at production plants.

## **2.8. – Conventional EC generation mode**

As discussed in §2.4, when eddy currents direction is perpendicular to the defect orientation, the EC suffer a greater deviation than a parallel one, which will result in a greater amplitude signal of the probe impedance. Obtaining the maximum signal amplitude for a defect is clearly one of the main goals when designing an EC probe thus, the orientation of the EC in the

specimen is crucial. It is also known that the EC in an isotropic specimen have the same path orientation as the shape of the coil used in the excitation.

On helicoidal bobbin probes ferrite cores and shields are sometimes used to change the magnetic field flow. When the bobbin coils are wound around a ferrite core, since ferrite is ferromagnetic, the magnetic flux produced by the coil concentrates on ferrite instead of the air. Therefore, the ferrite core concentrates the magnetic field near the centre of the probe. This, in turn, concentrates the eddy currents near the centre of the probe (Figure 2.14b). Probes with ferrite cores tend to be more sensitive than air core probes and less affected by probe wobble and lift-off [101].

On the other hand, probe shielding is used to prevent or reduce the interaction of the probe's magnetic field with nonrelevant features near the probe. Shielding could be used to reduce edge effects when testing near dimensional transitions such as a step or an edge. Shielding could also be used to reduce the effects of conductive or magnetic fasteners in the region of testing. Bobbin coils shielded have a ferrite, or other material with high permeability and very low electric conductivity, ring surrounding the coil. The shield creates an area of low magnetic reluctance and the probe's magnetic field is concentrated in this area rather than spreading beyond the shielding. This concentrates the magnetic field into a tighter area around the coil (Figure 2.14c). This interaction, between the magnetic field and high permeability materials, can have a huge potential in the ability to change the EC orientations without changing the coil geometry since the magnetic field is clearly affected by them.

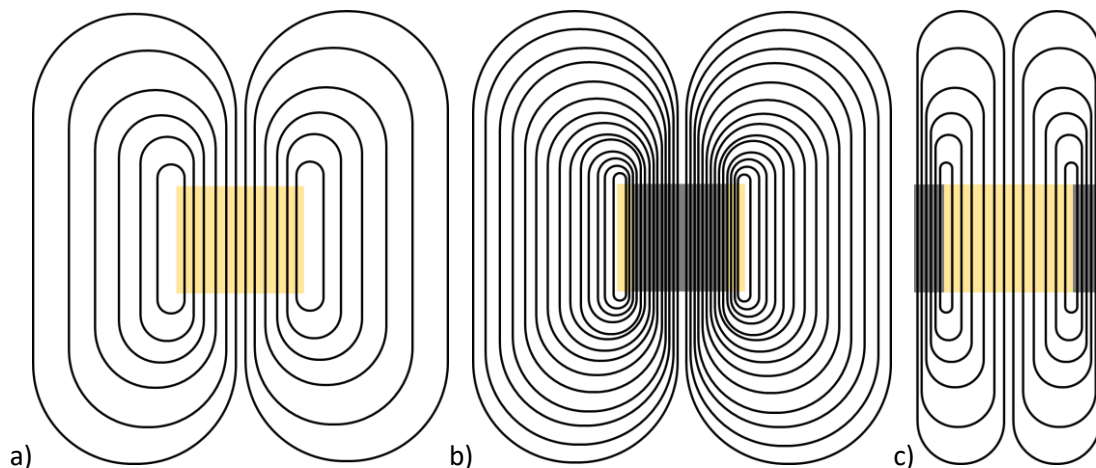


Figure 2.14 – Magnetic flux generated by a bobbin coil: a) without core nor shield; b) with a ferrite core; c) with a ferrite shield.

The need for greater sensitivity for all kind of defects and all kind of defect orientations is resulting in an increasingly complexity of EC probes since the EC have the same path orientation

as the shape of the coil used for the excitation. Excitation coils, as well as pick-up coils, are getting more and more complex with very complicated geometries. Many different coil structures of the eddy current coils have been designed such as a circular spiral structure [257], meandering winding magnetometer structure [258,259], parallelogram structure [118,165], double rectangle structure [260,261], rosette structure [131,262], D shaped differential structure [102,263], dual driver structure [98], gradient winding coil structure [264], mesh-winding structure [265], new rosette-like structure [266], same direction line structure [267], fractal geometry [268] and so on. Another example of a very complex probe geometry are the Meandering Winding Magnetometers (MWM®) sensors developed by JENTEK® Sensors [269–273] for damage detection and quality evaluation of metal structures which consists of a meandering primary winding for creating the spatially periodic magnetic field and meandering secondary windings for sensing the response both with a complex zigzag pattern.

This trend may lead to a level of probe complexity impossible to manage, and therefore alternative ways to create eddy currents in the materials should be researched and tested. The proposed MPPS concept (Chapter 6) is intended to be a contribution for that.

## **2.9. – Summary**

A bibliographic review was made, on the main topics involved in this thesis: non-destructive testing by eddy currents. An approach to NDT in general was performed in §2.4 followed by the EC method in particular. In the EC review the different operating modes (§2.4.1) are described as well as the different types of probe sensors geometries (§2.4.2). The inspection of tubular inner perimeters was discussed (§2.5) where the EC plays a major role. Nevertheless, EC probes have become very complex and expensive and lack the customization possibility. A new solution is required which should be reliable, simple, customizable to different diameters/geometries and cost effective.

Bimetallic joints in the automotive industry were discussed (§2.6) especially the quality control of the laser brazed weld beads. The quality control of these weld beads is currently being made with destructive testing. This testing method is not the ideal since it is not cost effective and does not guarantee the good quality of all the weld beads produced. A non-destructive solution was studied and from the several methods available, due to the specificities of the weld (geometry, accessibility and materials), the electromagnetic methods appeared to be the most suitable for this application.



Unidirectional carbon fibre reinforced polymer composites inspection was studied (§2.7). Most quality control is performed with non-destructive testing although, this concrete application requires no contact between the probe and the element and high-speed inspections (> 3 m/s). Once again, mainly due to the application requirements, electromagnetic methods are the best candidates for the inspection since the inspections can be performed with a lift-off and these speed ranges are well within the working speed range of EC.

Finally, the EC generation in the specimens is discussed focussing on the orientation it assumes. High permeability materials has shown as having the ability to interfere with the magnetic field and thus, having the potential to change the EC orientations as one may see fit in order to simplify an EC probe, for example.



# **CHAPTER 3**

## **CUSTOMIZED EC PROBES FOR CIRCULAR GEOMETRIES INSPECTIONS**

### **3.1. – Introduction**

This chapter presents a case study where a solution was developed for circular geometries inspections. The problem and objectives were addressed followed by the probe design in §3.2 and §3.4. The three key features of the probe were explained, and the target defects were characterized (§3.3). The experimental results were shown validating the probe concept in §3.5.

### 3.2. – Motivation

The inner surface of tubular components is very challenging in concern to the detection of some defect morphologies mainly, circumferentially oriented cracks. An example of a NDT application with particular demanding and complex technology is the detection of defects in one of the components that make up the International Thermonuclear Experimental Reactor (ITER). ITER consists of a nuclear fusion powerplant, which uses hydrogen to produce 500 MW of energy through nuclear fusion process (Figure 3.1). The project was born from an international cooperation involving China, European Union, United States, India, Japan, South Korea and Russia. It is under construction, will be located in south of France and should have its first operation in 2026. The component in question is a tube with a particular profile that can be visualized in Figure 3.2.

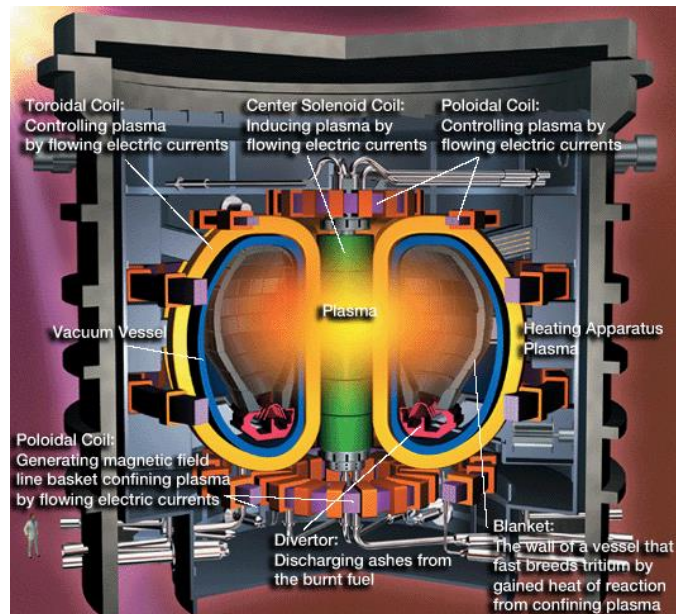


Figure 3.1 – ITER main components illustration [274].

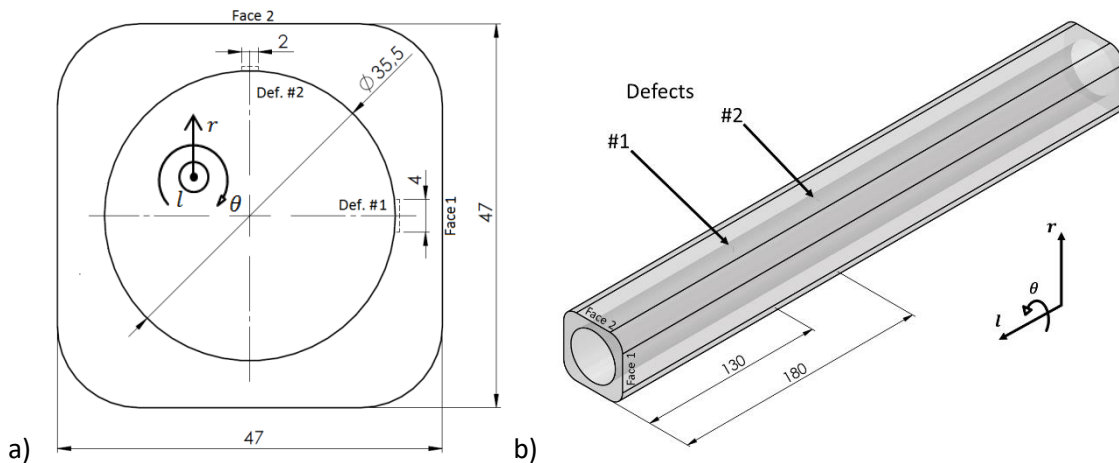


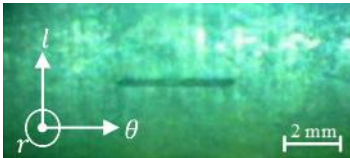
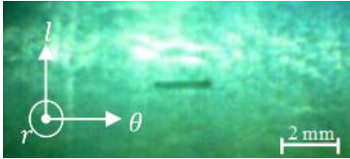
Figure 3.2 – ITER tubular sample. a) profile view with dimensions in mm, b) isometric view.

The component is designated as a poloidal coil and Inside it will have superconductors so any defect unnoticed can cause incalculable damage. In Figure 3.1 it is possible to identify the location of the component to be tested (Poloidal Coil) in the reactor. As shown in Figure 3.1, the tube will be bent but, the NDT concerned here are carried out before they are folded.

### 3.3. – Material and defects characterization

Target defects are small cracks, up to 2 mm length 0.5 mm depth and 0.2 thickness, whether arranged in the axial or tangential direction. Currently, conventional EC probes allow the detection of axial defects (l direction) with some ease. However, it has been found that tangential ( $\theta$  direction) defects of less than 4 mm in length are very difficult to detect. The component to be investigated is composed of 316LN steel (JK2LB). It is known as 18/8 stainless because of its chemical composition, which includes about 18% chromium and 8% nickel in weight. The steel is easily shaped, weldable and very resistant to corrosion, it has low conductivity and the magnetic permeability is similar to the air ( $\mu_r \approx 1$ ). Two artificial defects were produced using electro erosion on an austenitic steel 316LN (JK2LB) round-in-square jacket, which is used in Central Solenoid coils in the ITER. Figure 3.2 shows the tube profile with its dimensions and isometric view. It is also possible to visualize the position of the defects in the pipe. The two defects were circumferentially oriented and apart from each other 50 mm in the axial direction. Other defects characteristics are presented in Table 3.1 such as: dimension, morphology and location. A remote visual inspection (RVI) with an endoscope was previously performed and the defect pictures obtained are also displayed in Table 3.1.

Table 3.1 – Artificial defects in the ITER sample.

Defect	Face	Dimension (mm)			Visual inspection (endoscopy)
		Length	Thickness	Depth	
#1	1	4	0,2	0,5	
#2	2	2	0,2	0,5	

### 3.4. – Probe design

In the context of previously performed work [166], EC probes were developed for inspection of circular geometry components with very promising results. In the continuation of this work an improvement of these probes was done resulting in a new probe [118,165].

A set of functional requirements for the probe was defined in order to increase the inspection reliability, compared to existing commercial EC probes. The new probes should: i) have a high sensitivity to detect small size defects with a very good signal-to-noise ratio when handled with conventional EC equipment; ii) be capable of detecting defects with any orientation (axial, tangential or oblique); iii) provide information on both axial and tangential position of the defect; iv) be easily customizable, economic and cost effective.

Fill factor was also considered in order to improve the response to potential cracks. The fill factor is the ratio between the cross-section areas of the probe and the pipe. Therefore, the ideal fill factor is to be as close as possible to the unity. The fill factor of the manufactured probes was around 0.95.

#### 3.4.1. Excitation winding – Element 1

The excitation is characterized by a twisted zigzag excitation winding, i.e., non-axial zigzag. The inclination allows the generated eddy currents to be disturbed by axial, tangential or oblique defects.

The excitation angle ( $\beta$ ) is a function of  $\Delta\theta_{\text{ext.}}$  and  $\Delta l$ , and it must be such that, a defect passing through the sensitive coil crosses the excitation coil at least once. According to this criteria  $\beta$  should follow the identity  $\tan(\beta) > \Delta l / \Delta\theta_{\text{ext.}}$ . This allows to make sure that there are currents flowing through the defect at some point, while under the sensitive coil, as shown in Figure 3.3.

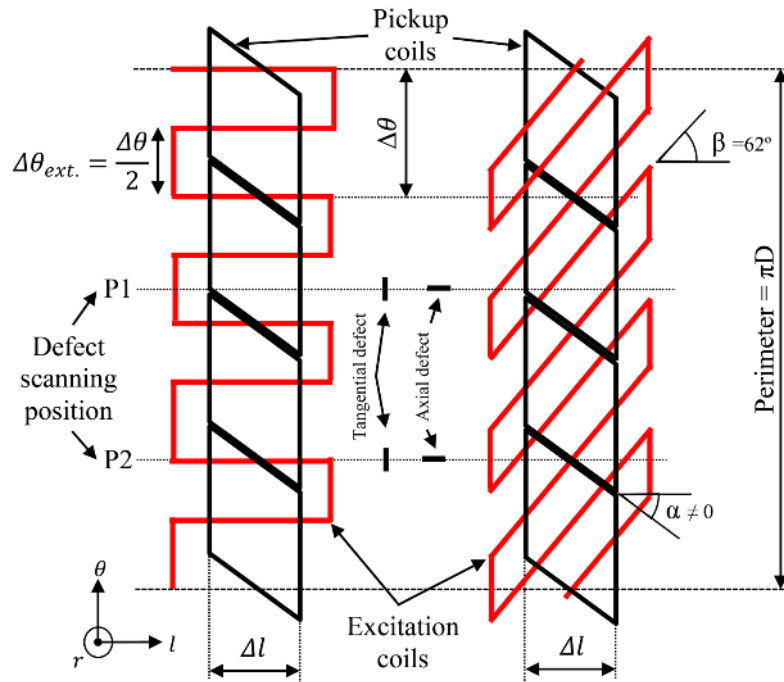


Figure 3.3 – Schematic of the sensitive and excitation coils with axial zigzag (left side) and twisted zigzag (right side). The twisted excitation coil ensures that the defect will have EC passing through it at least once.

### 3.4.2. Pick-up coils array – Element 2

The probe pick-up coil comprises a linear array of planar parallelogram spiral coils produced by Print Circuit Board (PCB) in a flexible substrate. This feature was selected for three main reasons: i) to maximise the proximity to the pipe inner surface and, hence, to the defect, allowing a superior sensitivity; ii) to provide a constant lift-off by simple adjustment to the pipe surface, since it is flexible; iii) and, finally, its simplicity to produce. In fact, the low production cost leads the sensor to be disposable and modular, that is, the same linear array pattern may be used together with different probe chassis and excitation coils, allowing different probe arrangements. The probe architecture is scalable, to different diameters, and its geometry can be adapted to exterior tube surfaces, involving the entire perimeter, or, in cases where the diameter is too big, a tangential section only.

The pick-up coil array is rolled over the chassis, if it is for an inner surface inspection probe, or on the inner surface of the chassis, if it is for an external surface inspection probe.

The sensitive plane is perpendicular to the  $r$  direction. The parallelogram coils have a width of  $\Delta l$ , an angle between 2 consecutive coils of ( $\alpha$ ) about  $45^\circ$  (Figure 3.5) and a number of elements determined by  $\pi D / \Delta \theta$ , where  $D$  [m] is the pipe perimeter and  $\Delta \theta$  [m] is the length of each coil. The number of coils and their dimension in each array depends on the spatial resolution envisaged. Increasing the number of coils improves the spatial resolution.

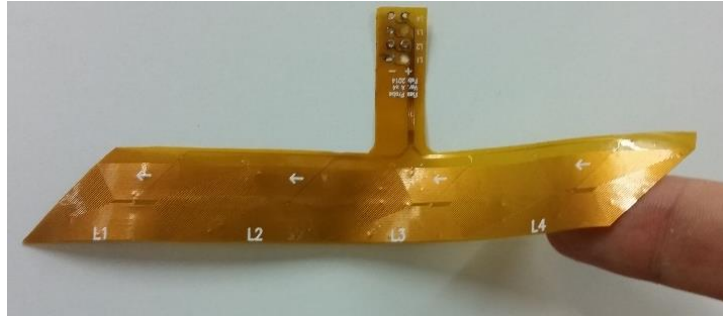


Figure 3.4 – Pick-up coils - Planar parallelogram spiral coils in flexible PCB.

Conventional EC probes composed of planar circular spiral coils present a common problem which is the existence of a blind zone in the interface between two consecutive sensitive coils. In this zone, the detection of defects becomes compromised or even impossible (Figure 3.5). To overcome this problem, there is a need for a second linear array with an offset from the first array, to ensure that all the tangential positions of the pipe are covered by EC. An evident benefit of the proposed parallelogram spiral coil configuration is that, a single array can avoid the blind zones and cover the whole pipe perimeter as well (Figure 3.5). Nevertheless, it must be noticed that the density of eddy currents can exhibit a spread over the material surface, and thus, the blind zones may be narrower than schematically depicted in Figure 3.5.

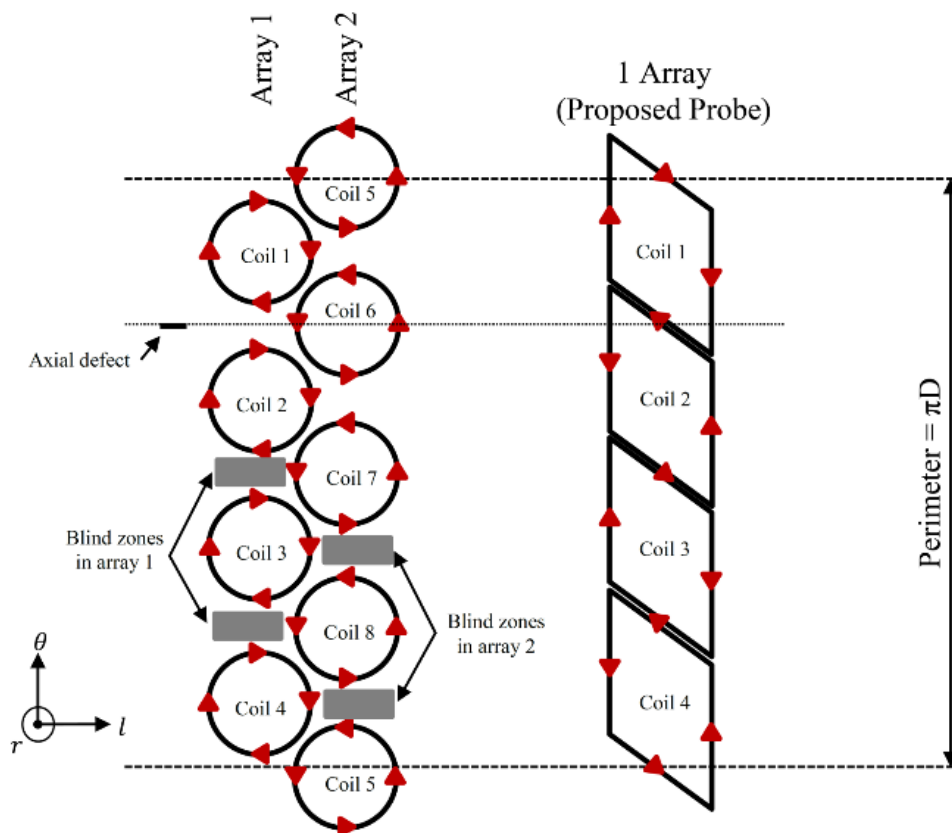


Figure 3.5 – Schematic of currents flow direction in circular spiral (left) and in parallelogram spiral coils (right). The proposed EC probe with parallelogram spiral coils avoids, with one array, the blind zones of the conventional probes.



Another advantage of this parallelogram configuration is that, for the same number of coils in the array, the spatial resolution of the probe is superior. In fact, if circular or rectangular spiral coils are used [275], there would be an Area of Exclusive Sensitivity (AES) in which the spatial resolution is dispersed. Using the proposed parallelogram coils, the AES is much smaller, reducing the uncertainty and, thus, increasing its spatial resolution (Figure 3.6). An axial defect that passes under the interface between two consecutive rectangular spiral coils may not be detected, as shown in Figure 3.6, whereas with the parallelogram geometry the defect is always detected and can be detected by two adjacent coils. Moreover, the signal indication will be the combination of the two coils result, which may indicate more accurately if the defect is closer to one or the other coil (depending on each coil signal intensity contribution), thus increasing the accuracy of the tangential position of the defect (Figure 3.6).

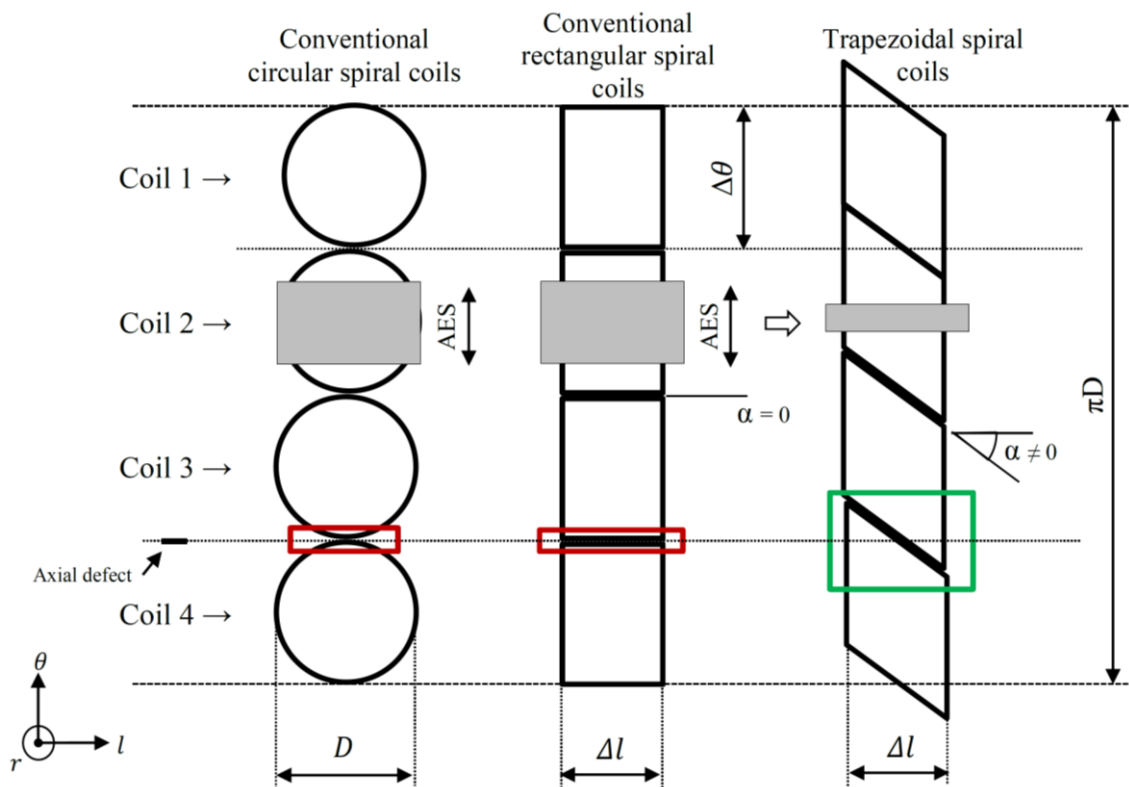


Figure 3.6 – Circular spiral coils (left) vs rectangular spiral coils (middle) vs parallelogram spiral ones (right). An axial defect may not be detected by a conventional circular or rectangular spiral coil where both parallelogram spiral coils would.

The coil array may have "N" parallelogram coils with multiple turns, depending on its use. The coil has a particular characteristic, which consists in windings on both sides of the substrate in the same direction, thus doubling the number of turns, and consequently, increasing the signal amplitude. The turns width was  $150 \mu\text{m}$ , as well as, the spacing between them, and the thickness was of  $25 \mu\text{m}$  (Figure 3.7).

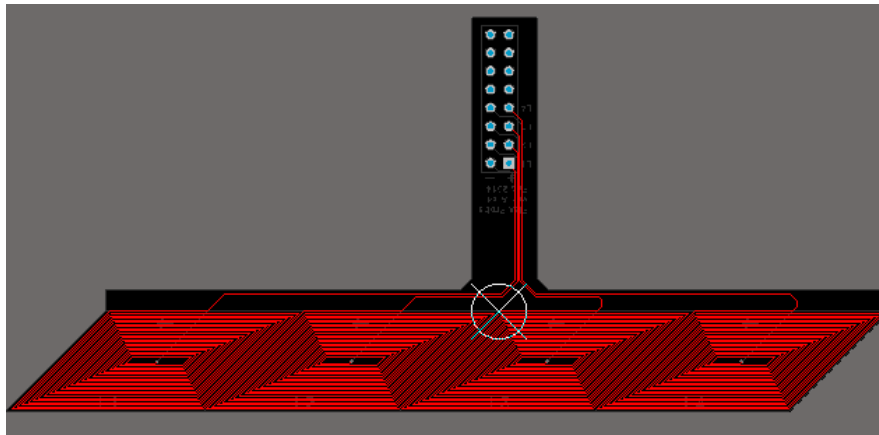


Figure 3.7 – Probe designed in Altium Design software.

### 3.4.3. Probe chassis – Element 3

The probe chassis is concentric with the tubular geometry and is responsible for the excitation winding and pick-up coil array support. The probe chassis can be produced in a polymeric material, namely, polylactic acid (PLA), which allows its production by 3D additive manufacturing, using fused deposition modelling (FDM) technique [276–278]. This process allows a quick, economical and easily customizable solution.

The elements characteristics that make up the probe allow a scalable architecture, with different diameters, also allowing adaptation to outer tube surfaces surrounding the entire perimeter or, in cases where the diameter is too large or inaccessible, only one section (Figure 3.8).

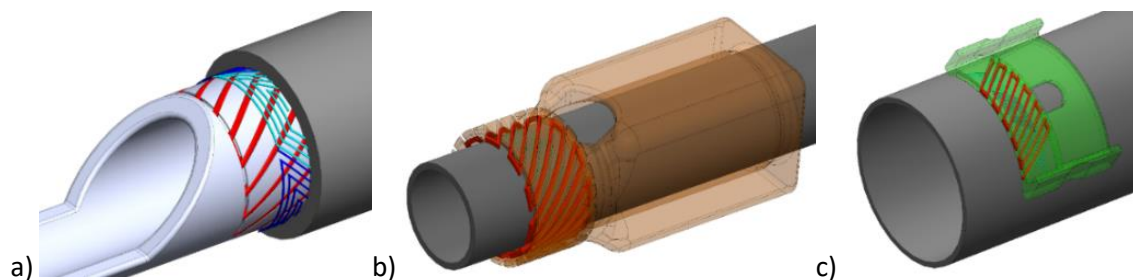


Figure 3.8 – Chassis examples; a) inner surface inspection probe; b) outer surface inspection probe; c) outer surface section inspection probe.

## 3.5. – Experimental results and discussion

The ITER tube inspection was performed with the inner perimeter inspection probe shown in Figure 3.9. The chassis geometry was designed having in mind: the diameter of the sample, the excitation windings as they are placed in depressions created in the chassis model and the part 3D printing feasibility.

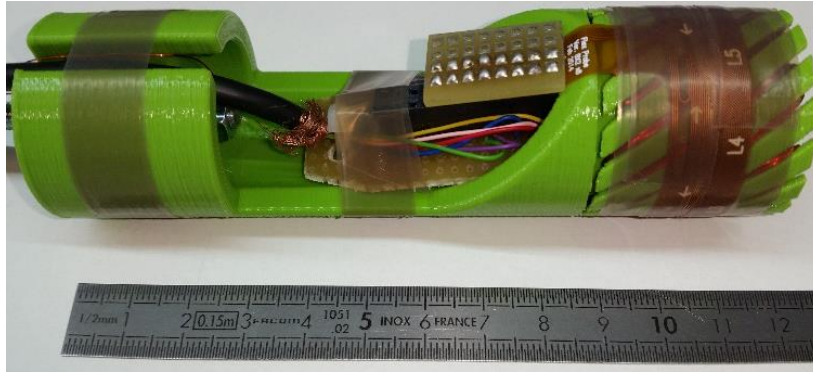


Figure 3.9 – Inner surface inspection probe for the inspection of the ITER sample.

The movement, as well as the signal acquisition, were controlled and programmed in LabVIEW environment and commercial EC testing equipment (Nortec 500) was used for impedance measurements. A commercial probe was tested in the same conditions and testing parameters for comparison purposes. This commercial probe was designed and produced for this particular ITER pipe application. It is composed of two parallel coaxial windings with the same diameter as the pipe tested. This type of probe is one of the most standard and used probes for pipe inspection and thus, constitute a good basis for comparison. Figure 3.10 shows the results of each probe. The commercial probe was tested at 200 kHz in a bridge differential mode which provided the best signal output. Both defects caused a perturbation on the signal, but defect #2 is almost unnoticeable. The customized probe result was obtained at a frequency of 500 kHz. The probe revealed a clear output signal for each defect with a good signal-to-noise ratio. The results were performed with the defect aligned with the centre of the flat parallelogram spiral coil (position 1 of Figure 3.10).

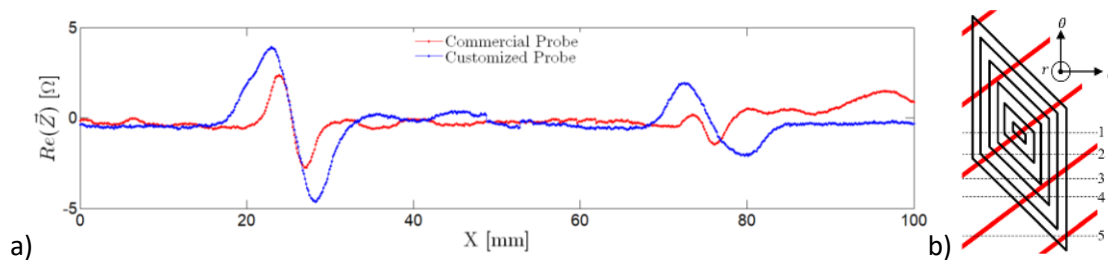


Figure 3.10 – Output signal obtained with each probe when scanning defect #1 and #2 in the axial scanning position 1.

Figure 3.11 depicts the output signal obtained from a pick-up coil scanning in different positions. As observed, the defect is detected in all tested positions and starts to lose amplitude as it moves away from position 1. However, even though the defect is detected with a small signal amplitude in position 5, it must be taken into account that the adjacent coil would detect it with a much more intense signal since for this coil the defect would pass through a position equivalent to position 1.

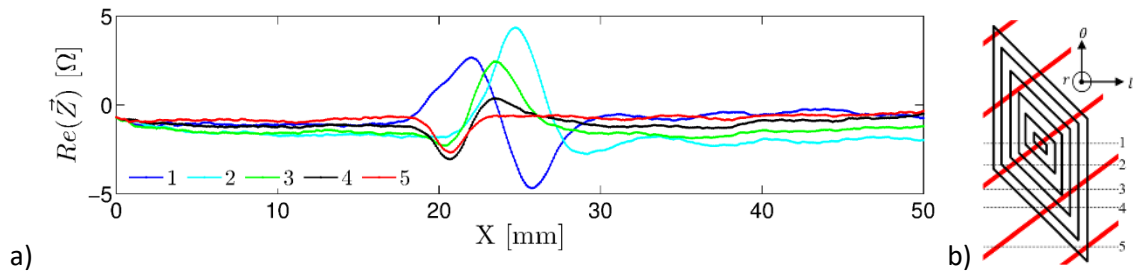


Figure 3.11 – Output signal obtained at 500 kHz of defect #2 in different axial scanning positions (1 to 5).

The inner perimeter inspection probe, shown in Figure 3.12a, was tested on a steel pipe ST 52 with a 35.5 mm internal diameter. Three artificial defects were made in the tube consisting of 4 mm diameter holes with different depths depicted in Figure 3.12b.

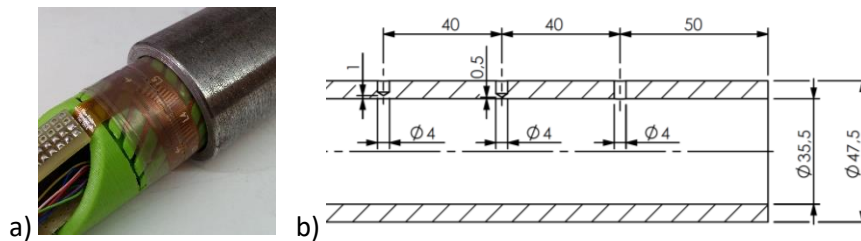


Figure 3.12 – EC probe and steel sample; a) inner perimeter inspection probe; b) tube cut view with defects represented.

Figure 3.13 illustrates the output signal obtained at a frequency of 500 kHz. Defects have been detected even though only the through hole has a good signal-to-noise ratio. The results were performed with the defects aligned with the centre of the flat parallelogram spiral coil (position 1 of Figure 3.13).

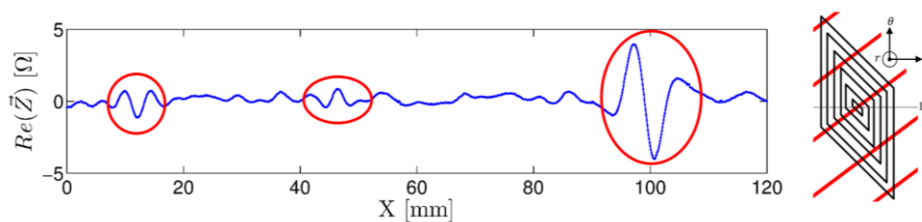


Figure 3.13 – Output signal obtained at 500 kHz of the steel sample in the axial scanning position 1.

A different ST 52 steel tube sample was tested with an outer surface inspection probe shown in Figure 3.14. The tube has 45 mm outside diameter and four defects have been made on its outer surface. The defects are shown in Figure 3.15 and their dimensions in Table 3.2.

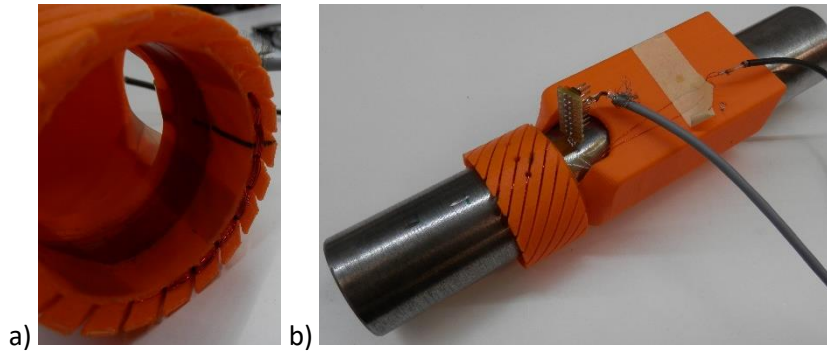


Figure 3.14 – Outer surface inspection probe; a) flat flexible pick-up coils inside the chassis; b) EC probe around the steel sample.

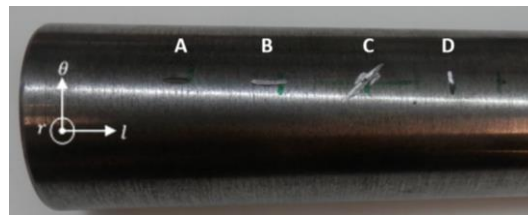


Figure 3.15 – ST 52 steel sample with the four artificial defects depicted.

Table 3.2 – ST 52 steel sample defects dimensions.

Defect	Length (mm)	Thickness (mm)	Depth (mm)
A	5	1	0.4
B	7	1	0.3
C	8	1	0.2
D	5	0.5	0.3

The output signal obtained at a frequency of 750 kHz is shown in Figure 3.16. The probe revealed a clear signal for each defect with a good signal-to-noise ratio. The results were performed with the defect aligned with the centre of the flat parallelogram spiral coil (position 1 of Figure 3.16).

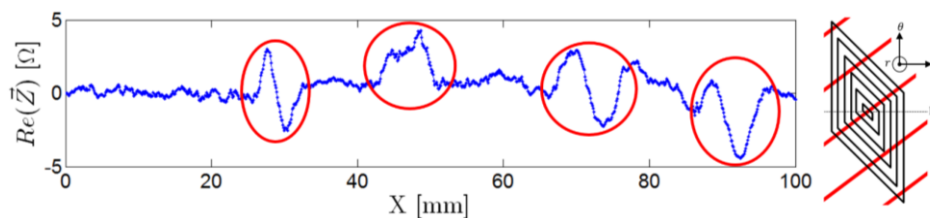


Figure 3.16 – Output signal obtained at 500 kHz of the steel sample in the axial scanning position 1.

A 120 mm outer diameter AA2024 aluminium tube was also inspected. Since the diameter is too big for a probe to be wrapped around, a different probe which inspects only one section at a time was used as shown in Figure 3.17. This probe has a great potential for applications in

pipes whose end has a difficult or impossible access. Five artificial defects on the outer surface were produced and are depicted in Figure 3.18 and their dimensions are shown in Table 3.3.

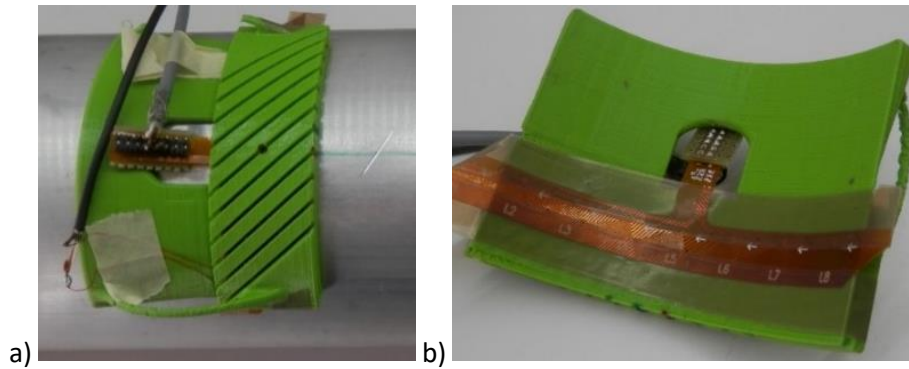


Figure 3.17 – Outer surface section inspection probe; a) probe over the sample; b) pick-up coils of the probe.

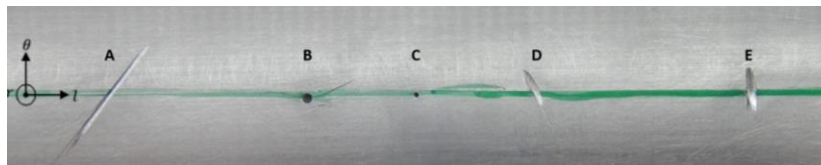


Figure 3.18 – Aluminium AA2024 120 mm diameter pipe with artificial produced defects.

Table 3.3 – Aluminium AA2024 artificial produced defects dimensions.

Defect	Length (mm)	Thickness (mm)	Depth (mm)	Diameter (mm)
A	8	0.5	0.2	-
B	-	-	-	1.5
C	-	-	-	0.6
D	4	1	0.2	-
E	5	1	0.3	-

The experimental results on the aluminium sample are shown in Figure 3.19 with a frequency of 750 kHz. The five defects were detected, with a good signal to noise ratio. The result was done with the defect aligned with the centre of the flat parallelogram spiral coil (position 1 of Figure 3.19).

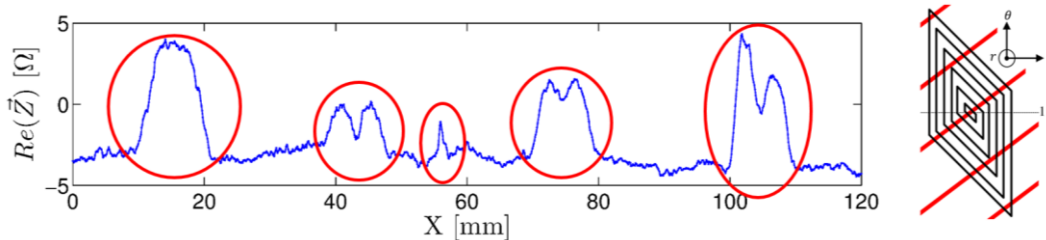


Figure 3.19 – Output signal obtained at 500 kHz of the aluminium sample in the axial scanning position 1.

### **3.6. – Summary**

New concepts of eddy current probes were designed, manufactured, validated and the experimental results in ITER CS jackets pipes were presented.

Target defects were characterized followed by the experimental validation where the proposed probe concept successfully demonstrated its superiority against commercially available EC probes. Different probe chassis geometries were tested and a few more specimens were added to the probe experimental validation.

The probe concept is composed by three main features which were described and explained: the excitation winding; the pick-up coils and the probe chassis. The proposed linear array of trapezoidal spiral sensing coils allows the elimination of blind zones of the conventional circular spiral coil arrays. It also increases the accuracy of the defect location in circumferential direction, since one single array with N coils allow to distinguish 2N regions. The flexible substrate allows a closer proximity to the tube surface, thus increasing the coil sensitivity.

The probes exhibit superior sensitivity to detect circumferential defects when compared to existing commercial ones. Reflection type probes presented enhanced signals when compared to the absolute type probes. Twisted excitation windings and trapezoidal sensing coils evidenced a superior reliability, since it was able to detect all defects, with a depth of 0.5 mm, in any scanning position.

3D printing proved to be a very good alternative in the production of the chassis as it allows a faster, cheaper and easily customizable solution.

The trapezoidal spiral coils are made in a PCB flexible substrate which is simple to produce and inexpensive, so that they can be disposable, allowing an easy customization to any specific application.





# **CHAPTER 4**

## **NON-DESTRUCTIVE INSPECTION OF LASER BRAZED WELD BEADS**

### **4.1. – Introduction**

This chapter presents the second case study where a technological solution was developed for non-destructive inspection of laser brazed weld beads for automotive industry. Extensive materials and geometrical characterization were performed in order to address the issue (§4.3). Numerical simulations were presented which were essential for the probe development (§4.4). A functional prototype for the inspection scanning was also described and the laboratorial setup was depicted in §4.5.4. The results are then presented in laboratorial conditions and in industrial environment in §4.6.1 and §4.6.2.

## 4.2. – Motivation

The roof top connection to the side panel of automobiles is extremely important in what concerns its structural integrity. Therefore, it is important to assure that the joint does not have any type of critical defect that may compromise it. In the automotive industry, most of the quality control is typically done with destructive testing. In every 200-500 cars one is destroyed in order to evaluate the weld quality with, for example, a macro as seen in Figure 4.1, and the weld quality of the rest of the lot is statistically estimated based on these.

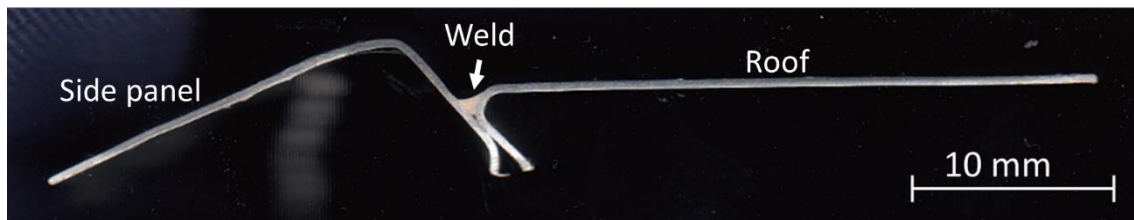


Figure 4.1 –Weld profile macro.

This is not an ideal method to assess the process quality, since it does not guarantee the good quality of all the welds nor allows the quick correction of the weld parameters if needed, for example. Hence, the need for a different approach. A non-destructive solution can guarantee the conformity, or not, of all the welds inspected since, it can be done with haste and without destruction of the product. Also, if done right after the weld production, it can indicate that some weld parameters can be adjusted preventing the production of more defective welds.

Being a structural joint, in which the weld bead shape and integrity is crucial, defects like: porosities, internal cracks, one side wetting and the lack of bead height compromises the mechanical resistance of the joint. Therefore, in the event of a collision or rollover of the vehicle, endangers the safety of the occupants. Given the importance of this joint, it is necessary to ensure that there are no internal defects and the bead height must comply with the construction standards. Depending on the manufactures, it must be equal or greater than 70% of the filler thickness, to give an example. Under that (around 0.5 mm) is considered that the joint has no structural strength. The brazed joint is established between two thin curved steel sheets, which makes non-destructive inspection particularly difficult. From Table 2.1, it is possible to reason that NDT techniques based on electromagnetic phenomena such as eddy current (EC) or electrical phenomena, such as Alternating Current Potential Drop Measurement (ACPD), are best suited to the nature of the inspection problem (Figure 4.2). However, given the technological specificity of the application in question, a solution is not commercially available, and it is therefore necessary to design, produce and validate a dedicated NDT system.

So, the concept solution proposed consisted on the development of a dedicated inspection system based on two distinct NDT techniques, to create redundancy and complementarity in the inspection process, increasing the reliability of the results and identifying all defect morphologies respectively.

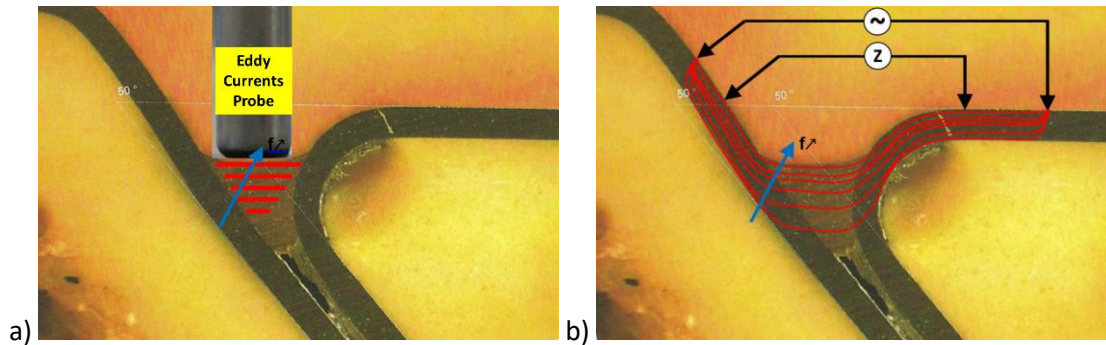


Figure 4.2 – Inspection methods envisaged.

a) eddy currents testing b) potential drop measurement.

#### Alternating Current Potential Drop Measurement (ACPDM)

The ACPDM technique consists in imposing an alternating electric current  $I$  [A], with a given frequency  $f$  [Hz] between two external points, simultaneously measuring the electrical impedance  $Z$  [ $\Omega$ ] (or simply voltage  $V$  [V]) at two internal points, for example in a configuration called a 4-point probe, although the points may not be collinear. Variations in the measurements of impedance  $Z$  [ $\Omega$ ] mean that there are material heterogeneities, namely surface or sub-surface defects. Impedance variations may also indicate a local change in electrical conductivity or a reduction in material thickness. This technique can also be used by imposing a Direct Current (DC) and simply measure the electrical resistance, instead of impedance.

In the case of the brazed joint inspection, it is proposed to adapt this technique to the geometry in question and to the inspection conditions, namely: high speed inspection required and impossibility of dragging the contact points (needles with low curvature radius) along the material surface. It is not convenient to drag the needles because this can damage the surface of the steel sheets as well as the rapid wear of the probe contacts (needles). Indeed, the effectiveness of the technique requires contact pressures greater than 500 g on each needle, especially at the inner points, where the impedance measurement is performed.

### Eddy currents

The conventional EC technique (cylindrical helical absolute probe with a ferrite core - pencil probe type) allows the identification of porosity defects or cracks on the surface and inside the brazed bead. With the correct choice of probe geometry and inspection parameters it is possible to inspect the whole height of the bead.

Given the specificity of the application and the small size of the bead surface it will be necessary to design and produce a dedicated EC probe, eventually with a tungsten carbide tip, to resist abrasion during contact with the bead surface.

### 4.3. – Geometrical and material characterization

The weld profile uniformity was evaluated along its length. From a complete weld sample of 3 meters, various profiles were sectioned and digitalized like the one from Figure 4.1. With a CAD software these profiles were recreated in 3D models as seen in Figure 4.3. Overlapping these profiles allowed an evaluation of its uniformness. From Figure 4.4a it is possible to observe that the zone with most variance corresponds to the position of the rear wheel and it is about 2,5 mm. As observed in Figure 4.4b, the variation in inspection zone is pretty much inexistent and it was considered not significant from the point of view of prototype coupling.

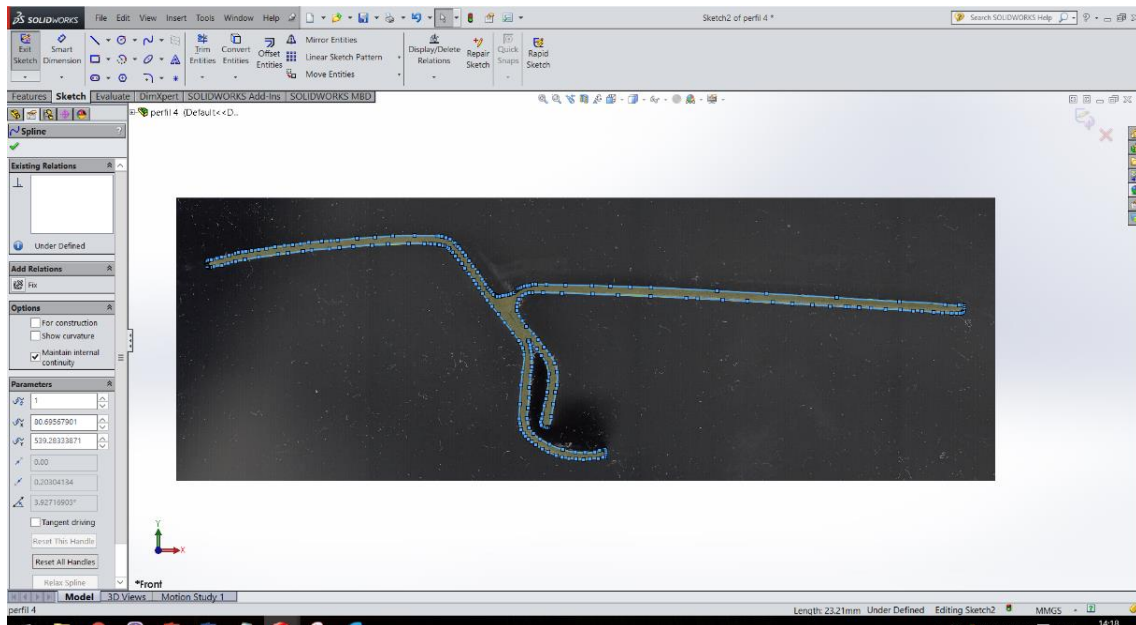


Figure 4.3 – Weld profile being digitalized to a CAD model.

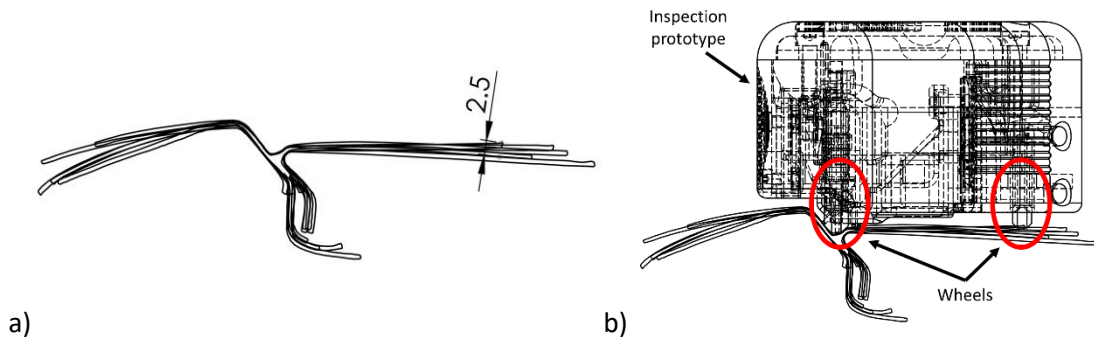


Figure 4.4 – Weld profile uniformness along its length.

a) profiles overlapped to access its uniformness along its length; b) Profile variation is not significant in the inspection zone.

The electrical conductivity was measured in all three materials involved in the weld. The weld is composed of two base materials, the side panel and the roof (both steels), and a filler material (Figure 4.5). The conductivity was measured with a commercial four-point probe with a spacing between pins of 0.635 mm as seen in Figure 4.5b. Table 4.1 shows the measured and tabled values provided by the manufacturer.

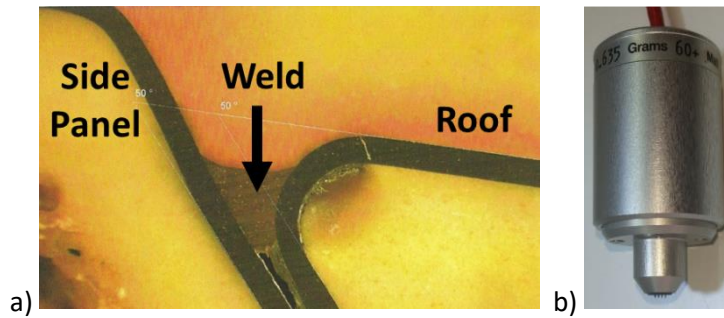


Figure 4.5 – a) Weld profile macrograph with the different components; b) four-point probe used to measure the electrical conductivity.

Table 4.1 – Resistivity and conductivity measured with four-point probe.

Component	Material (Alloys not specified due to confidential agreements)	Resistivity	Conductivity		Source
		Ω.m	× 10 <sup>6</sup> S/m	%IACS <sup>1</sup>	
Roof	Steel	1.46E-07	6.85	11.8	Tabled
		1.92E-07	5.21	8.9	Measured
Side panel	Steel	1.14E-07	8.77	15.1	Tabled
		1.55E-07	6.44	11.1	Measured
Weld	Copper alloy	4.93E-07	2.03	3.5	Measured

<sup>1</sup> International Annealed Copper Standard (IACS) establishes a standard for the conductivity of commercially pure annealed copper. The Commission established that, at 20°C, commercially pure, annealed copper has a resistivity of  $1.7241 \times 10^{-8} \Omega.m$  or  $5.8001 \times 10^7 S/m$  and may be expressed as 100 %IACS [101].

In order to get a precise value of the filler material electrical conductivity, a filler wire 1 mm diameter and 5,175 m was used. A current was imposed in its ends and the resistance was acquired which values are presented in Table 4.2.

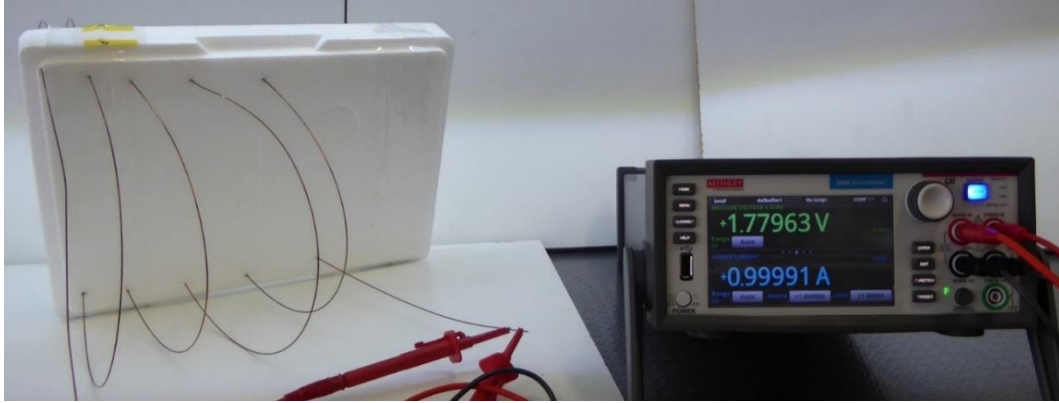


Figure 4.6 – Set up for the resistance measurement of the filler wire.

Table 4.2 – Voltage and resistance measured with different currents.

Current [mA]	Voltage [mV]	Resistance [ $\Omega$ ]
10	17.788	1.7788
50	88.914	1.77828
100	177.812	1.77812
500	888.79	1.77758
1000	1779.21	1.77941

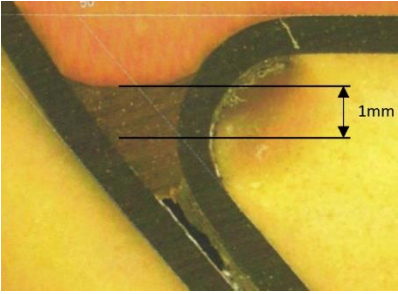
The mean resistance measured was 1.778  $\Omega$  which according to Eq. 4.1, in which R [ $\Omega$ ] is the resistance, L [m] is the length of the wire, A [ $m^2$ ] is the section area of the wire and  $\rho$  [ $\Omega.m$ ] the resistivity, which translates into a resistivity of  $2.7 \times 10^{-7} \Omega.m$  of a conductivity of  $3.7 \times 10^6 S/m$  or 6.39 %IACS.

$$R = \frac{\rho \times L}{A} \quad \text{Eq. 4.1}$$

The eddy currents penetration depth in the material depends on the frequency used, the material magnetic permeability and its electrical conductivity according to Eq. 2.5. Being magnetic permeability and electric conductivity intrinsic to the material, the only way to change penetration depth is by varying the EC probe frequency. The penetration depth was calculated

for some frequencies in order to understand how deep it could go in this specific case and the results are presented in Table 4.3.

Table 4.3 – Penetration depth for different frequencies.

Frequency [kHz]	Penetration depth [mm]	Profile macro
100	<b>1.117</b>	
250	<b>0.706</b>	
500	<b>0.500</b>	
750	<b>0.408</b>	
1.000	<b>0.353</b>	
2.000	<b>0.250</b>	
3.000	<b>0.204</b>	

Considering: Magnetic permeability  $\mu = 4\pi \times 10^{-7}$  [H/m] and electric conductivity  $\sigma = 2.03 \times 10^6$  [S/m]

#### 4.4. – Numerical simulations

Numeric simulations were performed aiming to understand electric and magnetic phenomena involved in the probe operation in this geometry and materials. A CAD model was designed from a profile macro, digitalized according to Figure 4.3, to be as similar as possible to reality (Figure 4.7a). The material properties were inserted according to the measured proprieties mentioned above. For this, a numerical simulation software (ANSYS Electronics) was used, and it calculates an approximate numerical solution of Maxwell's equations in their full formulation, Finite Integration Technique (FIT). In Figure 4.7b is depicted the model used and the tetrahedral mesh representation which contains about 2.7 M elements.

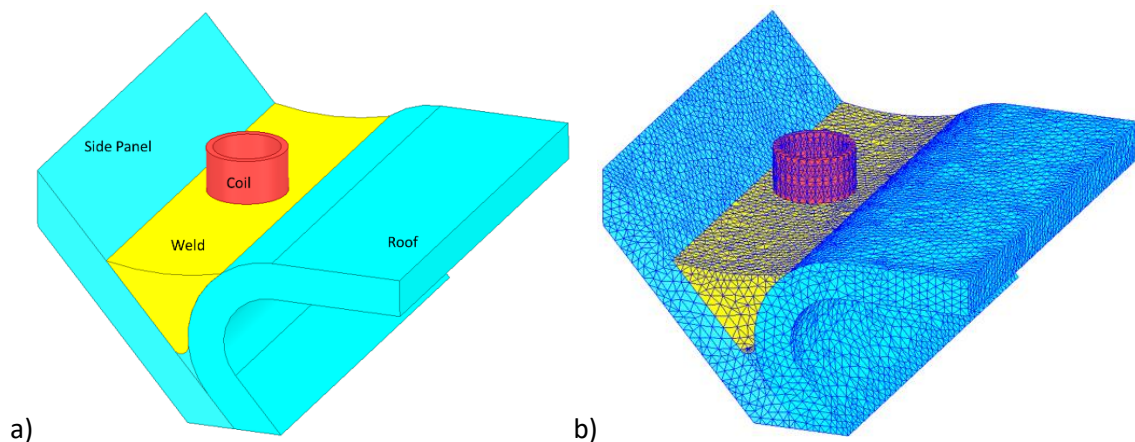


Figure 4.7 – a) CAD model used in the numeric simulations; b) Mesh representation with the tetrahedral elements.



Figure 4.8 depicts the result obtained of eddy current testing simulation at a frequency of 10 kHz and 3 MHz. The coil used for this simulation has 1.8 mm diameter, 1 mm of height and 0.15 mm thickness. It has 100 windings, 0.2 mm lift-off and an alternated current of 1 A was imposed. The eddy currents concentrate on the weld and cover most of its depth at lower frequencies (10 kHz) and at higher frequencies (3 MHz) the current density concentrates mostly on the weld surface as expected.

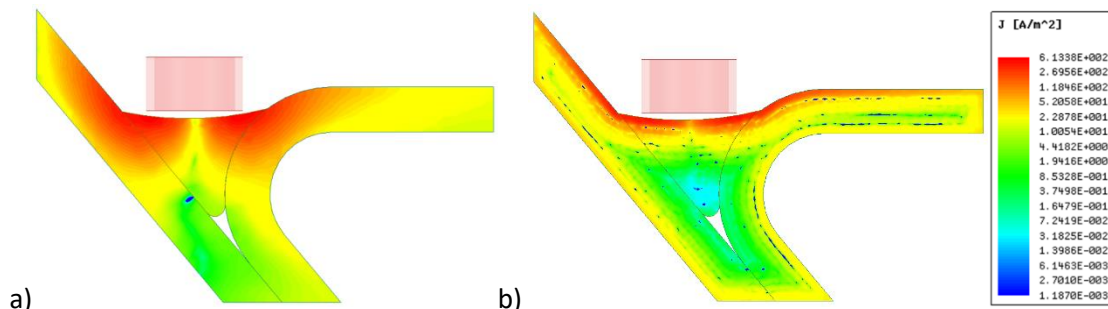


Figure 4.8 – Eddy current testing simulation with a 100-winding coil at a frequency of:  
a) 10 kHz; b) 3 MHz.

Potential drop measurement technique was also simulated in order to understand the ideal 4-point configuration for the case. The 4 points conventional position was tested in a line in which in the extreme pins, shown in red in Figure 4.9a, the current is injected, and the reading is made between the two central pins represented in green. Figure 4.9b allows to observe the currents behaviour passing through the material when there is no defect present.

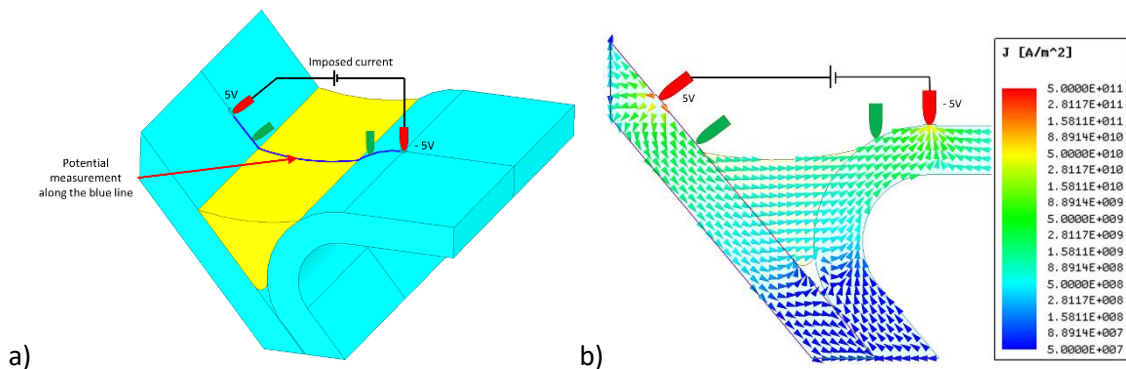


Figure 4.9 – Four-point probe simulation: a) pins positioning towards the profile; b) current flow through the weld.

Figure 4.10 shows the results obtained with different defect morphologies/locations. The current flow is deviated by the present defects. Figure 4.11 depicts the potential along the current flow direction with different defects. These results acknowledge that there are changes in the current flow and potential throughout the weld in the presence of defects. Current density vector field is greatly affected by surface and sub surface defects while defects away from the inspection surface do not affect the current density vector field. Although the potential drops



significantly throughout the way, the potential drop between the middle needles does not change much with a defect.

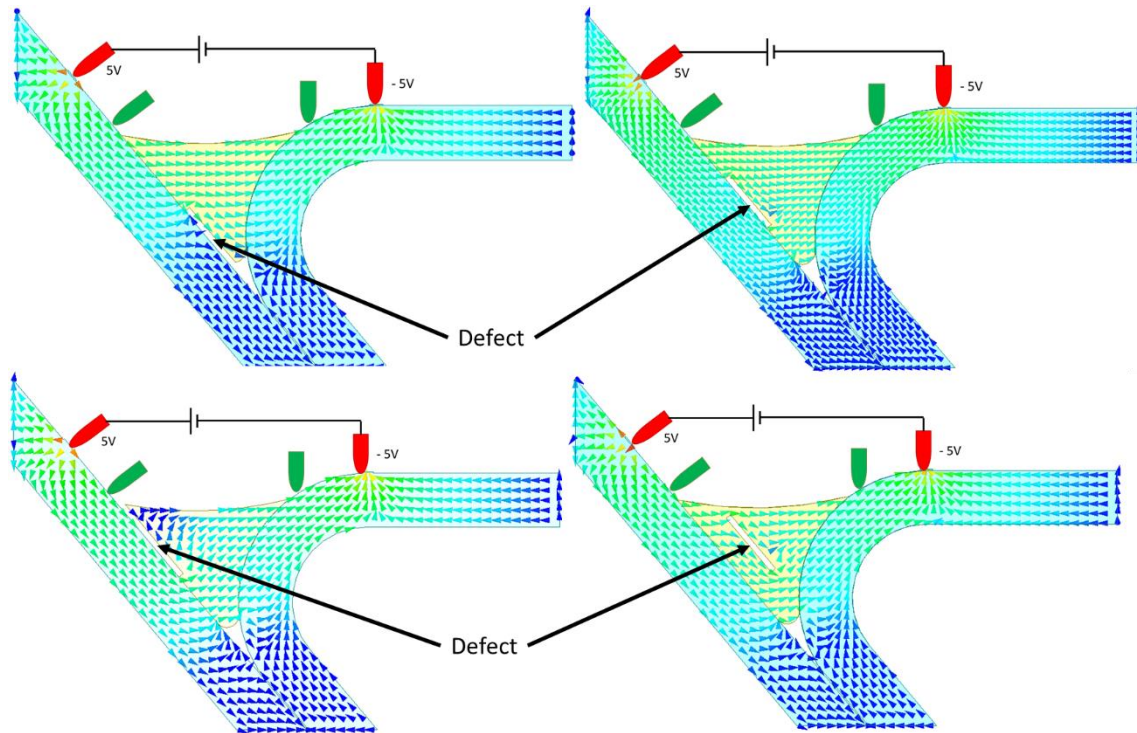


Figure 4.10 – Current flow behaviour in a weld with different defects.

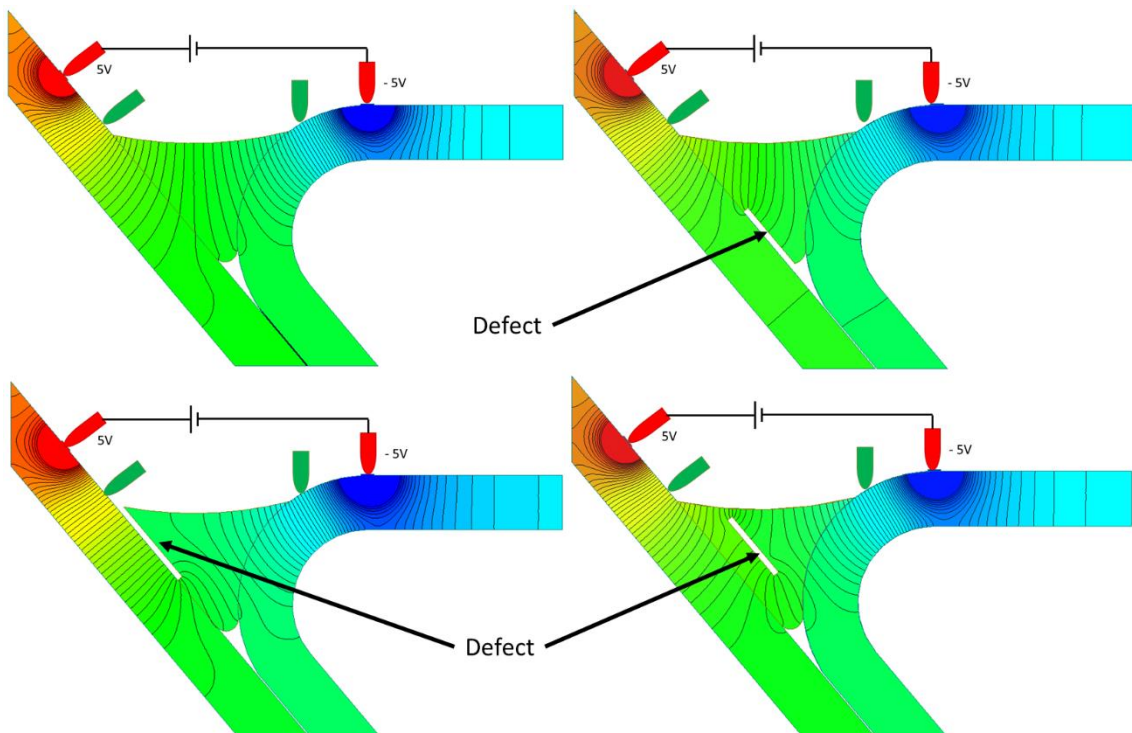


Figure 4.11 – Potential along the current flow direction with different defects.

However, although it is interesting to see what is happening in the material, experimentally, only the two interior points are available to measure from. A line was created between the two

extreme current injection pins and a plot was built with the potential along that line. This way, it is possible to understand if the potential drop between the selected points (internal pins) is significant. These two pins must necessarily be outside the weld bead to ensure that any defect in the weld is between them (including lack of fusion), otherwise it will not be detected. However, as seen in Figure 4.12 the potential drop between the green pins' little changes regardless of the defect. For this reason, other ways of solving this problem were sought.

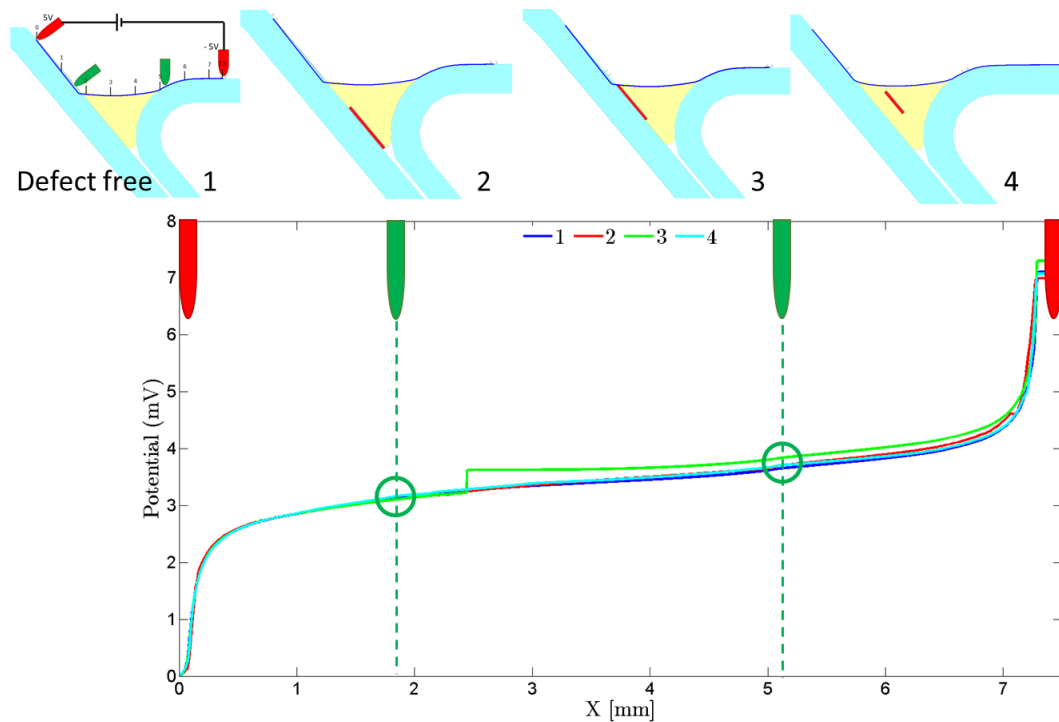


Figure 4.12 – Potential drop along the transversal line that contains all the pins.

The approach taken was to perform different simulations and evaluate the potential distribution on the weld and base materials surface. The results obtained, shown in Figure 4.13, allowed to understand that the aligned pins could not be the best solution. Arranged in a cross shape, keeping the current injection pins in the same place and placing the sensitive ones on the weld bead apart from each other according to the Figure 4.14, could be a better solution.

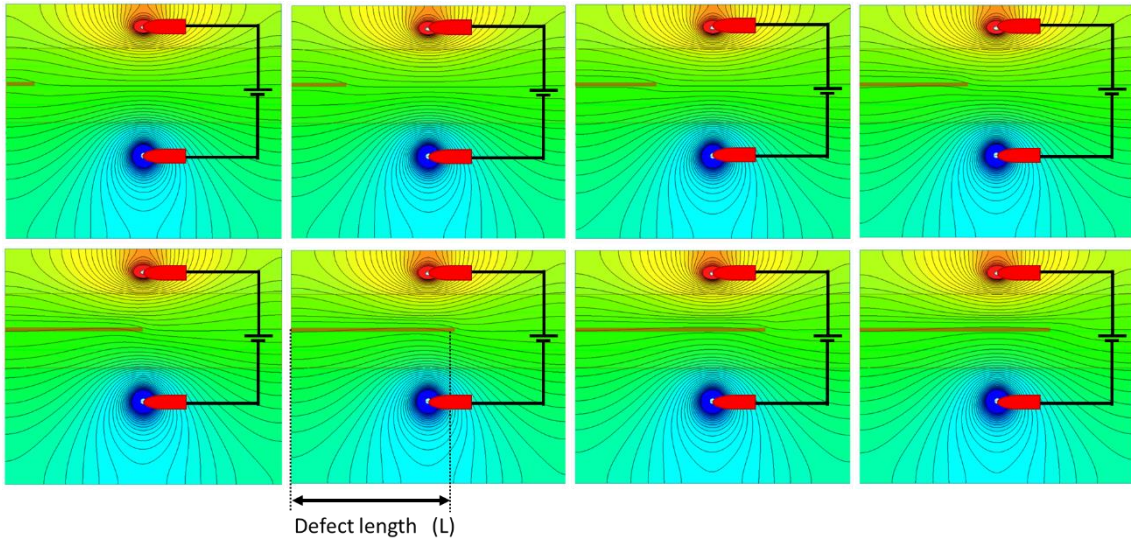


Figure 4.13 – Potential distribution from the top with an increasing defect.

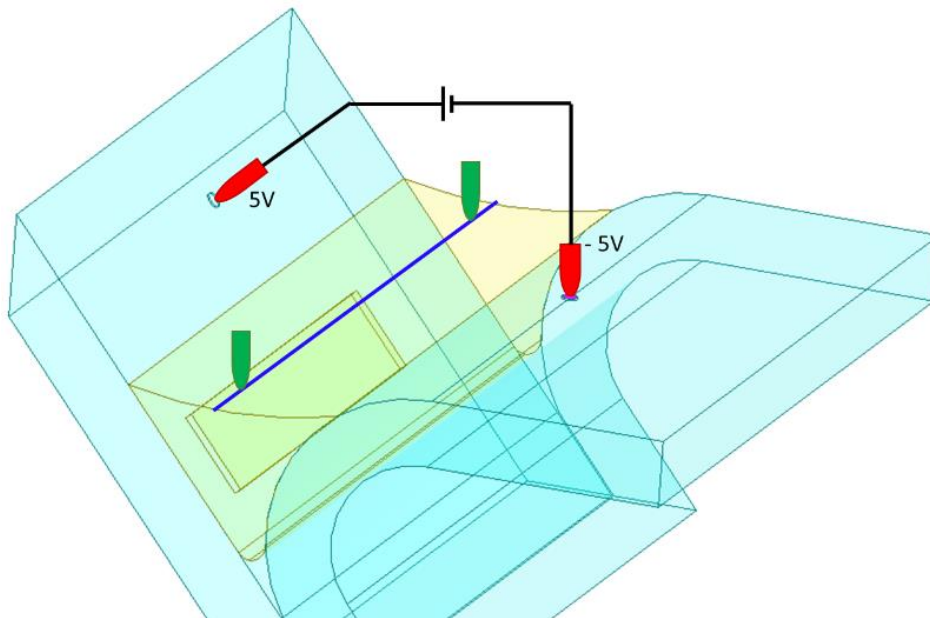


Figure 4.14 – Alternative pin distribution (cross shape).

Several simulations were performed and the potential along a longitudinal line in the middle of the weld bead (blue line in Figure 4.15) was evaluated. In the graph, in Figure 4.15, each line represents the potential variation along the weld bead for each defect length. From these curves, two locations were selected in which the difference between the potentials were higher, this variation is represented by another line with a red arrow pointing towards it. These locations correspond to the positions 1 mm and 6 mm which corresponds to an offset of 4 and 1 mm, respectively, from the transversal line that contains the current imposing pins.

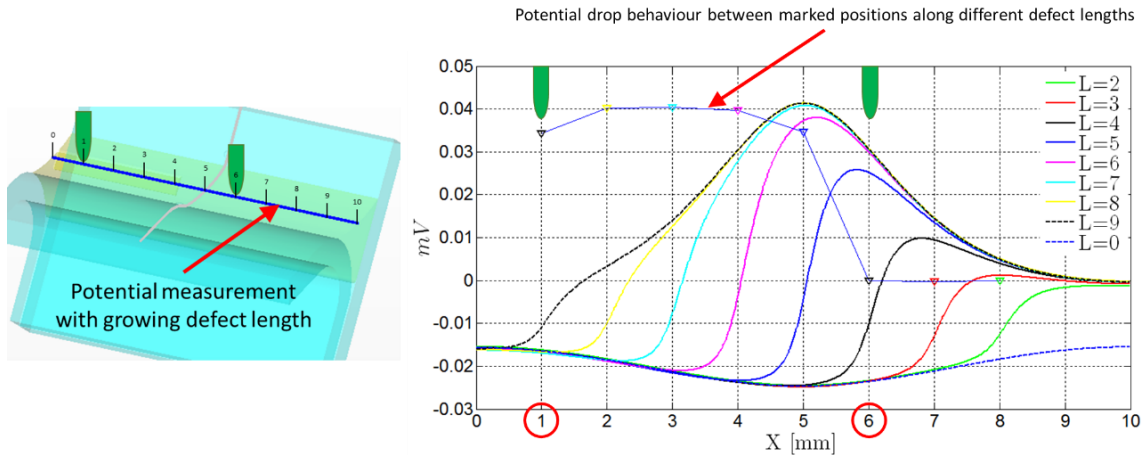


Figure 4.15 – Potential distribution along the blue longitudinal line for different defects with increasing length L.

## 4.5. – Customized NDT system development

### 4.5.1.– Functional prototype chassis

The design of the functional prototype for the weld inspection took into account the following requirements:

- The device should be coupled to the weld allowing only one degree of freedom which corresponds to the linear movement along the weld;
- The device should be prepared to be operated by robot and by hand;
- The device should be ergonomic to the hand for manual operation;
- The device should hold one four-point probe;
- The device should hold two EC probes to operate with two different frequencies at the same time;
- The device should be parametrizable for easy adaptation to different inspection geometries.

The manufacturing process chosen to produce the prototype was 3D printing as it allows a faster, cheaper and easily customizable solution. And it can also be used for the final product as has been seen before [279].

Figure 4.16 depicts several preliminary test chassis to reach the final solution. The first five chassis were focused on ergonomics and an attempt to take advantage of 3D printing specificities in favour of the pretended solution.



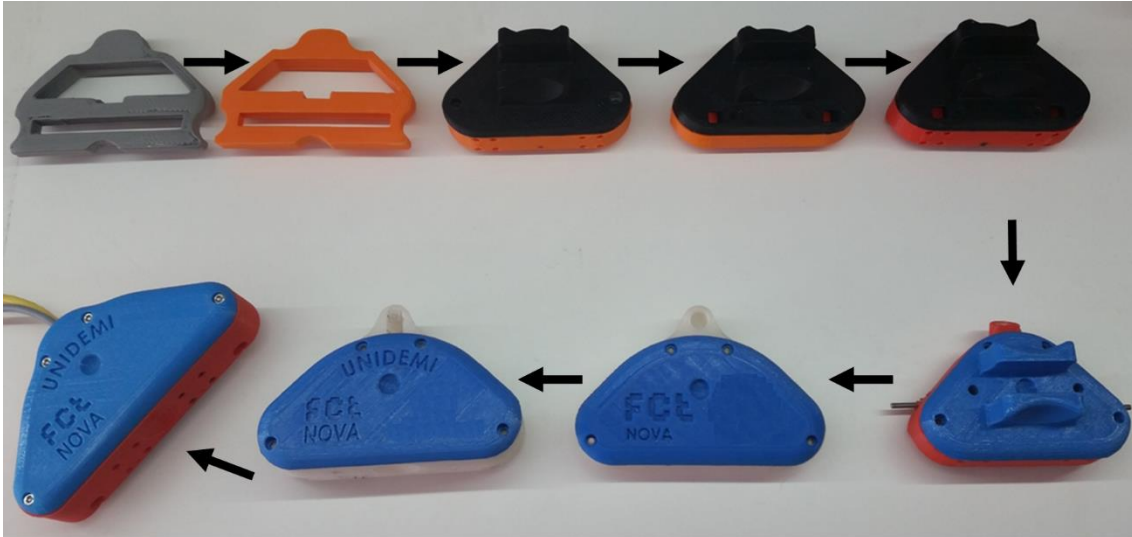


Figure 4.16 – Device chassis designed in the iterative process to reach the pretended solution.

On a first approach, the chassis had three footholds in which two would be over the weld bead forcing the device to move in the weld direction solely. To make sure the foothold would not slip off the weld bead, while handheld, a set of magnets was incorporated in the chassis.

The friction between the device and the weld bead generated too much vibration and was subjected to wear too fast. The footholds were replaced by three bearing wheels to cancel the vibration and wear which resulted in a bigger chassis to accommodate them. On a first approach, the wheels were tin machined and inserted in a radial bearing. This solution cancelled the vibration but added too much noise so, polymer 3D printed wheels replaced tin ones as seen in Figure 4.17.

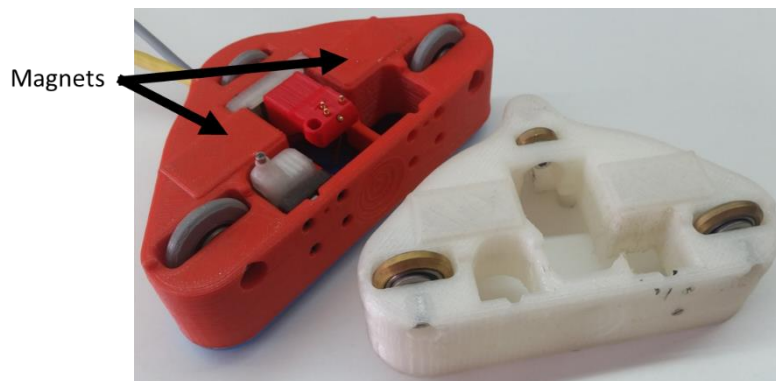


Figure 4.17 – Preliminary device chassis with bearing tin wheels on the right and bearing 3D printed on the left.

For demonstration purposes and laboratorial experimental tests, two step motors were coupled to the weld bead wheels to automate the weld scanning. On a final implementation, this movement would be done with a robot arm. The final iteration of the autonomous

movement prototype is depicted in Figure 4.18. And, in Figure 4.19 is shown the final product to implement in real environment to be coupled with an arm robot.

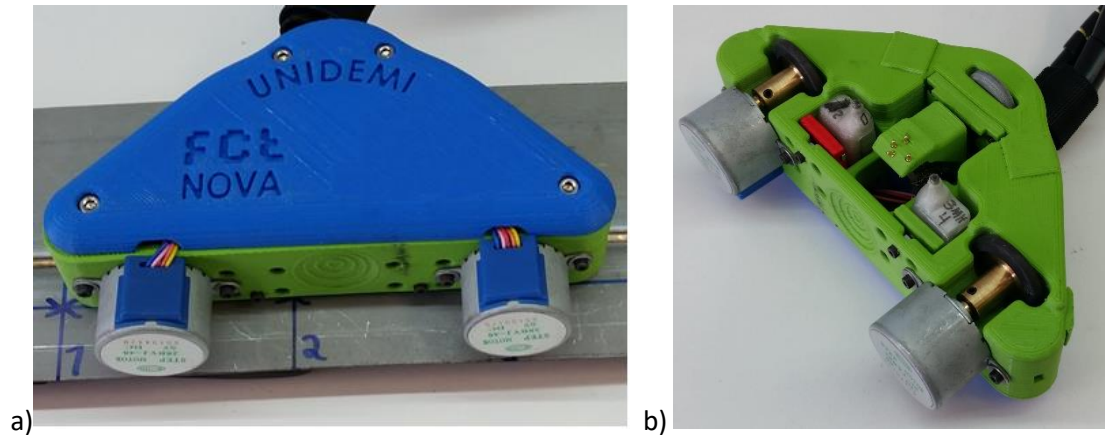


Figure 4.18 – Scanning device with step motors for movement.  
a) top view of the device over a weld specimen; b) bottom view;

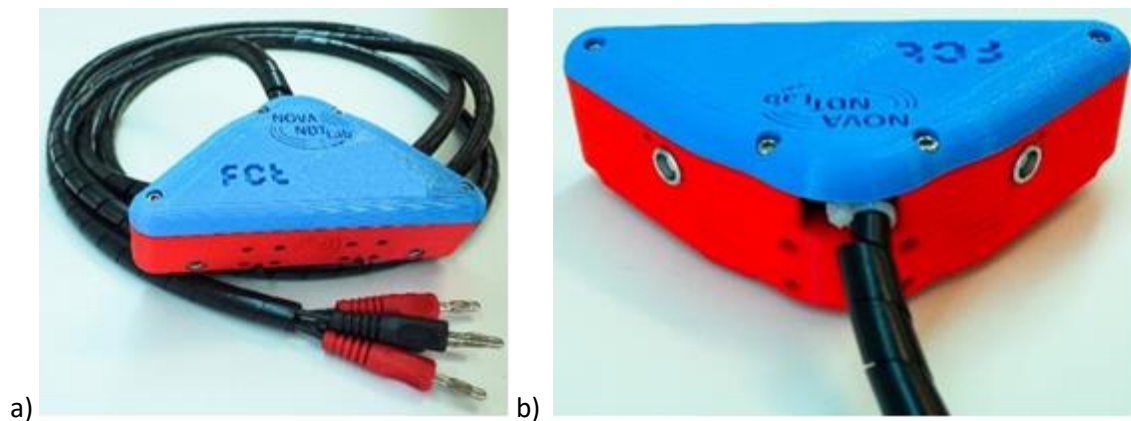


Figure 4.19 – Final scanning device for robotic arm movement.  
a) front view of the device; b) back view;

#### 4.5.2.– Eddy current probes

Tailored made eddy current probes were designed to fit the chassis of the inspection prototype. Bobbin coils with a reduced diameter were created specifically to fit the weld bead.

Weld bead materials and geometry are a design constraint so, in order design customized EC probes for this specific problem the frequency range at which the probes should operate was calculated as shown in Figure 4.20, depending on the penetration depth desired. Low frequencies for surface and sub-surface defects and higher frequencies for surface defect only. Having the target frequencies been selected, different probe characteristics were numerically simulated and experimentally tested. Parameters like number of windings, wire diameter, wire material, core material, core dimensions, core geometry, shield, material, shield dimensions, shield geometry, etc which are all characteristics that highly influence the probe behaviour at

different frequencies (Figure 4.21b). Several EC probes were produced with different characteristics combinations. Each bobbin coil produced was thoroughly characterized (Figure 4.21a) with numerous frequency sweeps with several materials with different electrical conductivities and lift-offs. The characterization allowed through trial and error with help from the numerical simulations and prior knowhow with an increased technical sensitivity to find the best combinations for the desired purpose.

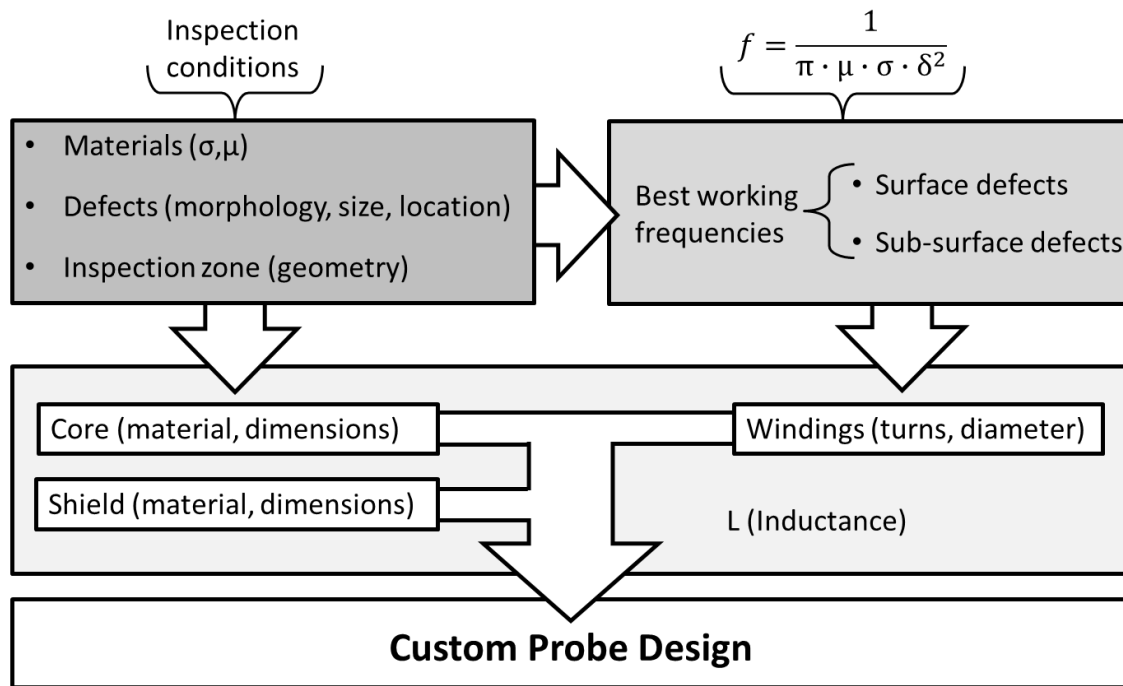


Figure 4.20 – Probe design sequence.

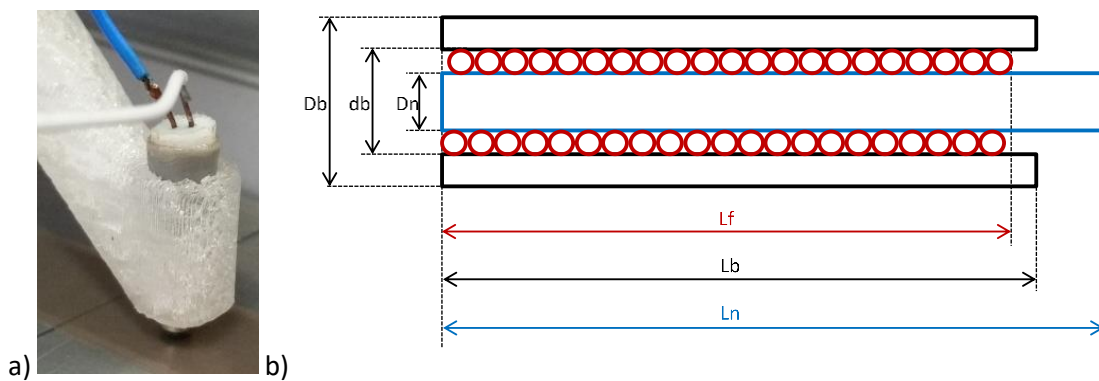


Figure 4.21 –EC bobbin probe: a) final probe assembled over a conductivity standard for impedance characterization; b) probe geometric parameters.

A probe holder was designed and produced to hold two bobbins together (Figure 4.22). One bobbin travel through the weld bead and is connected in bridge differential with the other that is pointed in the opposite direction and in contact with a small specimen of a good weld. Operating in bridge differential allows a greater sensibility since the inspected weld is being compared with a good one. In Figure 4.23a is depicted one probe encapsulated and in

Figure 4.23b the device that holds two identical probes. This device that holds the probes is attached to the chassis by a linear bearing and a spring which ensures a constant lift-off (Figure 4.23c).

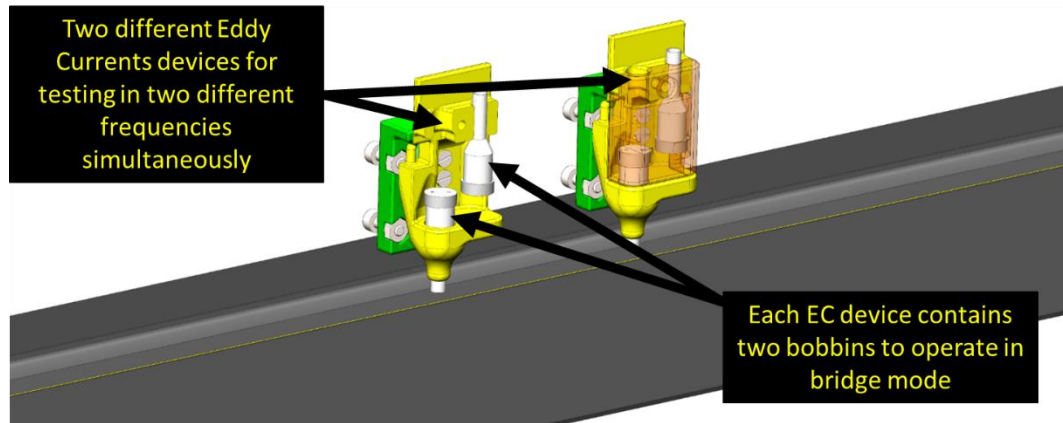


Figure 4.22 – Set of tailored EC probe holder.

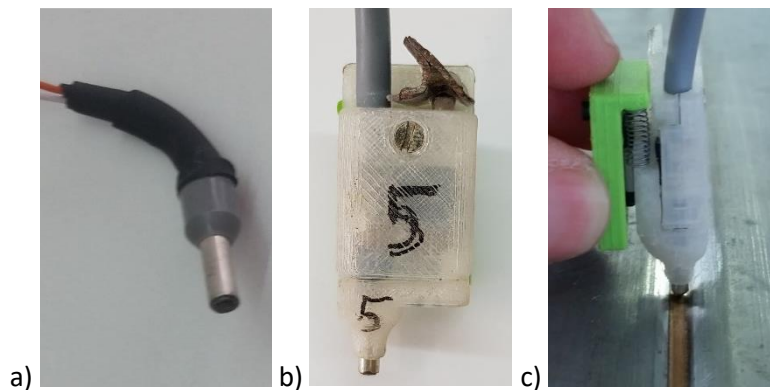


Figure 4.23 – Tailored EC probes.

a) EC individual bobbin; b) device with a set of two bridge differential bobbins; c) device over the weld testing the spring that maintains the probe constant lift-off.

#### 4.5.3.– Four-point probe for potential drop measurement

A four-point probe holder was designed and produced with 3D printing. The location of the probe pointers is defined in a CAD model which is created as well when printing the holder. Four spring loaded connectors were assembled in the holder and welded to the cables that will connect the probe to the source meter unit. The simulations performed in §4.4 were crucial to determine the pins locations. The probe is depicted in Figure 4.24.





Figure 4.24 – Four-point probe.

#### 4.5.4.– Laboratorial set up

In order to perform the experimental tests, both in laboratorial [280] and relevant environment, a structure that holds all the equipment required for the inspection was designed and produced (Figure 4.25a). The structure holds the impedance analyser, the SMU, and the inspection device. Also, there is a voltage source and step motors drivers for the device movement (Figure 4.25b). The structure top also allows the landing of a laptop which connects to the system through a communication DAC and a dedicated LabVIEW software controls the movement and signal acquisition.

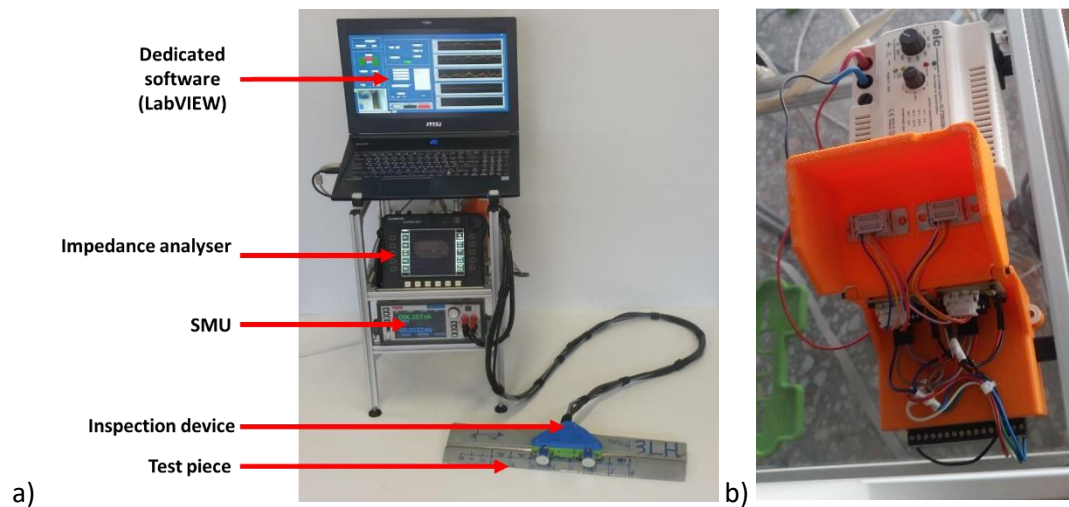


Figure 4.25 – Inspection set-up: a) equipment structure; b) voltage source and drivers for the step motors.

## 4.6. – Experimental results and discussion

### 4.6.1.– Industrial environment – Real defects

Experimental tests were made in relevant environment. The movement, as well as the signal acquisition, were controlled and programmed in LabVIEW environment and commercial EC

testing equipment (Nortec 500) was used for impedance measurements. A van chassis weld was inspected without prior knowledge of its condition. The eddy currents system detected a few extremely small defects, notches with diameters of about 0,13-0,27 mm. Figure 4.26 to Figure 4.29 depict the impedance measured and the respective defect picture. Frequencies of 250 kHz, 750 kHz and 1 MHz were used. The defects were detected with the different frequencies being the 250 kHz the one with the greater signal to noise ratio. Since the probes are operating in bridge mode but only one bobbin is over the weld the result obtained is an absolute type, represented by a peak. The results obtained present a very good signal to noise ratio considering the extremely small defects dimensions.

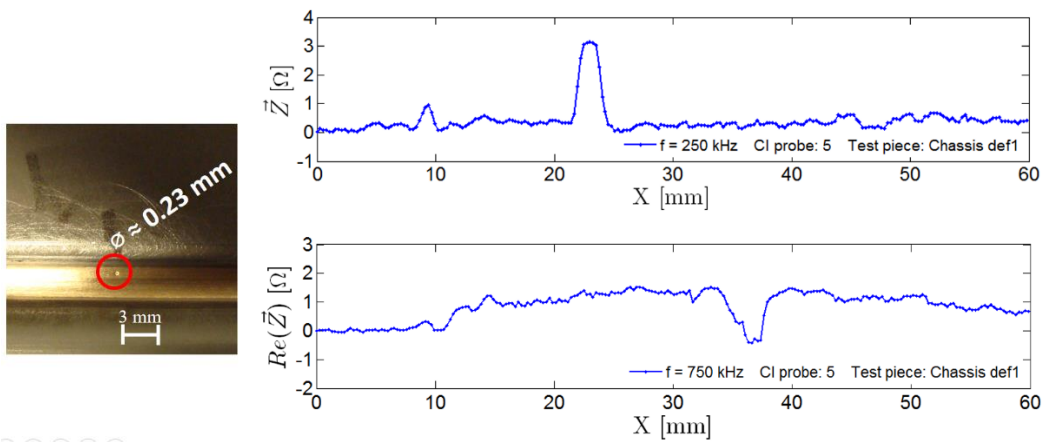


Figure 4.26 – Relevant environment experimental result where a 0,23 mm diameter notch was detected with 250 kHz and with 750 kHz.

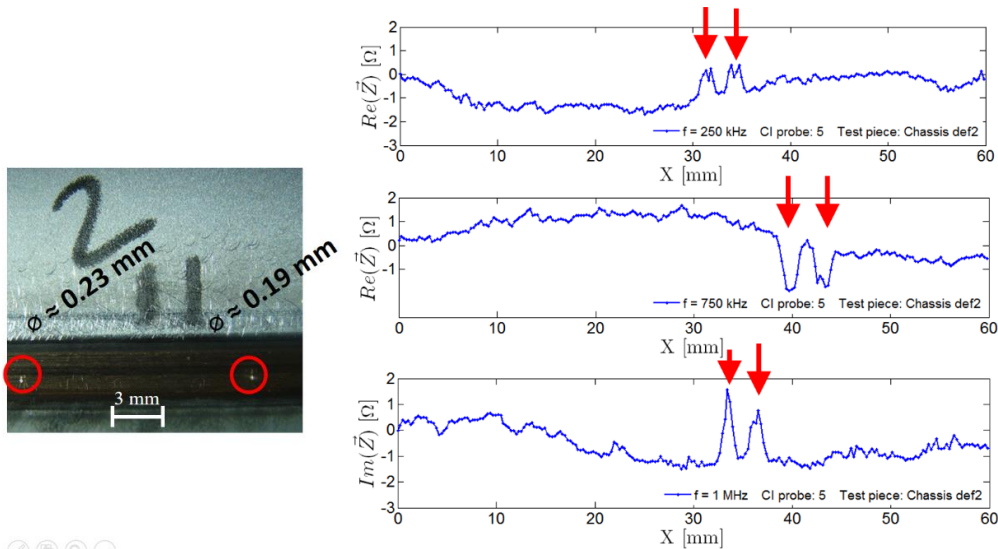


Figure 4.27 – Relevant environment experimental result where two notches were found with 250 kHz, 750 kHz and 1 MHz.

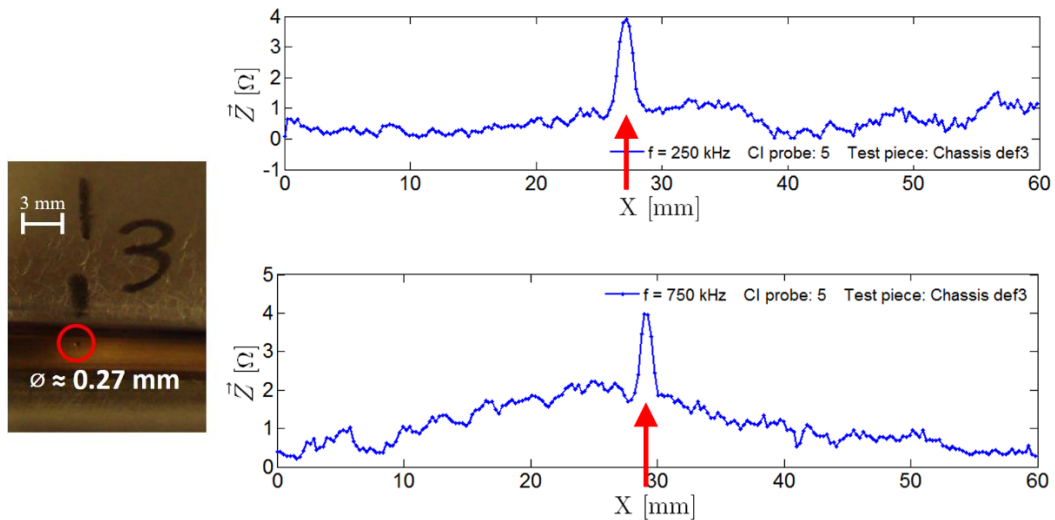


Figure 4.28 – Relevant environment experimental result where a notch was detected with 250 kHz and 750 kHz.

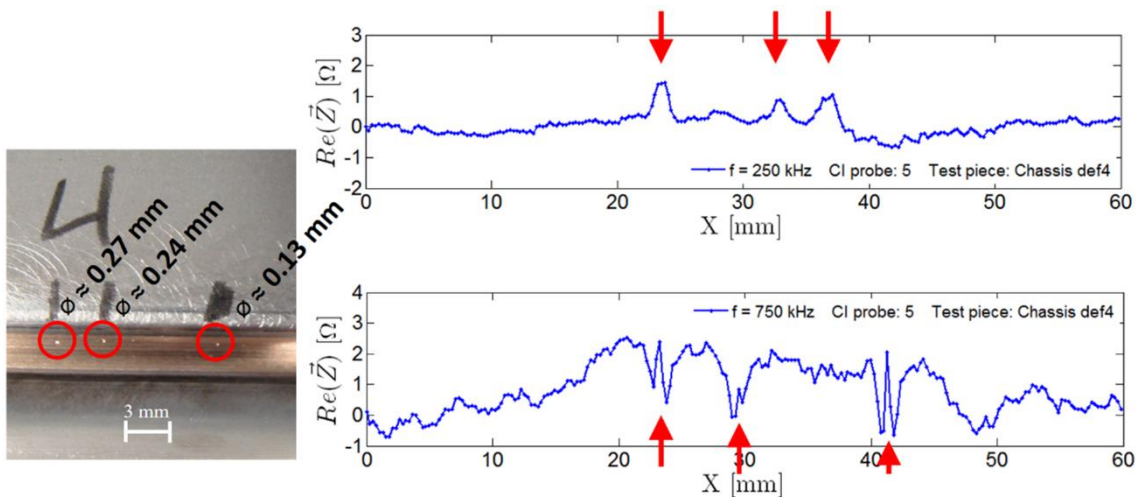


Figure 4.29 – Relevant environment experimental result where three notches were found with 250 kHz and 750 kHz.

#### 4.6.2.– Laboratory conditions – Artificial defects

Several experimental tests were done in laboratorial environment using specimens with artificially made defects. Drilled holes with several different orientations and longitudinal milling and electrical discharge machining EDM defects were done. Figure 4.30 and Figure 4.31 depict sample 2LH with enlarged defect pictures.

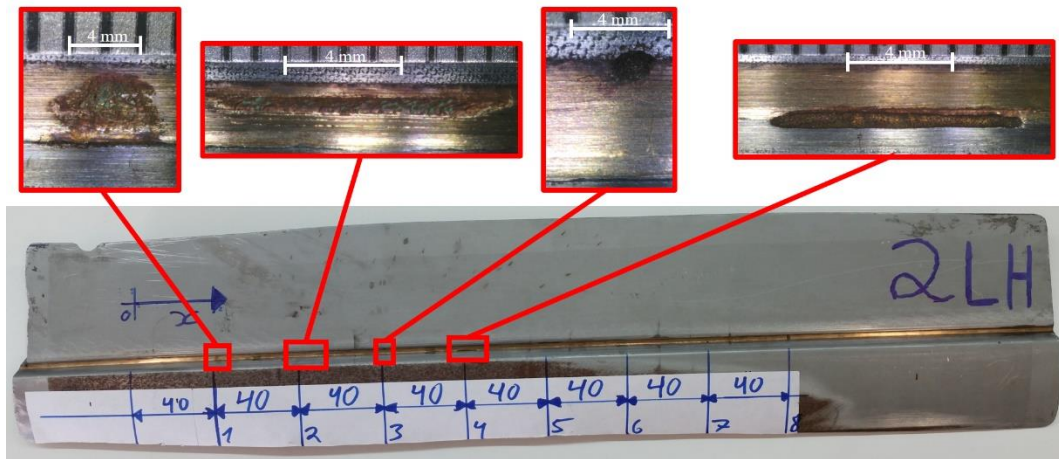


Figure 4.30 – Sample 2LH with enlarged defects 1 to 4.

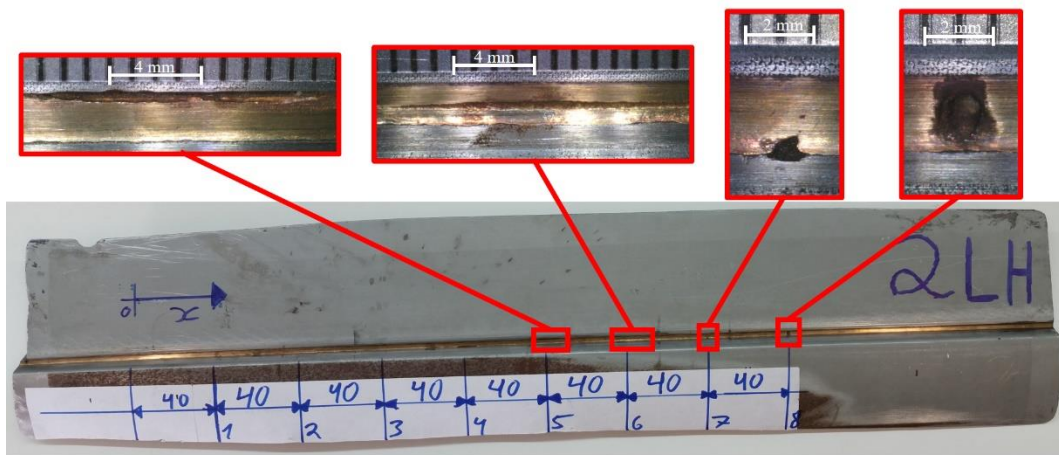


Figure 4.31 – Sample 2LH with enlarged defects 5 to 8.

Figure 4.32 presents an eddy current test on sample 2LH at a frequency of 250 kHz. Defects 3, 4 and 7 did not create a visible signal amplitude since they are too close to the interface and therefore too far away from the EC probe. Defect 5 did create a very visible signal output, despite the defect being in the interface, because the probe was scanning closer to this interface. The probe would have a better performance if its outside diameter was the same as the space between interfaces but that could lead to getting the probe stuck in between or jumping over changing the lift off in case the weld bead width decreases. The remaining defects were detected but without the best SNR. Using a 750 kHz frequency, the resulted improved considerably and a better signal to noise ratio was achieved as depicted in Figure 4.33. Increasing the frequency to 1 MHz did not improve the output as depicted in Figure 4.34.



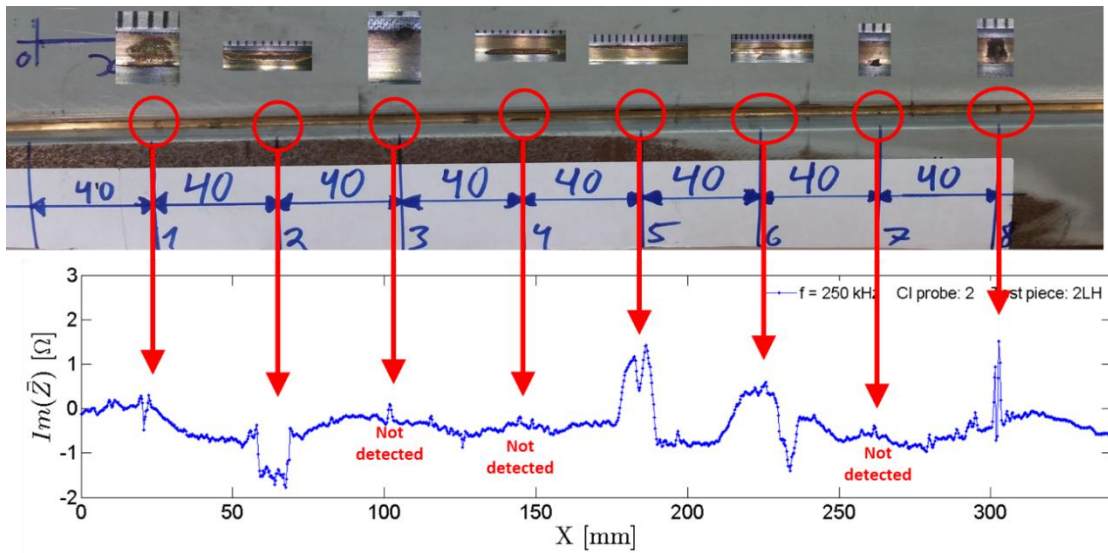


Figure 4.32 – EC probe output signal of sample 2LH at a frequency of 250 kHz.

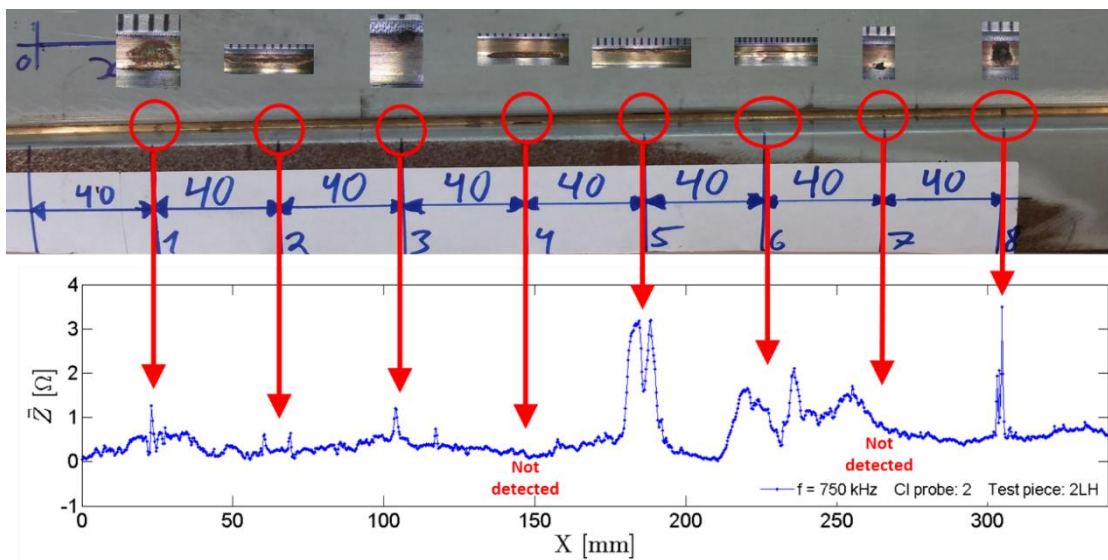


Figure 4.33 – EC probe output signal of sample 2LH at a frequency of 750 kHz.

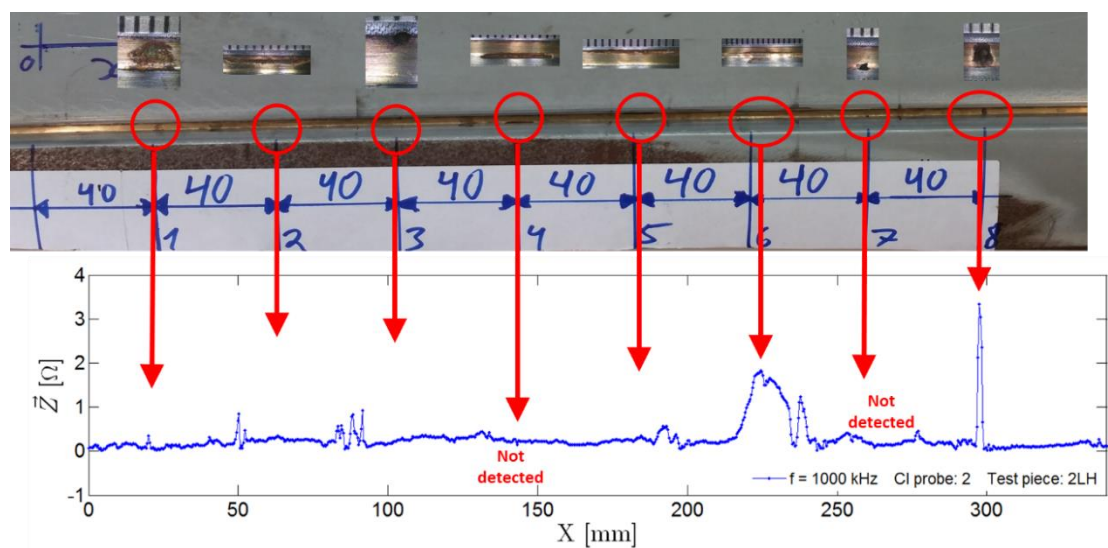


Figure 4.34 – EC probe output signal of sample 2LH at a frequency of 1 MHz.

A potential drop measurement using the four-point probe of the device was used to inspect the sample 2LH (which can be made at the same time the EC testing is done). A current of 1 A was imposed on the outer pins. Figure 4.35 depicts the output of the four-point probe. This technique allows the detection of longitudinal defects, with a sinusoidal shape, near the interface that the EC cannot reach like the defect 4 that was detected here but not with the EC testing.

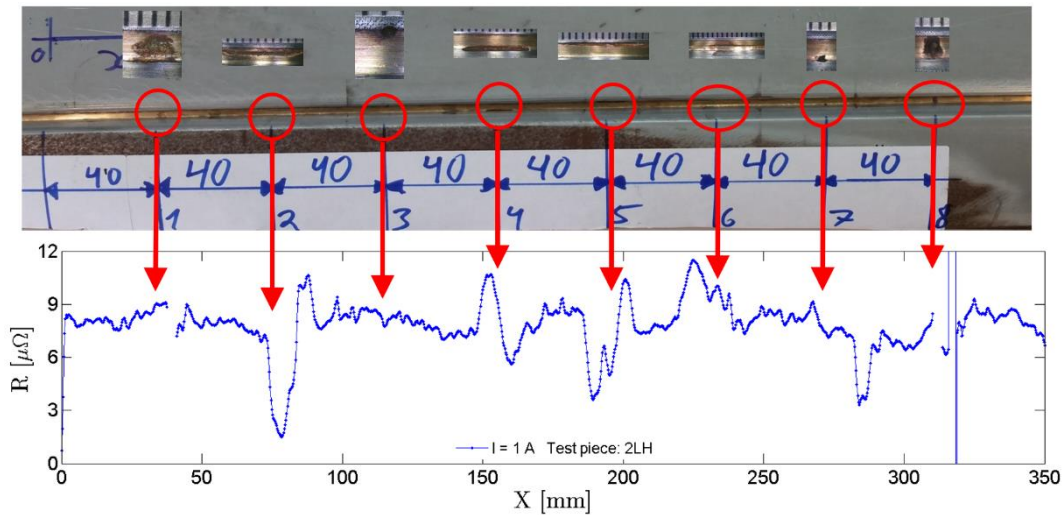


Figure 4.35 – Four-point probe output signal of sample 2LH.

Another sample, with different defects, was tested. Denominated 3LH it is composed of seven defects, five drilled holes and two longitudinal defects. Figure 4.36 and Figure 4.37 depict the specimens with the respective zoomed defects and their characterization.

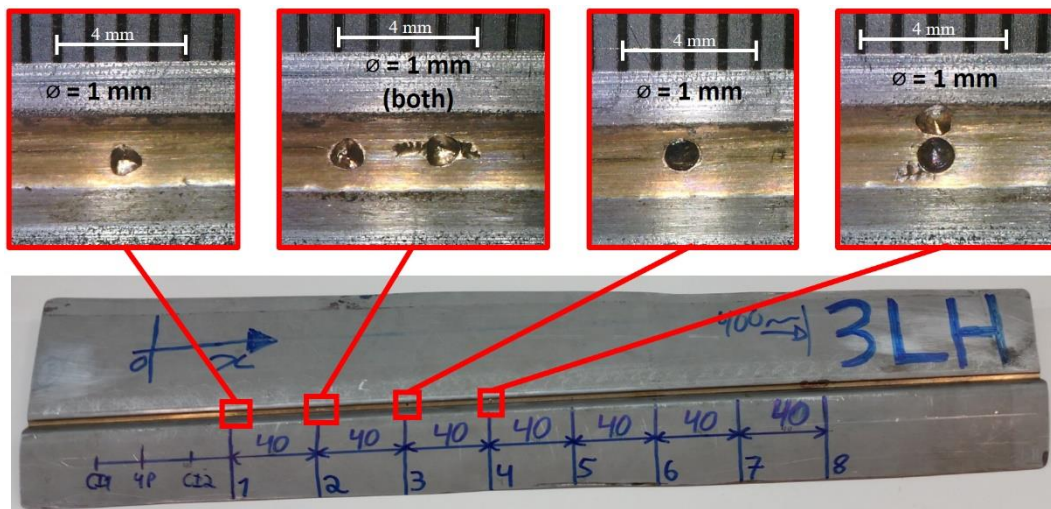


Figure 4.36 – Sample 3LH with enlarged defects 1 to 4.

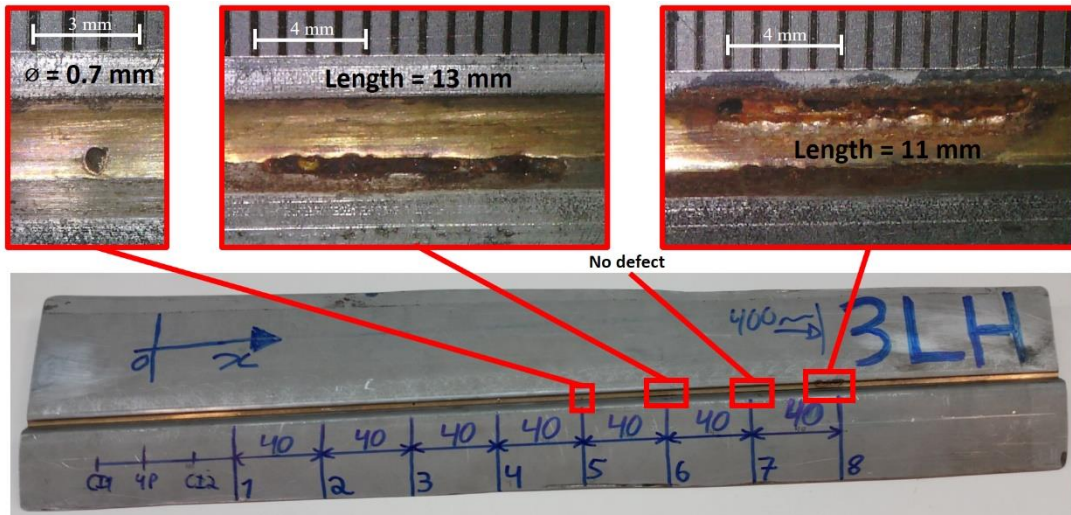


Figure 4.37 – Sample 3LH with enlarged defects 5 to 8.

In Figure 4.38 is shown the output signal of the EC testing at 750 kHz in of the test piece 3LH. The defects are very well defined with a very good signal-to-noise ratio. Defect 6 may not have been detected due to the probe being too distant.

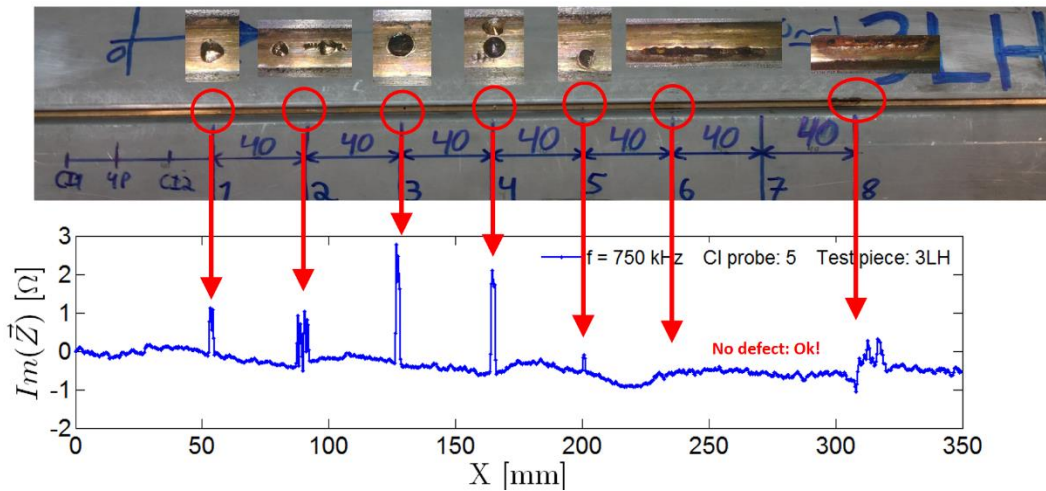


Figure 4.38 – EC probe output signal of sample 3LH at a frequency of 750 kHz.

Test piece 4LH is shown in Figure 4.39 where seven artificial defects were produced. These defects consist on drilled holes, some performed from the bottom and others from the side as illustrated. Two of the defects are not visible from the weld surface.



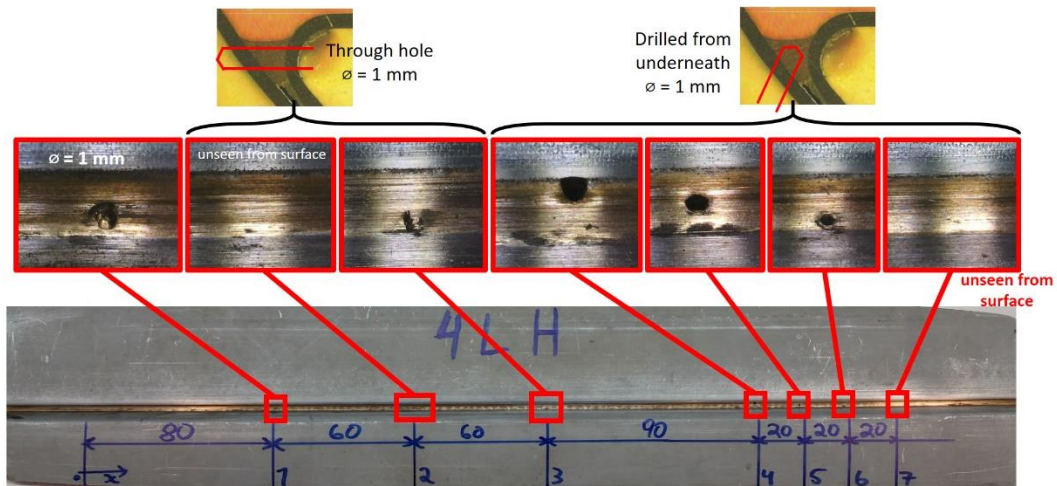


Figure 4.39 – Sample 4LH with enlarged defects 1 to 7.

Apart from defect number 2, all the defects are clearly detected by the EC probe at frequencies of 250, 750 and 1000 kHz as shown respectively in Figure 4.40, Figure 4.41 and Figure 4.42. Defect number 2 is too far away from the weld bead surface meaning, the probe is too far away from the defect to measure eventual deflections of the EC. Although defect number 7 was not at the surface, it was also detected but with a lower amplitude.

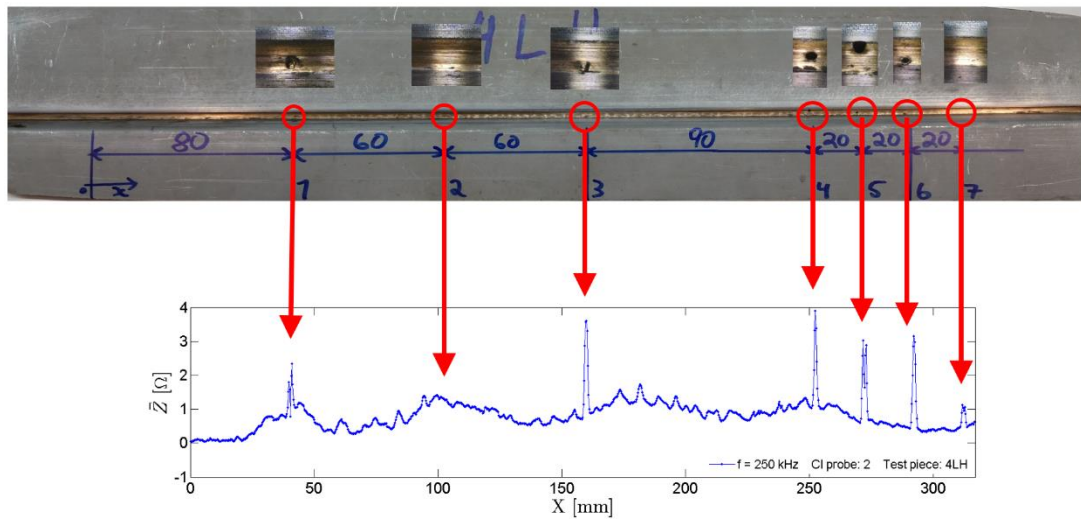


Figure 4.40 – EC probe output signal of sample 4LH at a frequency of 250 kHz.



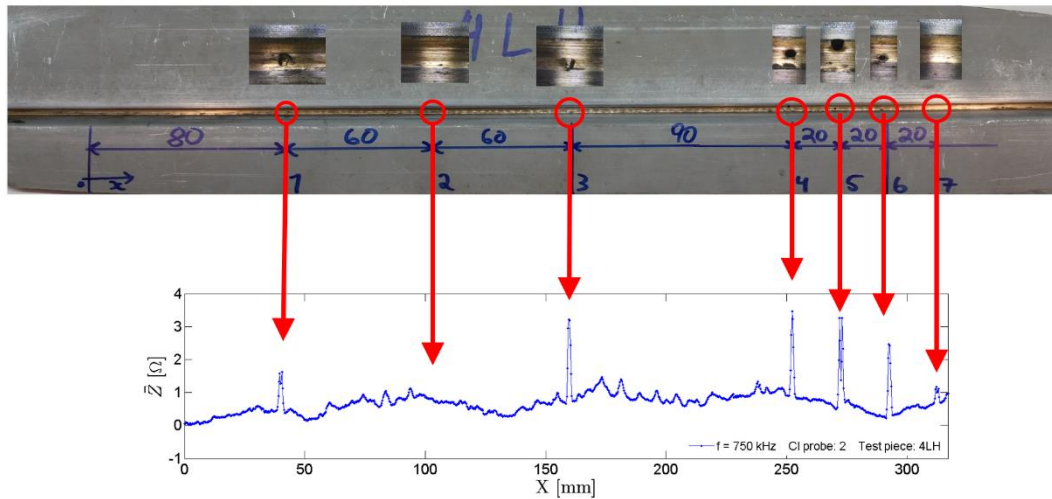


Figure 4.41 – EC probe output signal of sample 4LH at a frequency of 750 kHz.

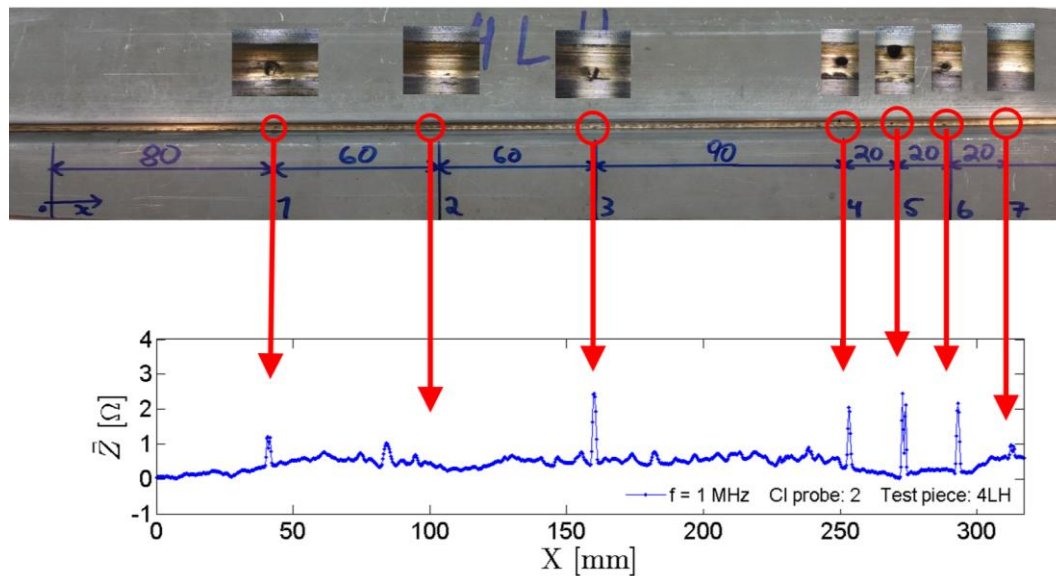


Figure 4.42 – EC probe output signal of sample 4LH at a frequency of 1 MHz.

In order to distinguish surface from sub-surface defects, high and low frequency probes were produced. The idea consists in detecting surface defects with both probes but, detecting sub-surface defects with only the low frequency probe since it has a higher penetration depth. A sample with 1 surface defect (drilled hole) and 2 sub-surface defects (not visible from the weld bead surface) was inspected to validate this. As seen in Figure 4.43 the surface defect was detected by both bobbins and the low frequency bobbin coil detected all the defects. The high frequency probe operated at 3 MHz and the low frequency probe at 20 kHz. The same probe was tested in Figure 4.44 but with different defects. Two drilled holes were produced one from the bottom and one from the top simulating one surface defect and one sub surface. As envisaged, the low frequency probe detected both defects and the high frequency bobbin coil detected the surface one only.

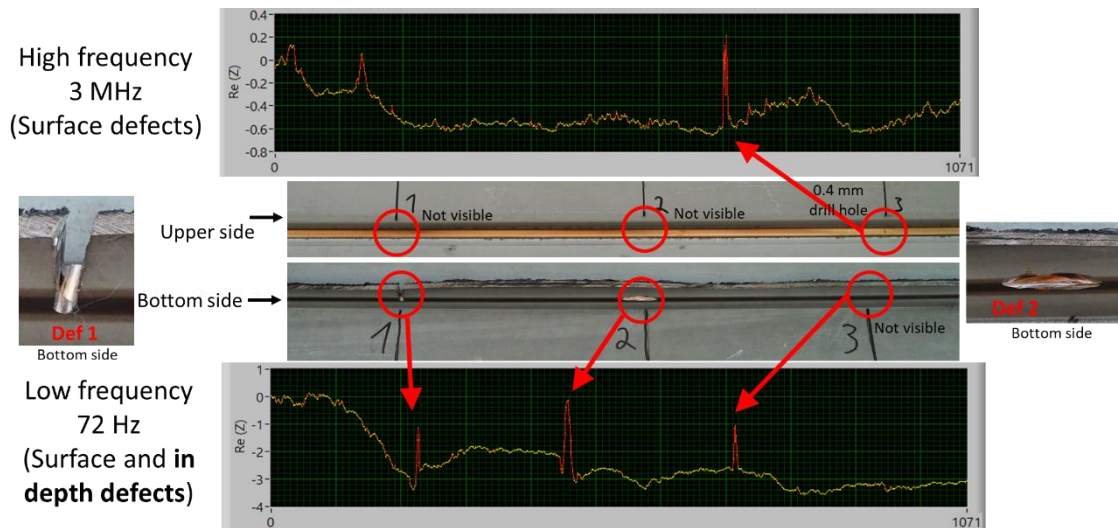


Figure 4.43 – Test piece with 1 surface and 2 sub-surface defects and respective output signals at high and low frequency.

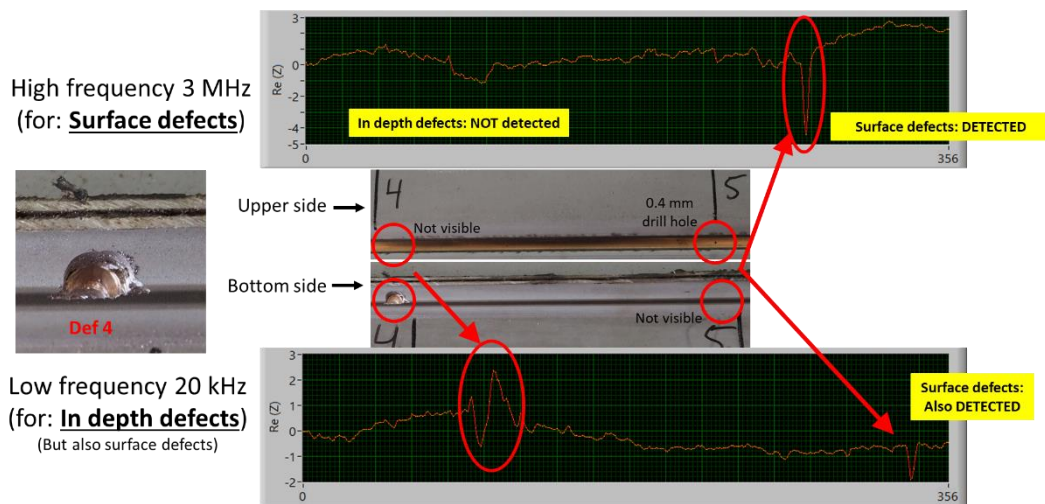


Figure 4.44 – Test piece with one surface and one sub-surface defect and respective output signal at high and low frequency.

The results presented were performed at low velocity due to the step motors limitation. To demonstrate the capacity of the EC system at higher speeds, closer to an eventual integration in an assembly line, a linear guide belt driven was adapted to push the device chassis at a speed of 20 mm/s. A new prototype was also developed to support this guide and 3 m long weld samples as shown in Figure 4.45.

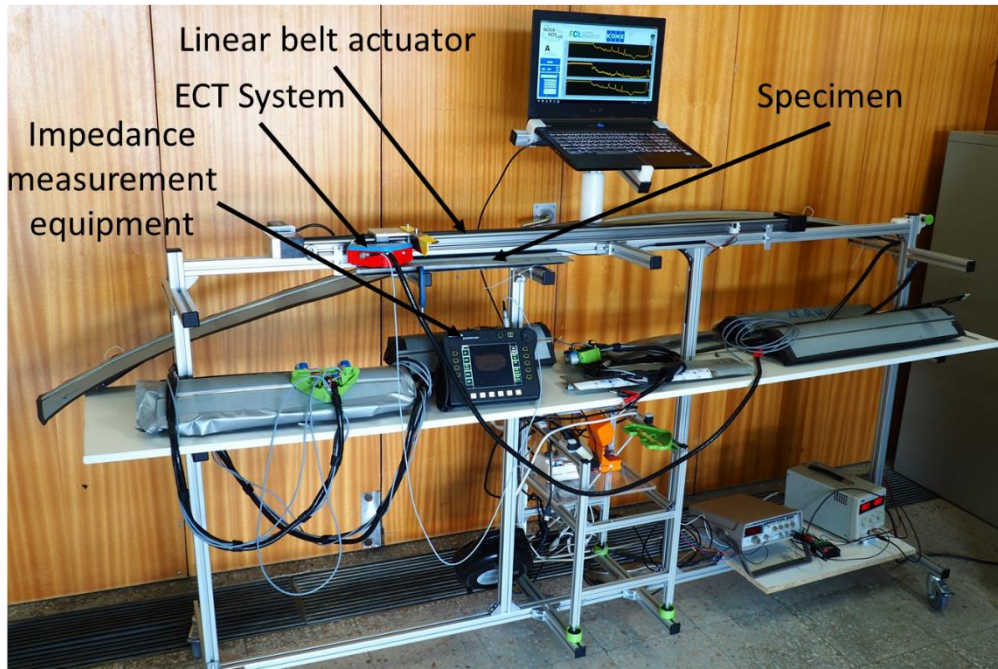


Figure 4.45 – Prototype developed for the inspection of 3 m long samples at higher speeds.

Sample 3LH was inspected at this higher speed and the output signal is displayed in Figure 4.46. In order to reduce the vibration of the device, an acceleration gap in which the probe is stationary, was required and it also assured constant speed during the test. As depicted, the defects are still detectable and well defined.

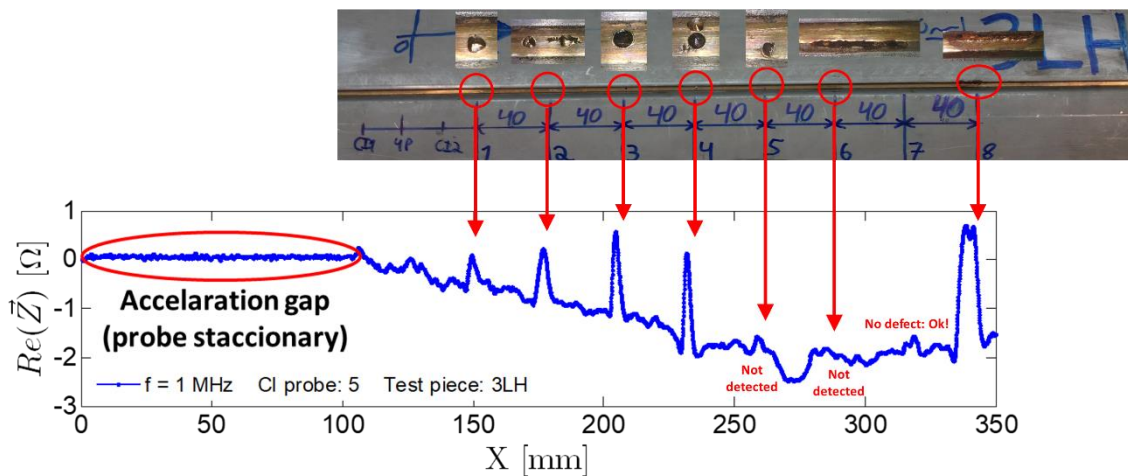


Figure 4.46 – EC probe output signal of sample 3LH at a higher speed.

#### **4.7. – Summary**

An extensive materials and geometrical characterization were performed on the bimetallic joint. The electrical conductivity of the materials involved was measured and the weld bead was sectioned in order to access its uniformness (§4.3). Numerical simulations were presented which were essential for the probe development in §4.4.

The prototype developed for the inspection of the laser brazed weld beads was successfully validated in laboratorial conditions and in industrial setting. Surface and sub-surface defects were detected with about 0.13 mm diameter, and that distinction was possible with two set of eddy current probes, one designed for low frequencies (20 kHz) and the other for high frequencies (3 MHz). For the lack of bonding, the potential drop measurement technique was used, with a customized four-point probe, which was also part of the prototype. The conventional linear pins position was numerically simulated and was considered unfit for this specific application. Different pins positions were simulated and a new disposition for the pins that made the inspection possible was found, in a cross shape. However, the target defects, lack of fusion, were quite hard to recreate artificially.

An extensive probe characterization was performed for the several bobbins produced in order to evaluate the best combination of bobbin characteristics for the weld in question. Higher speeds (20 mm/s) were also tested, with a very good feedback, in order to access the feasibility of the device working with a robot arm.

# **CHAPTER 5**

## **CONTACTLESS HIGH-SPEED ECT OF CARBON FIBER REINFORCED POLYMER**

### **5.1. – Introduction**

This chapter presents the last case study where a solution is developed for contactless high-speed inspection of a carbon fibre reinforced polymer. A material characterization is performed (§5.2), and several artificially made defects are presented (§5.3). A numerical simulation analysis was made (§5.4) to assist the probes design (§5.7). Two functional prototypes, in which the tests were made, are described and depicted: a low speed (§5.5) and a high-speed (§5.6) prototype. Finally, the experimental results and the conclusions are presented in §5.8 and §5.8.2.



## 5.2. – Material characterization

The carbon fibre tension member is a structural system consisting of four pultruded unidirectional (UD) Carbon Fibre elements protected by a polyurethane coating with an average thickness of about 1.2 mm (Figure 5.1). Each load carrying Carbon Fibre element has a cross section dimension of 5.0 mm  $\times$  2.5 mm (Figure 5.2). The CFRP elements are pultruded composite rods consisting of carbon fibre reinforcement embedded in an epoxy matrix. As the elements are manufactured using a pultrusion line, they are not laminates and do not consist of plies like most CFRP structures (Figure 5.3). However, they behave in a similar manner as UD laminates [223]. Like laminated structures, the microstructure of the pultruded elements contains resin rich zones, but their orientation varies. Failure due to excessive shear stresses and impact loading results in near-planar matrix cracks that closely resemble delamination commonly seen in laminates. Henceforth we call such matrix cracks delamination.

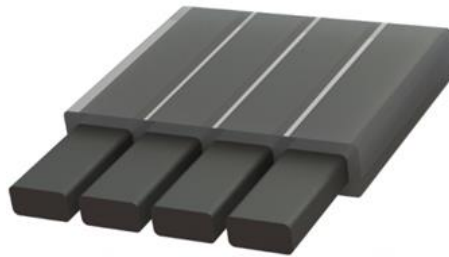


Figure 5.1 – 3D perspective of the carbon fibre tension member system with four parallel CFRP elements, protected by a polymer coating.

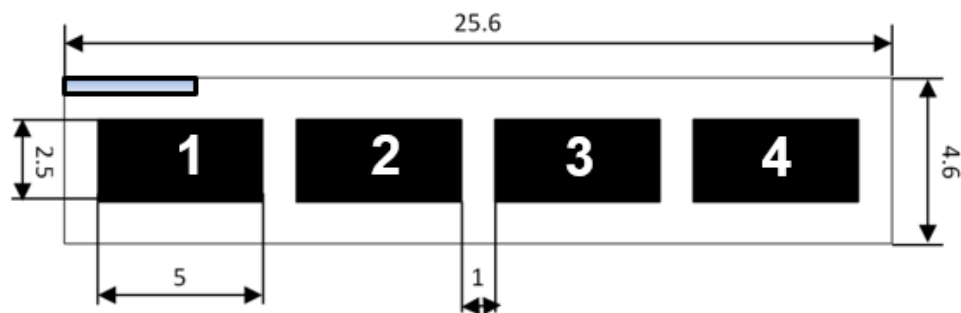


Figure 5.2 – Dimensions of the cross-section of the individual CFRP elements (in millimetres).

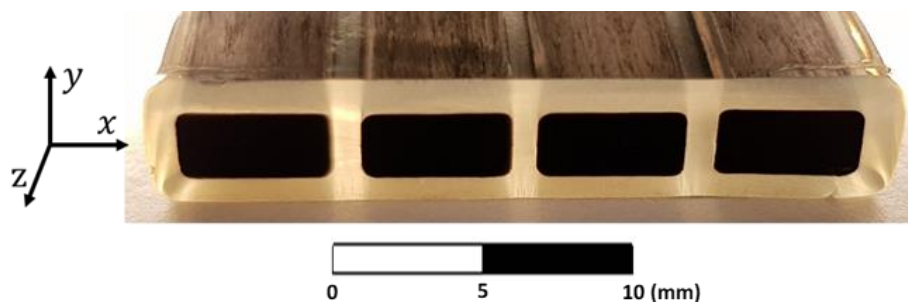


Figure 5.3 – Cross-section of the tension member evidencing the four CFRP elements with 5  $\times$  2.5 mm cross section and the polyurethane coating with about 1 mm thickness.

The electrical conductivity  $\sigma$  [S/m] of the CFRP elements was measured using different methods. It is the reciprocal of electrical resistivity  $\rho$  [ $\Omega \cdot \text{m}$ ], according to the equation  $\sigma = 1/\rho$ , and its relation with the electrical field  $\vec{E}$  [V/m] and the current density  $\vec{J}$  [A/m<sup>2</sup>] is given by Eq. 5.1. Since  $\vec{E}$  and  $\vec{J}$  are vectors,  $\rho$  is, in general, a tensor. Meaning the current does not necessarily flow in the same direction as the applied electric field [281].

$$\vec{E} = \rho \cdot \vec{J} \quad \text{Eq. 5.1}$$

The resistivity of the elements was measured along three perpendicular directions (XYZ) represented in Figure 5.4, using two redundant methods: local measurement, using a colinear four-point probe (potential drop measurement); and bulk measurement, through two contacts on both ends of a sample (applying Pouillet's law - in this case four-point measurements were performed using both source meter unit (SMU) and a LRC meter). The mean tensor of the electrical conductivity is represented by Eq. 5.2. It must be noticed that the tensor is diagonal because the XYZ coordinate system corresponds to the principal directions of the tensor (eigenvectors). Therefore, the electrical conductivity along those axes corresponds to the extreme maximum and minimum values (eigenvalues). As expected, the electrical bulk conductivity in the longitudinal direction (Z) is much higher than in X and Y directions, since this is the alignment direction of the fibres. This result shows the high electrical anisotropy of the material, and it was considered during EC probe design.

The results obtained with the potential drop measurement are presented in Table 5.1. The electrical conductivity in the longitudinal direction (Z) is much higher than in the other two directions due to the unidirectional orientation of the fibres. However, there is also transverse bulk conductivity because the fibres are closely packed (Figure 5.5). The fibres do not run in parallel either (fibre waviness), which leads to occasional contact with all its neighbours (Figure 5.6).

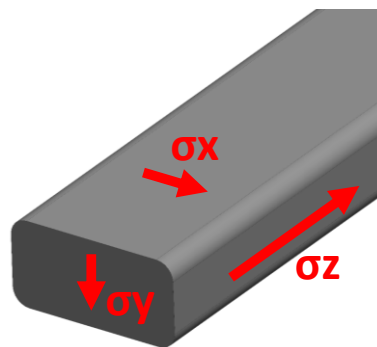


Figure 5.4 – Directions used to measure the electrical conductivity of the CFRP element.

$$\sigma_{ij} = \begin{bmatrix} \sigma_{xx} & 0 & 0 \\ 0 & \sigma_{yy} & 0 \\ 0 & 0 & \sigma_{zz} \end{bmatrix} = \begin{bmatrix} 117 & 0 & 0 \\ 0 & 78.1 & 0 \\ 0 & 0 & 13000 \end{bmatrix} \text{ [S/m]} \quad \text{Eq. 5.2}$$

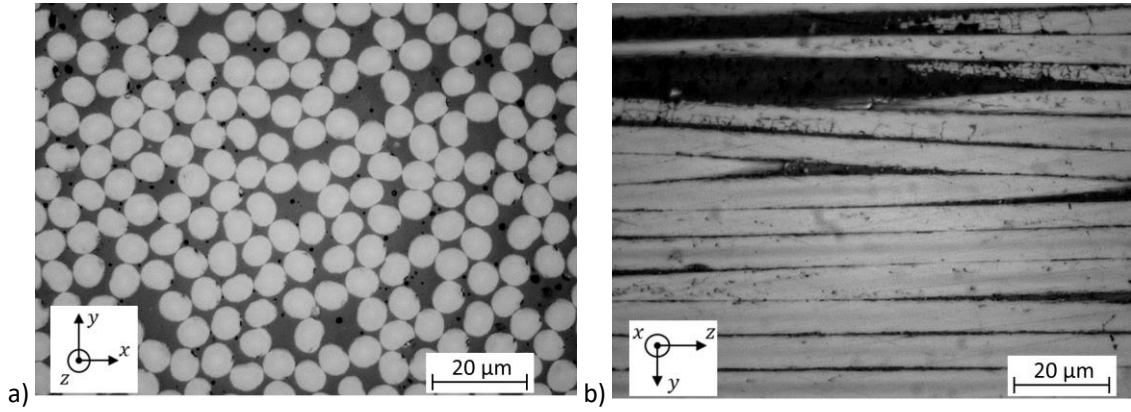


Figure 5.5 – Micrographs showing the contact between individual carbon fibres: a) Transversal view; b) Longitudinal view

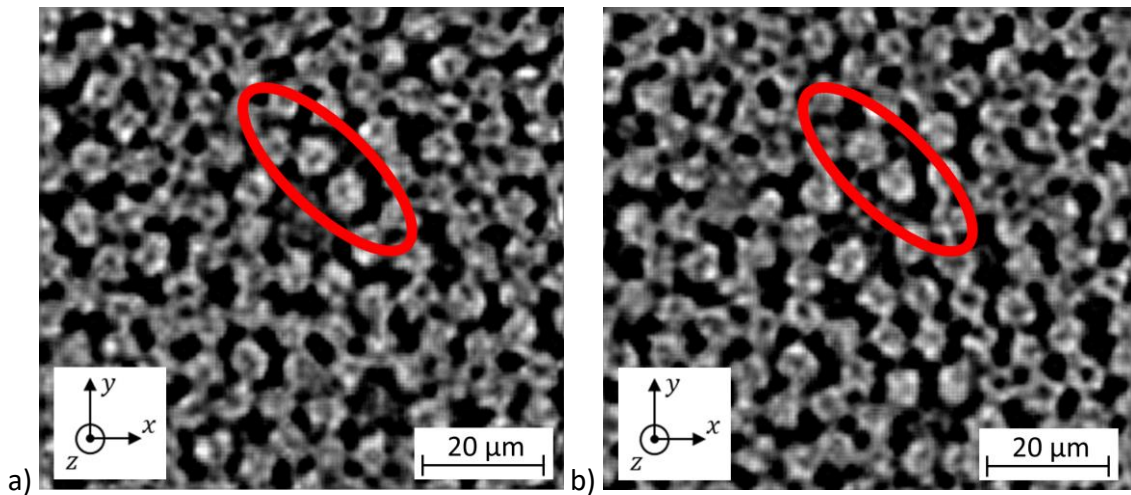


Figure 5.6 – X-ray microtomography 50 µm apart showing the fibre waviness and contact: a) transversal section (Z = 0); b) transversal section (Z = 50 µm)

The electrical conductivity in the X and Y directions are a slightly different, maybe because the sample length in those directions is short, which increases the measurement error.

Table 5.1 – Electrical resistivity and conductivity of the CFRP sample for XYZ directions.

Direction	X	Y	Z
Electrical Resistivity [mΩ.m]	8.57	12.8	0.077
Electrical Conductivity [S/m]	117	78.1	13000



### 5.3. – Defects Characterization

Artificial defects were produced, and quasi-realistic damage was induced, to the individual CFRP system. Samples with artificial damage were produced by machining, via drilling of flat-bottomed holes in the individual CFRP elements and partial through-thickness sawing of the CFRP system. The quasi-realistic damages were induced with mechanical loading to the individual elements, via three-point bending, inducing delamination damage, and to the whole tension member system, via low-velocity drop-weight loading, inducing multiple (complex) damage [282].

The size of machined defects was controllable, and the resulting defects were reproducible. However, they are not very realistic with respect to real-life applications. Therefore, three-point bending was used to induce delamination. The loading conditions followed EN ISO 14130 [283]. The support span was 12.8 mm and a roller diameter of 6.0 mm was used. A test speed of 1 mm/min was used and the bending was interrupted when a drop-in force was observed, usually accompanied by an audible crack. The delamination typically extends through the width (X direction) and in the case of a relatively short sample, they also propagate all the way to one end (Z direction) of the sample. Using longer samples, such as 1000 mm, resulted in delamination slightly longer than the support span.

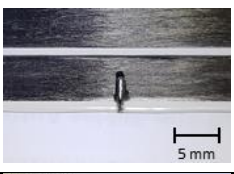
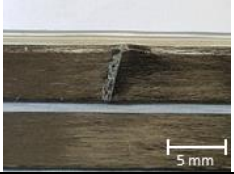
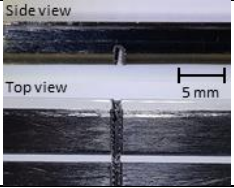
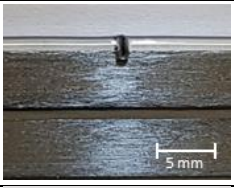

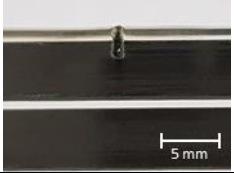


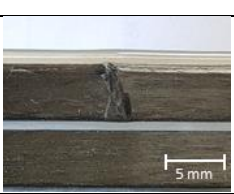

Coated samples were subjected to low-velocity drop-weight loading according to ASTM D5628-10 [284]. A weight of 1530 g with a hemispherical 16 mm diameter impact head was dropped from various heights to produce impact energies between 5 and 15 J. The samples were clamped to a steel frame with an  $\varnothing$  76 mm opening during the impact test, making it essentially a constrained three-point bending setup. Large fibre breaks were produced by sawing a transverse cut in the sample approximately 1 mm deep. The width of the cut was 2 mm.

Damage in the conducting constituents, namely carbon fibres, can cause changes in the eddy current paths, which alters the secondary magnetic field when compared to undamaged material. However, the damage does not necessarily have to be in the conductive constituents, because the quasi-UD carbon fibres are in contact with each other, leading to transverse bulk conductivity. Therefore, delamination could, in theory, be detected as well, although the transverse bulk conductivity is much lower than the longitudinal conductivity [282].

Table 5.2 describes the defects created for each of the four CFRP samples. The defects position along Z direction corresponds to the ones presented in Figure 5.7, in the same element of the CFRP.

Natural defects in this application can be very much alike the artificial ones. Damage can occur on the transport, assembly and use and that damage can be originated by objects falling over the CFRP (similar to broken fibres induced by ball-peen hammering) or some object that gets between the CFRP and the pulley in hoisting applications (similar to 3-point bending). The CFRP ropes are tensioned so fibre breaks will show the clear separation which makes cutting the fibres artificially a very close comparison.

Table 5.2 – Machined and real defects in the four CFRP samples.

Defect	Type of defect	Picture	Defect	Type of defect	Picture
LC05	Lateral Cut 0.5 mm length of width		3PTB	Broken fibres or Delamination induced by 3 ptb	
TC05	Cross Top Cut 0.5 mm depth of thickness		LC02	Lateral Cut 0.2 mm length of width)	
TH05	Top Hole 0.5 mm depth of thickness		LC05	Lateral Cut 0.5 mm length of width	
SH2	Side Hole 2 mm depth		BFH	Broken fibres induced by ball-peen hammering	
BFH	Broken fibres induced by ball-peen hammering		LC025	Lateral Cut 0.25 mm length of width	

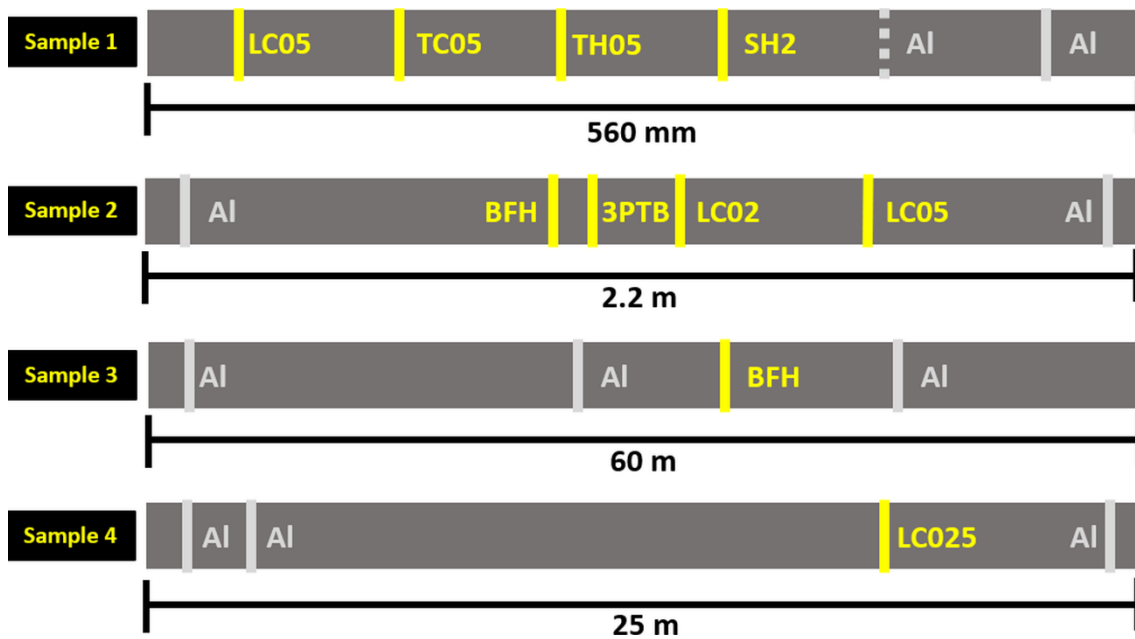


Figure 5.7 – Tested CFRP samples with the location of the defects.

#### 5.4. – Numerical simulation of Eddy Currents in CFRP

Numerical simulation was performed in order to evaluate the behaviour of eddy currents in the CFRP material. For this, a numerical simulation software (ANSYS Electronics) was used, and it calculates an approximate numerical solution of Maxwell's equations in their full formulation, Finite Integration Technique (FIT). The simulation comprises of one carbon fibre element and an excitation coil. The element has the same section as the individual CFRP elements,  $5 \times 2.5$  mm, and 100 mm length. The excitation coil was placed 3 mm above the element to allow some clearance even in the presence of a protective coating and 1 A current was used with a frequency of 6 MHz. The excitation element section used was  $1 \times 1$  mm where 10 parallel conductors pass. In Figure 5.8 is depicted the model used and the tetrahedral mesh representation which contains 1.700.000 elements. An isotropic material (aluminium) was first considered in order to understand the different behaviour of eddy current in an isotropic and anisotropic material.

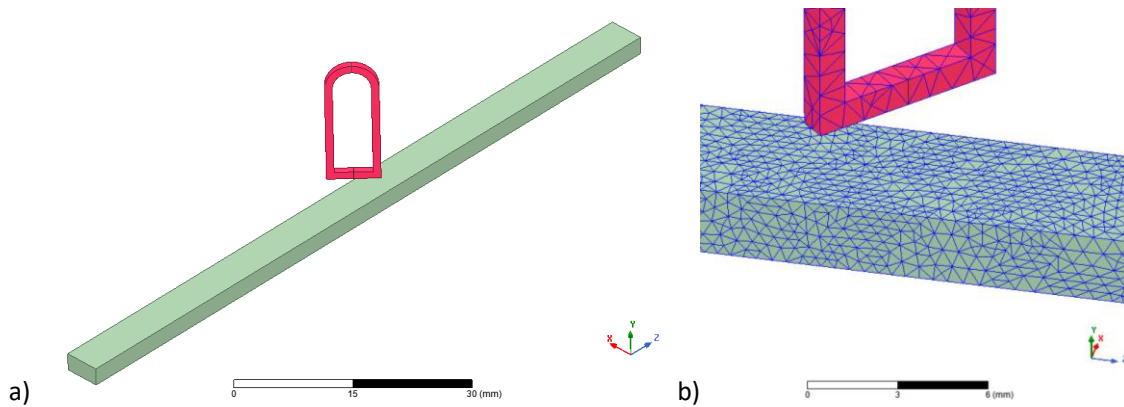


Figure 5.8 – Geometrical model used in the simulation of the eddy current induced by the excitation filament of the EC probe: a) geometric model; b) mesh representation.

In Figure 5.9 can be observed the field of current density in one electric conductivity isotropic element with different excitation coil orientations: transversely to the element (a), at a 45° angle (b) and aligned with the element (c). The current field is condensed near the excitation coil and symmetric with it. There is a noticeable edge effect of the eddy current in the transversal excitation. Edge effect is a phenomenon that occurs when an inspection coil is at the end of the test piece. In these instances, eddy current flow is distorted, as currents cannot flow at the edge [18].

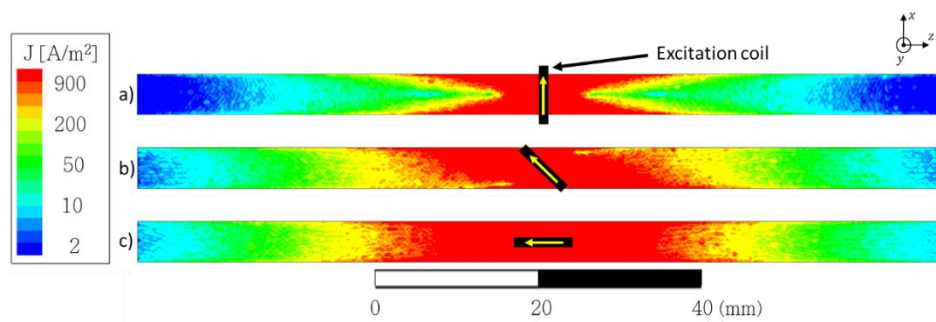


Figure 5.9 – Field of eddy current density on an isotropic material (Aluminium) with different excitation orientations: a) excitation with 90°; b) excitation with 45°; c) excitation with 0°.

The carbon fibre material properties used for the simulation were the measured electrical conductivity (Figure 5.10) and a relative magnetic permeability of  $\mu_r = 1$ . Figure 5.10 shows the field of eddy current density in the carbon fibre with different excitation orientations. Four loops are created in the edges of the element and away from the excitation when a transversal excitation is used (Figure 5.10a). Applying a small angle (5°) to the excitation, it is possible to observe a preferred flow direction, which is the most conductive direction (Z direction) of the element, consistent with the high electric conductivity anisotropy of the CFRP. Increasing this angle will facilitate this flow as depicted. With the carbon fibre, the excitation spreads along the element and its direction is not as distinct as in an isotropic material.

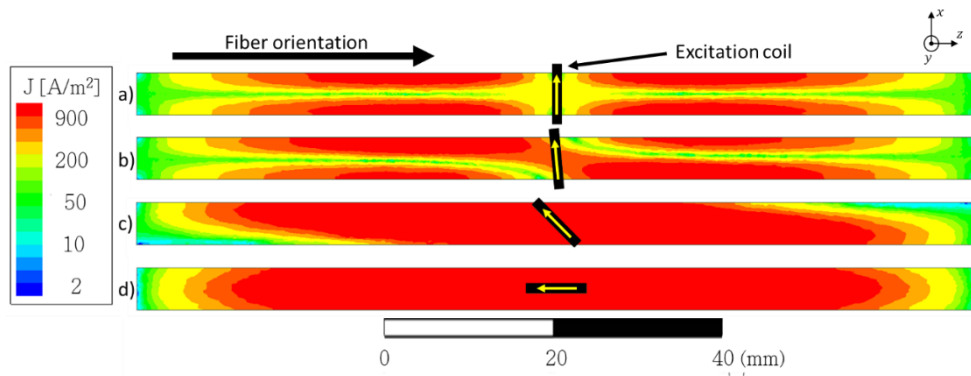


Figure 5.10 – Field of eddy current density on an CFRP anisotropic material (carbon fibre) with different excitation orientations: a) excitation with  $90^\circ$ ; b) excitation with  $85^\circ$ ; c) excitation with  $45^\circ$ ; d) excitation with  $0^\circ$ .

### 5.5. – Functional prototype for low speed inspection

In order to conduct the EC probes experimental validation a prototype was designed, manufactured and assembled. This prototype is responsible for the EC probe fastening and for the element specimen movement in relation to the EC probe (Figure 5.11). This prototype fixes the element through four V shaped bearing wheels resulting in only one degree of freedom for the element which corresponds to the longitudinal direction. A step motor was used to transmit the movement to the CFRP element. The probes are coupled to the prototype which allows a precision lift-off adjustment with a screw. The prototype is connected to a laptop where a customized LabVIEW program controls the movement and the EC probe data acquisition.

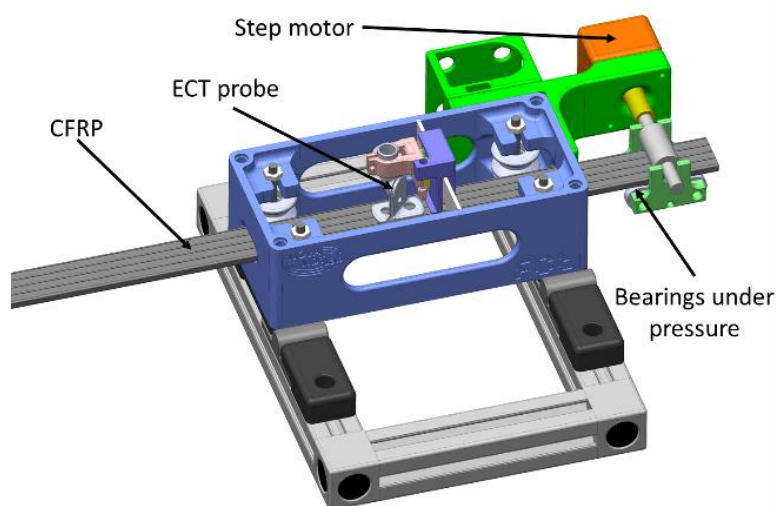


Figure 5.11 – Inspection prototype CAD design.

The prototype is mounted on an aluminium Bosch profile [285] frame with two hinges which allow the prototype rotation for vertical or horizontal tests (Figure 5.12).

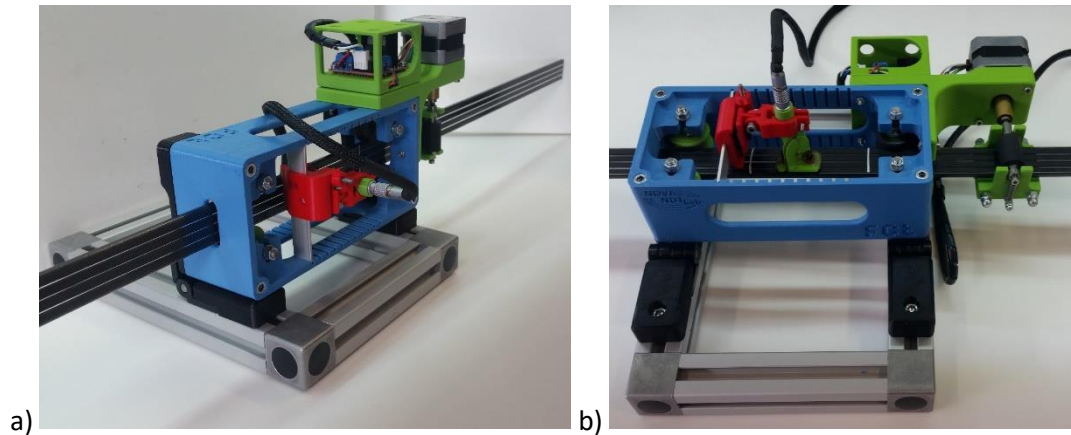


Figure 5.12 – Low speed inspection prototype. a) inspection with the prototype at the vertical position; b) inspection with the prototype at the horizontal position.

The probe is placed in a support which allows the adjustment in the transversal direction as well as the angle between the probe and the CFRP element. The support also contains a linear bearing screw thread regulated which allows a precise adjustment between the probe and the CFRP reducing its lift-off to the minimum although maintaining its contact non-existent (Figure 5.13).

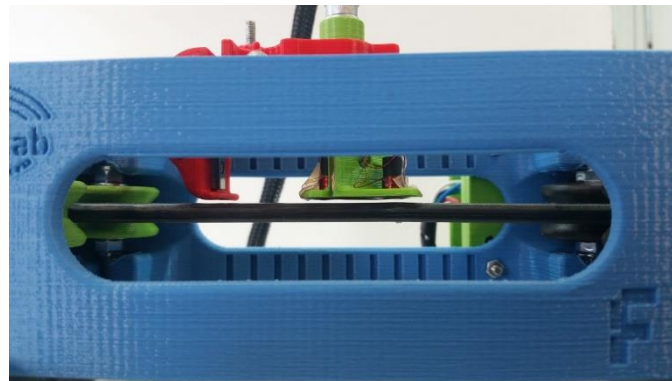


Figure 5.13 – Lift-off regulation by screw.

### 5.6. – Functional prototype for high speed inspection

A high-speed functional prototype was designed and assembled in order to experimentally test the most reliable tailored EC probes at high speed (1 to 4 m/s). Since a final implementation envisages the use of the inspection prototype, in real environment, in a moving CFRP, a programmable high speed belt driven linear actuator was used to provide high speed movement to the CFRP element. The chosen linear actuator is a 5.5 m long belt driven slide system



LCB060LG05500SLN from Parker [286] and it is powered by a SMH100 brushless motor also from Parker, both depicted in Figure 5.14a and Figure 5.14b. It can accelerate at a rate of  $20 \text{ m/s}^2$  and achieve a maximum speed of  $8 \text{ m/s}$ . Also, it includes a rotary encoder to provide feedback to the Compax3 Single Axis Drive (Figure 5.14c) also by Parker which is powered by a regulated  $24 \text{ V}$  power supply. A  $180 \text{ W}$  Ballast Resistor was also used for the deceleration. The acceleration/deceleration routine was programmed with CoDeSys according to the international industrial standard IEC 61131-3 which can be seen in Appendix 1.

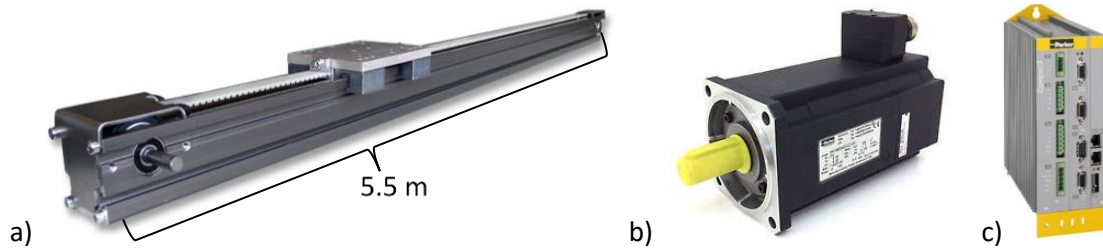


Figure 5.14 – Equipment acquired for the high speed movement; a) Slider bearing rodless linear actuator - LCB060; b) SMH100 brushless motor; c) Compax3 Single Axis Drive [286].

An aluminium Bosch profile [285] frame was designed and assembled to accommodate all the devices required for the CRFP movement: the compax3 drive, the brushless motor, the  $24 \text{ V}$  power supply, the braking resistor and the switches to control the system (Figure 5.15).

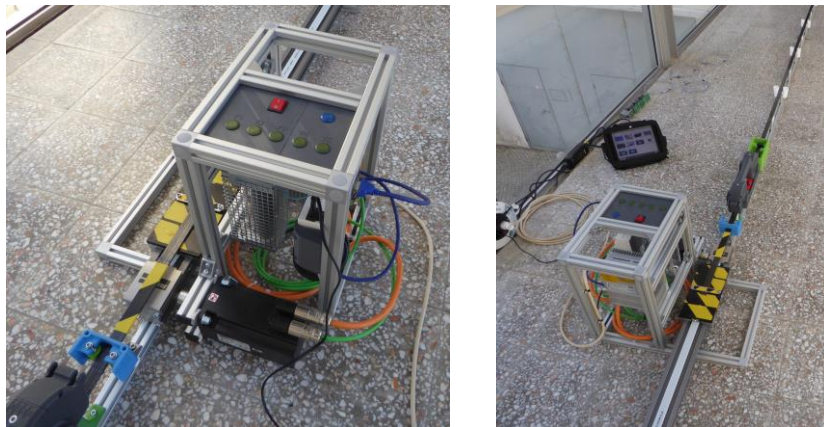


Figure 5.15 – Aluminium frame with all the devices required for the actuator operation.

In Figure 5.16 is represented a schematic with the set up required for the high-speed inspection. An aluminium structure had to be created in order to guide the CFRP and also to elevate it to the carriage height. Also, there had to be a clear zone, before the belt, where the hand-held device could be used without any interference underneath the CFRP element. Figure 5.17 depicts both the linear guide and the CFRP guiding structure.

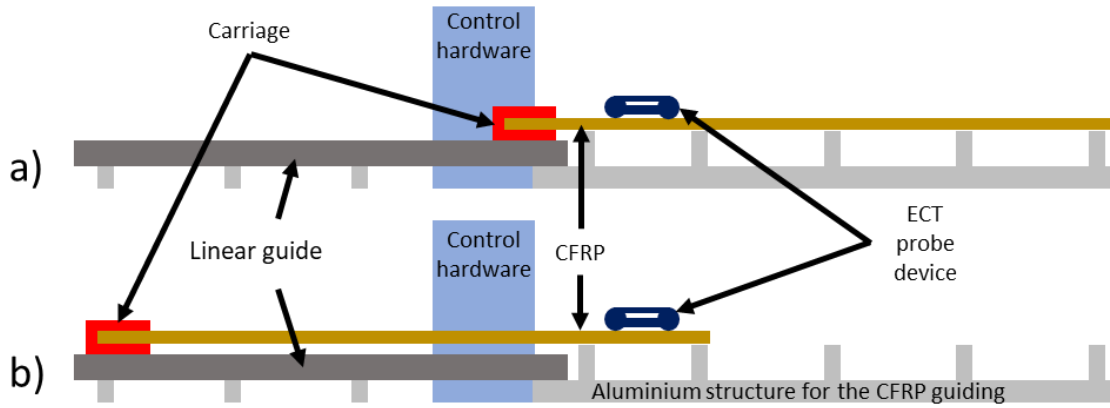


Figure 5.16 – Schematic design of the high-speed inspection prototype (not to scale), a) before the inspection; b) after the inspection.



Figure 5.17 – Set up for the high-speed inspection with the linear guide and the CFRP guiding structure.

A 3D printed handheld chassis with two wheels was designed, produced and assembled to couple the EC probes for the high-speed inspection (Figure 5.18). Due to its size, the chassis is composed of multiple parts which are assembled together later. The parts are connected with glue and screws inside them, which space was already assigned in the design, increasing the robustness of the device. The EC probe is placed in the middle of the chassis and its positioning and constant lift-off is assured by it. The probe holder allows four degrees of freedom as shown in Figure 5.19. The wheels work like train wheels and the CFRP serves as a rail. This guarantees the transversal positioning of the probe relative to the CFRP.



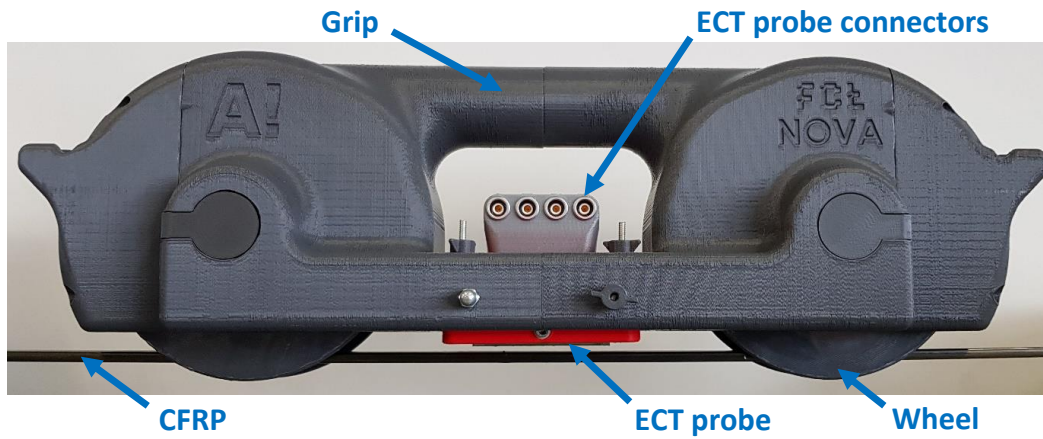


Figure 5.18 – Hand held device used in the high-speed tests [287].

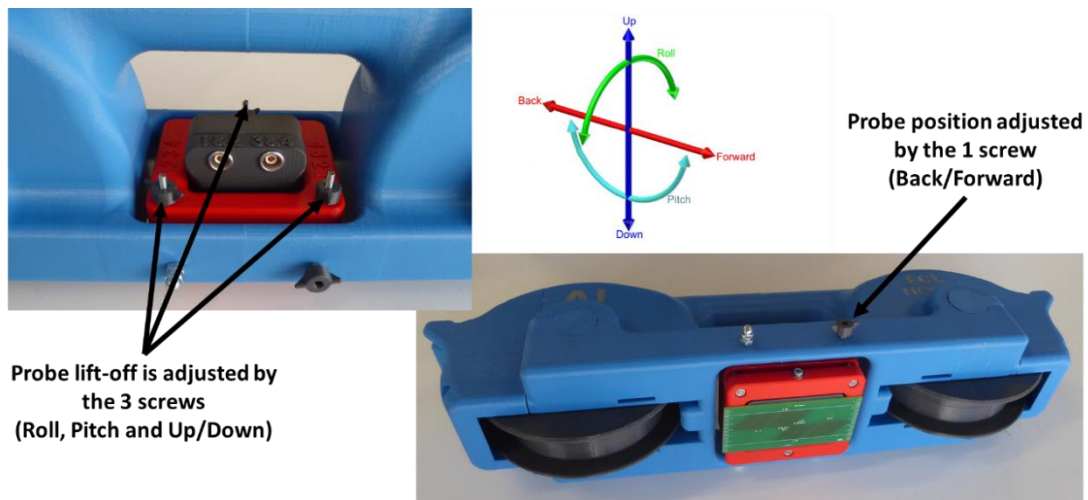


Figure 5.19 – The EC probe can be adjusted with relative precision to the CFRP elements.

A dock support was created to assist the inspection when the inspection device is not being used (stationary). This support has an aluminium structure with a defective CFRP at its base. The inspection device is placed over the CFRP and fixed by the aluminium. The support has two main functions, to hold the inspection device in place when not it is not being used and also serves has a defect reference test. Before performing the inspection, it is possible to run the device along the CFRP to check if everything is working as intended.

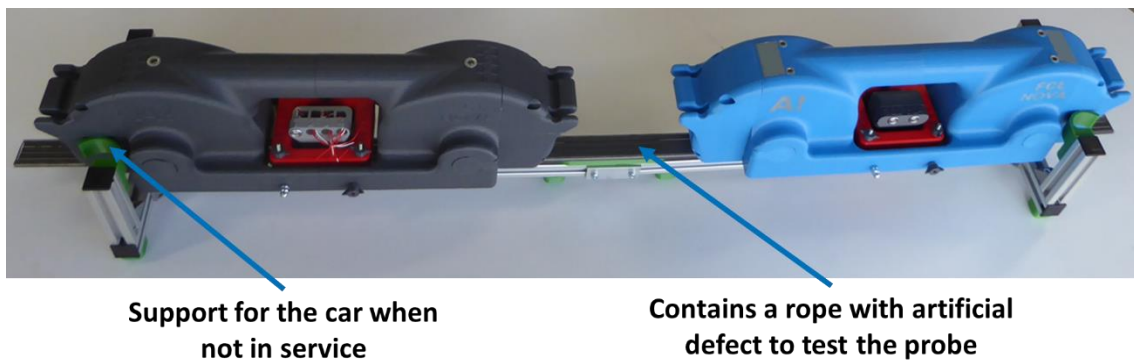


Figure 5.20 – Inspection device holder and test reference.


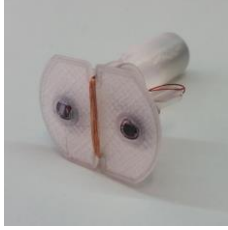





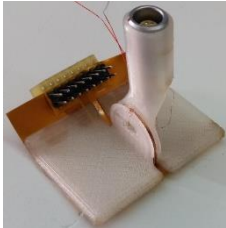
### 5.7. – Probe design

Several EC tailored probes were designed, produced and validated experimentally for the inspection of different kinds of imperfections in carbon fibre reinforced polymers. Probes composed of excitation windings and pairs of sensitive coils were produced with the ability to operate in reflection differential or bridge differential mode. When operating in bridge differential, the excitation winding is ignored and both sensitive coils work as excitation and sensors. Several configurations were created where different parameters were changed like the: number of excitation windings, diameter of the excitation wire, orientation of the excitation winding towards the CFRP, number of sensitive coils, sensing coils wire diameter, sensing coils with or without core, core material, distance from the excitation winding to the sensing coils, diameter of the sensing coils, geometry of the sensitive coils, etc. Table 5.3 depicts some of the first prototypes created which were assembled in 3D printed chassis with FDM technology modelled in CAD environment. The complete set of probes can be found in Appendix 2.

After this first iteration with the 3D printed probes, with a deeper understanding on what seemed to work for this composite inspection, a step was taken to get improved results with flat PCB probes.

A set of functional requirements for the probes was defined in order to specify the inspection needs. The new customized probes should: i) have a high sensitivity to detect small defects with a very good signal-to-noise ratio when handled with conventional EC testing equipment; ii) be capable of detecting distinct kinds of defects (morphology and locations); iii) provide the accurate position of the defect in Z direction; iv) be easily customizable and affordable. Four different probe geometries were designed, created and produced via Printed Circuit Board (PCB) technology on a rigid substrate (Figure 5.21). This configuration was selected to maximize the proximity of all the winding to the surface of the CRFP and, hence, to the defect, allowing a superior sensitivity due to the proximity to the EC changes. PCB probes are also inexpensive to produce.

Table 5.3 – First EC tailored probes prototypes.

Probe	Picture	
#5	 A photograph of probe #5 from a side perspective. It features a white cylindrical probe tip mounted on a white base. A blue component is visible at the base, and several thin wires are connected to the assembly.	 A photograph of probe #5 from a top-down perspective. The probe tip is a light-colored, circular disc with two dark circular spots. Wires are visible extending from the base.
#6B	 A photograph of probe #6B from a side perspective. The probe tip is a white, rectangular block with a cylindrical protrusion. It is secured with two orange elastic bands. Wires are attached to the base.	 A photograph of probe #6B from a top-down perspective. The rectangular probe tip is clearly visible, showing the two orange elastic bands and the cylindrical protrusion. Wires are connected to the base.
#9C	 A photograph of probe #9C from a side perspective. The probe tip is a white, rectangular block with a cylindrical protrusion. It features an orange component on the side and is secured with orange elastic bands. Wires are attached to the base.	 A photograph of probe #9C from a top-down perspective. The rectangular probe tip is visible, showing the orange component and the cylindrical protrusion. Wires are connected to the base.
#10	 A photograph of probe #10 from a side perspective. The probe tip is a rectangular, orange-colored pad with a grid of small square elements. It is mounted on a white handle. Wires are attached to the back.	 A photograph of probe #10 from a top-down perspective. The orange rectangular pad is clearly visible, showing the grid pattern. The white handle and wires are also visible.

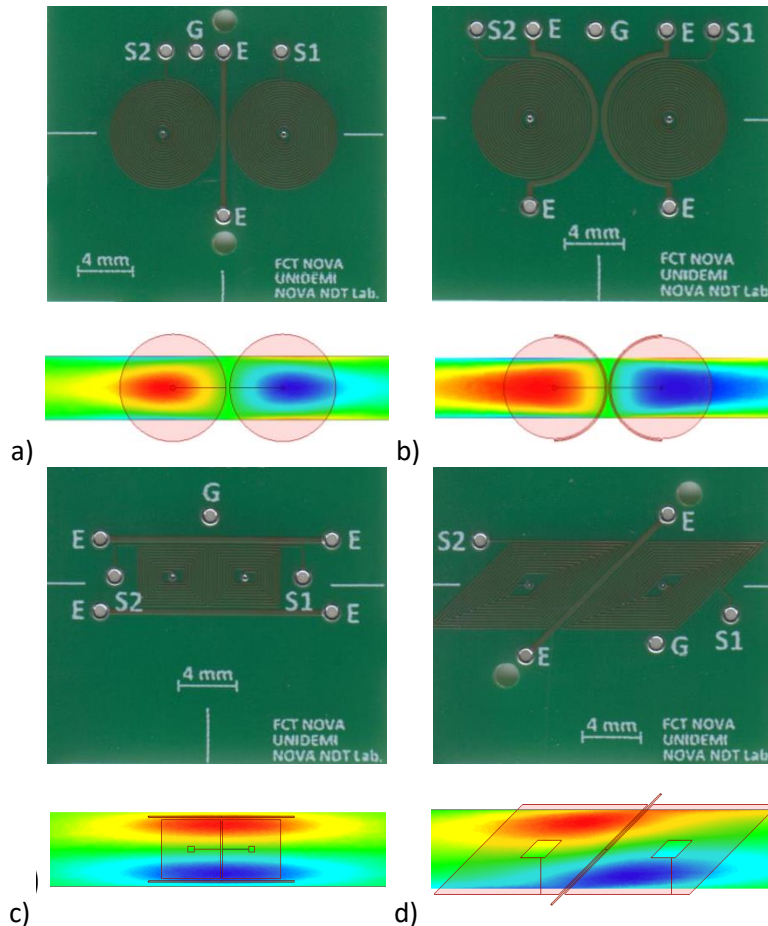


Figure 5.21 – PCB EC probes designed and manufactured for testing with correspondent secondary magnetic field: a) Circular spiral coil probe with transversal excitation – PCB Probe #1; b) Circular spiral coil probe with curved excitations – PCB Probe #2; c) Rectangular spiral coil probe with parallel excitation – PCB Probe #3; d) 45° parallelogram spiral coil probe with transverse excitation – PCB Probe #4.

The probes consisted of two planar pickup spiral coils and one or more excitation driver(s) tracks between them. The probe architecture is scalable to different widths according to the components to be inspected. Each of the probes can operate in two different modes. Reflection mode: using the middle track as a driver while the spiral pickup coils operate in differential mode. Using the same spiral coils, and ignoring the middle track in the probe, it can operate in bridge differential mode. PCB Probe #1 uses planar circular spiral coils wound in opposition, and a rectilinear excitation filament placed in the symmetry plane, for reflection mode purposes (Figure 5.21a). The secondary magnetic field, when operating in bridge mode, is also presented and it is possible to observe that the field is stronger under the sensing coils and spreads in the length direction of the CFRP. To decrease the distance between the excitation and the pickup spiral coils, PCB Probe #2 was designed so that EC would be closer to the pickup coils (Figure 5.21b) and will impose a more circular EC path. From the numeric simulation presented, while operating in reflection mode, it is possible to observe that the field is stronger and spreads

more than with the previous probe. PCB Probe #3 attempts to induce the EC in the direction of the fibres, with the two paths at the top and bottom of the pickup coils and allows the current input in the same or opposite direction in these tracks, depending on the connection made (Figure 5.21c). The secondary magnetic field, when operating in reflection mode, is displayed. The field spreads along the element near the edges and under the sensing coils. This probe was also tested with an excitation coil wound as seen in Figure 5.23. PCB Probe #4 comprises of two 45° parallelogram spiral coils with a 45° excitation track in the middle (Figure 5.21d). From Figure 5.10 it was possible to understand that a transversal excitation (90°) should be avoided and a longitudinal direction preferred, so a 45° parallelogram coil with only 0° and 45° segments fulfils these conditions best. A pair of 45° parallelogram coils avoids undesired transversal excitation and creates a known output signal when working in bridge differential mode. As seen in Figure 5.22, the EC are stronger in the length direction of the element which is expected to be very suitable to fibre breaks detection. The secondary magnetic field, when operating in reflection mode, is spread with an angle under the sensing coils. The parallelograms width is about the same as the element, maximizing the sensitive area, and either operating in reflection or bridge mode, the excitation is never transversal to the element as preferred considering the numeric simulation in Figure 5.10. More numerical simulation results of the probes, where the EC density, EC vectors and secondary magnetic field for different operation modes, are shown in the Appendix 3.

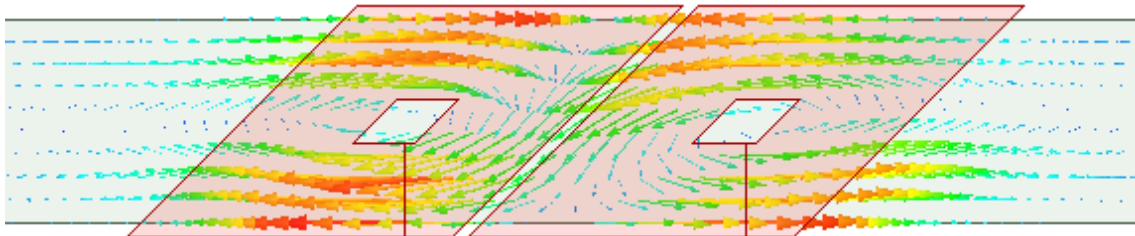


Figure 5.22 – Vectorial field of the EC in the CFRP element when excited with a parallelogram probe when operating in bridge differential mode.

PCB Probe #4 with dual 45° parallelogram spiral coils, was numerically simulated in order to get insight and assess its feasibility to inspect imperfections in the CFRP material. The probe operates in differential bridge mode with a 3 mm lift-off. The coils were simplified in order to decrease the number of elements required for the mesh and hence the simulation time (Figure 5.24a). The parallelogram's outer dimensions are 5.7 mm width, 8 mm length and 35  $\mu\text{m}$  thickness and it contains 12 turns (Figure 5.24b). The model used for the simulation comprises only of one CFRP element and the respective probe. The CFRP element is modelled with the same section as the specimen, 5  $\times$  2.5 mm, and 100 mm length. In Figure 5.25 is depicted the

geometric model developed and the tetrahedral mesh representation which contains 2.7 million elements. The coils were excited with 1 A current at a frequency of 6 MHz. Two artificial defects were simulated. One was a top horizontal cut through the whole CFRP element with 0.5 mm thickness and depth as depicted in Figure 5.25. The other defect was a lateral cut through the whole element height also with 0.5 mm thickness and depth, as depicted in Figure 5.25. Figure 5.26 depicts the EC density induced by the 45° parallelogram coils in the top surface of the element, where its behaviour around the defect can be seen.

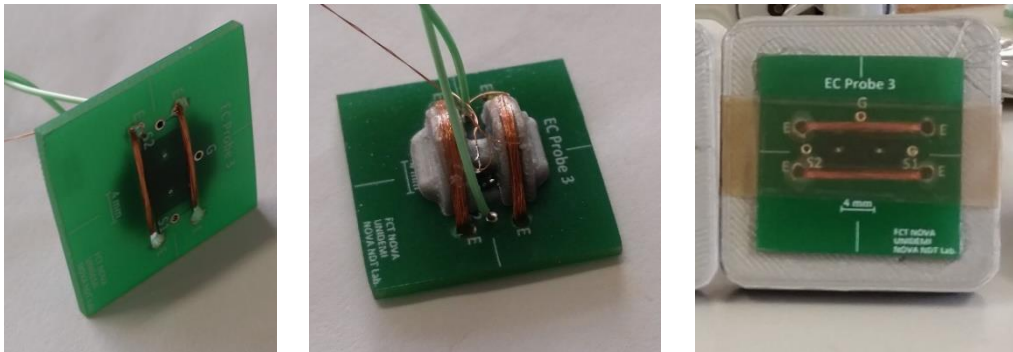


Figure 5.23 – PCB probe #3 variant with winded excitation coil.

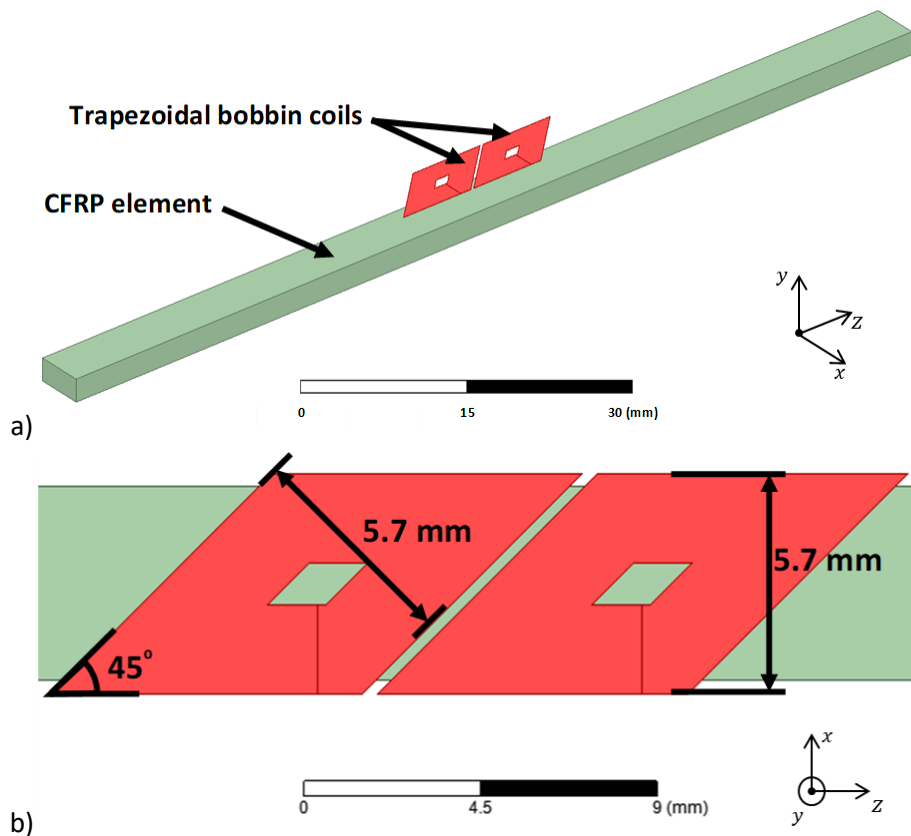


Figure 5.24 – Schematic representation of the model used for the probe simulation:  
 a) Isometric view of the element with the two coils; b) Top view of the coils and its dimensions.



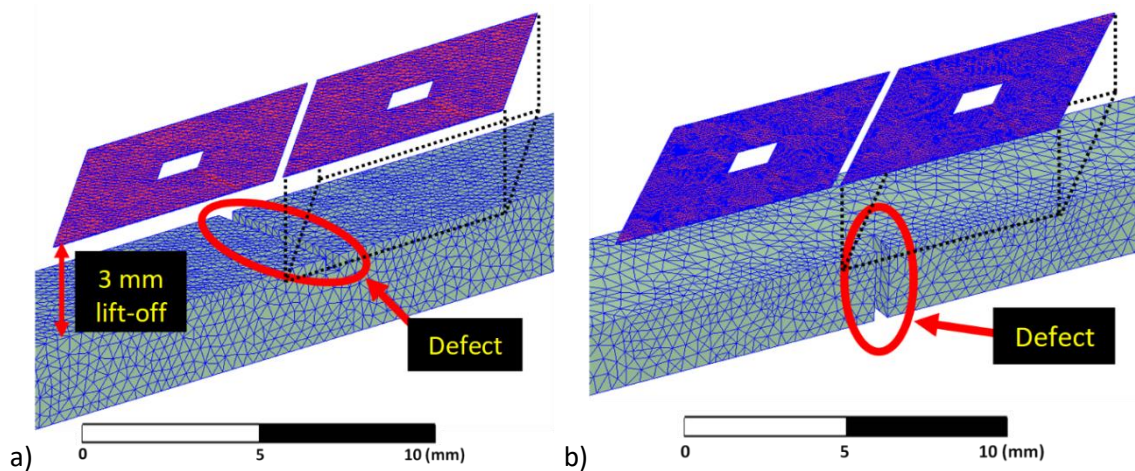


Figure 5.25 – Mesh representation with about 2.7 million tetrahedral elements:  
 a) With a top cross cut defect; b) With a lateral cut defect.

To simulate the inspection procedure, when the probe is scanning a defect, various defect positions along Z direction were simulated, keeping the probe at the same position. Figure 5.26 illustrates the EC density produced by the probe in one CFRP element, with the defect in three different positions, and its behaviour around the lateral cut defect. The output signal of the bobbin coils, in differential bridge operation, is shown in Figure 5.27, where the blue line represents the output signal of the cross top cut defect, while the red line represents the side defect. According to the numerical simulations, both defects are detected with a clear output signal and with a good signal-to-noise ratio, especially the top cut defects. It must be noticed that these output signals are the result of the compilation of the simulations performed with different defect positions. Each dot in Figure 5.27, results from the simulation at that point and the defect is moved 500  $\mu\text{m}$  between consecutive simulations. The distance was increased for probe positions longer than  $\pm 15$  mm away from the defect.

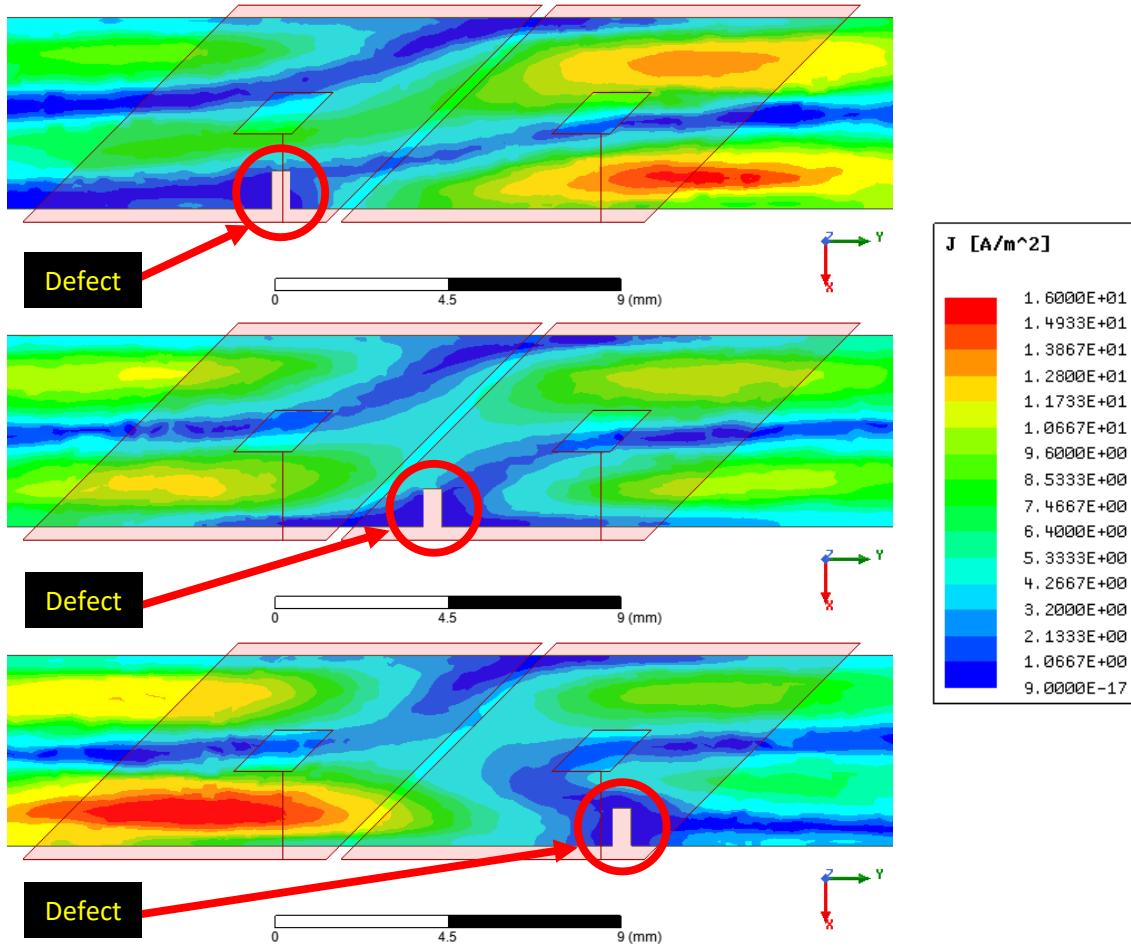


Figure 5.26 – Field of EC density on the top of the element with the lateral cut defect in three distinct positions.

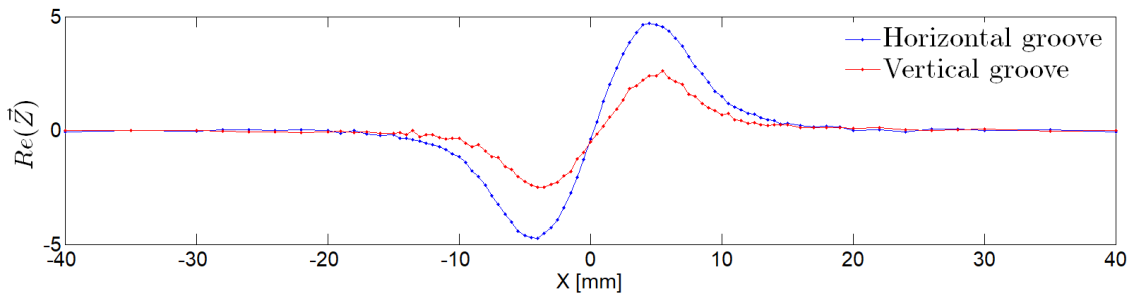


Figure 5.27 – Numerical simulated output signal of the parallelogram bridge differential probe of a top cross and lateral cut defect scanning.

Figure 5.28 depicts the probe 3D printed chassis and connector designed for the benchmarking of the PCB probes. Two array versions of PCB Probe #4 were produced and tested to allow the inspection of the four CFRP elements simultaneously (Figure 5.29). Figure 5.29a shows the array version of PCB Probe #4 with four individual 45° parallelogram spiral coils for the entire inspection the CFRP allowing monitoring each CFRP element separately but requiring four simultaneous impedance reading channels. Figure 5.29b shows an array version that requires only two impedance channels for measuring two pairs of merged elements. Figure 5.30



depicts the probes 3D printed chassis and correspondent connectors and Figure 5.31 combines all the EC probes produced.

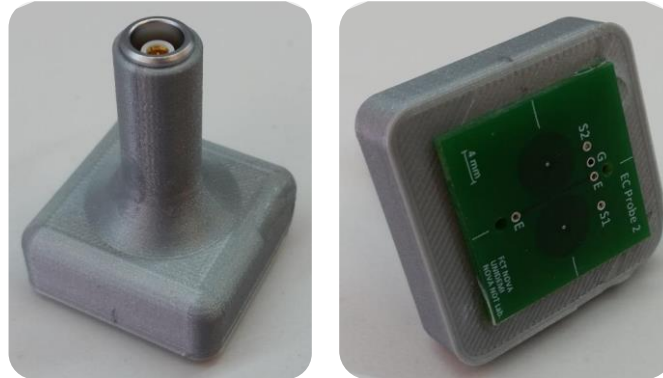


Figure 5.28 – PCB probes assembled in the 3D printed chassis.

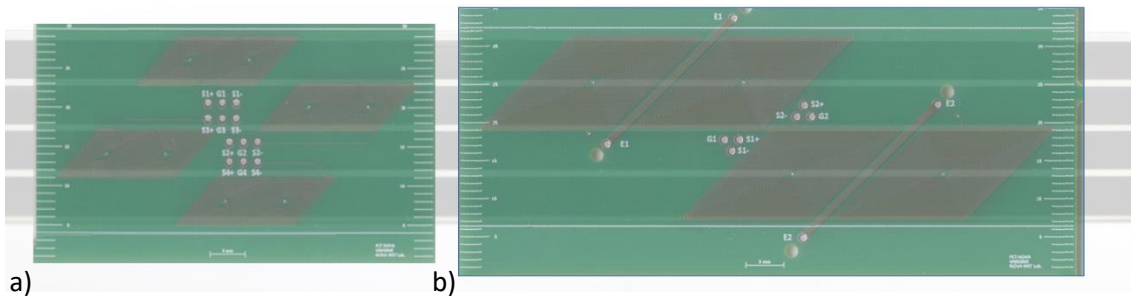


Figure 5.29 – Array versions of the PCB Probe #4 with 45° parallelogram spiral coil overlapped with the four CFRP elements: a) Version with four individual coils; b) Version with two individual coils.



Figure 5.30 – PCB probes assembled in the 3D printed chassis.

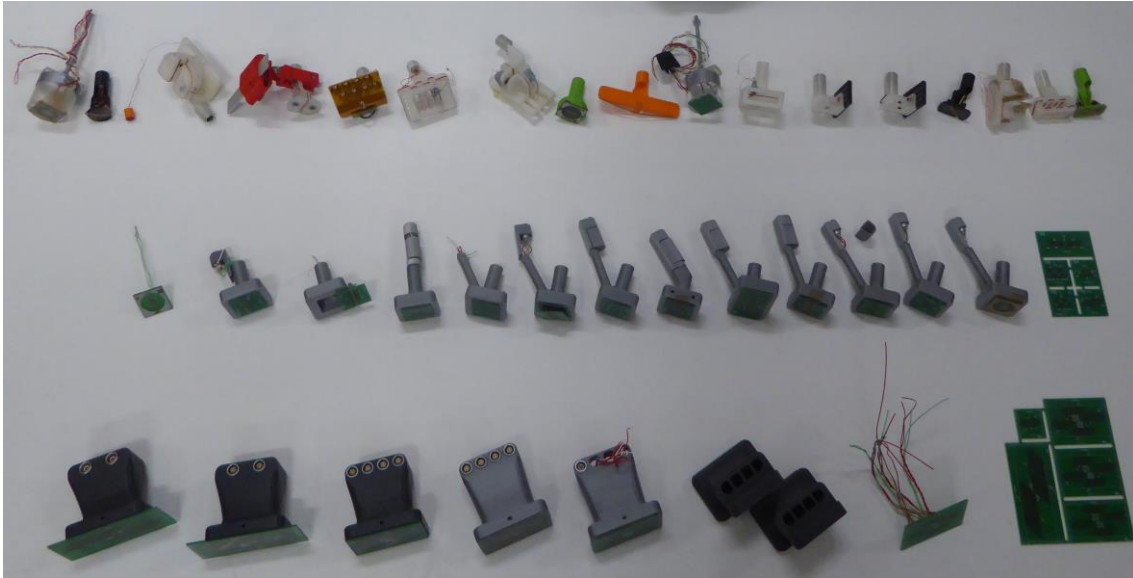


Figure 5.31 – Total of EC tailored probes produced and experimentally tested.

## 5.8. – Experimental results and discussion

### 5.8.1.– Low speed experimental tests

The experimental implementation of the tailored EC probes was performed by means of an automated scanning device responsible for the carbon fibre system movement while the probe remains stationary. Each one of the four CFRP elements was inspected, at a time. The movement, as well as the signal acquisition, were controlled and programmed in LabVIEW environment. Between each acquisition, the sample moved  $\Delta Z = 500 \mu\text{m}$  and the equipment responsible for the impedance measurement was the Nortec 500. The sampling rate of the equipment is 6 kHz. Absolute commercial pencil probes of different manufacturers were tested under the same inspection conditions without success. The distance between the probe and the carbon fibre system was about 3 mm. The Figure 5.32 exhibits both probes lift-off to the inspected component.

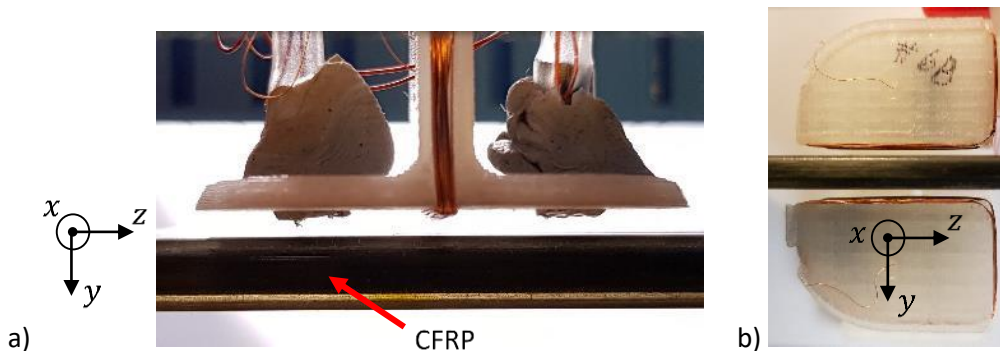


Figure 5.32 – EC probes lift-off: a) EC probe #5; b) EC probe #6b.

Figure 5.33 depicts one scanned CFRP element with the sawed defect using EC probe #5 and a 6 MHz commercial absolute pencil probe. The operating mode used was reflection at 4 MHz. The output signal is the well-known shape due to the differential sensing arrangement.

With the same probes and operating parameters, the sample with the impact damage 15 J was inspected. This sample was longer, which allows identifying how high the signal-to-noise ratio is (Figure 5.34).

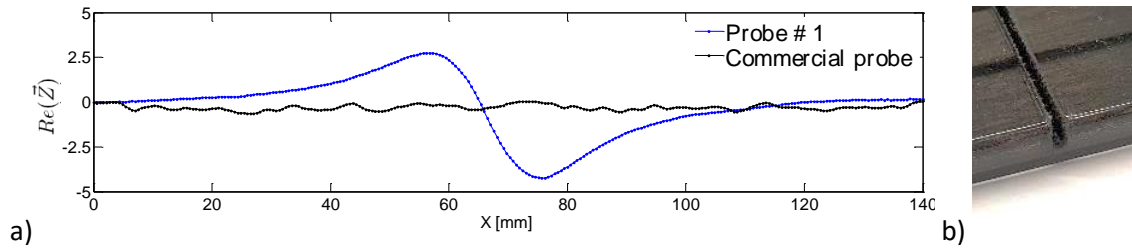


Figure 5.33 – Output signal of EC probe #5 inspecting a saw cut sample at 4 MHz, assessed from the defective side.

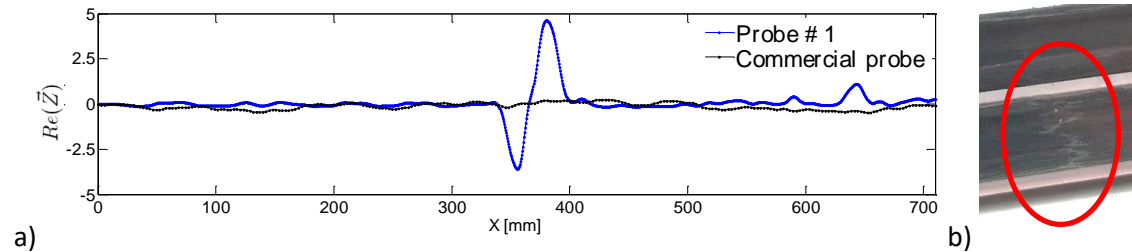


Figure 5.34 – Output signal of EC probe #5 inspecting an impact damage sample at 4 MHz, assessed from the defective side.

Although EC probe #5 presented very good results, defects assessed from the other side of the CFRP element were not detected. Thus, the need for the EC probe #6b.

The same two samples were inspected with the EC probe #6b. This probe also operates in reflection mode and the test were done at 4 MHz. In Figure 5.35 and Figure 5.36 are presented the results for the sawed defect and impact defect respectively.

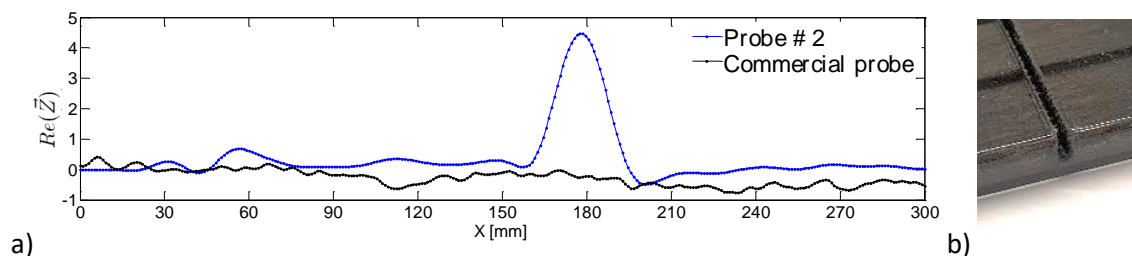


Figure 5.35 – Output signal of EC probe #6b inspecting a saw cut sample at 4 MHz.

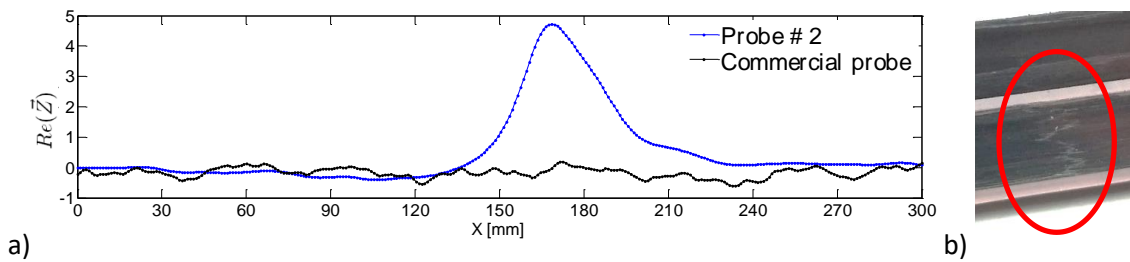


Figure 5.36 – Output signal of EC probe #6b inspecting an impact damage sample at 4 MHz.

In order to benchmark the tailored EC PCB probes, CFRP Sample 1 was inspected at low speed (20 mm/s). The experimental implementation was performed by means of an automated scanning device responsible for the CFRP movement while the probe remains stationary. The movement, as well as the signal acquisition, were controlled and programmed in LabVIEW environment and commercial EC testing equipment (Nortec 500) was used for impedance measurements. Figure 5.37 shows the output signal from CFRP Sample 1 with the different EC tailored probes with the best frequencies for each probe (all at 8 MHz except PCB Probe #4 in bridge mode at 6 MHz). Regarding PCB Probe #1, operating in bridge differential mode, the defect TH05 (drilled hole from the top), as well as the aluminium mark on the opposite side of the probe were not detected. This probe operating in reflection mode was not suitable due to the excitation track being too far away from the pickup coils. The second output signal corresponds to PCB Probe #2 operating in reflection mode. Defects TH05 and SH2 were not detected, as well as, the aluminium mark on the opposite side of the inspection. The third output signal corresponds to PCB Probe #3 operating in bridge differential mode. Reflection mode did not show any improvement. All the defects were detected except TH05. The fourth output signal corresponds to PCB Probe #4 operating in reflection mode. All the defects were detected except the aluminium mark on the opposite side of the inspection. The signal characteristic changed as well, since the “8” shape characteristic was lost, which means that the excitation does not induce currents under the whole sensing coils, only in the windings near the excitation track. The last output signal corresponds to PCB Probe #4 operating in bridge differential mode at 6 MHz. All the defects were detected with good signal-to-noise ratio. Probe #4 can detect all the defects because of its geometry. It induces the EC in the fibres preferential orientation as observed in the simulation. This maintains the EC pattern in the fibre as constant as possible in flawless fibres. So, when a fibre break occurs, a greater EC disturbance is created and measured by the probe.

Figure 5.38 depicts the output signal of PCB Probe #4 in an enlarged graph comparing to Ionic Probe [263] at 8 MHz, as well as, to commercial EC absolute pencil probe with 3 mm diameter with a fixed air-loaded reference coil in bridge mode at 6 MHz and a circular planar EC absolute probe with 8 mm diameter with a fixed loaded reference coil over a good specimen in

bridge mode at 6 MHz. Even though the defects are close to each other, all four defects and both aluminium marks are spotted by PCB Probe #4 while the circular planar EC absolute probe detected only three of them and the Ionic probe detected all but one with an inferior signal amplitude. On the other hand, the commercial probe managed to detect merely the top aluminium mark. This demonstrates the superior performance of planar PCB coils and the impact different geometries have for the same operation modes. The cut-like defects signal has a bigger amplitude than the through-hole defects.

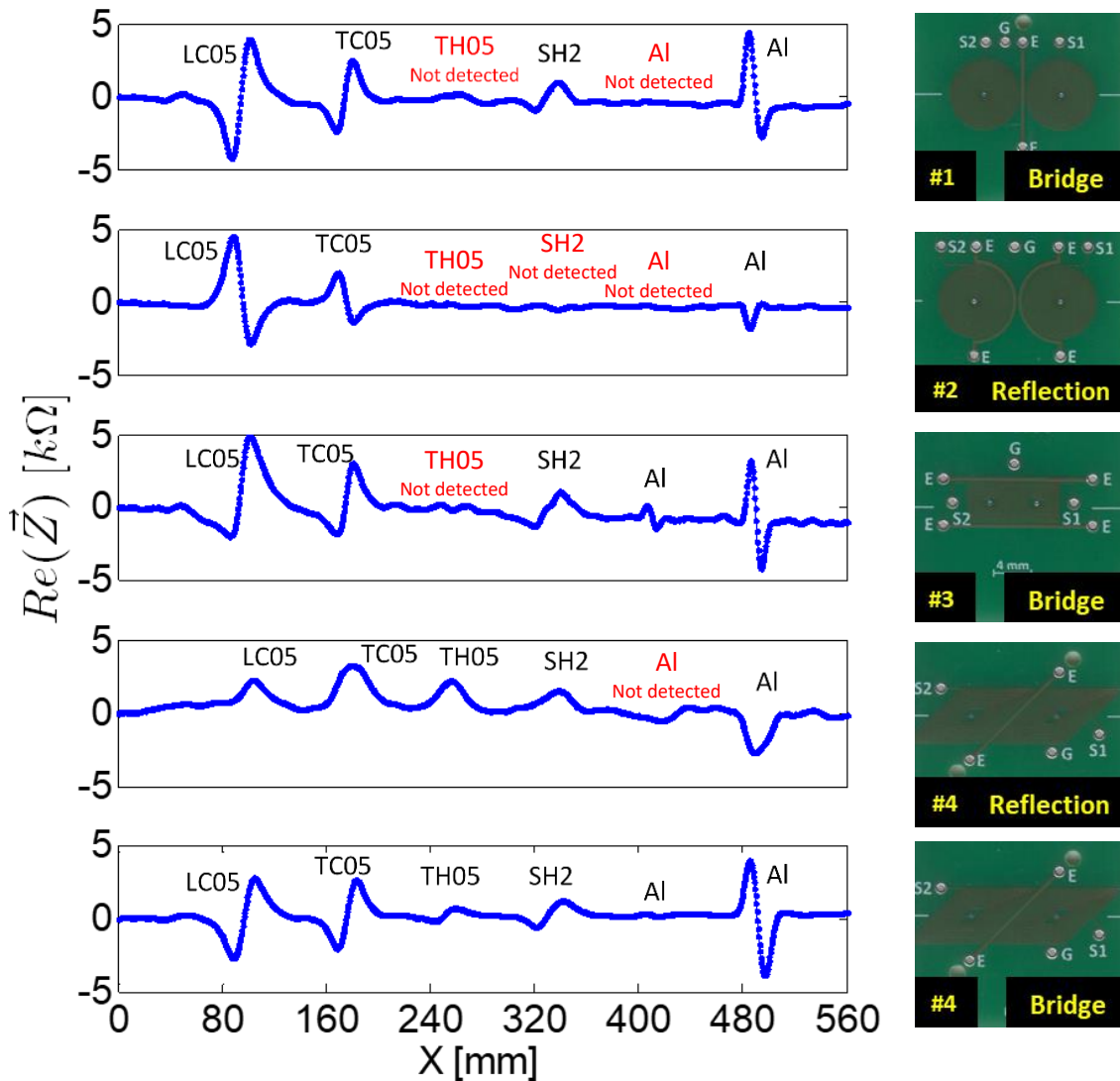


Figure 5.37 – Output signal of tailored EC Probes inspecting the Sample 1 at low speed at 8 MHz, except PCB Probe #4 in bridge mode at 6 MHz.

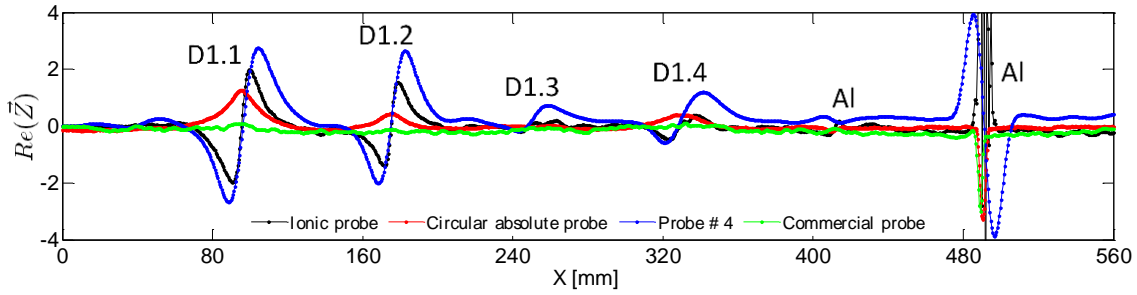


Figure 5.38 – Output signal of EC PCB Probe #4 inspecting the Sample 1 at 8 MHz at low speed comparing to the Ionic Probe at 8 MHz and commercially EC absolute pencil probe with 3 mm diameter with a fixed air loaded reference coil in bridge mode at 6 MHz.

### 5.8.2.– High speed experimental tests

The most reliable tailored EC probes were experimentally tested by the high-speed prototype with the automated high-speed linear guide belt driven (1 to 4 m/s). A commercial GE Mentor EM impedance measure equipment was used. Figure 5.39 shows the output signal of PCB Probe #4 operating in bridge differential mode at 6 MHz when inspecting CFRP Sample 2 at 3.5 m/s. The first and last differential signals were obtained from the aluminium markers that mark the beginning and the end of constant speed conditions. All four defects are clearly detected with excellent signal-to-noise ratio. As anticipated by the numerical simulations, top cut-like defects (BFH and 3PTB) produce signals with superior amplitude compared to lateral cut defects (LC02 and LC05). Zooming in on the lateral cut signals and overlapping with the numerical simulation results allows the comparison between them. Figure 5.40 and Figure 5.41 depict the experimental results (lateral cut LC05 and top cut 3PTB zoomed in, respectively) overlapping the numerical simulation results for the same defects. This provides an identification of the defect and they clearly agree in the exhibited trend.

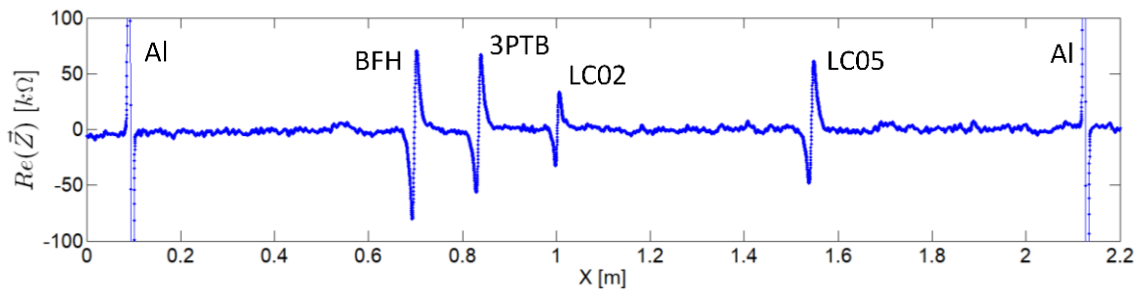


Figure 5.39 – Output signal of EC PCB Probe #4 operating in bridge differential mode inspecting Sample 2 at 6 MHz at 3.5 m/s.

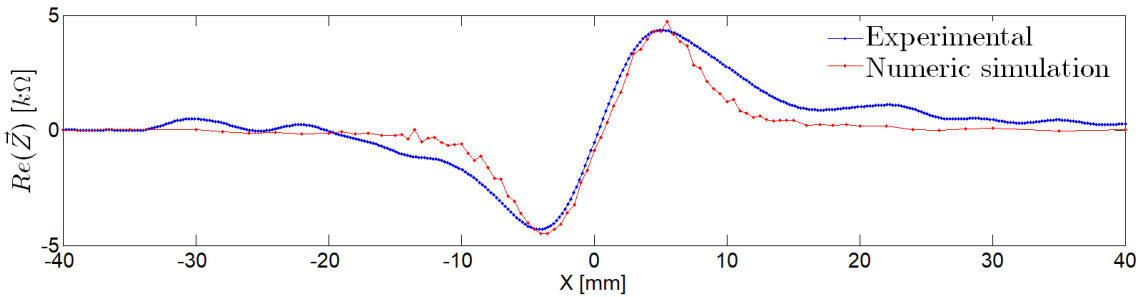


Figure 5.40 – Comparison between experimental results and numerical simulation by Finite Element Method (FEM) testing the lateral cut defect LC05 at 6 MHz and 3.5 m/s.

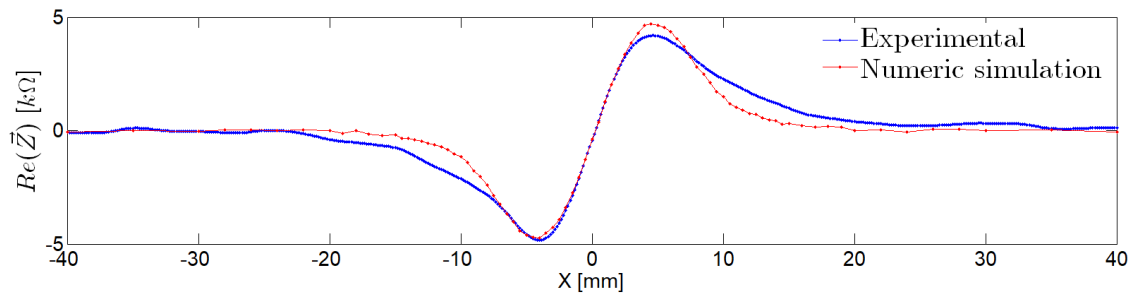


Figure 5.41 – Comparison between experimental results and numerical simulation by Finite Element Method (FEM) testing the cross top cut defect 3PTB at 6 MHz and 3.5 m/s.

Figure 5.42 depicts the output signal of the array versions of the PCB Probe #4 with two  $45^\circ$  parallelogram spiral coils (Figure 5.29b) operating in bridge differential mode at 6 MHz and inspecting Sample 2 at 3.5 m/s. In fact, since this probe inspects two elements with the same channel, the results correspond to two elements: one without defects and one that corresponds to Sample 2. All the defects are detected but the signal amplitude has decreased, and the smallest lateral cut defect is barely noticeable. Figure 5.43 shows the output signal of PCB Probe #4 inspecting Sample 2 at a velocity of 2 m/s, operating in reflection mode at 3 MHz. All the defects are distinguished although with an inferior signal to noise ratio. A commercial EC absolute pencil probe with 3 mm diameter with a fixed air loaded reference coil in bridge mode at 6 MHz was tested in the same inspection conditions for comparison purposes, but only the aluminium strip marks were found (Figure 5.44). This probe has a circular geometry which create and apply an axisymmetric magnetic field over the highly anisotropic CFRP material. Therefore, the EC generated are free spread along the fibre direction. This phenomenon increases the EC circulation area and, since the probe is small and can only measure what is beneath it, defect disturbance of EC outside this area cannot be detected.



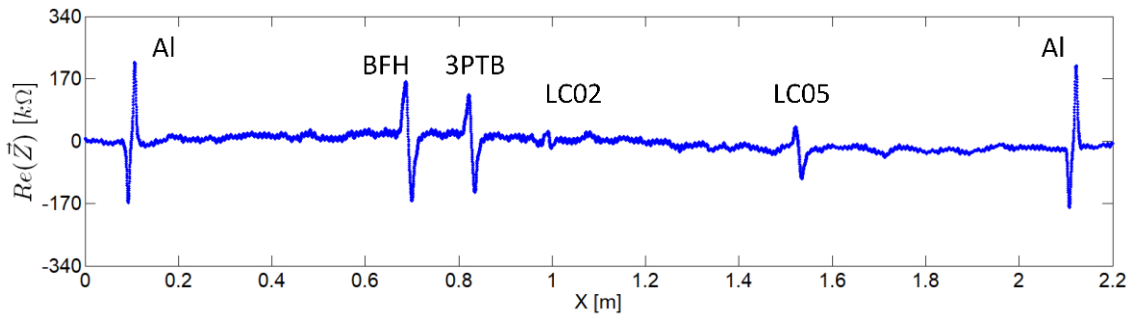


Figure 5.42 – Output signal of EC PCB Probe #4 (Figure 5.29 – b) operating in bridge differential mode inspecting Sample 2 at 6 MHz at 3.5 m/s.

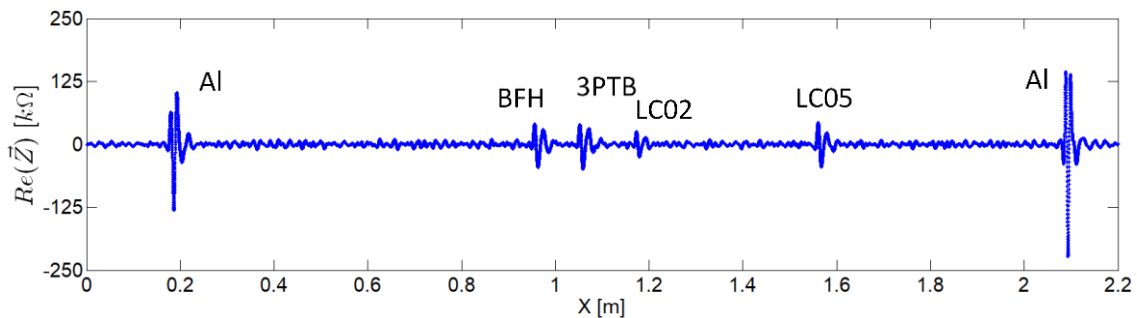


Figure 5.43 – Output signal of EC PCB Probe #4 operating in reflection mode inspecting Sample 2 at 3 MHz at 2 m/s.

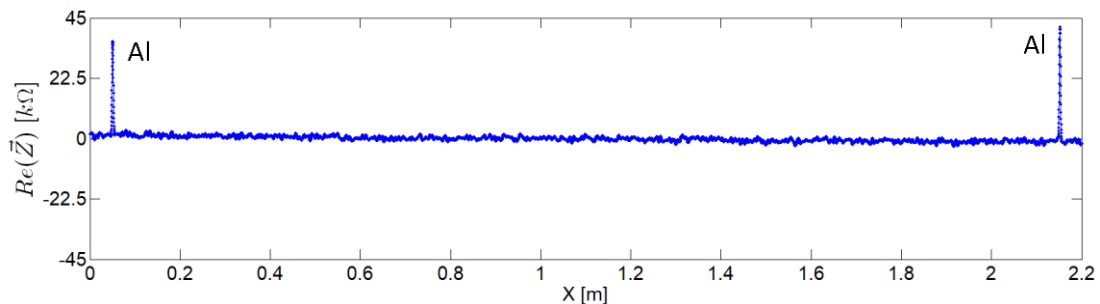


Figure 5.44 – Output signal of EC commercial probe inspecting Sample 2 at 6 MHz at 2 m/s.

Figure 5.45 shows the output signal of PCB Probe #4 when inspecting a 60 m Sample 3 at a velocity of 4 m/s operating in bridge differential mode at 6 MHz. The defect BFH is clearly detected with a good signal to noise ratio. Figure 5.46 illustrates the output signal of PCB Probe #4 when inspecting a 25 m Sample 4 at a velocity of 4 m/s operating in bridge differential mode at 6 MHz. The defect (LC025) is clearly detected with a good signal to noise ratio which characteristic signal can be seen zoomed in Figure 5.47.



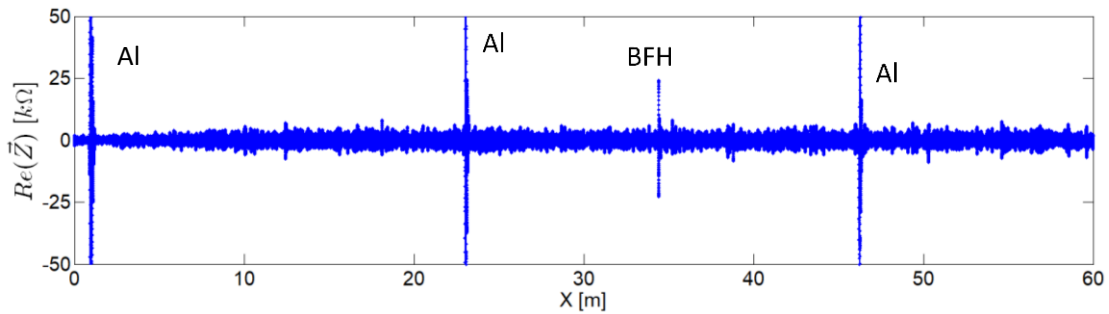


Figure 5.45 – Output signal of EC PCB Probe #4 inspecting Sample 3 at 6 MHz at 4 m/s.

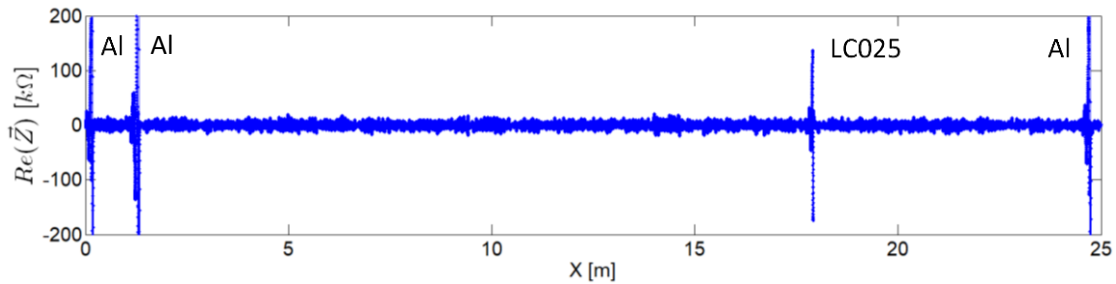


Figure 5.46 – Output signal of EC PCB Probe #4 inspecting Sample 4 at 6 MHz at 4 m/s.

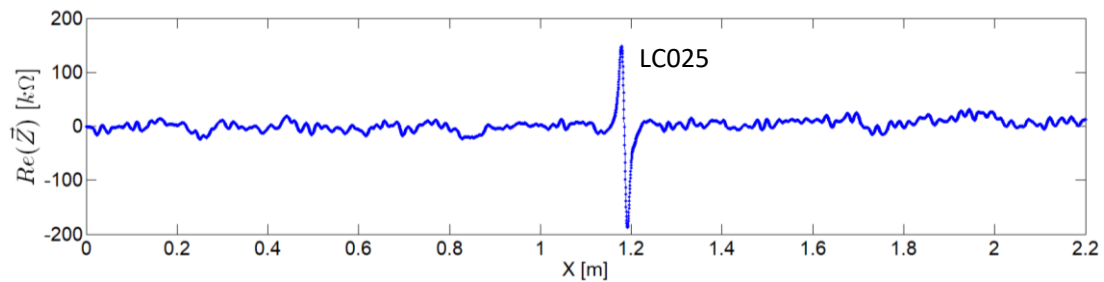


Figure 5.47 – Output signal of EC PCB Probe #4 inspecting Sample 4 at 6 MHz at 4 m/s zoomed in on the lateral cut defect.

### 5.9. – Summary

EC testing proved to be the most suitable NDT method for this specific inspection. It allows the inspection of the CFRP tension members at a high-speed velocity (4 m/s) and doing so without contact which was not an option in other methods like US.

Several tailored planar EC probes were designed, manufactured and experimentally validated. These probes demonstrated superior performance when compared to commercial pencil probes or conventional circular spiral absolute probes. The four main features that contributed to this technological development were: the planar configuration which allows a closer proximity of all windings to the specimen; the size of the sensing coils which cover the full width of each CFRP element; the differential operation mode that allows a continuous comparison of two portions of the specimen; and the geometry of the coils itself are responsible

for the EC and magnetic fields directions. These four features combined allowed a superior sensitivity of the EC probes despite the high lift-off used.

The 45° parallelogram spiral coils probe demonstrated the best performance especially when operating in bridge differential mode at a frequency of 6 MHz. Speeds of 2-4 m/s were used in the CFRP inspections and the smallest lateral cuts (0.2 of the width) and fibre breaks were detected with a clear signal.

Using the PCB technology to produce the probes enabled a faster and consistent reproducibility and parametrization for different specimen dimensions.

Numerical simulations allowed better understanding of the EC behaviour in the CFRP component and thus were an essential tool in assisting the probe design. The experimental results were consistent with the numerical simulations performed. It was also understood from the simulations, and confirmed experimentally, that the probes are not able to detect defects on the other side of the CFRP since, although there are currents flowing there, there is not a sensor to measure the local EC deviations. Future work will focus on an integral CFRP inspection (both sides) and different defects like delamination.

# **CHAPTER 6**

## **MAGNETIC PERMEABILITY PATTERN**

### **SUBSTRATE**

#### **6.1. – Introduction**

This chapter presents the development of a disruptive conceptual approach to the creation of EC in materials to be inspected, creating substrates/films with patterns of different magnetic permeabilities, called Magnetic Permeability Pattern Substrate (MPPS). Numerical simulations were performed to assess its viability (§6.2) and experimental validation was done using permanent magnets (§6.3.1) and induction heating thermography (§6.3.2). A new probe concept using this technology is also presented (§6.4).

## 6.2. – Motivation

As discussed in §2.4, when eddy currents direction is perpendicular to the defect orientation, the EC suffer a greater deviation than towards a parallel one, which will result in a greater signal amplitude of the probe impedance. Obtaining the maximum signal amplitude for a defect is clearly one of the main goals when designing an EC probe thus, the orientation of the EC in the specimen is crucial. It is also known that the EC in an isotropic specimen have the same orientation as the coil used for the excitation.

The need for greater sensitivity for all kind of defect morphologies and all kind of defect orientation is resulting in an increasingly complexity of EC probes. Excitation coils as well as pick-up coils are getting more and more complex with very complicated geometries [268].

The aim of this chapter is to propose a new way to induce eddy currents in a specimen reducing the EC probe complexity. In fact, the idea is to use coils geometries as simple as possible, namely: linear segments or circular coils. And, from these simple geometries create complex eddy currents patterns. As seen in §2.8, materials with high magnetic permeability, namely ferrites, have the ability to change the magnetic field near them. Conventionally, these ferrites are used as shields to confine the magnetic field or, as cores to concentrate the field in the centre of the probe. This change in the magnetic field with high magnetic permeability materials can therefore be exploited in order to change the eddy currents orientations.

## 6.1. – Theoretical concept

The proposed concept for introducing complex EC paths in the material consist in creating customized substrates/films with patterns with different magnetic permeabilities, called Magnetic Permeability Pattern Substrate (MPPS). These substrates/filters consist in a plate, for example, in a high magnetic permeability material and a specific pattern drawn in it as seen in Figure 6.1. It may be produced by 3D printing with FDM technology with magnetic iron PLA filament.

The eddy currents will be stronger in the MPPS gaps,  $\mu_r = 1$ , and lower under the substrate (where  $\mu_r \gg 1$ ), originating EC with the same orientation of the pattern present in the MPPS. The MPPS film complexity may not be simplified but the probe production process is. The coil windings can be the simplest possible and the complex pattern may be produced by the 3D printer.

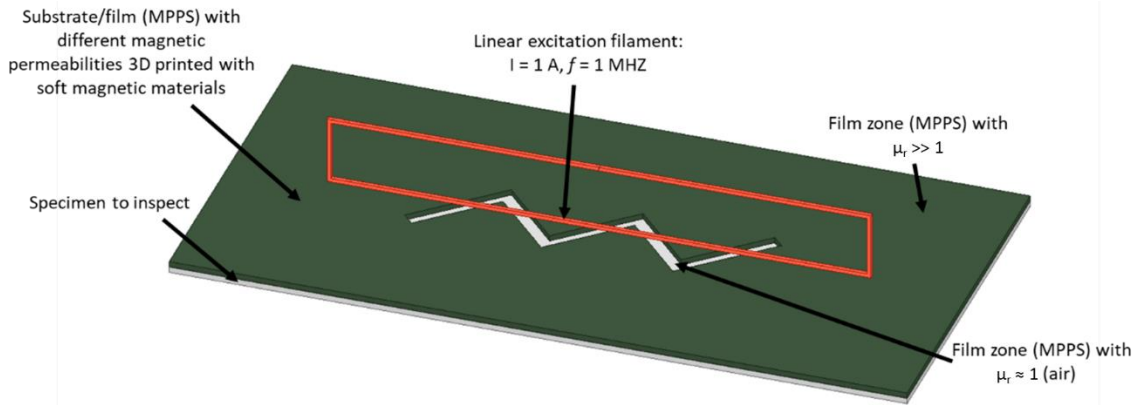


Figure 6.1 – Model used for the simulation of a zigzag pattern substrate.

## 6.2. – Numeric simulation of the MPPS

In order to access the feasibility of the concept, several numerical simulations were performed. For this, a numerical simulation software (ANSYS Electronics) was used, which calculates an approximate numerical solution of Maxwell's equations in their full formulation, Finite Integration Technique (FIT). Tetrahedral meshes of around 2 million elements were used. This specimen simulated was a standard aluminium with 3 mm thickness and an area of  $380 \times 190$  mm. The MPPS was modelled as a non-electrical conductor and with a relative magnetic permeability of  $\mu_r = 2000$ , with the same dimensions as the specimen, containing a zigzag shape without material with a thickness of 8 mm. A current of 1 A was imposed in the excitation coil at 1 MHz (Figure 6.1). As depicted in Figure 6.2, the eddy currents are stronger in the zones where there is no substrate creating the same pattern of the MPPS. However, that is not entirely true, on a closer look the EC density is stronger in the interface of the pattern. Just like the ferrite shields in EC probes confine the magnetic field here the magnetic field is concentrated on the interface creating a stronger field in the pattern perimeter.

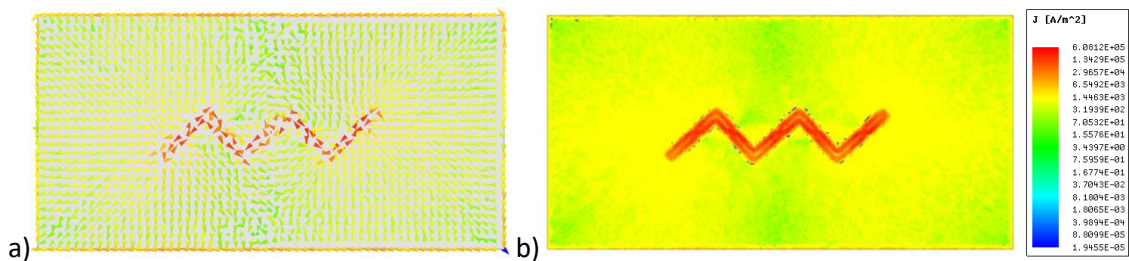


Figure 6.2 – Simulation results using a zigzag pattern on an aluminium specimen; a) eddy currents vector field; b) eddy currents density intensity.

Other geometries were simulated in order to understand the capabilities of the MPPS using only circular or linear windings since the main goal was to simplify the coils windings. In Figure 6.3 is represented a model of a cross pattern using a circular coil. The substrate has the

same dimensions as the specimen to inspect and has a cross shape pattern inside. Figure 6.4 shows that even though the coil is circular, the EC induced in the plate are not circular. The substrate creates a cross shaped pattern in the eddy currents density.

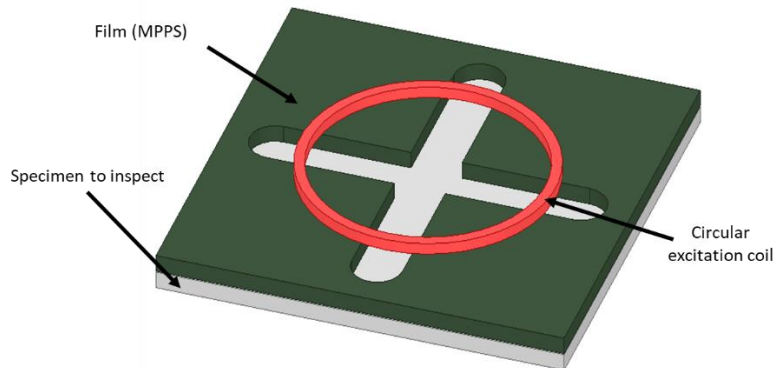


Figure 6.3 – Model of the simulation using a circular coil and a cross shaped pattern.

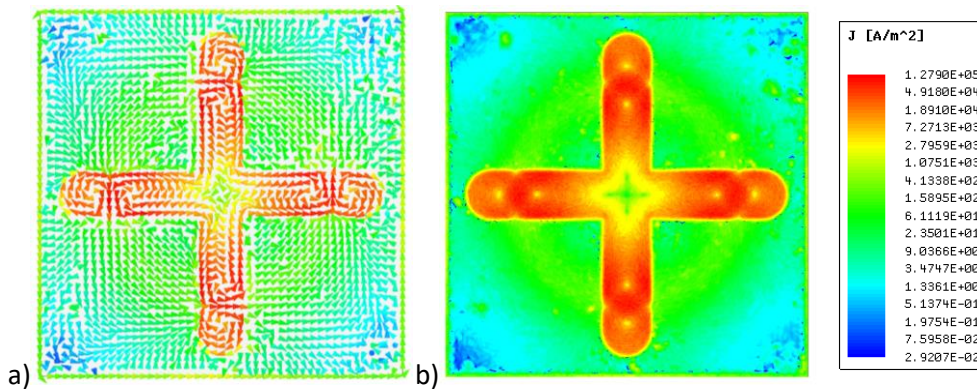


Figure 6.4 – Simulation results using a circular coil and a cross shaped pattern; a) eddy currents vector field; b) eddy currents density intensity.

Figure 6.5 depicts the simulation model using a ring-shaped pattern and a linear coil. The eddy currents are induced mainly in the ring perimeter being stronger near the excitation filament (Figure 6.6).

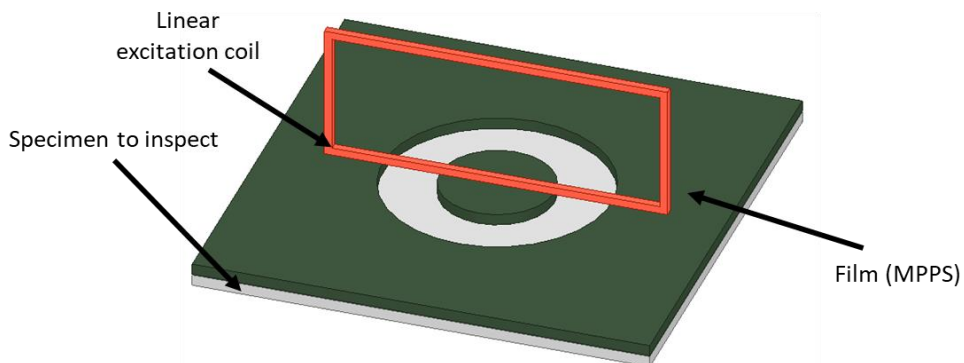


Figure 6.5 – Model of the simulation using a linear excitation and a ring-shaped pattern.



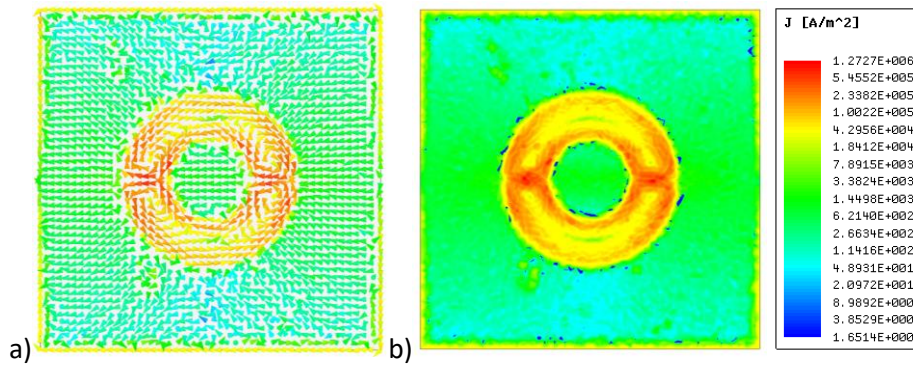


Figure 6.6 – Simulation results using a linear excitation and a ring-shaped pattern; a) eddy currents vector field; b) eddy currents density intensity.

Other approaches were made using several parts of MPPS in order slightly deviate the EC (Figure 6.7). An EC zigzag like pattern is created as depicted in Figure 6.8 when using a linear excitation and several MPPS rectangles. The results obtained in Figure 6.9 somewhat resemble the deviation EC suffer when encountering a crack.

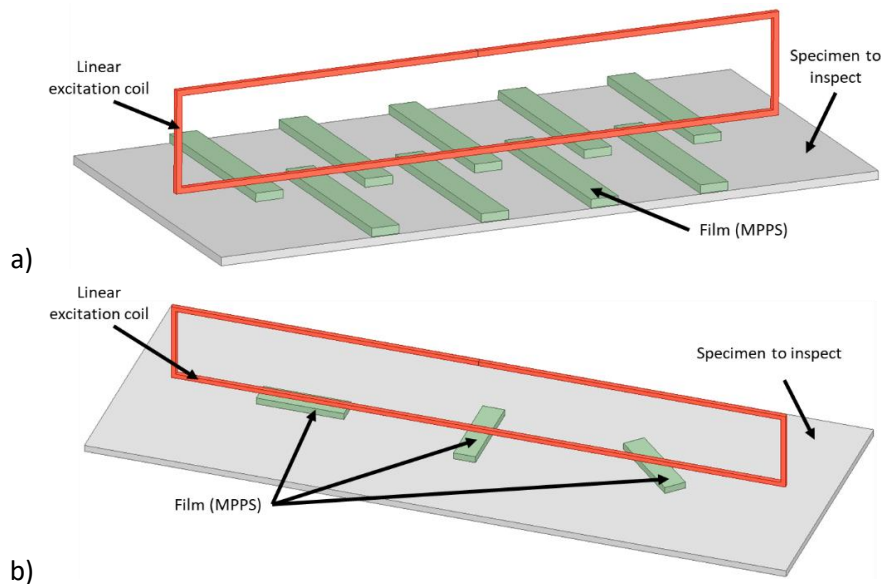


Figure 6.7 – Model of the simulation; a) using a linear excitation and several substrate rectangles creating a zigzag EC pattern; b) using a linear excitation and three substrate rectangles with different orientations.

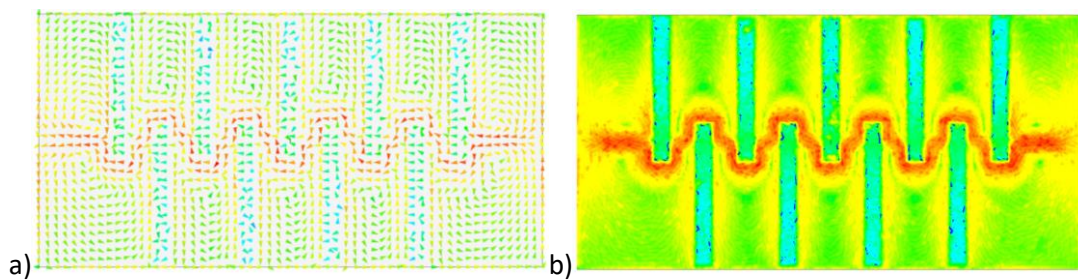


Figure 6.8 – Simulation results using a linear excitation and several substrate rectangles creating a zigzag EC pattern; a) eddy currents vector field; b) eddy currents density intensity.

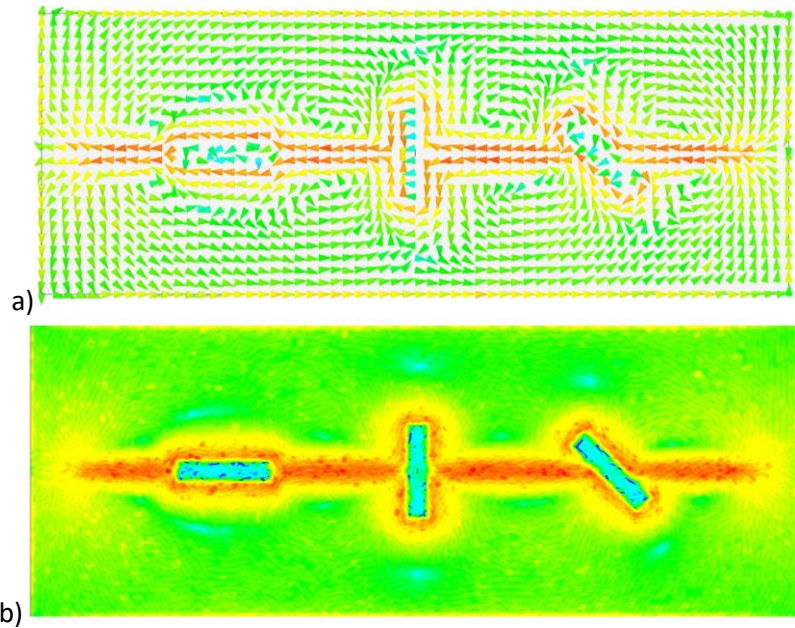


Figure 6.9 – Simulation results using a linear excitation and three substrate rectangles with different orientations; a) eddy currents vector field; b) eddy currents density intensity.

### 6.3. – Experimental concept validation

#### 6.3.1.– Magnetic field measurement

The numerical simulation demonstrated that the MPPS does indeed change the EC direction on an isotropic specimen. However, if the same is replicated in an experimental testing these results cannot be confirmed, since the EC are not visible by naked eyes. A different approach was taken in order to validate the concept experimentally. It consisted in applying the MPPS over a source of a strong magnetic field and measuring the magnetic field filtered through a Hall sensor.

A neodymium permanent magnet block with  $110.6 \times 89 \times 19.5$  mm was used as a permanent magnetic field source depicted in Figure 6.10. The magnetic field was measured with a Hall sensor Honeywell SS496A1.

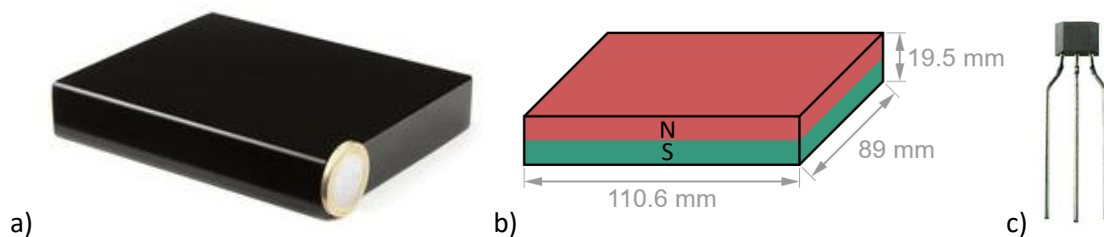


Figure 6.10 – Neodymium permanent magnet: a) image; b) magnetic poles and dimensions [288], c) Hall sensor Honeywell SS496A1.



The sensor was placed above the magnet at 64 mm where the magnetic field was around 300 Gauss (0.03 T), and a C-scan was made under a  $100 \times 100 \text{ mm}^2$  area with 1 mm resolution. In Figure 6.11 is displayed the Hall sensor scan of the magnetic without any filter between them. It is possible to observe that the magnetic field is not uniform over its entire area. So, any result made with a filter must be subtracted to cancel this.

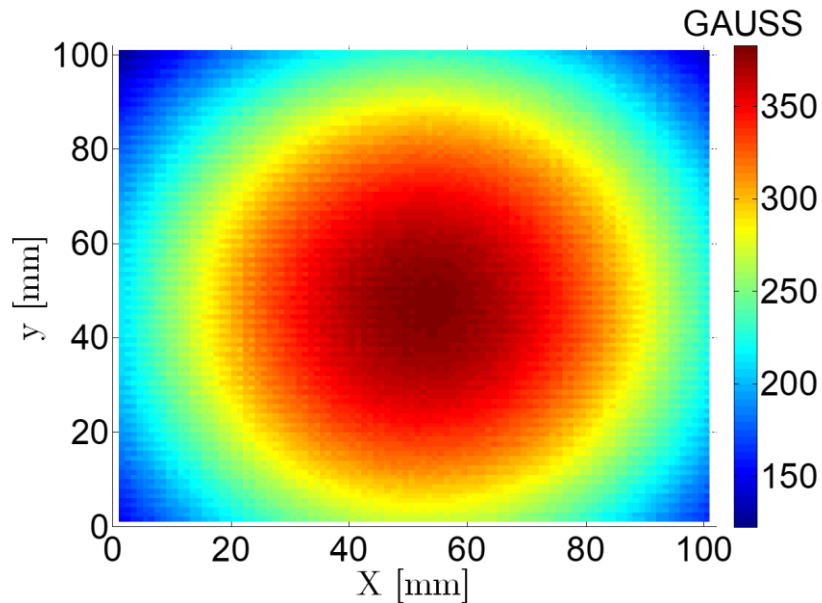


Figure 6.11 – Magnetic field measured with a Hall sensor at 64 mm with 1 mm resolution.

A filter was 3D printed with a magnetic iron PLA filament [289]. A zigzag pattern was designed in a rectangle shaped filter with  $110 \times 90 \text{ mm}$  as depicted in Figure 6.12.

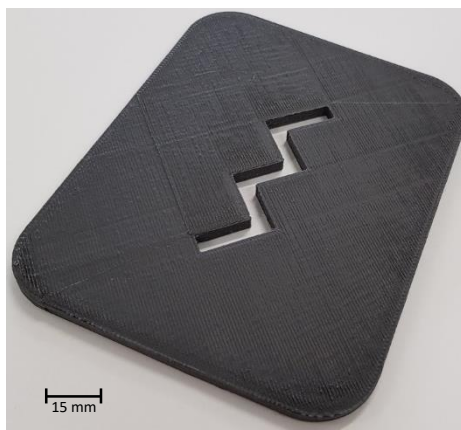


Figure 6.12 – 3D printed magnetic iron PLA filter with zigzag pattern.

With the same set up used to measure the magnet magnetic field the 3D printed filter was placed in between the Hall sensor, around 3 mm under it, and the magnet (Figure 6.13a). Figure 6.13b depicts the magnetic field obtained by the Hall sensor with 1 mm resolution. The

zigzag shape is clearly seen in the results which means that the magnetic field is indeed filtered by the MPPS.

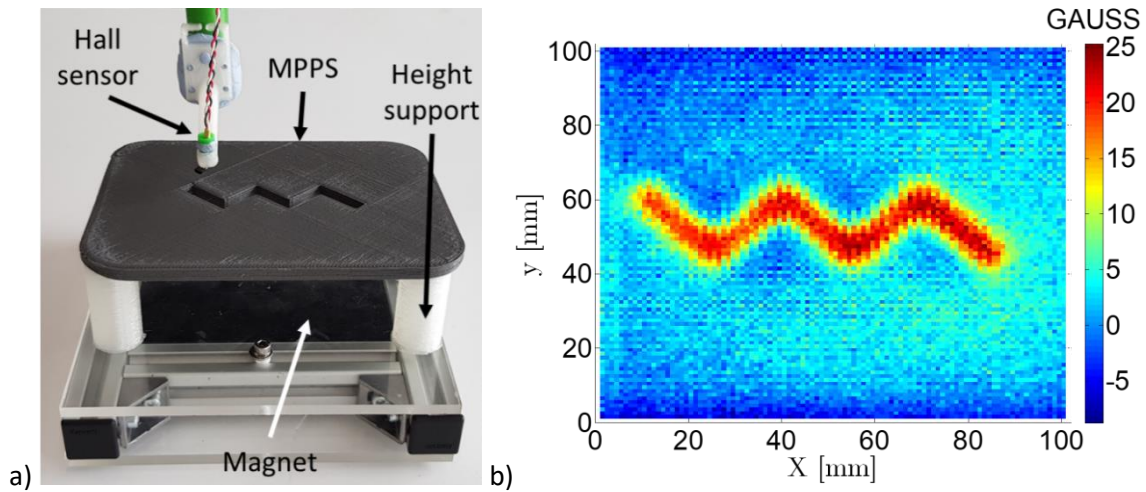


Figure 6.13 – Validation of the MPPS as a magnetic filter; a) set up used; b) magnetic field measured by the Hall sensor.

### 6.3.2.– Induction heating with thermography

Another approach to confirm this hypothesis consisted on the measurement of the heat produced by the EC induced by an excitation coil. An induction oven with 1.8 kW and a circular planar bobbin coil was used for the heating of a ferromagnetic steel plate. MHLL12060-000 ferrite sheet was used as the substrate (Figure 6.14b). The sheets have 0.35 mm thickness and a relative magnetic permeability of 130-200.

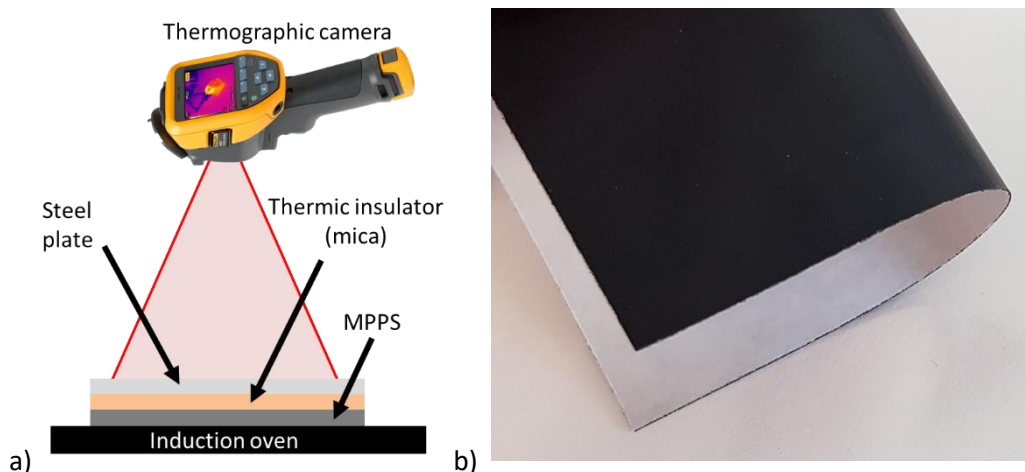


Figure 6.14 – Induction heating for thermography: a) setup used for the validation; b) ferrite sheet used as MPPS.

For the capture and visualization of the infrared radiation, a Fluke Ti400, marketed by Fluke® [290] was used. This camera has a temperature measuring range from -20 °C to 1200 °C, with a temperature measurement accuracy of  $\pm 2$  °C and an infrared spectral band of 7.5  $\mu\text{m}$  to 14  $\mu\text{m}$ .

It also features a 9 Hz image capture frequency, a field of view  $24^\circ \times 17^\circ$  and a spatial resolution of 1.31 mRad.

Figure 6.15 depicts a test performed without the MPPS substrate. As expected, the steel plate is heated by the induction oven and the shape of the coil is clearly visible in the thermographic image. The eddy currents, which are responsible for the heating, have the same orientation as the exciting coil.

Between the steel plate and the induction oven different patterns of MPPS were placed as depicted in Figure 6.14 and the schematic representation of these MPPS patterns towards the coil position and the respective thermographic images are displayed in Table 6.1. It was possible to change the eddy currents pattern from a circular geometry to a triangular or square one meaning that with the MPPS the EC in isotropic materials are no longer restricted to the excitation coil geometry. Table 6.2 shows other geometries of MPPS namely, small parts with the intent to create EC voids and force the EC to contour the MPPS.

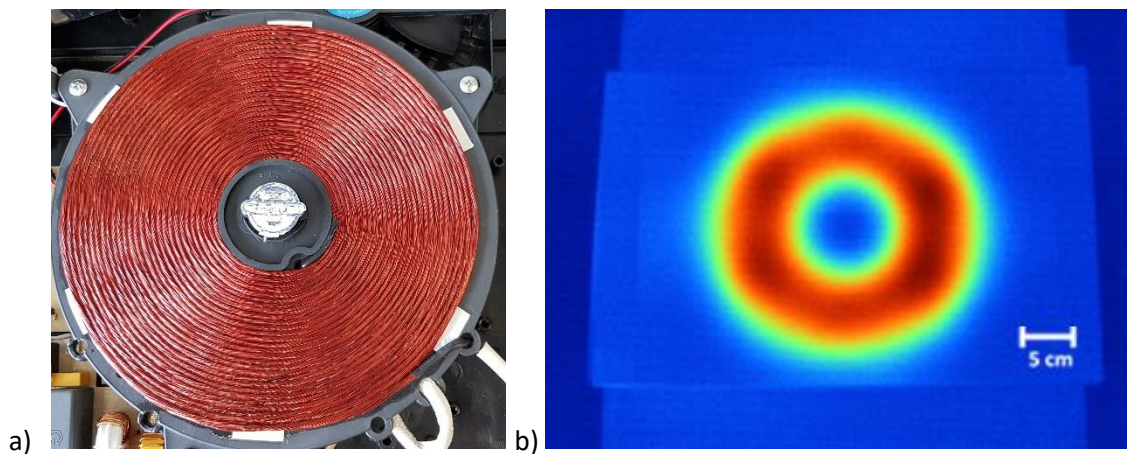


Figure 6.15 – Test performed without MPPS: a) induction coil; b) thermography image of the heat produced by the eddy currents.

Table 6.1 – Schematic representation of the MPPS geometry and its respective thermography.


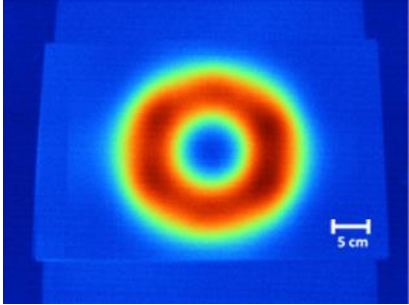
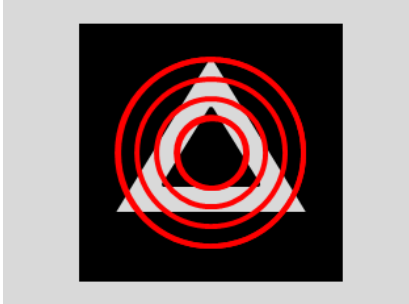
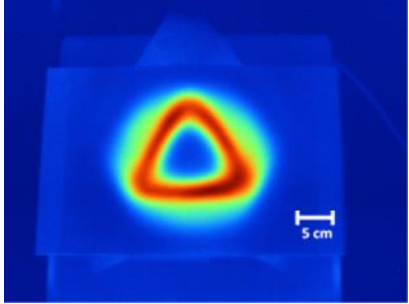
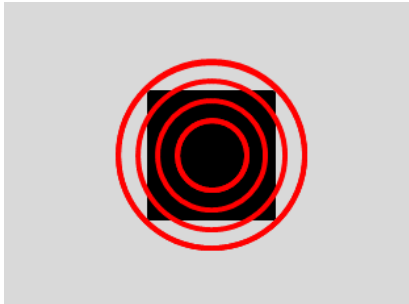
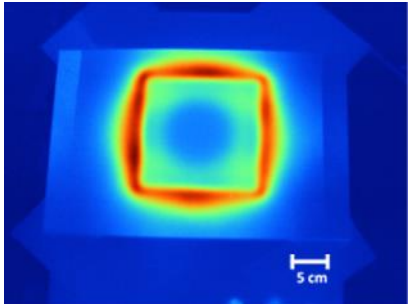
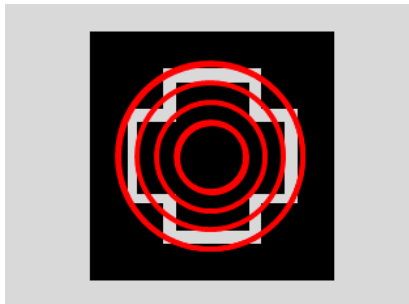
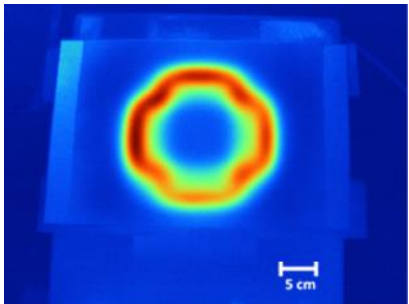

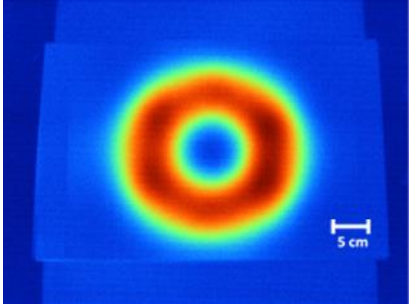

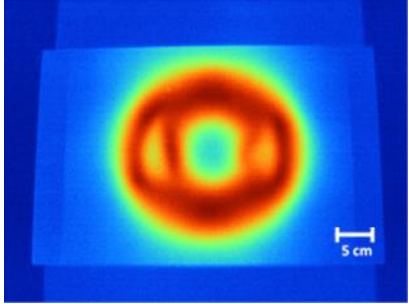

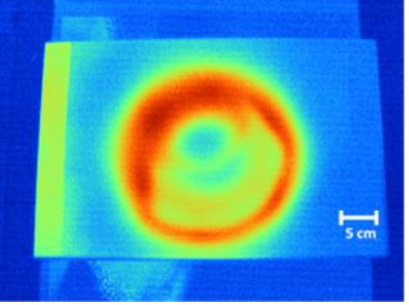

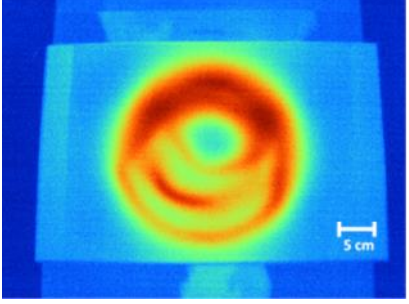
Schematic representation of the MPPS geometry towards the coil position	Thermographic image
 <p data-bbox="421 696 600 719">Steel Coil</p>	
 <p data-bbox="371 1081 647 1104">Steel MPPS Coil</p>	
 <p data-bbox="371 1462 647 1485">Steel MPPS Coil</p>	
 <p data-bbox="371 1843 647 1865">Steel MPPS Coil</p>	

Table 6.2 – Schematic representation of the MPPS geometry and its respective thermography.

Schematic representation of the MPPS geometry towards the coil position	Thermographic picture
 <p data-bbox="421 696 600 719">Steel Coil</p>	
 <p data-bbox="371 1081 647 1104">Steel MPPS Coil</p>	
 <p data-bbox="371 1467 647 1489">Steel MPPS Coil</p>	
 <p data-bbox="371 1852 647 1874">Steel MPPS Coil</p>	



#### 6.4. – Eddy current probe with the MPPS technology

A probe application that seemed obvious as a potential candidate for this technology was the probe for circular geometries presented in §3.4. In order to create the twisted excitation which proved to be the best solution, a complex chassis had to be designed and 3D printed, and a complex winding had to be wound which is very time consuming. Figure 6.16 depicts the three main components required to assemble the probe currently.

With the MPPS technology a different alternative can be considered. Instead of complex excitation winding, a simple coaxial circular winding would replace the complex one and a MPPS sheet with the desired geometry would be assembled over it (Figure 6.17). The assembly process would be: i) 3D print the chassis; ii) wound a copper wire coated with a nonconductive insulation in a circular shape; iii) cover with winding with the MPPS sheet; iv) place over the MPPS the sensitive coils array (Figure 6.18).

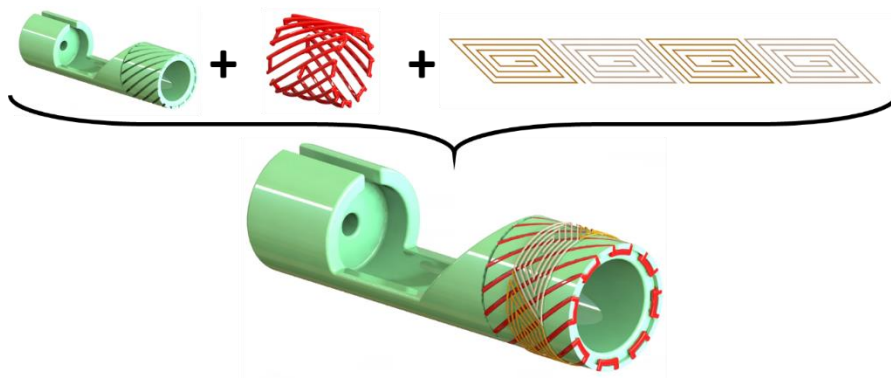


Figure 6.16 – Components required for the EC probe assembly as presented in §3.4: 3D printed chassis; complex twisted excitation coil; sensitive coils array.

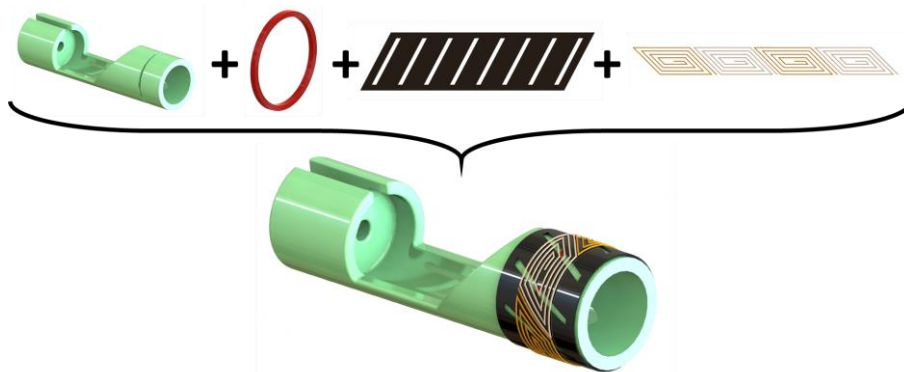


Figure 6.17 – Components required for the MPPS EC probe assembly: 3D printed chassis; simple circular winding; MPPS; sensitive coils array.

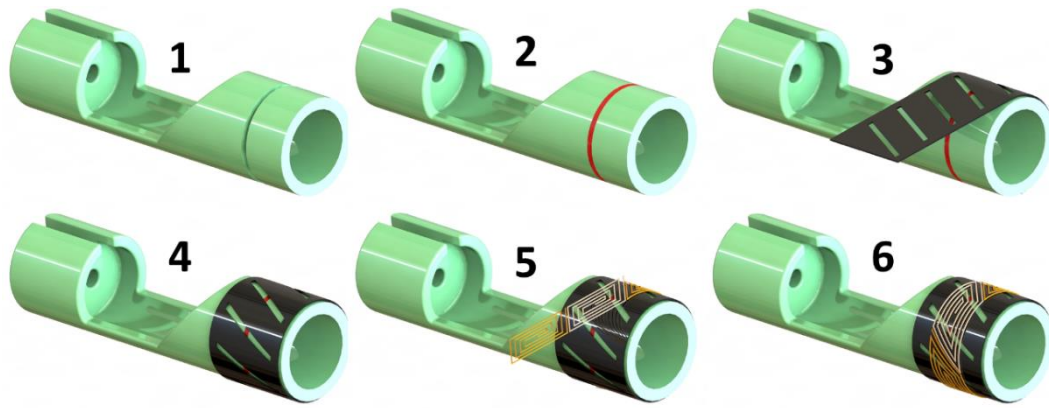


Figure 6.18 – Eddy current probe for inner diameter tube inspection with the MPPS technology assembly sequence.

Numerical simulations were performed in order to determine the pattern that creates EC with an orientation closer to the twisted winding. Tetrahedral meshes of around 2 million elements were used. This specimen simulated was a standard aluminium with 3 mm thickness and an area of  $380 \times 190$  mm. The MPPS was considered not electrical conductor and with a relative magnetic permeability of 2000, with the same dimensions as the specimen, containing the shape that simulates the twisted excitation without material with a thickness of 8 mm. A current of 1 A was imposed in the excitation coil at 1 MHz. As depicted in Figure 6.19, the eddy currents are stronger in the zones where there is no substrate creating the same pattern of the MPPS. The MPPS sheet generated EC with the same orientation as the complex twisted excitation coil used previously.

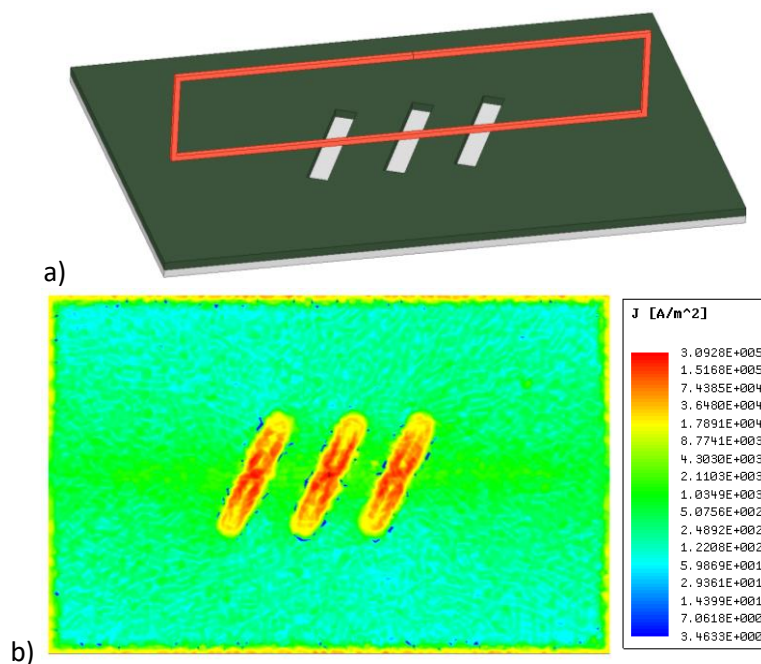


Figure 6.19 – Simulation using a linear excitation and pattern simulating the twisted excitation; a) model of the simulation; b) simulation result of the eddy currents density intensity.

### **6.5. – Summary**

The necessity for different EC orientations in the detection of imperfections is briefly presented as is the consequently increase of the EC probes complexity. A new alternative for other EC orientations different from the exciting coils is introduced denominated MPPS.

The MPPS technology is still at an early stage and there is still some work ahead. Despite, the concept has been validated by both simulation and experimental testing. The numerical simulations have demonstrated that the eddy currents acquired the shape of the MPPS pattern as predicted. The experimental validation was not as straightforward since the eddy currents visualization is not possible directly. Two different validation techniques were used. The technique with a permanent magnet and magnetic fields measurement with a Hall sensor allowed the visualization of the pattern designed in a 3D printed filter. It is possible to conclude that the MPPS does indeed change the magnetic field and that the eddy currents created by it do change accordingly. With the thermography technique, it was possible to visualize the heat produced by the eddy currents and the different patterns when applying different MPPS geometries. It was possible to change a circular heat pattern to square and triangular patterns as well as create voids where there should be EC. Summing up, it was possible to conclude that the MPPS does indeed change the EC paths. Finally, a probe concept, for tubular geometries, was designed with this technology which allows a faster and simplified probe assembly which was numerically simulated.



# **CHAPTER 7**

## **CONCLUSIONS AND FUTURE WORK**

### **7.1. – Introduction**

This chapter summarizes the research conclusions and future work is discussed. Since the most relevant conclusions are in the obtained results comments, and synthetized at the end of each chapter, this chapter pretends to recap the conclusions in a broader spectrum. Future work is also discussed.

## **7.2. – Conclusions**

This work consisted in the development of applied research, innovation, numerical simulation and knowledge generation for the development of eddy current probes for customized non-destructive systems for highly demanding industrial inspection conditions.

Technological innovations were developed in order to produce and experimentally validate customized eddy current systems for three highly demanding engineering applications, namely the inspection of: micro defects in tubular geometries; brazed joints for the automotive industry and high-speed moving composite materials.

### **Inspection of micro defects in tubular geometries**

New geometries of eddy current probes were designed, manufactured, validated and the experimental results in ITER CS jackets pipes were presented. The proposed linear array of trapezoidal spiral sensing coils allows the elimination of blind zones of the conventional circular spiral coil arrays. It also increases the accuracy of the defect location in circumferential direction, since one single array with N coils allow to distinguish 2N regions. The flexible substrate allows a closer proximity to the tube surface, thus increasing the coil sensitivity. The probes exhibit superior sensitivity to detect circumferential defects when compared to existing commercial ones. Reflection type probes presented enhanced signals when compared to the absolute type probes. Twisted excitation windings and trapezoidal sensing coils evidenced a superior reliability, since it was able to detect all defects, with a depth of 0.5 mm thickness of 0.2 mm and length of 2 mm, in any scanning position. 3D FDM printing proved to be a very good alternative in the production of the chassis as it allows a faster, cheaper and easily customizable solution. The trapezoidal spiral coils are made in a PCB flexible substrate which is simple to produce and inexpensive, so that they can be disposable, allowing an easy customization to any specific application. This innovative probe has a Portuguese patent pending (PT N. º 109373) in the final stage of the process.

### **Inspection of brazed joints for the automotive industry**

The prototype designed and produced for the inspection of the laser brazed weld beads was successfully validated. The prototype holds two sets of EC probes, one designed for low frequencies and the other for high frequencies that aim the detection of sub-surface and surface defects, respectively. Each probe was comprised of two bobbin probes operating in bridge mode, one bobbin was over the weld being inspected while the other was over a reference (good weld).

That distinction was possible with the two set of probes since the low frequency (20 kHz) EC probe was able to detect both surface and sub-surface cracks and porosities and the high frequency (3 MHz) probe detected the surface ones only, as intended. For the lack of bonding, the potential drop measurement technique was used, with a customized four-point probe, which was also part of the prototype. The conventional pins position, linear, was numerically simulated and was considered unfit for this specific application. Different pins positions were simulated and a new disposition for the pins that made the inspection possible was found, in a cross shape. However, the aimed defects were quite hard to recreate artificially. Pores with 0.13 mm diameter and internal artificial defects 1 mm from the weld surface were successfully detected.

### **Inspection of high-speed moving composite materials**

Several tailored planar EC probes were designed, manufactured and experimentally validated. These probes demonstrated superior performance when compared to commercial pencil probes or conventional circular spiral absolute probes. The four main features that contributed to this technological development were: the planar configuration which allows a closer proximity of all windings to the specimen; the size of the sensing coils which cover the full width of each CFRP element; the differential operation mode that allows a continuous comparison of two portions of the specimen; and the geometry of the coils itself are responsible for the EC and magnetic fields directions. These four features combined allowed a superior sensitivity of the EC probes despite the high lift-off used (about 3 mm). Using the PCB technology to produce the probes enabled a faster and consistent reproducibility and parametrization for different specimen dimensions. Numerical simulations allowed better understanding of the EC behaviour in the CFRP component and thus were an essential tool in assisting the probe design. The experimental results were consistent with the numerical simulations performed. It was also understood from the simulations, and confirmed experimentally, that the probes are not able to detect defects on the other side of the CFRP since, although there are currents flowing there, there is not a sensor to measure the local EC deviations. Defects under 1 mm at speeds up to 4 m/s and 3 mm lift-off were successfully detected.

### **Magnetic Permeability Pattern Substrate (MPPS)**

Another innovation of a more scientific and disruptive nature was the new technique for the generation of EC in the materials to be inspected, an alternative to the conventional use of bobbin coils. This technique, Magnetic Permeability Pattern Substrate (MPPS), consisted on the

development of substrates/films with patterns of different magnetic permeabilities rather than the use of excitation bobbin coils or filaments of complex geometry to provide the desired EC orientation.

The MPPS technology is still at an early stage and there is still some work ahead. Despite, the concept has been validated both by numerical simulation and by experimental validation. The numerical simulations have demonstrated that the eddy currents acquired the shape of the MPPS pattern. The experimental validation was not as straightforward since the eddy currents visualization is not possible directly. Two different validation techniques were used:

1) A technique with a permanent magnet and magnetic fields measurement with a Hall sensor which allowed the visualization of the pattern designed in a 3D printed filter. It was possible to conclude that the MPPS does indeed change the magnetic field and that the eddy currents created by it do change accordingly.

2) Thermography technique, which allowed to visualize the heat produced by the eddy currents and the different patterns when applying different MPPS. It was possible to change a circular heat pattern to square and triangular patterns as well as create voids where there should be EC. Summing up, it was possible to conclude that the MPPS does indeed change the EC paths. A probe concept, for tubular geometries, was designed with this technology which allows a faster and simplified probe assembly which was numerically simulated.

### **7.3. – Future work**

The customized EC probe for circular geometries production process may be possible to simplify with the MPPS technology. The 3D printed chassis can be made with magnetic permeable PLA in the excitation zone which could have the complex geometry of the excitation. This would allow for the excitation coil to be a simple coaxial winding like the one used in conventional circular bobbin coils for piping applications.

The weld bead inspection prototype is currently at a TRL  $\approx$  5, since it has been validated in relevant environment, but there is still a long way to go, since it has been demonstrated that a commercial product could emerge from it.

Future work in the CFRP inspection will focus on an integral inspection (both sides) and different defect morphologies such as delamination. Higher velocities may be tested as well. This prototype has great potential to be turned into a commercial product since it is already

working for some morphologies with very good results. Future work should also include dedicated electronics for the probe drivers and sensors. These dedicated electronics could be included in the prototype chassis and a single wireless connection to a laptop or the cloud.

The MPPS technology still has a long way to go. Different kinds of materials for the filters must be tested as well as different geometries and thicknesses. A new signal measurement method should also be studied.

#### 7.4. – Publications and Patents

##### Papers in Peer-Reviewed Journals (indexed ISI/Scopus):

- [2] Miguel A. Machado, Kim-Niklas Antin, Luis S. Rosado, Pedro Vilaça, Telmo G. Santos, “Contactless high-speed eddy current inspection of unidirectional carbon fiber reinforced polymer”, *Composites Part B: Engineering*, 168 pp. 226-235, 2019. doi:10.1016/j.compositesb.2018.12.021
- [1] Miguel A. Machado, Luis Rosado, Nuno Pedrosa, Alexander Vostner, R.M. Miranda, Moisés Piedade, Telmo G. Santos, “Novel eddy current probes for pipes: Application in austenitic round-in-square profiles of ITER”, *NDT&E International*, 87 pp. 111–118, 2017. doi:10.1016/j.ndteint.2017.02.001.

##### Conference papers (indexed ISI/Scopus):

- [4] Fernando S. Crivellaro, Ana Peixoto, Miguel A. Machado, José P. Sousa, António Custódio, J. Pamies Teixeira, Telmo G. Santos, “Analysis of high temperature pipe integrity using customized eddy-current system”, 6th International Conference Integrity-reliability-failure, Lisbon, Portugal, 22-26/07/2018
- [3] Miguel A. Machado, Fernando S. Crivellaro, Ana Peixoto, Pedro H.G. Riscado, José P. Sousa, António Custódio, Rosa M. Miranda, J. Pamies Teixeira, Telmo G. Santos, “Customized eddy current probes for pipe inspection at high temperatures”, 12th European Conference on Non-Destructive Testing, Gothenburg, Sweden, 11-15/06/2018.
- [2] Telmo G. Santos, Patrick L. Inácio, Miguel A. Machado, J.J. Pamies Teixeira, Carla M. Machado, Rosa Miranda, Carla C.C.R. Carvalho, *Advances in non destructive testing and evaluation (ndt&e): developments and applications. Proceedings of 7th International Conference on Mechanics and Materials in Design*, pp. 1857-1858, Albufeira, Portugal, 11-15/06/2017
- [1] Miguel A. Machado, Luís Rosado, Nuno Pedrosa, R. M. Miranda, Moisés Piedade, Telmo G. Santos, “Customized Eddy Current Probes for Pipe Inspection”, *Electromagnetic Nondestructive Evaluation (XX) Studies in Applied Electromagnetics and Mechanics*, vol.42 pp.283-290, 2016. doi:10.3233/978-1-61499-767-2-283.

**Conference papers (non-indexed):**

- [4] Miguel A. Machado, Fernando Crivellaro, Pedro H.G. Riscado, José P. Sousa, António Custódio, Rosa M. Miranda, Telmo G. Santos, “Sondas de correntes induzidas customizadas para inspeção de tubagens a alta temperatura”, 4CNEND- 4ª Conferência Nacional em Ensaios Não Destrutivos, PCTA, Évora, Portugal, 14-15/12/2017.
- [3] Miguel A. Machado, Pedro Riscado, Frederico Coelho, Carlos Simão, Carla C.C.R. de Carvalho, Telmo G. Santos, “Ensaios não destrutivos customizados: exemplos de aplicação”, 13º Congresso Ibero-americano de Engenharia Mecânica, Lisboa, Portugal, 23-26/10/2017.
- [2] Telmo G. Santos, Patrick Inácio, Miguel Machado, Pamies Teixeira, Carla C.C.R. de Carvalho, Rosa M. Miranda, Técnicas avançadas de inspeção: desenvolvimento e aplicações, I Workshop Luso-Brasileiro de Fabricação e Tecnologias de Inspeção (WLBFI), (Congresso Nacional de Ensaios Não Destrutivos - CONAEND), São Paulo, Brasil, 25/08/2016.
- [1] Machado, M.A., Miranda, R.M., Pedrosa, N., Rosado, L., Santos, T.G., “Design, Simulation and Experimental Validation of Eddy Current Probes for Non-Destructive Testing of Tubular Geometries”, 3rd National Conference in Non-Destructive Testing, Estado Maior da Força Aérea (EMFA), Amadora, Portugal, 15-16/12/2014, pp. 111-112.

**Patents:**

- [2] European and US Patent Pending (EU N°17211045,4-1017): Method and arrangement for condition monitoring of a rope of a hoisting apparatus. Date of patent application: 29-12-2017. Inventors from Portugal: Telmo Santos, Miguel Machado. Inventors from Finland: Antin Kim, Juntunen Mika, Puranen Mikko, Valjus Petteri. Assignee: KONE, Finland; Current status: Patent Pending.
- [1] Portuguese Patent Pending PT N.º 109373 - *New eddy currents probe for tubular geometries*, Date of patent application: 09-05-2017. Inventors: Telmo Santos, Miguel Machado. Assignee: FCT NOVA. Current status: PEDIDO-ESTUDO EM CURSO / EXAME DE FUNDO since 09-07-2018.  
<https://servicosonline.inpi.pt/pesquisas/main/patentes.jsp?lang=PT>

## REFERENCES

- [1] Prakash R. Non-destructive testing techniques. Tunbridge Wells, United Kingdom: New Age Science; 2012.
- [2] European Federation for Non-Destructive Testing (EFNDT) 2008. [www.efndt.org](http://www.efndt.org) (accessed May 10, 2018).
- [3] GUIDELINES E. Overall Ndt Quality System. Eur Fed Non-Destructive Test 2008. [http://www.efndt.org/Portals/14/doc/EFNDT Guidelines Issue 1.pdf](http://www.efndt.org/Portals/14/doc/EFNDT%20Guidelines%20Issue%201.pdf) (accessed February 10, 2018).
- [4] Dwivedi SK, Vishwakarma M, Soni PA. Advances and Researches on Non Destructive Testing: A Review. *Mater Today Proc* 2018;5:3690–8. doi:10.1016/j.matpr.2017.11.620.
- [5] Lavender JD. Introduction to nondestructive testing. *NDT Int* 1988;21:189–90. doi:10.1016/0308-9126(88)90483-X.
- [6] Kumar S, Mahto D. Recent Trends In Industrial And Other Engineering Applications Of Non Destructive Testing: A Review. *Int J Sci Eng Res* 2013;4:183–95. doi:10.1016/S1365-1609(03)00027-3.
- [7] Jolly M, Prabhakar A, Sturzu B, Hollstein K, Singh R, Thomas S, et al. Review of Non-destructive Testing (NDT) Techniques and their Applicability to Thick Walled Composites. *Procedia CIRP* 2015;38:129–36. doi:10.1016/j.procir.2015.07.043.
- [8] Lim MK, Cao H. Combining multiple NDT methods to improve testing effectiveness. *Constr Build Mater* 2013;38:1310–5. doi:10.1016/j.conbuildmat.2011.01.011.
- [9] LAMET UFRGS. Nondestructive Evaluation and Quality Control. vol. 17. 8th ed. ASM International; 1997.
- [10] Spencer FW. Visual Inspection Research Project Report on Benchmark Inspections. U.S. Department of Transportation, Federal Aviation Administration, Washinton D.C.: 1996.
- [11] Pedrini G, Gusev M, Schedin S, Tiziani HJ. Pulsed digital holographic interferometry by using a flexible fiber endoscope. *Opt Laser Eng* 2003;40:487–99. doi:DOI: 10.1016/S0143-8166(02)00077-5.
- [12] Zhu YK, Tian GY, Lu RS, Zhang H. A review of optical NDT technologies. *Sensors* 2011;11:7773–98. doi:10.3390/s110807773.
- [13] Santos TG, Miranda RM, De Carvalho CCCR. A new NDT technique based on bacterial cells to detect micro surface defects. *NDT E Int* 2014;63:43–9. doi:10.1016/j.ndteint.2014.01.006.
- [14] Santos TG, Miranda RM, Vieira MTF, Farinha AR, Ferreira TJ, Quintino L, et al. Developments in micro- and nano-defects detection using bacterial cells. *NDT E Int* 2016;78:20–8. doi:10.1016/j.ndteint.2015.11.002.
- [15] Ferreira TJ, Farinha AR, Santos TG, Miranda R, Carvalho CCCR, Vieira MT. Nondestructive testing in microfabrication using bacteria. *Cienc e Tecnol Dos Mater* 2017;29:e262–4. doi:10.1016/j.ctmat.2016.09.002.
- [16] Santos TG, Inácio PL, Costa AA, Miranda RM, Carvalho CCCRDE. Applications of a new NDT technique based on bacterial cells. 19th World Conf. Non-Destructive Test. 2016, Munich: 2016,

- p. 1–7.
- [17] Santos TG, Inácio P, Costa AA, Vilaça P, Miranda RM, Carvalho CCCR De. Micro Surface Defects Detection by Bacterial Cell Suspension. 11th ECNDT, Prague: 2014.
- [18] Santos TG, Inácio PL, Costa AA, Miranda RM, De Carvalho CCCR. Nova Técnica de END baseada em células bacterianas para detecção de micro e nano defeitos superficiais. *Soldag e Insp* 2015;20:253–9. doi:10.1590/0104-9224/SI2002.12.
- [19] Santos TG, Inácio P, Machado M, Teixeira P, Miranda RM, De Carvalho CCCR. Técnicas avançadas de inspeção: desenvolvimento e aplicações. I Work. Luso-Brasileiro Fabr. e Tecnol. Inspeção (WLBFI), (Congresso Nac. Ensaio Não Destrutivos - CONAEND), São Paulo: 2016.
- [20] Santos TG, Inácio PL, Machado M, Teixeira JJP, Machado CM, Miranda R, et al. Advances in non destructive testing and evaluation (ndt&e): developments and applications. *Proc. 7th Int. Conf. Mech. Mater. Des., Albufeira: 2017*, p. 1857–8.
- [21] Pinto F, Barata J, Barros P. Ensaio Não destrutivos. Edições técnicas do Inst. Sold. e Qual., 1992, p. 1–30.
- [22] Luk BL, Alan HSC. Human Factors and Ergonomics in Dye Penetrant and Magnetic Particles Nondestructive Inspection Methods 2007:1–7.
- [23] De Schryver T, Dhaene J, Dierick M, Boone MN, Janssens E, Sijbers J, et al. In-line NDT with X-Ray CT combining sample rotation and translation. *NDT E Int* 2016;84:89–98. doi:10.1016/j.ndteint.2016.09.001.
- [24] Yanhong J, Hao L, Lin Z, Dan L. X-ray Inspection of MIM 418 Superalloy Turbine Wheels and Defects Analysis. *Rare Met Mater Eng* 2017;46:317–21.
- [25] Stamopoulos AG, Tserpes KI, Dentsoras AJ. Quality assessment of porous CFRP specimens using X-ray Computed Tomography data and Artificial Neural Networks. *Compos Struct* 2018;192:327–35. doi:10.1016/j.compstruct.2018.02.096.
- [26] Nghiep TD, Cong NT. Analysis of gamma ray incoherent scattering for non-destructive testing. *Int J Nucl Energy Sci Technol* 2008;4:2008. doi:10.1504/IJNEST.2008.020531.
- [27] Peng PC, Wang CY. Use of gamma rays in the inspection of steel wire ropes in suspension bridges. *NDT E Int* 2015;75:80–6. doi:10.1016/j.ndteint.2015.06.006.
- [28] Priyada P, Ramar R, Shivaramu. Application of gamma ray scattering technique for non-destructive evaluation of voids in concrete. *Appl Radiat Isot* 2013;74:13–22. doi:10.1016/j.apradiso.2012.12.020.
- [29] Casalta S. Digital image analysis of X-ray and neutron radiography for the inspection and the monitoring of nuclear materials. *NDT E Int* 2003;36:349–55. doi:10.1016/S0963-8695(03)00008-2.
- [30] Vedula VSVM, Munshi P. An improved algorithm for beam-hardening corrections in experimental X-ray tomography. *NDT E Int* 2008;41:25–31. doi:10.1016/j.ndteint.2007.06.002.
- [31] Chankow N, Punnachaiya S, Wonglee S. Neutron radiography using neutron imaging plate. *Appl Radiat Isot* 2010;68:662–4. doi:10.1016/j.apradiso.2009.09.021.
- [32] Shukla M, Roy T, Kashyap Y, Shukla S, Singh P, Ravi B, et al. Development of neutron imaging beamline for NDT applications at Dhruva reactor, India. *Nucl Instruments Methods Phys Res Sect A Accel Spectrometers, Detect Assoc Equip* 2018;889:63–8. doi:10.1016/j.nima.2018.01.097.



- 
- [33] Kaestner AP, Hovind J, Boillat P, Muehlebach C, Carminati C, Zarebanadkouki M, et al. Bimodal Imaging at ICON Using Neutrons and X-rays. *Phys Procedia* 2017;88:314–21. doi:10.1016/j.phpro.2017.06.043.
- [34] Rosc J, Hammer VMF, Brunner R. X-ray computed tomography for fast and non-destructive multiple pearl inspection. *Case Stud Nondestruct Test Eval* 2016;6:32–7. doi:10.1016/j.csnedt.2016.08.002.
- [35] Zhou Y, Zheng X, Jiang J, Kuang D. Modeling of rail head checks by X-ray computed tomography scan technology. *Int J Fatigue* 2017;100:21–31. doi:10.1016/j.ijfatigue.2017.03.005.
- [36] Wang Y, Burnett T, Chai Y, SOUTIS C, Hogg P, Withers P. X-ray computed tomography study of kink bands in unidirectional composites. *Compos Struct* 2017;160:917–24. doi:10.1016/j.compstruct.2016.10.124.
- [37] Jones GA, Huthwaite P. Limited view X-ray tomography for dimensional measurements. *NDT E Int* 2018;93:98–109. doi:10.1016/j.ndteint.2017.09.002.
- [38] Zheng S, Vanderstelt J, McDerimid JR, Kish JR. Non-destructive investigation of aluminum alloy hemmed joints using neutron radiography and X-ray computed tomography. *NDT E Int* 2017;91:32–5. doi:https://doi.org/10.1016/j.ndteint.2017.06.004.
- [39] Lopes Ribeiro A, Geirinhas Ramos H, Postolache O. A simple forward direct problem solver for eddy current non-destructive inspection of aluminum plates using uniform field probes. *Meas J Int Meas Confed* 2012;45:213–7. doi:10.1016/j.measurement.2011.03.029.
- [40] Arenas MP, Rocha TJ, Angani CS, Ribeiro AL, Ramos HG, Eckstein CB, et al. Novel austenitic steel ageing classification method using eddy current testing and a support vector machine. *Measurement* 2018;127:98–103. doi:10.1016/j.measurement.2018.05.101.
- [41] Shu L, Songling H, Wei Z, Peng Y. Study of pulse eddy current probes detecting cracks extending in all directions. *Sensors Actuators, A Phys* 2008;141:13–9. doi:10.1016/j.sna.2007.07.008.
- [42] Vacher F, Alves F, Gilles-Pascaud C. Eddy current nondestructive testing with giant magneto-impedance sensor. *NDT E Int* 2007;40:439–42. doi:10.1016/j.ndteint.2007.02.002.
- [43] Rocha TJ, Ramos HG, Lopes Ribeiro A, Pasadas DJ. Magnetic sensors assessment in velocity induced eddy current testing. *Sensors Actuators A Phys* 2015;228:55–61. doi:10.1016/j.sna.2015.02.004.
- [44] Hatsukade Y, Miyazaki A, Matsuura H, Maeda T, Suzuki A, Tanaka S. Study of inspection of wire breakage in aluminum transmission line using SQUID. *NDT E Int* 2009;42:170–3. doi:10.1016/j.ndteint.2008.09.004.
- [45] Thirunavukkarasu S, Rao BPC, Vaidyanathan S, Jayakumar T, Raj B. Influence of sodium deposits in steam generator tubes on remote field eddy current signals. *Int J Press Vessel Pip* 2008;85:211–8. doi:10.1016/j.ijpvp.2007.10.010.
- [46] Fukutomi H, Takagi T, Nishikawa M. Remote field eddy current technique applied to non-magnetic steam generator tubes. *NDT E Int* 2001;34:17–23. doi:10.1016/S0963-8695(00)00026-8.
- [47] O'Connor S, Clapham L, Wild P. Magnetic flux leakage inspection of tailor-welded blanks. *Meas Sci Technol* 2002;13:157–62. doi:10.1088/0957-0233/13/2/303.
- [48] Zhang Y, Ye Z, Wang C. A fast method for rectangular crack sizes reconstruction in magnetic flux leakage testing. *NDT E Int* 2009;42:369–75. doi:10.1016/j.ndteint.2009.01.006.

- [49] Park GS, Jang PW, Ruho YW. Optimum Design of a Non-Destructive Testing System to Maximize Magnetic Flux Leakage. *J Magn* 2001;6:31–5. doi:10.1109/20.996326.
- [50] Guo-ming C, Wei L, Ze-xin W. Structural optimization of 2-D array probe for alternating current field measurement. *NDT E Int* 2007;40:455–61. doi:10.1016/j.ndteint.2007.03.002.
- [51] Ravan M, Sadeghi SHH, Moini R. Using a wavelet network for reconstruction of fatigue crack depth profile from AC field measurement signals. *NDT E Int* 2007;40:537–44. doi:10.1016/j.ndteint.2007.04.001.
- [52] Saguy H, Rittel D. Flaw detection in metals by the ACPD technique: Theory and experiments. *NDT E Int* 2007;40:505–9. doi:10.1016/J.NDTEINT.2007.04.003.
- [53] Lugg MC. Data interpretation in ACPD crack inspection. *NDT Int* 1989;22:149–54. doi:10.1016/0308-9126(89)90002-3.
- [54] RUDLIN JR, KARE R. Crack Depth Measurement using an Advanced ACPD Technique on a Large Tubular Joint. *Impact Non-Destructive Test.*, Elsevier; 1990, p. 221–30. doi:10.1016/B978-0-08-040191-1.50028-X.
- [55] Zilberstein V, Schlicker D, Walrath K, Weiss V, Goldfine N. MWM eddy current sensors for monitoring of crack initiation and growth during fatigue tests and in service. *Int J Fatigue* 2001;23.
- [56] Dover WD, Collins R, Michael DH. Review of developments in ACPD and ACFM. *Br J Non-Destructive Test* 1991;33:121–7. doi:10.1016/S0963-8695(98)90785-X.
- [57] Dover WD, Monahan CC. the Measurement of Surface Breaking Cracks By the Electrical Systems Acpd/Acfm. *Fatigue Fract Eng Mater Struct* 1994;17:1485–92. doi:10.1111/j.1460-2695.1994.tb00790.x.
- [58] Dixon S, Hill S, Fan Y, Rowlands G. The wave-field from an array of periodic emitters driven simultaneously by a broadband pulse. *J Acoust Soc Am* 2013;133:3692–9. doi:10.1121/1.4802648.
- [59] Baby S, Balasubramanian T, Pardikar RJ. Ultrasonic study for detection of inner diameter cracking in pipeline girth welds using creeping waves. *Int J Press Vessel Pip* 2003;80:139–46. doi:10.1016/S0308-0161(03)00003-6.
- [60] Drinkwater BW, Wilcox PD. Ultrasonic arrays for non-destructive evaluation: A review. *NDT E Int* 2006;39:525–41. doi:10.1016/j.ndteint.2006.03.006.
- [61] Satyanarayan L, Sridhar C, Krishnamurthy C V., Balasubramaniam K. Simulation of ultrasonic phased array technique for imaging and sizing of defects using longitudinal waves. *Int J Press Vessel Pip* 2007;84:716–29. doi:10.1016/j.ijvpv.2007.08.002.
- [62] Baskaran G. Shear-wave time of flight diffraction (S-TOFD) technique. *NDT E Int* 2006;39:458–67. doi:10.1016/j.ndteint.2006.01.003.
- [63] Beard MD, Lowe MJS. Non-destructive testing of rock bolts using guided ultrasonic waves. *Int J Rock Mech Min Sci* 2003;40:527–36. doi:10.1016/S1365-1609(03)00027-3.
- [64] Chaki S, Bourse G. Guided ultrasonic waves for non-destructive monitoring of the stress levels in prestressed steel strands. *Ultrasonics* 2009;49:162–71. doi:10.1016/j.ultras.2008.07.009.
- [65] Mazeika L, Kazys R, Raisutis R, Sliteris R. Ultrasonic guided wave tomography for the inspection of the fuel tanks floor. *Int J Mater Prod Technol* 2011;41:128. doi:10.1504/IJMPT.2011.040291.
- [66] Ke W, Castaings M, Bacon C. 3D finite element simulations of an air-coupled ultrasonic NDT system.

- Springer Proc Phys 2009;128:195–206. doi:10.1007/978-3-540-89105-5\_17.
- [67] Dutton B, Clough AR, Rosli MH, Edwards RS. Non-contact ultrasonic detection of angled surface defects. *NDT E Int* 2011;44:353–60. doi:10.1016/j.ndteint.2011.02.001.
- [68] Zahran O, Shihab S, Al-Nuaimy W. Recent Developments in Ultrasonic Techniques For Rail-Track Inspection. *Northampt Br Inst Non-Destructive Test* 2002:55–60.
- [69] Borza DN. High-resolution time-average electronic holography for vibration measurement. *Opt Lasers Eng* 2004;41:515–27. doi:10.1016/S0143-8166(03)00016-2.
- [70] Jacquot M, Sandoz P, Tribillon G. High resolution digital holography. *Opt Commun* 2001;190:87–94.
- [71] Pickering SG, Almond DP. Matched excitation energy comparison of the pulse and lock-in thermography NDE techniques. *AIP Conf Proc* 2009;1096:533–40. doi:10.1063/1.3114301.
- [72] Omar MA, Zhou Y. A quantitative review of three flash thermography processing routines. *Infrared Phys Technol* 2008;51:300–6. doi:10.1016/j.infrared.2007.09.006.
- [73] Bates D, Smith G, Lu D, Hewitt J. Rapid thermal non-destructive testing of aircraft components. *Compos Part B Eng* 2000;31:175–85. doi:10.1016/S1359-8368(00)00005-6.
- [74] Titman DJ. Applications of thermography in non-destructive testing of structures. *NDT E Int* 2001;34:149–54. doi:10.1016/S0963-8695(00)00039-6.
- [75] Carlomagno GM, Meola C. Comparison between thermographic techniques for frescoes NDT. *NDT E Int* 2002;35:559–65. doi:10.1016/S0963-8695(02)00029-4.
- [76] Di Gianfrancesco A. The fossil fuel power plants technology. *Mater Ultra-Supercritical Adv Ultra-Supercritical Power Plants* 2017:1–49. doi:10.1016/B978-0-08-100552-1.00001-4.
- [77] Karabutov A, Devichensky A, Ivochkin A, Lyamshev M, Pelivanov I, Rohadgi U, et al. Laser ultrasonic diagnostics of residual stress. *Ultrasonics* 2008;48:631–5. doi:10.1016/j.ultras.2008.07.006.
- [78] Yashiro S, Takatsubo J, Miyauchi H, Toyama N. A novel technique for visualizing ultrasonic waves in general solid media by pulsed laser scan. *NDT E Int* 2008;41:137–44. doi:10.1016/j.ndteint.2007.08.002.
- [79] Dutton B, Boonsang S, Dewhurst RJ. A new magnetic configuration for a small in-plane electromagnetic acoustic transducer applied to laser-ultrasound measurements: Modelling and validation. *Sensors Actuators, A Phys* 2006;125:249–59. doi:10.1016/j.sna.2005.07.026.
- [80] Dixon S, Palmer SB. Wideband low frequency generation and detection of Lamb and Rayleigh waves using electromagnetic acoustic transducers ( EMATs ) 2004;42:1129–36. doi:10.1016/j.ultras.2004.02.019.
- [81] Mabrouki F, Thomas M, Genest M, Fahr A. Frictional heating model for efficient use of vibrothermography. *NDT E Int* 2009;42:345–52. doi:10.1016/j.ndteint.2009.01.012.
- [82] Mian A, Han X, Islam S, Newaz G. Fatigue damage detection in graphite/epoxy composites using sonic infrared imaging technique. *Compos Sci Technol* 2004;64:657–66. doi:10.1016/j.compscitech.2003.07.005.
- [83] Tschelisnig P. Acoustic emission testing (AET) an integral non-destructive testing method. *Int J Mater Prod Technol* 2001;3:267–75.

- [84] Shrivastava S, Prakash R. Future research directions with Acoustic emission and Acousto-ultrasonic technique. *Int J Biomed Eng Technol* 2011;6. doi:10.1504/IJBET.2011.041775.
- [85] Hosoi A, Yamaguchi Y, Ju Y, Sato Y, Kitayama T. Detection and quantitative evaluation of defects in glass fiber reinforced plastic laminates by microwaves. *Compos Struct* 2015;128:134–44. doi:10.1016/j.compstruct.2015.03.050.
- [86] Chen X, Hou D, Zhao L, Huang P, Zhang G. Study on defect classification in multi-layer structures based on Fisher linear discriminate analysis by using pulsed eddy current technique. *NDT E Int* 2014;67:46–54. doi:10.1016/j.ndteint.2014.07.003.
- [87] Burrows SE, Fan Y, Dixon S. High temperature thickness measurements of stainless steel and low carbon steel using electromagnetic acoustic transducers. *NDT E Int* 2017;68:221. doi:10.1016/j.ndteint.2014.07.009.
- [88] Machado MA, Crivellaro FS, Riscado P, Sousa JP, Custódio A, Miranda RM, et al. Sondas De Correntes Induzidas Customizadas Para Inspeção De Tubagens a Alta Temperatura. 4CNEND- 4ª Conferência Nac. em Ensaios Não Destrutivos, 2017.
- [89] Machado MA, Riscado P, Coelho F, Simão C, Carvalho CCCR, Santos T. Ensaios Não Destrutivos Customizados: Exemplos De Aplicação. 13º Congr. Ibero-americano Eng. Mecânica, Lisbon: 2017.
- [90] Machado MA, Crivellaro FS, Peixoto A, Riscado PHG, Sousa JP, Custódio A, et al. Customized eddy current probes for pipe inspection at high temperatures. *Ecndt18*, Gothenburg: 2018.
- [91] Lopez A, Bacelar R, Pires I, Santos TG, Sousa JP, Quintino L. Non-destructive testing application of radiography and ultrasound for wire and arc additive manufacturing. *Addit Manuf* 2018;21:298–306. doi:10.1016/j.addma.2018.03.020.
- [92] Waller JM, Parker BH, Hodges KL, Burke ER, Walker JL. Nondestructive Evaluation of Additive Manufacturing State-of-the-Discipline Report. *Nasa/Tm-2014-218560* 2014:1–36. doi:10.13140/RG.2.1.1227.9844.
- [93] Cerniglia D, Montinaro N. Defect Detection in Additively Manufactured Components: Laser Ultrasound and Laser Thermography Comparison. *Procedia Struct Integr* 2018;8:154–62. doi:10.1016/J.PROSTR.2017.12.016.
- [94] Zheng X. On some basic problems of fatigue research in engineering. *Int J Fatigue* 2001;23:751–66. doi:10.1016/S0142-1123(01)00040-8.
- [95] Zuluaga-Ramírez P, Frövel M, Belenguer T, Salazar F. Non contact inspection of the fatigue damage state of carbon fiber reinforced polymer by optical surface roughness measurements. *NDT E Int* 2015;70:22–8. doi:10.1016/j.ndteint.2014.12.003.
- [96] Heideklang R, Shokouhi P. Multi-sensor image fusion at signal level for improved near-surface crack detection. *NDT E Int* 2015;71:16–22. doi:10.1016/j.ndteint.2014.12.008.
- [97] Garcia-Martin J, Gomez-Gil J, Vezquez-Sanchez E, García-Martín J, Gómez-Gil J, Vázquez-Sánchez E. Non-destructive techniques based on eddy current testing. *Sensors* 2011;11:2525–65. doi:10.3390/s110302525.
- [98] Rosado LS, Santos TG, Ramos PM, Vilaça P, Piedade M. A new dual driver planar eddy current probe with dynamically controlled induction pattern. *NDT E Int* 2015;70:29–37. doi:10.1016/j.ndteint.2014.09.009.
- [99] Bird J. *Electrical Circuit Theory and Technology*. Newnes 2007:1-. doi:10.4324/9780080549798.

- 
- [100] Eddy Current Electromagnetic Induction 2018. <http://www.victor-aviation.com/Eddy-Current-Inspection.php> (accessed May 20, 2018).
- [101] Iowa State University. NDT Resource center 2012. [https://www.nde-ed.org/index\\_flash.htm](https://www.nde-ed.org/index_flash.htm) (accessed February 23, 2018).
- [102] Rosado LS, Santos TG, Ramos PM, Vilaça P, Piedade M. A differential planar eddy currents probe: Fundamentals, modeling and experimental evaluation. *NDT E Int* 2012;51:85–93. doi:10.1016/j.ndteint.2012.06.010.
- [103] Kontroll Technik - Eddy Current Inspection Solutions. *Kontroll Tech* 2018. <http://www.kontrolltechnik.com/methods/eddy-current-principle> (accessed May 18, 2018).
- [104] Santos T. Ensaio Não Destrutivo por Correntes Induzidas: Desenvolvimento e Aplicação à Soldadura por Fricção Linear. Instituto Superior Técnico PhD thesis, 2009.
- [105] Tian GY, Sophian A. Reduction of lift-off effects for pulsed eddy current NDT. *NDT E Int* 2005;38:319–24. doi:10.1016/j.ndteint.2004.09.007.
- [106] Yu Y, Yan Y, Wang F, Tian G, Zhang D. An approach to reduce lift-off noise in pulsed eddy current nondestructive technology. *NDT E Int* 2014;63:1–6. doi:10.1016/j.ndteint.2013.12.012.
- [107] Rosado LS, Santos TG, Piedade M, Ramos PM, Vilaça P. Advanced technique for non-destructive testing of friction stir welding of metals. *Meas J Int Meas Confed* 2010;43:1021–30. doi:10.1016/j.measurement.2010.02.006.
- [108] CIVA E. Eddy current testing 2018. <http://www.extende.com/eddy-current-testing-for-education> (accessed August 10, 2018).
- [109] NDT Resource Center. American Society For Nondestructive Testing 2018. <https://www.asnt.org/MajorSiteSections/NDT-Resource-Center> (accessed January 9, 2018).
- [110] TPUB. Nondestructive Inspection Methods Manual. *Integr Publ* 2018. [http://chemical-biological.tpub.com/TM-1-1500-335-23/css/TM-1-1500-335-23\\_338.htm](http://chemical-biological.tpub.com/TM-1-1500-335-23/css/TM-1-1500-335-23_338.htm) (accessed May 22, 2018).
- [111] Joubert PY, Vourc'H E, Thomas V. Experimental validation of an eddy current probe dedicated to the multi-frequency imaging of bore holes. *Sensors Actuators, A Phys* 2012;185:132–8. doi:10.1016/j.sna.2012.07.009.
- [112] Yusa N, Hashizume H, Urayama R, Uchimoto T, Takagi T, Sato K. An arrayed uniform eddy current probe design for crack monitoring and sizing of surface breaking cracks with the aid of a computational inversion technique. *NDT E Int* 2014;61:29–34. doi:10.1016/j.ndteint.2013.09.004.
- [113] Rosado L, Santos TG, Piedade M, Ramos PM, Vilaça P. New Non Destructive Test technique on Metal Inspection. *IMEKO 2009 - Fundam. Appl. Metrol.*, 2009, p. 443–8.
- [114] Mandache C, Dubourg L, Merati A, Jahazi M. Pulsed eddy current testing of friction stir welds. *Mater Eval* 2008;66.
- [115] Smith RA. The potential for friction stir weld inspection using transient eddy currents. *Insight Non-Destructive Test Cond Monit* 2005;47:133–43. doi:10.1784/insi.47.3.133.61314.
- [116] Olympus Scientific Solutions Americas Corp 2014:0–2. <https://www.olympus-ims.com/pt> (accessed May 23, 2018).
- [117] Kosmas K, Sargentis C, Tsamakidis D, Hristoforou E. Non-destructive evaluation of magnetic metallic

- materials using Hall sensors. *J Mater Process Technol* 2005;161:359–62. doi:10.1016/j.jmatprotec.2004.07.051.
- [118] Machado MA, Rosado L, Pedrosa N, Vostner A, Miranda RM, Piedade M, et al. Novel eddy current probes for pipes: Application in austenitic round-in-square profiles of ITER. *NDT E Int* 2017;87:111–8. doi:10.1016/j.ndteint.2017.02.001.
- [119] Fava J, Ruch M. Design, construction and characterisation of ECT sensors with rectangular planar coils. *Insight - Non-Destructive Test Cond Monit* 2004;46:268–74. doi:10.1784/insi.46.5.268.55568.
- [120] Sadler DJ, Ahn CH. On-chip eddy current sensor for proximity sensing and crack detection. *Sensors Actuators A Phys* 2001;91:340–5. doi:10.1016/S0924-4247(01)00605-7.
- [121] Ptchelintsev A, de Halleux B. Two-dimensional finite element model for a long rectangular eddy current surface coil. *Rev Sci Instrum* 2000;71:571–6. doi:10.1063/1.1150244.
- [122] Ebine N, Ara K. Magnetic measurement to evaluate material properties of ferromagnetic structural steels with planar coils. *IEEE Trans Magn* 1999;35:3928–30. doi:10.1109/20.800711.
- [123] Ptchelintsev A, de Halleux B. Thickness and conductivity determination of thin nonmagnetic coatings on ferromagnetic conductive substrates using surface coils. *Rev Sci Instrum* 1998;69:1488–94. doi:10.1063/1.1148784.
- [124] Tsopelas N, Siakavellas NJ. Performance of circular and square coils in electromagnetic-thermal non-destructive inspection. *NDT E Int* 2007;40:12–28. doi:10.1016/j.ndteint.2006.07.011.
- [125] Ditchburn RJ, Burke SK. Planar rectangular spiral coils in eddy-current non-destructive inspection. *NDT E Int* 2005;38:690–700. doi:10.1016/j.ndteint.2005.04.001.
- [126] Santos T, Vilaça P, Dos Santos J, Quintino L. A new NDT system for micro imperfections detection: Application to FSW and FSpW. *Weld World* 2009;53:361–6.
- [127] Santos TG, Vilaça P, dos Santos J, Quintino L, Rosado L, Thompson DO, et al. INNOVATIVE EDDY CURRENT PROBE FOR MICRO DEFECTS, 2010, p. 377–84. doi:10.1063/1.3362418.
- [128] Naidjate M, Helifa B, Feliachi M, Lefkaier I-K, Heuer H, Schulze M. A Smart Eddy Current Sensor Dedicated to the Nondestructive Evaluation of Carbon Fibers Reinforced Polymers. *Sensors* 2017;17:1996. doi:10.3390/s17091996.
- [129] Brown DJ. Massively Multiplexed Eddy Current Testing and its Comparison with Pulsed Eddy Current Testing. *AIP Conf. Proc.*, vol. 700, AIP; 2004, p. 390–7. doi:10.1063/1.1711649.
- [130] Chen X, Ding T. Flexible eddy current sensor array for proximity sensing. *Sensors Actuators, A Phys* 2007;135:126–30. doi:10.1016/j.sna.2006.06.056.
- [131] Li P, Cheng L, He Y, Jiao S, Du J, Ding H, et al. Sensitivity boost of rosette eddy current array sensor for quantitative monitoring crack. *Sensors Actuators, A Phys* 2016;246:129–39. doi:10.1016/j.sna.2016.05.023.
- [132] Grimberg R, Udpa L, Savin A, Steigmann R, Palihovici V, Udpa SS. 2D Eddy current sensor array. *NDT E Int* 2006;39:264–71. doi:10.1016/J.NDTEINT.2005.08.004.
- [133] Gear Test 2018. <http://geartest.com.au> (accessed June 26, 2018).
- [134] Koyama K, Hoshikawa H. Influence of Speed Effect in Eddy Current Nondestructive Testing. *Nondestruct Test Eval* 1992;7:73–82. doi:10.1080/10589759208952989.

- 
- [135] Ida N. Modeling of velocity effects in eddy current applications. *J Appl Phys* 1988;63:3007–9. doi:10.1063/1.340929.
- [136] Rocha TJ. Velocity Induced Eddy Current Testing. Instituto Superior Técnico PhD thesis, 2016.
- [137] Feng CC, Deeds WE, Dodd C V. Analysis of eddy-current flowmeters. *J Appl Phys* 1975;46:2935–40. doi:10.1063/1.322032.
- [138] EN 10246-2. Non-destructive testing of steel tubes - Part 2: Automatic eddy current testing of seamless and welded austenitic and austenitic-ferritic steel tubes for verification of hydraulic leak-tightness 2000:2–3.
- [139] 25902-1 I. Titanium pipes and tubes – Non-destructive testing – Part 1: Eddycurrent examination 2009:2–3.
- [140] Förster F. Sensitive eddy-current testing of tubes for defects on the inner and outer surfaces. *Non-Destructive Test* 1974;7:28–36. doi:10.1016/0029-1021(74)90023-1.
- [141] IAEA. Training Guidelines in Non-destructive Testing Techniques 2002.
- [142] Kim YJ, Lee SS. Eddy current probes of inclined coils for increased detectability of circumferential cracks in tubing. *NDT E Int* 2012;49:77–82. doi:10.1016/j.ndteint.2012.04.004.
- [143] Xin J, Lei N, Udpa L, Udpa SS. Rotating field eddy current probe with bobbin pickup coil for steam generator tubes inspection. *NDT E Int* 2013;54:45–55. doi:10.1016/j.ndteint.2012.12.002.
- [144] Ye C, Huang Y, Udpa L, Udpa SS. Novel Rotating Current Probe With GMR Array Sensors for Steam Generate Tube Inspection. *IEEE Sens J* 2016;16:4995–5002. doi:10.1109/JSEN.2016.2556221.
- [145] Santos T, Vilaça P, Quintino L, Tecnologia S De. Developments in Ndt for Detecting Imperfections in Friction Stir Welds in Aluminium Alloys Developments in Ndt for Detecting Imperfections in Friction Stir Welds in Aluminium Alloys n.d.:30–7.
- [146] Yamada S, Katou M, Iwahara M, Dawson FP. Eddy current testing probe composed of planar coils. *IEEE Trans Magn* 1995;31:3185–7. doi:10.1109/20.490322.
- [147] Ditchburn RJ, Burke SK, Posada M. Eddy-current nondestructive inspection with thin spiral coils: Long cracks in steel. *J Nondestruct Eval* 2003;22:63–77. doi:10.1023/A:1026340510696.
- [148] Krampfner YD, Johnson DD. Flexible substrate eddy current coil arrays. *NDT Int* 1990;23:366. doi:10.1016/0308-9126(90)90968-T.
- [149] A.E. Crouch, T. Goyen PP. New method uses conformable array to map external pipeline corrosion. *Oil Gas J* 2004;102:55–9.
- [150] Uesaka M, Hakuta K, Miya K, Aoki K, Takahashi A. Eddy-current testing by flexible microloop magnetic sensor array. *IEEE Trans Magn* 1998;34:2287–97. doi:10.1109/20.703868.
- [151] N. Goldfine, D. Schlicker, Y. Sheiretov, A. Washabaugh, V. Zilberstein TL. Conformable eddy-current sensors and arrays for fleetwide gas turbine component quality assessment. *J Eng Gas Turbines Power* 2002;124:904–9.
- [152] Papazian JM, Nardiello J, Silberstein RP, Welsh G, Grundy D, Craven C, et al. Sensors for monitoring early stage fatigue cracking. *Int J Fatigue* 2007;29:1668–80. doi:10.1016/j.ijfatigue.2007.01.023.
- [153] Zilberstein V, Walrath K, Grundy D, Schlicker D, Goldfine N, Abramovici E, et al. MWM eddy-current arrays for crack initiation and growth monitoring. *Int J Fatigue* 2003;25:1147–55.
-

- doi:10.1016/j.ijfatigue.2003.08.010.
- [154] Olympus IMS. Olympus 2018. <https://www.olympus-ims.com/pt> (accessed May 23, 2018).
- [155] Eddyfi. Eddyfi 2018. <http://www.eddyfi.com/tubing-probes> (accessed May 20, 2018).
- [156] Jentek sensors. Jentek 2018. <http://www.jenteksensors.com/index.php> (accessed May 20, 2018).
- [157] GE Measurement. Gen Electr 2018. <https://www.gemeasurement.com/inspection-ndt> (accessed May 20, 2018).
- [158] Lion precision. Lion Precis 2018. <http://www.lionprecision.com/eddy-current-sensors> (accessed May 20, 2018).
- [159] Zetec. Zetec 2018. <http://www.zetec.com> (accessed May 20, 2018).
- [160] NDTs - NDT Solutions. NDTs 2018. <http://www.ndts.com> (accessed May 20, 2018).
- [161] Liu Z, Hu Y, Fan J, Yin W, Liu X, He C, et al. Longitudinal mode magnetostrictive patch transducer array employing a multi-splitting meander coil for pipe inspection. *NDT E Int* 2016;79:30–7. doi:10.1016/j.ndteint.2015.11.009.
- [162] Kalinin G, Gauster W, Matera R, Tavassoli AAF, Rowcliffe A, Fabritsiev S, et al. Structural materials for ITER in-vessel component design. *J Nucl Mater* 1996;233–237:9–16. doi:10.1016/S0022-3115(96)00316-9.
- [163] Shi Y, Wu Y, Li S, Liu B, Long F. Performance evaluation and analysis of ITER poloidal field conductors. *Fusion Eng Des* 2012;87:1801–4. doi:10.1016/j.fusengdes.2012.06.006.
- [164] Liu X, Wu Y, Qin J, Li L, Deng M, Wang W, et al. Developments of non-destructive test method of jacket section for ITER Poloidal Field (PF) coils. *IEEE Trans Appl Supercond* 2016:1–1. doi:10.1109/TASC.2016.2527635.
- [165] Machado MA, Rosado L, Pedrosa N, Miranda RM, Piedade M, Santos TG. Customized Eddy Current Probes for Pipe Inspection. *Stud Appl Electromagn Mech* 2017;42:283–90. doi:10.3233/978-1-61499-767-2-283.
- [166] Machado M. *Conceção, Simulação e Validação Experimental de Sondas de Correntes Induzidas para Ensaio Não Destrutivos de Geometrias Tubulares*. NOVA School of Science and Technology, NOVA University Lisbon - Master Thesis, 2014.
- [167] Riedelsberger H. Laser brazing in the automotive industry. 87th Fabtech / AWS Weld Show Atlanta 2006.
- [168] Krishnaja D, Cheepu M, Venkateswarlu D. A Review of Research Progress on Dissimilar Laser Weld-Brazing of Automotive Applications. *IOP Conf Ser Mater Sci Eng* 2018;330:012073. doi:10.1088/1757-899X/330/1/012073.
- [169] Frank S, Ungers M, Rolser R. Coaxial Control of Aluminum and Steel Laser Brazing Processes. *Phys Procedia* 2011;12:752–60. doi:10.1016/j.phpro.2011.03.094.
- [170] Lexus IS Body Structure. Boron Extrication 2018. <https://www.boronextrication.com/2014/07/10/2014-lexus-body-structure/> (accessed August 1, 2018).
- [171] Klocke F, Frank S. Surface deposits in laser brazing. *Sci Technol Weld Join* 2013;18:62–9. doi:10.1179/1362171812Y.0000000075.



- [172] Park HJ, Rhee S, Kang MJ, Kim DC. Joining of Steel to Aluminum Alloy by AC Pulse MIG Welding. *Mater Trans* 2009;50:2314–7. doi:10.2320/matertrans.M2009105.
- [173] Wang P, Chen X, Pan Q, Madigan B, Long J. Laser welding dissimilar materials of aluminum to steel: an overview. *Int J Adv Manuf Technol* 2016;87:3081–90. doi:10.1007/s00170-016-8725-y.
- [174] Lv SX, Jing XJ, Huang YX, Xu YQ, Zheng CQ, Yang SQ. Investigation on TIG arc welding–brazing of Ti/Al dissimilar alloys with Al based fillers. *Sci Technol Weld Join* 2012;17:519–24. doi:10.1179/1362171812Y.0000000041.
- [175] Venkateswarlu D, Nageswara rao P, Mahapatra MM, Harsha SP, Mandal NR. Processing and Optimization of Dissimilar Friction Stir Welding of AA 2219 and AA 7039 Alloys. *J Mater Eng Perform* 2015;24:4809–24. doi:10.1007/s11665-015-1779-4.
- [176] Yigezu BS, Venkateswarlu D, Mahapatra MM, Jha PK, Mandal NR. On friction stir butt welding of Al+12Si/10wt%TiC in situ composite. *Mater Des* 2014;54:1019–27. doi:10.1016/j.matdes.2013.09.034.
- [177] Kumar A, Mahapatra MM, Jha PK, Mandal NR, Devuri V. Influence of tool geometries and process variables on friction stir butt welding of Al–4.5%Cu/TiC in situ metal matrix composites. *Mater Des* 2014;59:406–14. doi:10.1016/j.matdes.2014.02.063.
- [178] K. Kimapong TW. Friction Stir Welding of Aluminum Alloy to Steel. *Weld Res* 2004;278–S:277–82.
- [179] Xie G hua, Yin J, Liu R gui, Chen B, Cai D sheng. Experimental and numerical investigation on the static and dynamic behaviors of cable-stayed bridges with CFRP cables. *Compos Part B Eng* 2017;111:235–42. doi:10.1016/j.compositesb.2016.11.048.
- [180] Chen Y. Study on the Joining of Titanium and Aluminum Dissimilar Alloys by Friction Stir Welding. *Open Mater Sci J* 2011;5:256–61. doi:10.2174/1874088X01105010256.
- [181] Muralimohan C., Haribabu S, Hari prasada Reddy Y, Muthupandi V, Sivaprasad K. Joining of AISI 1040 Steel to 6082-T6 Aluminium Alloy by Friction Welding. *J Adv Mech Eng Sci* 2015;1:57–64. doi:10.18831/james.in/2015011006.
- [182] Muralimohan CH, Haribabu S, Reddy YH, Muthupandi V, Sivaprasad K. Evaluation of Microstructures and Mechanical Properties of Dissimilar Materials by Friction Welding. *Procedia Mater Sci* 2014;5:1107–13. doi:10.1016/j.mspro.2014.07.404.
- [183] Muralimohan CH, Muthupandi V, Sivaprasad K. The influence of aluminium intermediate layer in dissimilar friction welds. *Int J Mater Res* 2014;105:350–7. doi:10.3139/146.111031.
- [184] Taban E, Gould JE, Lippold JC. Dissimilar friction welding of 6061-T6 aluminum and AISI 1018 steel: Properties and microstructural characterization. *Mater Des* 2010;31:2305–11. doi:10.1016/j.matdes.2009.12.010.
- [185] Cheepu M, Muthupandi V, Loganathan S. Friction Welding of Titanium to 304 Stainless Steel with Electroplated Nickel Interlayer. *Mater Sci Forum* 2012;710:620–5. doi:10.4028/www.scientific.net/MSF.710.620.
- [186] Muralimohan CH, Ashfaq M, Ashiri R, Muthupandi V, Sivaprasad K. Analysis and Characterization of the Role of Ni Interlayer in the Friction Welding of Titanium and 304 Austenitic Stainless Steel. *Metall Mater Trans A* 2016;47:347–59. doi:10.1007/s11661-015-3210-z.
- [187] Muralimohan CH, Muthupandi V. Friction Welding of Type 304 Stainless Steel to CP Titanium Using Nickel Interlayer. *Adv Mater Res* 2013;794:351–7. doi:10.4028/www.scientific.net/AMR.794.351.

- [188] Futamata M, Fuji A. Friction welding of titanium and SUS 304L austenitic stainless steel. *Weld Int* 1990;4:768–74. doi:10.1080/09507119009452178.
- [189] Cheepu M, Muthupandi V, Srinivas B, Sivaprasad K. Development of a Friction Welded Bimetallic Joints Between Titanium and 304 Austenitic Stainless Steel. *Techno-Societal 2016*, Cham: Springer International Publishing; 2018, p. 709–17. doi:10.1007/978-3-319-53556-2.
- [190] Hokamoto K, Izuma T, Fujita M. New Explosive Welding Technique to Weld Aluminum Alloy and Stainless Steel Plates Using a Stainless Steel Intermediate Plate. *Metall Trans A* 1993;24A:2289–97.
- [191] Calderon PD, Walmsley DR, Munir ZA. Investigation of Diffusion Welding of Pure and Alloyed Aluminum To Type 316 Stainless Steel. *Weld J (Miami, Fla)* 1985;64.
- [192] Ghosh M, Bhanumurthy K, Kale G., Krishnan J, Chatterjee S. Diffusion bonding of titanium to 304 stainless steel. *J Nucl Mater* 2003;322:235–41. doi:10.1016/j.jnucmat.2003.07.004.
- [193] Kapil A, Sharma A. Magnetic pulse welding: An efficient and environmentally friendly multi-material joining technique. *J Clean Prod* 2015;100:35–58. doi:10.1016/j.jclepro.2015.03.042.
- [194] Racineux G, Manogaran AP, Pereira D, Miranda RM. Dissimilar Welding Using Spot Magnetic Pulse Welding. *Adv. Intell. Syst. Comput.*, vol. 280, 2014, p. 525–31. doi:10.1007/978-3-642-55182-6\_45.
- [195] Pereira D, Oliveira JP, Pardal T, Miranda RM, Santos TG. Magnetic pulse welding: machine optimisation for aluminium tubular joints production. *Sci Technol Weld Join* 2018;23:172–9. doi:10.1080/13621718.2017.1355425.
- [196] Muralimohan CH, Muthupandi V, Sivaprasad K. Properties of Friction Welding Titanium-stainless Steel Joints with a Nickel Interlayer. *Procedia Mater Sci* 2014;5:1120–9. doi:10.1016/j.mspro.2014.07.406.
- [197] Li P, Li J, Xiong J, Zhang F, Raza SH. Diffusion bonding titanium to stainless steel using Nb/Cu/Ni multi-interlayer. *Mater Charact* 2012;68:82–7. doi:10.1016/j.matchar.2012.03.016.
- [198] Cheepu M, Ashfaq M, Muthupandi V. A New Approach for Using Interlayer and Analysis of the Friction Welding of Titanium to Stainless Steel. *Trans Indian Inst Met* 2017;70:2591–600. doi:10.1007/s12666-017-1114-x.
- [199] Srivastava N, Upadhyay A, Kumar S, Diva, Singh J, Agarwal A. Explosive Welding of SS304 and Al6061 Using Copper as Interlayer – Development of Trial Methodology and its Optimisation. *Mater Sci Forum* 2015;830–831:306–9. doi:10.4028/www.scientific.net/MSF.830-831.306.
- [200] Saida K, Song W, Nishimoto K. Diode laser brazing of aluminium alloy to steels with aluminium filler metal. *Sci Technol Weld Join* 2005;10:227–35. doi:10.1179/174329305X37060.
- [201] Miao YG, Han DF, Yao JZ, Li F. Microstructure and interface characteristics of laser penetration brazed magnesium alloy and steel. *Sci Technol Weld Join* 2010;15:97–103. doi:10.1179/136217109X12518083193676.
- [202] Donst D, Abels P, Ungers M, Klocke F, Kaieler S. On-line quality control system for laser brazing. *Proc 28th Int Congr Appl Laser Electro Opt* 2009.
- [203] Ungers M, Fecker D, Frank S, Donst D, Märgner V, Abels P, et al. In-situ quality monitoring during laser brazing. *Phys Procedia* 2010;5:493–503. doi:10.1016/j.phpro.2010.08.077.
- [204] Grimm A, Schmidt M. Possibilities for online process monitoring at laser brazing based on two dimensional detector systems. *ICALEO 2009*:537–44.

- [205] Koltsov A, Bailly N, Cretteur L. Wetting and laser brazing of Zn-coated steel products by Cu–Si filler metal. *J Mater Sci* 2010;45:2118–25. doi:10.1007/s10853-009-3949-y.
- [206] Zhu G, Sun G, Li G, Cheng A, Li Q. Modeling for CFRP structures subjected to quasi-static crushing. *Compos Struct* 2018;184:41–55. doi:10.1016/j.compstruct.2017.09.001.
- [207] Hosen MA, Jumaat MZ, Alengaram UJ, Ramli Sulong NH. CFRP strips for enhancing flexural performance of RC beams by SNSM strengthening technique. *Constr Build Mater* 2018;165:28–44. doi:10.1016/j.conbuildmat.2017.12.052.
- [208] Rabinovitch O, Frostig Y. Experiments and analytical comparison of RC beams strengthened with CFRP composites 2003;34:663–77. doi:10.1016/S1359-8368(03)00090-8.
- [209] Sarasini F, Tirillò J, D’Altilia S, Valente T, Santulli C, Touchard F, et al. Damage tolerance of carbon/flax hybrid composites subjected to low velocity impact. *Compos Part B Eng* 2016;91:144–53. doi:10.1016/j.compositesb.2016.01.050.
- [210] Wang S-X, Wu L-Z, Ma L. Low-velocity impact and residual tensile strength analysis to carbon fiber composite laminates. *Mater Des* 2010;31:118–25. doi:10.1016/j.matdes.2009.07.003.
- [211] Cantwell WJ, Morton J. Geometrical effects in the low velocity impact response of CFRP. *Compos Struct* 1989;12:39–59. doi:10.1016/0263-8223(89)90043-3.
- [212] Lee HY, Jung WT, Chung W. Flexural strengthening of reinforced concrete beams with pre-stressed near surface mounted CFRP systems. *Compos Struct* 2017;163:1–12. doi:10.1016/j.compstruct.2016.12.044.
- [213] Brönnimann R, Nellen PM, Sennhauser U. Application and reliability of a fiber optical surveillance system for a stay cable bridge. *Smart Mater Struct* 1998;7:229–36. doi:10.1088/0964-1726/7/2/010.
- [214] Zhu P, Ai P, Zhou Y, Xu L, Fan H. Structural analyses of extruded CFRP tendon-anchor system and applications in thin-walled aluminum/CFRP bridge. *Thin-Walled Struct* 2018;127:556–73. doi:10.1016/j.tws.2018.02.029.
- [215] Rebel G, Verreet R, Ridge IM. Lightweight ropes for lifting applications. *OIPEEC Conf Proc* 2006;1:33–54.
- [216] Wang X, Wu G, Wu Z, Dong Z, Xie Q. Evaluation of prestressed basalt fiber and hybrid fiber reinforced polymer tendons under marine environment. *Mater Des* 2014;64:721–8. doi:10.1016/j.matdes.2014.07.064.
- [217] Silva LV da, Silva FW da, Tarpani JR, Forte MM de C, Amico SC. Ageing effect on the tensile behavior of pultruded CFRP rods. *Mater Des* 2016;110:245–54. doi:10.1016/j.matdes.2016.07.139.
- [218] Mironenko A, Sukhorukov V. Non-destructive testing of steel wire ropes in Russia. *Insight Non-Destructive Test Cond Monit* 1998;40:395–7.
- [219] Gholizadeh S. A review of non-destructive testing methods of composite materials. *Procedia Struct Integ* 2016;1:50–7. doi:10.1016/j.prostr.2016.02.008.
- [220] Schmieder A, Heinze T, Michael M. Failure Analysis of High-Strength Fiber Ropes. *Mater Sci Forum* 2015;825–826:891–8. doi:10.4028/www.scientific.net/MSF.825-826.891.
- [221] Smyl, D., Antin, K-N, Bossuyt, S. & Dong L. Coupled digital image correlation and quasi-static elasticity imaging of inhomogeneous orthotropic composite structures. *Inverse Probl* 2018.

- [222] Antin KN, Harhanen L, Bossuyt S. Damage detection in CFRP components using DIC. *Conf. Proc. Soc. Exp. Mech. Ser.*, vol. 3, 2016, p. 57–62. doi:10.1007/978-3-319-22446-6\_7.
- [223] Schumacher D, Antin K-N, Zscherpel U, Vilaça P. Application of Different X-ray Techniques to Improve In-Service Carbon Fiber Reinforced Rope Inspection. *J Nondestruct Eval* 2017;36:62. doi:10.1007/s10921-017-0441-5.
- [224] Irving PE, Thiagarajan C. Fatigue damage characterization in carbon fibre composite materials using an electrical potential technique. *Smart Mater Struct* 1998;7:456–66. doi:10.1088/0964-1726/7/4/004.
- [225] Rebel G, Chaplin CR, Groves-Kirkby C, Ridge IML. Condition monitoring techniques for fibre mooring ropes. *Insight Non-Destructive Test Cond Monit* 2000;42:384–90.
- [226] Benmokrane B, Ali AH, Mohamed HM, Robert M, ElSafty A. Durability Performance and Service Life of CFCC Tendons Exposed to Elevated Temperature and Alkaline Environment. *J Compos Constr* 2016;20:04015043. doi:10.1061/(ASCE)CC.1943-5614.0000606.
- [227] Meola C, Boccardi S, Carlomagno GM, Boffa ND, Monaco E, Ricci F. Nondestructive evaluation of carbon fibre reinforced composites with infrared thermography and ultrasonics. *Compos Struct* 2015;134:845–53. doi:10.1016/j.compstruct.2015.08.119.
- [228] Emery TR, Dulieu-Barton JM. Thermoelastic Stress Analysis of damage mechanisms in composite materials. *Compos Part A Appl Sci Manuf* 2010;41:1729–42. doi:10.1016/j.compositesa.2009.08.015.
- [229] Freire J. L. F., Waugh RC, Fruehmann R, Dulieu-Barton JM. Using Thermoelastic Stress Analysis to Detect Damaged and Hot Spot Areas in Structural Components. *J Mech Eng Autom* 2015;5:1–23. doi:10.17265/2159-5275/2015.11.005.
- [230] Ashizawa T, Mizutani Y, Toyama N, Todoroki A, Suzuki Y. Numerical analysis and experimental observation of ultrasonic wave propagation in CFRP with curved fibers. *Compos Struct* 2018;194. doi:10.1016/j.compstruct.2018.03.089.
- [231] Raiutis R, Kays R, Ukauskas E, Maeika L, Vladiauskas A. Application of ultrasonic guided waves for non-destructive testing of defective CFRP rods with multiple delaminations. *NDT E Int* 2010;43:416–24. doi:10.1016/j.ndteint.2010.04.001.
- [232] Feng B, Ribeiro AL, Ramos HG. A new method to detect delamination in composites using chirp-excited Lamb wave and wavelet analysis. *NDT E Int* 2018;100:64–73. doi:10.1016/j.ndteint.2018.08.004.
- [233] Mukherjee S, Tamburrino A, Haq M, Udpa S, Udpa L. Far field microwave NDE of composite structures using time reversal mirror. *NDT E Int* 2018;93:7–17. doi:10.1016/j.ndteint.2017.09.008.
- [234] Park JB, Okabe T, Takeda N, Curtin WA. Electromechanical modeling of unidirectional CFRP composites under tensile loading condition. *Compos Part A Appl Sci Manuf* 2002;33:267–75. doi:10.1016/S1359-835X(01)00097-5.
- [235] Kupke M, Schulte K, Schüler R. Non-destructive testing of FRP by d.c. and a.c. electrical methods. *Compos Sci Technol* 2001;61:837–47. doi:10.1016/S0266-3538(00)00180-9.
- [236] Todoroki A. Monitoring of electric conductance and delamination of CFRP using multiple electric potential measurements. *Adv Compos Mater* 2014;23:179–93. doi:10.1080/09243046.2013.844900.
- [237] Abry J., Choi Y., Chateauminois A, Dalloz B, Giraud G, Salvia M. In-situ monitoring of damage in

- CFRP laminates by means of AC and DC measurements. *Compos Sci Technol* 2001;61:855–64. doi:10.1016/S0266-3538(00)00181-0.
- [238] Almeida G, Gonzalez J, Rosado L, Vilaça P, Santos TG. Advances in NDT and materials characterization by eddy currents. *Procedia CIRP* 2013;7:359–64. doi:10.1016/j.procir.2013.05.061.
- [239] Cheng J, Qiu J, Xu X, Ji H, Takagi T, Uchimoto T. Research advances in eddy current testing for maintenance of carbon fiber reinforced plastic composites. *Int J Appl Electromagn Mech* 2016;51:261–84. doi:10.3233/JAE-150168.
- [240] Heuer H, Schulze M, Pooch M, Gäbler S, Nocke A, Bardl G, et al. Review on quality assurance along the CFRP value chain – Non-destructive testing of fabrics, preforms and CFRP by HF radio wave techniques. *Compos Part B Eng* 2015;77:494–501. doi:10.1016/j.compositesb.2015.03.022.
- [241] Mizukami K, Mizutani Y, Kimura K, Sato A, Todoroki A, Suzuki Y, et al. Visualization and size estimation of fiber waviness in multidirectional CFRP laminates using eddy current imaging. *Compos Part A Appl Sci Manuf* 2016;90:261–70. doi:10.1016/j.compositesa.2016.07.008.
- [242] Mizukami K, Mizutani Y, Todoroki A, Suzuki Y. Detection of in-plane and out-of-plane fiber waviness in unidirectional carbon fiber reinforced composites using eddy current testing. *Compos Part B Eng* 2016;86. doi:10.1016/j.compositesb.2015.09.041.
- [243] Mizukami K, Mizutani Y, Kimura K, Sato A, Todoroki A, Suzuki Y. Detection of in-plane fiber waviness in cross-ply CFRP laminates using layer selectable eddy current method. *Compos Part A Appl Sci Manuf* 2016;82:108–18. doi:10.1016/j.compositesa.2015.11.040.
- [244] Bouloudenine A, Feliachi M, Latreche MEH. Development of circular arrayed eddy current sensor for detecting fibers orientation and in-plane fiber waviness in unidirectional CFRP. *NDT E Int* 2017;92:30–7. doi:10.1016/j.ndteint.2017.07.011.
- [245] Cheng J, Ji H, Qiu J, Takagi T, Uchimoto T, Hu N. Role of interlaminar interface on bulk conductivity and electrical anisotropy of CFRP laminates measured by eddy current method. *NDT E Int* 2014;68:1–12. doi:10.1016/j.ndteint.2014.07.001.
- [246] Xu X, Ji H, Qiu J, Cheng J, Wu Y, Takagi T. Interlaminar contact resistivity and its influence on eddy currents in carbon fiber reinforced polymer laminates. *NDT E Int* 2018;94:79–91. doi:10.1016/j.ndteint.2017.12.003.
- [247] Mook G, Lange R, Koeser O. Non-destructive characterisation of carbon-fibre-reinforced plastics by means of eddy-currents. *Compos Sci Technol* 2001;61:865–73. doi:10.1016/S0266-3538(00)00164-0.
- [248] Cheng J, Qiu J, Ji H, Wang E, Takagi T, Uchimoto T. Application of low frequency ECT method in noncontact detection and visualization of CFRP material. *Compos Part B Eng* 2017;110:141–52. doi:10.1016/j.compositesb.2016.11.018.
- [249] Gros XE, Takahashi K. Monitoring Delamination Growth In Cfrp Materials Using Eddy Currents. *Nondestruct Test Eval* 1998;15:65–82. doi:10.1080/10589759908952865.
- [250] Schmidt C, Schultz C, Weber P, Denkena B. Evaluation of eddy current testing for quality assurance and process monitoring of automated fiber placement. *Compos Part B Eng* 2014;56. doi:10.1016/j.compositesb.2013.08.061.
- [251] Ryosi A, Valentino M, Peluso G, Pepe G. Analysis of low-velocity impact damage in reinforced carbon fiber composites by HTS-SQUID magnetometers. *IEEE Trans Applied Supercond* 2001;11:1172–5. doi:10.1109/77.919557.

- [252] Placko D, Dufour I. Eddy current sensors for nondestructive inspection of graphite composite materials. *Conf Rec 1992 IEEE Ind Appl Soc Annu Meet n.d.:1676–82*. doi:10.1109/IAS.1992.244235.
- [253] Rizzo P, di Scalea FL. Acoustic emission monitoring of carbon-fiber-reinforced-polymer bridge stay cables in large-scale testing. *Exp Mech* 2001;41:282–90. doi:10.1007/BF02323146.
- [254] Kwon D-J, Kim J-H, Park S-M, Kwon I-J, DeVries KL, Park J-M. Damage sensing, mechanical and interfacial properties of resins suitable for new CFRP rope for elevator applications. *Compos Part B Eng* 2019;157:259–65. doi:10.1016/j.compositesb.2018.08.049.
- [255] Yarn testing. *Suragus Sensors & Instruments* 2018. <https://www.suragus.com> (accessed October 31, 2018).
- [256] Bardl G, Nocke A, Hübner M, Gereke T, Pooch M, Schulze M, et al. Analysis of the 3D draping behavior of carbon fiber non-crimp fabrics with eddy current technique. *Compos Part B Eng* 2018;132:49–60. doi:10.1016/j.compositesb.2017.08.007.
- [257] Fulton JP, Hedengren KH, Young JD, Filkins R, Patton TC. *Optimizing the Design of Multilayer Eddy Current Probes — A Theoretical and Experimental Study*. *Rev. Prog. Quant. Nondestruct. Eval.*, Boston, MA: Springer US; 1997, p. 973–80. doi:10.1007/978-1-4615-5947-4\_127.
- [258] Sheiretov Y, Zahn M. Design and modeling of shaped-field magnetoquasistatic sensors. *IEEE Trans Magn* 2006;42:411–21. doi:10.1109/TMAG.2005.860960.
- [259] Jin-qiang D, Yu-ting H, Hua D, Liming W, Qing S. Simulation analysis of lift off on an eddy current sensor array's output characteristics based on finite element method. *2011 Int. Conf. Electron. Commun. Control, IEEE*; 2011, p. 2280–3. doi:10.1109/ICECC.2011.6066384.
- [260] Sun Z, Cai D, Zou C, Zhang W, Chen Q. A Flexible Arrayed Eddy Current Sensor for Inspection of Hollow Axle Inner Surfaces. *Sensors* 2016;16:952. doi:10.3390/s16070952.
- [261] Sun Z, Cai D, Zou C, Zhang W, Chen Q. Design and optimization of a flexible arrayed eddy current sensor. *Meas Sci Technol* 2017;28:045105. doi:10.1088/1361-6501/aa5b76.
- [262] He Y, Chen T, Du J, Ding H, Jiao S, Li P. Temperature-compensated rosette eddy current array sensor (TC-RECA) using a novel temperature compensation method for quantitative monitoring crack in aluminum alloys. *Smart Mater Struct* 2017;26:065019. doi:10.1088/1361-665X/aa6ee6.
- [263] Rosado LS, Gonzalez JC, Santos TG, Ramos PM, Piedade M. Geometric optimization of a differential planar eddy currents probe for non-destructive testing. *Sensors Actuators A Phys* 2013;197:96–105. doi:10.1016/j.sna.2013.04.010.
- [264] Peng X, Jun H. A new eddy current sensor composed of three circumferential gradient winding coils. *2013 Seventh Int. Conf. Sens. Technol., IEEE*; 2013, p. 912–5. doi:10.1109/ICSensT.2013.6727782.
- [265] Mukhopadhyay SC. Quality inspection of electroplated materials using planar type micro-magnetic sensors with post-processing from neural network model. *IEE Proc - Sci Meas Technol* 2002;149:165–71. doi:10.1049/ip-smt:20020340.
- [266] Chen G, Zhang W, Zhang Z, Jin X, Pang W. A new rosette-like eddy current array sensor with high sensitivity for fatigue defect around bolt hole in SHM. *NDT E Int* 2018;94:70–8. doi:10.1016/j.ndteint.2017.12.001.
- [267] Chen T, He Y, Du J. A High-Sensitivity Flexible Eddy Current Array Sensor for Crack Monitoring of Welded Structures under Varying Environment. *Sensors* 2018;18:1780. doi:10.3390/s18061780.

- [268] Chen G, Zhang W, Pang W. Koch curve fractal geometry excitation probe for eddy current non-destructive testing. *Measurement* 2018;124:470–8. doi:10.1016/j.measurement.2018.04.031.
- [269] Washabaugh A, Zilberstein V, Schlicker D, Goldfine N. Absolute Electrical Property Measurements Using Conformable MWM Eddy-Current Sensors for Quantitative Materials Characterization. 15th WCNDT, Rome: 2000.
- [270] Goldfine N, Manning B, Thomas Z, Sheiretov Y, Denenberg S, Dunford T, et al. IMAGING CORROSION UNDER INSULATION AND UNDER FIREPROOFING, USING MR-MWM®-ARRAY SENSORS. 7th Middle East NDT Conf. Exhib., Manama, Kingdom of Bahrain: 2015.
- [271] Goldfine N, Grundy D, Craven C, Washabaugh A, Zilberstein V, Sheiretov Y, et al. Damage and Usage Monitoring for Vertical Flight Vehicles. Am. Helicopter Soc. 63rd Annu. Forum, Virginia Beach: 2007, p. 949–57.
- [272] Goldfine N, Denenberg S, Manning B, Thomas Z, Rushaid R Al. Modeling and Visualization for Imaging of Subsurface Damage. 7th Middle East NDT Conf. Exhib., Manama, Kingdom of Bahrain: 2015, p. 1–9.
- [273] Sheiretov Y, Grundy D, Zilberstein V, Goldfine N, Maley S. MWM-Array Sensors for In Situ Monitoring of High-Temperature Components in Power Plants. *IEEE Sens J* 2009;9:1527–36. doi:10.1109/JSEN.2009.2019335.
- [274] Nuclear Fusion Energy Thermonuclear Test Reactor for Power Generation ITER n.d. <https://enerjienstitusu.org/2014/10/10/nukleer-fuzyon-enerjisi-guc-uretimi-amacli-termonukleer-deney-reaktoru-iter/> (accessed October 10, 2018).
- [275] Oligschläger D, Lehmkuhl S, Watzlaw J, Benders S, De Boever E, Rehorn C, et al. Miniaturized multi-coil arrays for functional planar imaging with a single-sided NMR sensor. *J Magn Reson* 2015;254:10–8. doi:10.1016/j.jmr.2015.02.001.
- [276] Huang SH, Liu P, Mokasdar A, Hou L. Additive manufacturing and its societal impact: a literature review. *Int J Adv Manuf Technol* 2013;67:1191–203.
- [277] Vaezi M, Seitz H, Yang S. A review on 3D micro-additive manufacturing technologies. *Int J Adv Manuf Technol* 2013;67:1721–54. doi:10.1007/s00170-012-4605-2.
- [278] Czyzewski J, Burzynski P, Gawe K, Meisner J. Rapid prototyping of electrically conductive components using 3D printing technology. *J Mater Process Technol* 2009;209:5281–5. doi:10.1016/j.jmatprotec.2009.03.015.
- [279] Wesdyne. ELSCAN™ Pipe and Elbow Scanner 2018. <http://amdataproducts.com/manual-scanners> (accessed June 19, 2018).
- [280] Santos TG, Machado MA, Inácio PL. NOVA NDT Lab. FCT UNL 2018. <https://sites.fct.unl.pt/labndt-demi/> (accessed April 23, 2018).
- [281] Miranda RM, Gandra JP, Vilaca P, Quintino L, Santos TG. Surface modification by solid state processing. *Surf. Modif. by Solid State Process.*, 2014, p. 1–183. doi:10.1533/9780857094698.
- [282] Antin K-N, Machado MA, Santos TG, Vilaça P. Evaluation of different non-destructive testing methods to detect imperfections in unidirectional CFRP ropes (submitted). *J Non-Destructive Test* 2018.
- [283] Norm DE. Fibre-reinforced plastic composites Determination of apparent interlaminar shear strength by short-beam method (ISO 14130 : 1997) 1998;3:1–9.

- [284] ASTM standard. Standard Test Method for Impact Resistance of Flat, Rigid Plastic Specimen by Means of a Striker Impacted by a Falling Weight (Gardner Impact). ASTM Int 1996;i:1–8. doi:10.1520/D5420-10.2.
- [285] Bosch. Bosch Rexroth 2018. <https://www.boschrexroth.com/en/xc/products/product-groups/assembly-technology/topics/aluminum-profiles-solutions-components/index> (accessed June 20, 2018).
- [286] Parker. Slider bearing rodless linear actuator - LCB060 2018. <http://ph.parker.com/us/en/lcb-series-lcb060-belt-driven-slider-bearing-rodless-linear-actuator/lcb060mg01500srn> (accessed June 20, 2018).
- [287] Machado MA, Antin K-N, Rosado LS, Vilaça P, Santos TG. Contactless high-speed eddy current inspection of unidirectional carbon fiber reinforced polymer. *Compos Part B Eng* 2019;168:226–35. doi:10.1016/j.compositesb.2018.12.021.
- [288] Supermagnet. MONOLITH Block magnet 2018. [https://www.supermagnete.de/eng/block-magnets-neodymium/block-magnet-110.6mm-x-89mm-x-19.5mm-neodymium-n45-epoxy-coating\\_Q-111-89-20-E](https://www.supermagnete.de/eng/block-magnets-neodymium/block-magnet-110.6mm-x-89mm-x-19.5mm-neodymium-n45-epoxy-coating_Q-111-89-20-E) (accessed August 10, 2018).
- [289] Proto-Pasta. Magnetic iron PLA 2018. <https://www.proto-pasta.com/pages/magnetic-iron-pla> (accessed July 10, 2018).
- [290] FLUKE. Fluke Ti400 Infrared Camera 2018. <https://www.fluke.com/en-gb/product/thermal-imaging/thermal-cameras/professional-series/fluke-ti400> (accessed October 22, 2018).



# APPENDIX

## Appendix 1 – CoDeSys routine

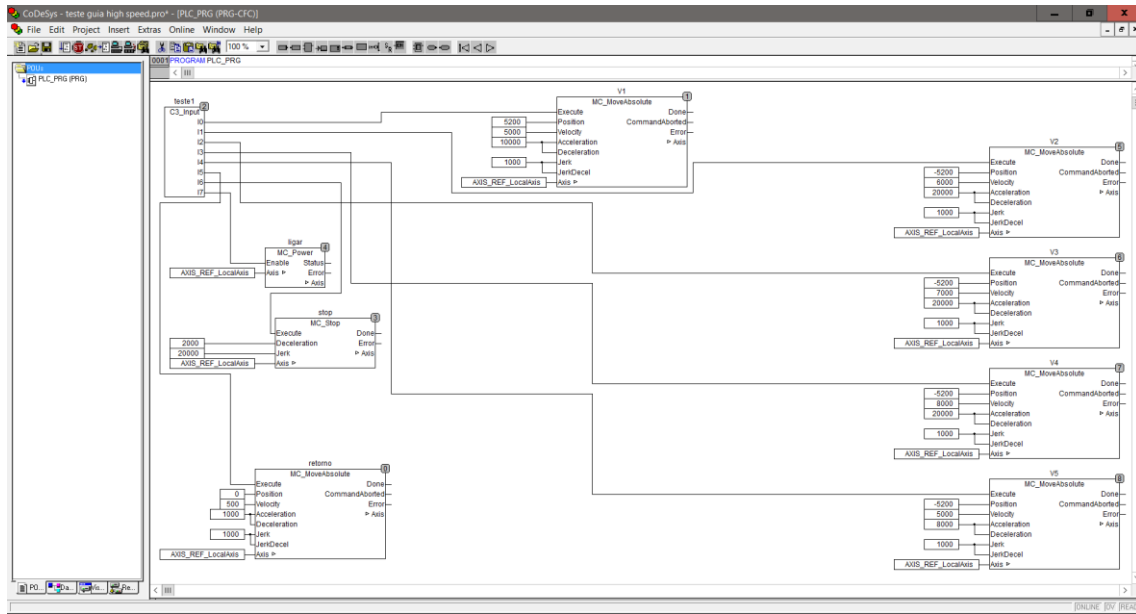


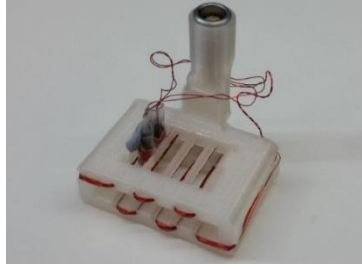
Figure A1 – CoDeSys routine programmed.

**Appendix 2 – EC tailored probes prototypes for the CFRP inspection**

Table A1 – First EC tailored probes prototypes.

Probe	Picture	
#1		
#2		
#3		
#4		
#5		

#6A



#6B



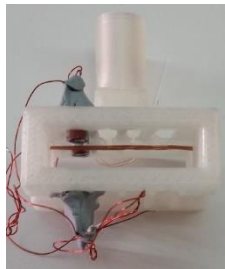
#7



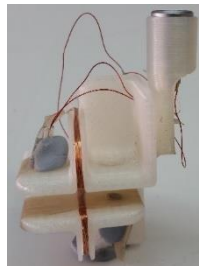
#8



#9A



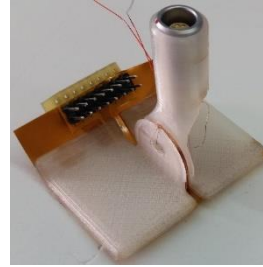
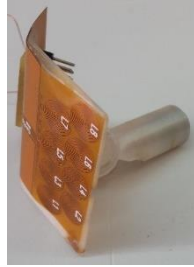
#9B



**#9C**



**#10**



Appendix 3 – EC tailored probes for the CFRP inspection numeric simulations

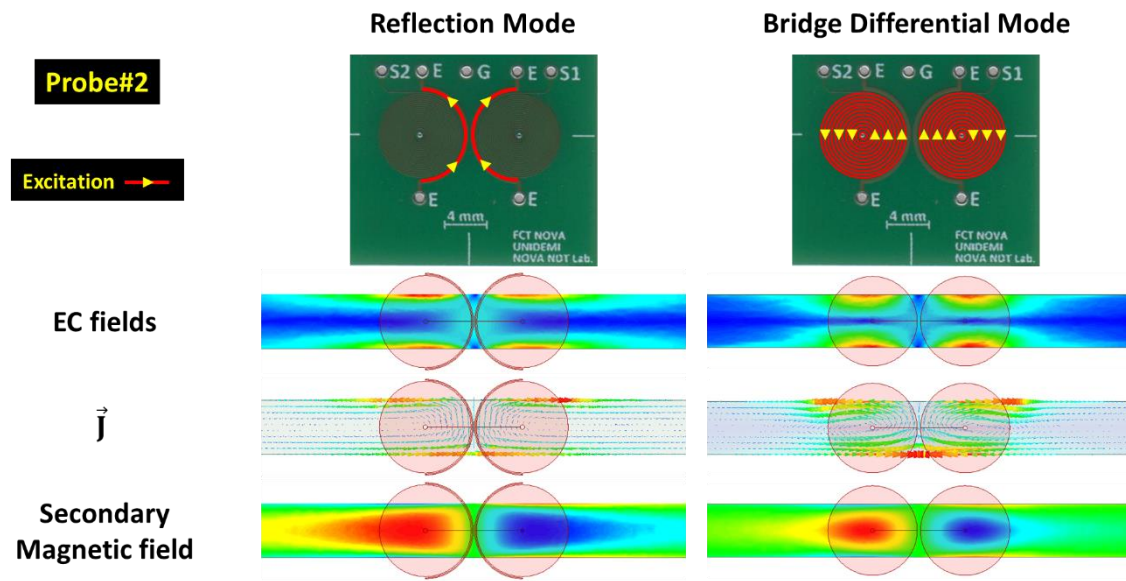


Figure A2 – PCB EC probe 2 EC density, EC vectors and secondary magnetic field for different probe operation modes.

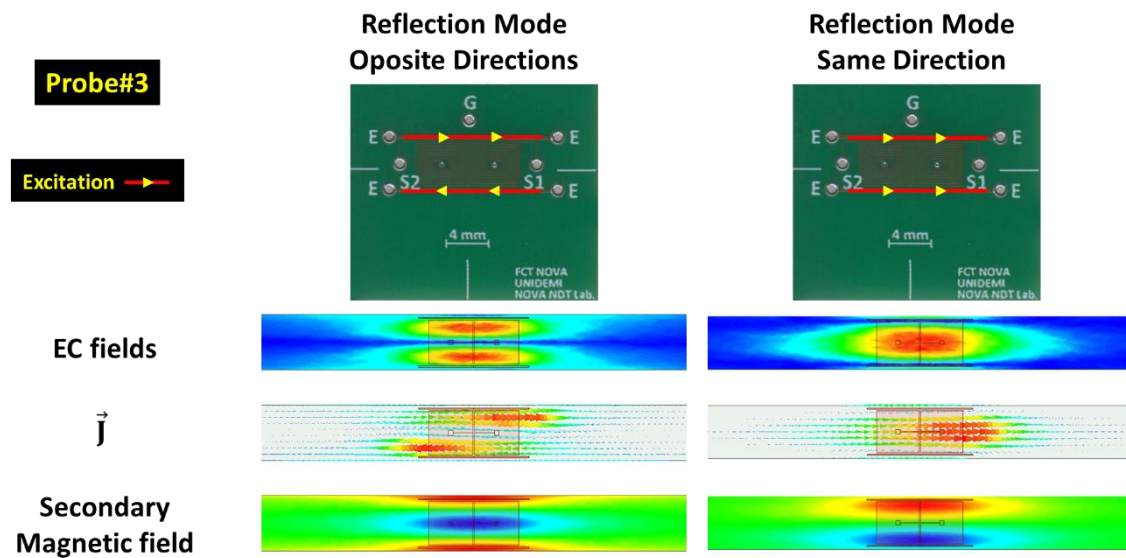


Figure A3 – PCB EC probe 3 EC density, EC vectors and secondary magnetic field for different probe operation modes.

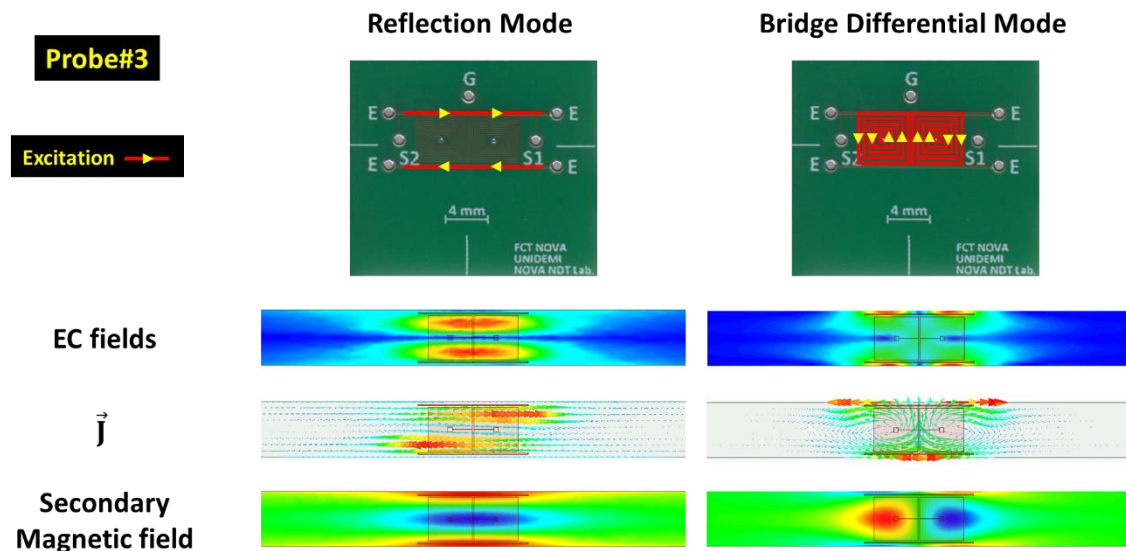


Figure A4 – PCB EC probe 3 EC density, EC vectors and secondary magnetic field for different probe operation modes.

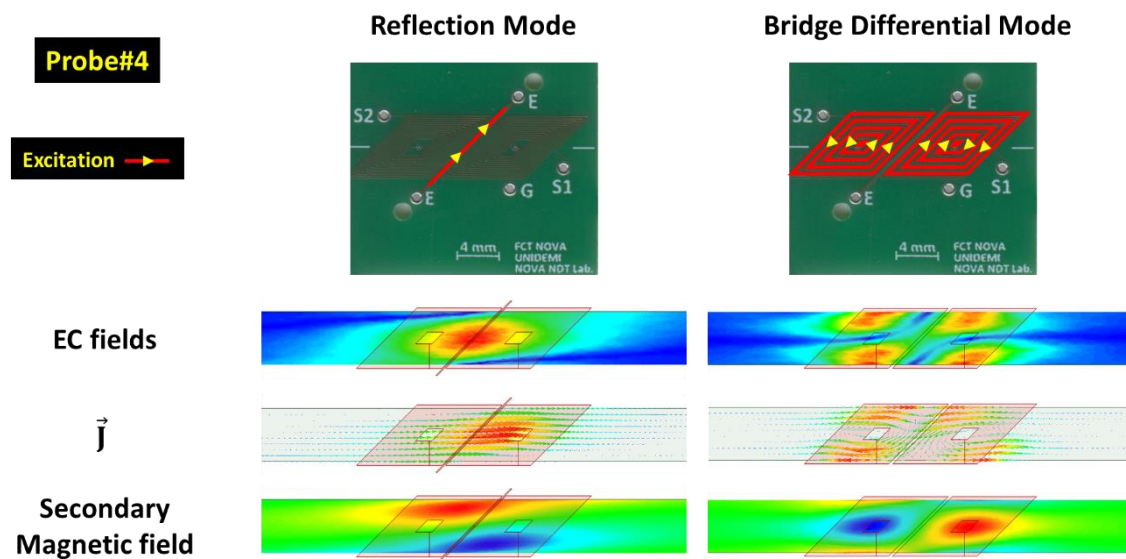


Figure A5 – PCB EC probe 4 EC density, EC vectors and secondary magnetic field for different probe operation modes.